Topics of LIGO physics: Template banks for the inspiral of precessing, compact binaries, and design of the signal-recycling cavity for Advanced LIGO

Thesis by

Yi Pan

In Partial Fulfillment of the Requirements

for the Degree of

Doctor of Philosophy

California Institute of Technology

Pasadena, California

2006

(Defended May 19, 2006)

Acknowledgements

First and foremost, I would like to thank Kip Thorne, for being a great advisor, for constant support and encouragement on my research, for stimulating discussions, and for painstakingly teaching me how to write scientific papers and give clear and well-organized presentations. I am deeply thankful to Alessandra Buonanno, Yanbei Chen and Michele Vallisneri, for inspiring collaborations that have contributed a great portion of what I have learned during my time as a graduate student, as well as 3 chapters of this thesis on the binary-inspiral project. They were not only close collaborators; they taught me a lot about compact-binary dynamics, post-Newtonian approximation, LIGO data analysis, general LIGO physics, and numerical techniques. Yanbei also taught me a great deal about quantum physics in LIGO. My special thanks go to Yanbei and Michele for sharing with me the LaTeX files of their theses, which greatly accelerated the preparation of this thesis.

I am very thankful to my former advisor, Tom Prince, for supporting my study and research for two years, and for guiding me into the exciting field of gravitational-wave physics. I am also thankful to Massimo Tinto for teaching me data analysis and for exciting collaboration on a binary-inspiral related project.

I wish to thank Theocaris Apostolatos, Leor Barack, Patrick Brady, Duncan Brown, Teviet Creighton, Curt Cutler, Johnathan Gair, and Peter Shawhan for discussions on post-Newtonian waveforms and/or data analysis issues in the binary-inspiral project.

I am very thankful to Rana Adhikari and Phil Willems for teaching me about the experimental (optical, mechanical, and thermal) physics in the gravitational-wave interferometers. I thank Guido Müller for discussing with and teaching me his design of non-degenerate recycling cavities. I especially thank Hiroaki Yamamoto for teaching me techniques of simulating optical-field propagations in gravitational-wave interferometers, and for an exciting collaboration on developing new simulation codes. I am also thankful to Biplab Bhawal, Peter Fritschel, William Kells, Malik Rakhmanov, and Stan Whitcomb for discussion on simulation and/or experimental issues in the project of the design of the signal-recycling cavity for Advanced LIGO.

In addition to the above, I would like to thank Mihai Bondarescu, Hua Fang, Shane Larson, Lee Lindblom, Geoffrey Lovelace, Ilya Mandel, and Pavlin Savov for useful discussions, and all others who attend Kip and Lee's group meeting, where I learned a lot of astrophysics and relativity through interesting discussions.

I thank Chris Mach for solving my computer problems, and I thank JoAnn Boyd, Donna Driscoll, and Shirley Hampton for helping me with administrative matters.

Finally, I would like to thank my parents Longfa and Jinglai, and my wife Rongmei. Without their love,

support, and encouragement, my accomplishments thus far would have been impossible.

Research presented in this thesis is supported by NSF grant PHY-0099568 and PHY-0601459, and NASA grant NAG5-12834.

Abstract

In the next decade, the detection of gravitational-wave signals by ground-based laser interferometric detectors (e.g., the Laser Interferometer Gravitational-Wave Observatory, or LIGO) will provide new information on the structure and dynamics of compact objects such as neutron stars (NS) and black holes (BH), both isolated and in binary systems. Efforts to detect the intrinsically weak gravitational-wave signals involve the development of high-quality detectors, the precise modeling of expected signals, and the development of efficient data analysis techniques. This thesis concerns two topics in these areas: methods to detect signals from the inspiral of precessing NS-BH and BH-BH binaries, and the design of the signal-recycling cavity for Advanced LIGO (the second generation LIGO detector).

The detection of signals from the inspiral of precessing binaries using the standard matched filter technique, is complicated by the large number (12 at least) of parameters required to describe the complex orbital-precession dynamics of the binary and the consequent modulations of the gravitational-wave signals. To extract these signals from the noisy detector output requires a discrete bank of a huge number of signal templates that cover the 12-dimensional parameter space; and processing data with all these templates requires computational power far exceeding what is available with current technology. To solve this problem, Buonanno, Chen, and Vallisneri (BCV) proposed the use of *detection template families* (DTFs) — phenomenological templates that are capable of mimicking rather accurately the inspiral waveform calculated by the post-Newtonian (PN) approach, while having a simpler functional form to reduce the computational cost. In particular, BCV proposed the so called BCV2 DTF for the precessing-binary inspiral, which has 12 parameters (most of them phenomenological). Of these, 8 are *extrinsic parameters* that can be searched over analytically, and only four of them are *intrinsic parameters* that need be searched over in a numerical one-by-one manner. The signal-matching efficiency of the BCV2 DTF has been shown to be satisfactory for signals from comparable mass BH-BH binaries.

In Chapter 2 (in collaboration with Alessandra Buonanno, Yanbei Chen, Hideyuki Tagoshi, and Michele Vallisneri), I test the signal-matching efficiency of the BCV2 DTF for signals from a wide sample of precessing BH-BH and NS-BH binaries that covers the parameter range of interest for LIGO and other ground-based gravitational-wave detectors, and I study the mapping between the physical and phenomenological parameters. My colleagues and I calculate the template-match metric, propose the template-placement strategy in the intrinsic parameter space and estimate the number of templates needed (and thus equivalently the com-

putational cost) to cover the parameter space. We also propose a so called BCV2P DTF that replaces the phenomenological parameters in the BCV2 DTF by physical parameters, which can be used to estimate the actual parameters of the binary that emitted any detected signal.

In Chapters 3 and 4 (in collaboration with Alessandra Buonanno, Yanbei Chen, and Michele Vallisneri), I investigate a *physical template family* (PTF) suggested by BCV. This PTF uses the most accurate known waveforms for inspiraling, precessing binaries (the adiabatic PN waveforms), formulated using a new *precessing convention* such that five parameters become extrinsic. PTF has the obvious advantages over the DTFs of a perfect match with target signals, a lower false-alarm rate at fixed threshold, and an ability to directly estimate the physical parameters of any detected signal.

In Chapter 3, we focus on the simpler single-spin binaries in which only four parameters out of nine remain intrinsic. We propose a two-stage scheme to search over the five extrinsic parameters quickly, and investigate the false-alarm statistics in each of the two stages. We define and calculate the metric of the full template space, and the projected metric and average metric of the intrinsic parameter subspace, and use these metrics to develop the method of template placement. Finally, we estimate that the number of templates needed to detect single-spin binary inspirals is within the reach of the current available computational power.

In Chapter 4, we generalize the use of the single-spin PTF to double-spin binaries, based on the fact that most double-spin binaries have similar dynamics to the single-spin ones. Since the PTF in this case is, strictly speaking, only quasi-physical, we test and eventually find satisfactory signal-matching performance. We also investigate, both analytically and numerically, the difference between the single-spin and double-spin dynamics, and gain an intuition into where in the parameter space the PTF works well. We estimate the number of templates needed to cover all BH-BH and NS-BH binaries of interest to ground-based detectors, which turns out to be roughly at the limit of currently available computational power. Since the PTF is not exactly physical for double-spin binaries, it introduces systematic errors in parameter estimation. We investigate these, and find that they are either comparable to or overwhelmed by statistical errors, for events with moderate signal-to-noise ratio. BCV and I are currently systematically investigating parameter estimation with the PTF.

The second part of this thesis concerns the design of the signal-recycling cavity for Advanced LIGO. In the planned Advanced-LIGO-detector upgrades from the first-generation LIGO, a signal-recycling mirror (SRM) is introduced at the dark output port. This SRM forms a signal-recycling cavity (SRC) with the input test masses. This signal-recycling design offers several advantages and brings new physics to LIGO. However, there is a problem in the current design of the SRC: The SRC is nearly degenerate, i.e., it does not distinguish transverse optical modes; and as a result, mode coupling due to mirror deformation will strongly reduce the optical power in the fundamental mode, and thus reduce the signal strength, which is roughly proportional to it.

In Chapter 5, I investigate this problem using a numerical simulation of the propagation of the optical field in an Advanced LIGO interferometer. I find that if the current degenerate design for the SRC is used,

there will be a serious and perhaps unattainable constraint on the magnitude of mirror deformations, in order to keep the reduction of signal-to-noise ratio below a few percent. This conclusion is consistent with previous order of magnitude estimates. This constraint poses practical difficulties on the quality of mirror polishing and the control of thermal aberration of the mirrors. Based on my simulation results, for a range of degeneracies of the SRC, I find the optimal level of degeneracy, which minimizes the reduction of signal-to-noise ratio. That optimum is nearly non-degenerate. I also discuss possible modifications to the current design that can achieve this optimal degeneracy.

Contents

List of Figures

List of Tables

Chapter 1

Introduction

After decades of planning and development, an international network of first-generation laser interferometric gravitational-wave detectors, consisting of LIGO [1], VIRGO [2], GEO600 [3], and TAMA300 [4] has begun scientific operation. In 2005, LIGO, the leading detector system in the network, reached its design sensitivity and started its fifth science run (S5) with the goal of collecting one year of scientific data in which all three LIGO interferometers are operating in their science mode. Data analysis has been done (by the LIGO Scientific Collaboration, LSC [5]) for previous science runs (S1, S2, S3 and S4) with shorter durations and lower sensitivity [6], to gain experience and insights for the challenging S5 data-analysis task. Although no detection has been made, the upper-limit results have entered the astrophysically interesting domain (e.g., Ref. [7]).

The detection and observation of gravitational waves will provide us a unique tool to study the physics of strong gravity experimentally, and open up a new "window" to observe the universe. We are at the exciting stage of creating "gravitational-wave astronomy," with the *analysis* of the S5 data from the first generation of LIGO, and the *planning* of future generations of LIGO detectors. This thesis presents research that deals with one topic from each of these issues: analysis and planning.

- *Detecting gravitational-waves from precessing, compact binaries with interferometric gravitational-wave detectors.* Detecting gravitational-waves from a precessing, compact binary (one made from black holes and/or neutron stars) is complicated by the large number of parameters needed to describe the waveform and the consequent huge computational cost to find the gravitational-wave signal in the noisy LIGO output. Section 1.1.2 and Chapter 2 describe research on the so called BCV2 detection template family, which uses approximate waveforms with simpler functional forms, and has been implemented in the LIGO data-analysis pipeline for the S3 and S4 data. Section 1.1.3 and Chapter 3 propose and investigate a physical template family that uses the exact physical waveforms for a special configuration of precessing binaries, and they describe a method to reduce greatly the computational costs associated with these physical waveforms. Section 1.1.4 and Chapter 4 generalize this physical template family to cover the general precessing binary signals targeted by LIGO. The implementation of this new template family in the data-analysis pipeline is ongoing. All my work on this topic is in

	NS-NS	NS-BH	BH-BH in field	BH-BH in clusters
Event rate in our galaxy ($\mathrm{yr}^{-}1$)	10^{-6}–5×10^{-4}	$\lesssim 10^{-7}$–10^{-4}	$\lesssim 10^{-7}$–10^{-5}	$\sim 10^{-6}$–10^{-5}
Visible range of LIGO	20Mpc	43Mpc	100Mpc	100Mpc
Event rate of LIGO ($\mathrm{yr}^{-}1$)	3×10^{-4}–0.3	$\lesssim 4\times10^{-4}$–0.6	$\lesssim 4\times10^{-3}$–0.6	$\sim$ 0.04–0.6
Visible range of Advanced LIGO	300Mpc	650Mpc	$z = 0.4$	$z = 0.4$
Event rate of Advanced LIGO ($\mathrm{yr}^{-}1$)	1–100	$\lesssim$ 1–1500	$\lesssim$ 30–4000	$\sim$ 300–4000

Table 1.1: Event rate estimates of binary inspirals ($\sim 1.4M_\odot$ for NS and $\sim 10M_\odot$ for BH) for LIGO and Advanced LIGO (broadband configuration) complied by Cutler and Thorne [10]

collaboration with Alessandra Buonanno (now at University of Maryland), Yanbei Chen (now at the AEI, Germany), and Michele Vallisneri (now at JPL), and for Chapter 2 also with Hideyuki Tagoshi (now with the TAMA project in Japan).

- *Analysis and design of a nondegenerate signal-recycling cavity in Advanced LIGO.* In Advanced LIGO [8] (the next generation of LIGO) a signal-recycling mirror is introduced at the dark output port and forms a signal-recycling cavity with the input test masses. This signal-recycling design offers several advantages and brings new physics to LIGO, but there is a flaw in the current design: The signal recycling cavity is very degenerate, so a tiny mirror deformation in the cavity will strongly deform the phase fronts of the light, and ultimately reduce the output signal-to-noise ratio. Section 1.2 and Chapter 5 describe an investigation of the reduction of signal-to-noise ratio (SNR) due to mirror figure error in the current Advanced LIGO design with its degenerate signal-recycling cavity, and prescribe possible solutions to fix this problem.

1.1 Detecting precessing, compact binaries with interferometric gravitational-wave detectors

The inspiral of a binary made from compact objects, neutron stars (NS), or black holes (BH) is among the most promising sources for ground-based laser interferometeric gravitational-wave detectors. Table 1.1 shows a brief summary [10] of estimates of inspiral event rates for the initial and advanced LIGO detectors.

The early inspiral of these binaries is well described by the Post-Newtonian (PN) approximation [9], and the orbits of these binaries are well circularized by gravitational radiation reaction by the time their orbital frequencies enter the initial LIGO band (40 Hz) or Advanced-LIGO band (10 Hz) [11]. The gravitational radiation reaction during the early inspiral slowly takes away orbital energy, and the binary is approximated to evolve on an adiabatic sequence of shrinking circular orbits. The gravitational waves generated by these systems have the feature of a *chirp*, which is periodic with increasing amplitude and frequency on a timescale much longer than a wave period.

These chirp waveforms are buried deep inside the overwhelming LIGO or Advanced LIGO noise. They

can be detected most efficiently by *matched filtering*, in which the interferometer output is correlated with theoretical signal templates, and a high correlation indicates a high probability of detection, i.e., of a true signal in the output resembling the template waveform. We should search over the entire parameter space of the template waveforms to find the maximum correlation. This is done with a discrete bank of templates that covers the parameter space, and we need to keep the number of templates below a limit set by the available computational power. This method relies on our capability to calculate theoretical waveforms that faithfully represent the physical gravitational waveforms radiated by inspirals of compact binaries. As NS-NS binaries pass through the LIGO frequency band, they are in their early inspiral stage, so the PN approximation can be trusted to model accurately the inspiral waveforms. For this reason, the PN templates have been implemented as the templates in the LIGO Scientific Collaboration's (LSC's) searches for waves from NS-NS binaries.

BH-BH binaries, by contrast, enter the LIGO band in their late inspiral stage, when the BHs are being accelerated to relativistic orbital velocities, and the orbit is shrinking into the strong gravity region. As a result, general relativistic effects strongly influence the binary evolution and complicate the matched-filter-based data analysis in the following ways:

(i) For spinning binaries, spin-orbit and spin-spin coupling cause the binary orbit to change its orientation (precess) on a timescale between those of the orbital motion and of the inspiral [13], producing complicated modulations of the inspiral waveforms [14, 15]. To describe such modulated waveforms, in general 12 parameter are required, which makes the matched-filter search over the template bank computationally extremely expensive.

(ii) As the relativistic effects get stronger, the adiabatic approximation breaks down and the PN approximation does not converge properly. Several techniques have been suggested to improve the convergence, but they have resulted in very different waveforms for the same physical situation. Therefore, no known theoretical waveforms can be trusted as faithful representations of the physical signals. (Recent exciting developments in *Numerical Relativity* [16], may lead, in a few years, to accurate numerically generated waveforms for these binaries.)

The late-stage inspiral of BH-BH binaries is very important for LIGO, since the gravitational waves in this stage are much stronger than in the early inspiral of lower-mass NS-NS binaries, and LIGO is therefore able to see BH-BH binaries to farther distances (recall that the event rate is proportional to the visible volume which scales as the cube of the distance). A quantitative example is shown in Figure 1.7 of Ref. [18]: for nonspinning binaries with comparable masses, the volume that Initial LIGO can survey is maximized for binaries with total mass around $35M_{\odot}$, and the volume is about 200 times that for $(1.4 + 1.4)M_{\odot}$ NS-NS binaries. In Table 1.1, we can see that NS-BH and BH-BH binaries are estimated to contribute the most significant event rate for LIGO and Advanced LIGO in compact binary inspiral sources.

This importance of BH-BH binaries forces us to confront the two difficulties, (i) and (ii), that complicate their data analysis. In the next section, 1.1.1, I will describe early work on solving the difficulties, work that forms the basis for research presented in this thesis.

1.1.1 Detecting high-mass BH-BH binaries with nonphysical template families

The second difficulty (relativistic effects invalidating the PN approximation) has been solved by Buonanno, Chen, and Vallisneri (BCV) for *nonspinning* BH-BH binaries in Ref. [19]. This solution is based on a nonphysical waveform that captures the common essential features of all existing theoretical waveforms while remaining flexible enough to match their different features by adjusting a set of nonphysical parameters. These waveforms have the following form in the frequency domain:

$$\tilde{h}(f) = f^{-7/6}(1 - \alpha f^{2/3})\Theta(f_{\rm cut} - f) \exp\left[i\left(2\pi f t_0 + \phi_0 + \psi_0 f^{-5/3} + \psi_{3/2} f^{-2/3}\right)\right]. \tag{1.1}$$

Here in the amplitude, α is a parameter used to fit the deviation from the Newtonian amplitude $f^{-7/6}$ and $f_{\rm cut}$ is a parameter used to terminate the waveform at the frequency where the adiabatic inspiral ends and the BHs begin to plunge toward each other; $\Theta(x)$ is the step function, i.e., it is 1 when $x > 0$ and 0 when $x < 0$. In the phase of $\tilde{h}(f)$, besides the time of arrival t_0 of the signal and the initial phase ϕ_0, there are two PN terms: the leading-order Newtonian term $\psi_0 f^{-5/3}$ and the 1.5PN correction $\psi_{3/2} f^{-2/3}$ (for the reasons BCV use only these two terms, see Section VI F of Ref. [19]). It has been shown [19] that this family of templates has high overlap with most theoretical signal waveforms from the inspiral of nonspinning BH-BH binaries; the *fitting factor* FF, (i.e., the overlap achievable by the template family for a target model) in this case is ≥ 0.96 for most well-behaved target signal models, which means the reduction of signal-to-noise ratio from using this family is no greater than $1 - 0.96 = 4\%$. Since this template family can mimic a wide variety of waveforms, it is plausible that it can also mimic the true signal. However, because we lack knowledge of the true possible signals, even if we can detect the signals, this family of templates is not good for parameter estimation. We refer to this kind of nonphysical template family as a *Detection Template Family* (DTF); and the particular DTF given in Eq. (1.1) is called the BCV DTF. The BCV DTF has been implemented and used in the standard search for nonspinning BH-BH binaries in LIGO data analysis.

What interests us most for this thesis is the fact that the computational cost associated with the BCV DTF is relatively low. There are six parameters, but three of them can be maximized over analytically: t_0, ϕ_0, and α. In particular, ϕ_0 and α are easily handled because they are essentially constant coefficients that linearly combine waveforms, and t_0 is handled with the *fast Fourier transform* (FFT) algorithm. This leaves us with only three parameters, ψ_0, $\psi_{3/2}$, and $f_{\rm cut}$, to search over in a one-by-one manner with a bank of templates, i.e., we need to lay down the template bank to cover only a 3-dimensional parameter space and it turns out that for initial LIGO we need only a few thousand templates, which is well manageable. We refer to parameters like t_0, ϕ_0, and α that can be searched over analytically as the *extrinsic parameters*, and those like ψ_0, $\psi_{3/2}$, and $f_{\rm cut}$ that have to be searched over numerically with a bank of templates as the *intrinsic parameters*. The reason for these names is that, usually but not always, intrinsic parameters are those that specify the physical configuration of the binary, while extrinsic parameters are those that specify the signal's initial conditions in time or the geometrical relation between the binary and the detector. By definition, extrinsic parameters

add little computational load to the data-analysis task, while the number of intrinsic parameters roughly determines the computational cost.

Now we turn to difficulty (i) (Sec. 1.1), waveform modulation due to spin-orbit and spin-spin coupling. This is the focus of Chapters 2–4. For spinning BH-BH or NS-BH binaries, self-consistent theoretical waveforms are only available up to the adiabatic 2PN order. The spin-orbit and spin-spin coupling first appear at 1.5PN and 2PN orders, respectively, where they induce precessions of the orbital plane and of the BH spins. Without other versions of waveforms for comparison, I take the adiabatic 2PN waveform to be my fiducial physical signal waveform for the inspiral of precessing binaries throughout this thesis.

Apostolatos, Cutler, Sussman, and Thorne (ACST) gave a (leading order) physical picture of the evolution and waveforms of precessing binaries in Ref. [14]. For the special cases (which we refer to as the *ACST configurations*) where only one compact object is spinning, or where the two objects have the same masses and with spin-spin coupling ignored, ACST gave a semi-analytical solution for the evolution of the binaries. They found that the direction of the total angular momentum $\mathbf{J}$ is roughly constant in space, while its amplitude shrinks slowly on the radiation reaction timescale; the orbital angular momentum $\mathbf{L}$ and the total spin $\mathbf{S}$ precess around $\mathbf{J}$ with shrinking $\mathbf{L}$ and with constant angle between $\mathbf{L}$ and $\mathbf{S}$. They called this picture *simple precession* and gave an analytical expression for the precession frequency of $\mathbf{L}$ and $\mathbf{S}$ around $\mathbf{J} = \mathbf{L}+\mathbf{S}$, which simplifies to a power law in orbital frequency in the limits $|\mathbf{L}| \ll |\mathbf{S}|$ and $|\mathbf{L}| \gg |\mathbf{S}|$:

$$f_{\rm precess} = \mathcal{B} f_{\rm orbit}^{-p} \,. \tag{1.2}$$

Here $p = 1$ or $2/3$ depending on which of the two limits the binary configuration is in. Apostolatos [17] suggested a DTF in which a phase modulation of the form

$$\Psi_{\rm mod} = C \cos(\mathcal{B} f^{-p} + \delta) \tag{1.3}$$

was introduced into the nonspinning binary waveform, based on the assumption that the leading-order modulation effect to the waveform has the same frequency as that of the precession. This is generally referred to as the *Apostolatos ansatz*. Unfortunately, this DTF is not very successful. The simple modification [Eq. (1.3)] to the nonspinning template cannot give a satisfactory overlap (correlation) with precessing waveforms (e.g., the FF for $(10 + 1.4)M_\odot$ NS-BH binaries on average is only $\simeq 0.8$), and even worse, three new intrinsic parameters C, $\mathcal{B}$, and δ are introduced, resulting in a several-orders-of-magnitude increase in the number of templates needed to cover the three new dimensions of the intrinsic-parameter space, which far exceeds the capacity of available computational power.

Buonanno, Chen, and Vallisneri (BCV), based on a better understanding of the precession effects, introduced a new *precessing convention* for writing the waveform. This new convention led BCV to introduce

another DTF to search for these precessing inspiral waveforms [20]. This DTF is given as

$$\begin{aligned}\tilde{h}(f) &= f^{-7/6}\Theta(f_{\rm cut}-f)\left[(C_1+iC_2)+(C_3+iC_4)\cos(\mathcal{B}f^{-2/3})+(C_5+iC_6)\sin(\mathcal{B}f^{-2/3})\right]\\ &\quad\times\exp\left[i\left(2\pi f t_0+\phi_0+\psi_0 f^{-5/3}+\psi_{3/2}f^{-2/3}\right)\right]. \end{aligned} \tag{1.4}$$

The only difference from the nonspinning BCV1 DTF [Eq. (1.1)] is that the correction to the Newtonian amplitude $(1-\alpha f^{2/3})$ is replaced by a complex amplitude consisting of a linear combination of six terms that include one version of the Apostolatos ansatz ($\mathcal{B}f^{-2/3}$), with combination coefficients $C_1\cdots C_6$. This complex amplitude produces amplitude and phase modulations into the waveform that mimic the effects of the orbit precession. At first glance, this DTF has 12 parameters: t_0, ϕ_0, $C_1\cdots C_6$, $f_{\rm cut}$, $\mathcal{B}$, ψ_0, and $\psi_{3/2}$, but in fact only the last four are intrinsic, and the computational cost turns out to be reasonable. The cleverness of this new DTF was its embodiment of the precessing effect in the extrinsic parameters $C_1\cdots C_6$. Since more extrinsic parameters ($C_1\cdots C_6$) are included to fit the precession-induced modulation, it has been shown [20] that this DTF has very high FF, on average ≥ 0.97 for spinning binary BHs with comparable masses and total mass in the range 6–30$M_\odot$, and $\simeq 0.93$ for $(10+1.4)M_\odot$ spinning NS-BH binaries. This DTF is now referred to as the BCV2 or spinBCV DTF.

The next section summarizes my follow-up research on the BCV2 DTF as presented in Chapter 2. In this research (performed jointly with BCV and Tagoshi), I have (i) produced a better understanding of the good performance of the BCV2 DTF, (ii) suggested a modified BCV2P DTF parameterized with physical parameters, (iii) tested the performance of the BCV2 DTF on asymmetric-mass-ratio compact binaries, (iv) scoped out the region of the nonphysical BCV2 parameters needed for a template-based search, (v) evaluated the template-match metric, (vi) discussed the template-placement strategy, and (vii) estimated the number of templates needed for search at the initial LIGO design sensitivity. All this work has led to the implementation of the BCV2 DTF into the LIGO data-analysis pipeline and its use in the LSC's searches for waves from spinning compact binaries starting with S3, the third science run.

1.1.2 Detecting precessing, compact binaries with the BCV2 detection template family [Chapter 2]

In Chapter 2 we begin by investigating a phenomenon seen by BCV in Ref. [20]. For waves from precessing binaries, BCV computed the best match with the BCV2 DTF and also the BCV2 parameters where this best match is achieved. They found that the value of the parameter $\mathcal{B}$ that gives the best match has a strong correlation with $\kappa \equiv \hat{\mathbf{L}}\cdot\hat{\mathbf{S}}$ (the inner-product between the directions of the orbital angular momentum and the total spin). In Eq. (1.4), we can see that $\mathcal{B}$ is a parameter that characterizes the frequency of the orbital precession, so this correlation means that the BCV2 template that best matches the target signal does capture a physical feature of the binary system: The precession frequency depends strongly on κ. What makes this especially interesting is that this correlation between $\mathcal{B}$ and κ is not one-to-one, and we explain this

phenomenon in detail in Chapter 2. It turns out that the explanation also gives a reason why the BCV2 DTF works so well. Following these improved insights on fitting the precession effects, we suggest a new DTF in which $\mathcal{B}$ is replaced by physical parameters of the binary. Since ψ_0 and $\psi_{3/2}$ can be replaced by physical parameters as well, we end up with a DTF parameterized completely by four intrinsic physical parameters. From this new DTF, which we refer to as the BCV2P DTF, we get not only high FFs but also estimates of the physical parameters for any detected waves.

When BCV first proposed the BCV2 DTF in Ref. [20], they tested it for precessing BH-BH binaries with total mass in the range of 6–30$M_\odot$ and comparable component masses, and for a single mass configuration $(10 + 1.4)M_\odot$ representing NS-BH binaries. In all cases, they found a good signal-matching efficiency (FF> 0.9). In Chapter 2, we extend this test to binary systems with component masses $(m_1, m_2) \in [6, 12]M_\odot \times [1, 3]M_\odot$, i.e., systems with an asymmetric mass ratio, so there is a large number of orbit and precession cycles and lower FFs are expected. The performance of the BCV2 DTF turns out to be good again, with the typical FF between 0.94 and 0.98.

Since the BCV2 DTF is parametrized by phenomenological parameters, we need to know what range of them to cover with a bank of templates in order to detect physical waveforms emitted by binaries with a realistic range of component masses. In testing the performance of the BCV2 DTF, we look for the template that best matches the target signal. This gives us the projection of target signals into the parameter space of the BCV2 DTF, and thence (by a large-scale computation of such projections), the range of parameters needed for a template-based search. In Chapter 2, we identify these ranges. We prescribe such regions for both comparable mass and asymmetric-mass-ratio BH-BH binaries and NS-BH binaries.

The next task is the placement of a discrete bank of templates that covers the parameter ranges. The correlation between the bank's neighboring templates should be larger than a certain threshold set by the desired minimum loss of SNR due to template discreteness, while the total number of templates should be as small as possible to save computational cost. The conventional method of template placement is based on Owen's *template-match metric* [21]: since the correlation between neighboring templates drops quadratically at leading order with increasing difference in parameters, a metric is naturally defined on the parameter space and the proper distance between two templates is thus the difference between their correlation (FF) and unity. In principle, the templates can be placed on a mesh formed by integral curves of the eigenvector fields of the metric, with proper distance between neighboring templates equal to the preset threshold; i.e., locally the templates can be placed on an n-dimensional (assuming n intrinsic parameters) cubic lattice (measured by the metric). A single such mesh might not exist smoothly throughout the entire parameter range we choose, but meshes can be found locally everywhere and patched together.

There is yet another subtlety with the metric. Since we need the template-bank placement only in the intrinsic-parameter subspace, we should use the *projected metric* of the subspace, not the full metric of the entire parameter space. However, the projected metric depends on the extrinsic parameters (i.e., full metrics with different extrinsic parameters and the same intrinsic parameters have different projections in the intrinsic-

parameter space). Therefore, at a given point in the intrinsic-parameter space, we have to use either a most conservative metric that gives equal or larger proper distance than all projected metrics at this point, or some sort of averaged projected metric. This issue is investigated in detail in Chapter 3. In Chapter 2, we simply choose the most conservative projected metric.

The full and projected metrics can be given analytically for the BCV2 DTF, while the most conservative projected metric has to be computed numerically by random sampling over the extrinsic-parameter subspace. Fortunately, the metric is independent of the intrinsic parameters ψ_0 and $\psi_{3/2}$, as they only appear linearly in the phase of the waveform. The intrinsic parameter $f_{\rm cut}$ cannot be properly described by a metric (because it characterizes a discontinuity in the waveform), but it is not very important for the sources targeted by the BCV2 DTF anyway, so we leave it to be specially handled after the main template-placement task and assume for the moment that it takes a fixed value of 400Hz. Thus, the metric depends only on one intrinsic parameter $\mathcal{B}$, and all we need to do is to determine the $\mathcal{B}$ distance between slices in the ψ_0-$\psi_{3/2}$ dimensions and place templates uniformly on each slice.

The proper volume of the parameter region we choose is given by the integral of the square root of the determinant of the metric, and the proper volume each template occupies is given by the cube of the proper distance between neighboring templates. From the proper volume per template, we can estimate the number of templates needed to cover the parameter range we choose. We require the correlation (FF) between neighboring templates to be at least 0.97. The resulting numbers of templates for comparable mass BH-BH binaries is computed in Chapter 2 to be 8×10^4, and for asymmetric-mass-ratio binaries it is 7×10^5. The larger number is roughly at the limit of the LSC's current computational power.

Although the BCV2 DTF has a high FF with target signals (precessing waveforms), and requires a computational cost that we can handle, there are two major shortcomings of using a DTF instead of a template family based on physically parametrized waveforms. First, we do not get a direct estimate of the physical parameters of detected binaries. Second, and more crucially, since the BCV2 DTF uses a family of very flexible phenomenological waveforms to get a good match to the complicated precessing signal waveforms, it also has a higher chance to match a random segment of noise than would a physical template family. This increases its false alarm rate. To keep a certain false alarm rate (say, one per year), we have to increase the threshold for detection, which reduces significantly or might even cancel the gain of FF that BCV2 DTF offers [20].

The main difficulty in using physical waveforms as templates is the huge computational cost associated with the large number of parameters. Nevertheless, in building the BCV2 DTF, Buonanno, Chen, and Vallisneri [20] made most of the parameters extrinsic to save computational cost, and they also proposed a possible way to do the same thing for the physical waveforms by reparameterizing them. In Chapter 3 and 4 of this thesis, I present my work (with BCV) on a new physical template family based on this re-parameterization. Naturally, we refer to this template family as the *physical template family* (PTF), in contrast to the DTF. The next two sections summarize Chapters 3 and 4.

1.1.3 Detecting single-spin precessing, compact binaries with the physical template family [Chapter 3]

In this section and Chapter 3, we start the building of a physical template family for spinning binary inspirals with a simpler but very important binary configuration: a binary where only one of the compact objects has significant spin. In astrophysical terms, this includes BH-BH binaries with only one BH spinning, and NS-BH binaries where the NS spin is generally expected to be small.

The observed gravitational waveform from a compact-binary inspiral is conventionally expressed as

$$h(t) = F_+(t)h_+(t) + F_\times(t)h_\times(t)\,. \tag{1.5}$$

Here $h_+(t)$ and $h_\times(t)$ are gravitational-wave fields in the "plus" and "cross" polarization in the "radiation reference frame" defined by the direction to the source and the source's instantaneous orbital plane, and $F_+(t)$ and $F_\times(t)$ are the so called *detector beam-pattern* coefficients that account for the projection from the radiation frame to the detector frame (Eq. (28) of Ref. [20]). For nonprecessing binaries, the orbital plane is fixed in space, and F_+ and $F_\times$ are constants in time, while for spinning, precessing binaries, they become time dependent. The beam-pattern coefficients F_+ and $F_\times$ depend on the geometrical parameters describing the direction of the source and the initial inclination of the orbit (as well as the subsequent orbital dynaics), and the waveform $h(t)$ in the LIGO output thus also depends on all these parameters. For single-spin binaries, the total number of parameters is 9, and the estimated number of templates needed far exceeds the LSC's computational capabilities.

This does not mean that matched filtering with physical waveforms is impossible. In Ref. [20], BCV introduced a new convention to express the leading-order mass-quadrupole gravitational waveform generated by inspiral of a spinning binary. Using this convention, the response of a ground-based interferometric detector to the GW signal is given by (adopting Einstein's summation convention on $i, j = 1, 2, 3$)

$$h = \underbrace{-\frac{2\mu}{D}\frac{M}{r}\Big([\mathbf{e}_+]^{ij}\,\cos 2(\Phi+\Phi_0) + [\mathbf{e}_\times]^{ij}\,\sin 2(\Phi+\Phi_0)\Big)}_{\text{factor Q: wave generation}}\underbrace{\Big([\mathbf{T}_+]_{ij}\,F_+ + [\mathbf{T}_\times]_{ij}\,F_\times\Big)}_{\text{factor P: detector projection}}\,. \tag{1.6}$$

Here the factor Q is the second time derivative of the mass-quadrupole moment of the binary, the factor P is the projection from the initial source frame (defined by the initial orbital plane) to the detector frame, $[\mathbf{e}_+]^{ij}$ and $[\mathbf{e}_\times]^{ij}$ are a basis for *symmetric trace free* (STF) tensors in the precessing orbital plane, and $[\mathbf{T}_+]_{ij}$ and $[\mathbf{T}_\times]_{ij}$ are a basis for STF tensors in the transverse plane of the GW propagation.

In this convention, all orbit precession information is contained in the $[\mathbf{e}_+]^{ij}$ and $[\mathbf{e}_\times]^{ij}$ tensors. As a result, the factor P is constant in time and collects terms that depend only on geometrical parameters, while the factor Q collects all dynamical terms describing the generation of the GWs. The geometrical parameters are thus separated from the dynamical terms. Since both Q and P are 3-dimensional STF tensors, they each

has five independent components, so decomposed into orthogonal STF tensor basis, the waveform is given by

$$h = Q^I(t; M, \eta, \chi, \kappa; t_0, \Phi_0) P_I(\Theta, \varphi, \alpha) \qquad I = 1, 2, \cdots, 5 \ . \tag{1.7}$$

Here Q^I depends on four intrinsic parameters (total mass M, mass ratio η, dimensionless magnitude of the single spin $\chi \equiv |\mathbf{S}_1|/m_1^2$, and $\kappa \equiv \hat{\mathbf{L}} \cdot \hat{\mathbf{S}}_1$) and two extrinsic parameters (time of arrival t_0 and initial phase Φ_0). By contrast, P_I depends on just three extrinsic parameters (direction of the detector seen in the source frame Θ and φ, and polarization angle of the detector α). See Secs. 3.3 and 3.4 for detailed definitions of these parameters. This waveform is in the linear combination form (linear combination of five time-dependent terms $Q^I(t)$ with coefficients P_I) that we have met in the BCV and BCV2 DTF, so here as there the maximization over the coefficients (P_I) is almost trivial. Although t_0 and Φ_0 appear in Q^I, maximization over them can be carried out analytically in the same way as for the BCV and BCV2 DTFs. Therefore, after this re-parameterization of the precessing waveform, we end up with only four intrinsic parameters that need to be searched over with a discrete bank of templates.

There is, however, a subtlety in the maximization over the P_I coefficients. Since the five components of P_I depend only on three parameters, they are not independent; i.e., P_I is a vector confined to a 3-dimensional hyper-surface in the 5-dimensional vector space. Thus, we need to add some constraints in the maximization over P_I, and the maximization over Θ and φ has to be done numerically. This does not mean, however, that Θ and φ become intrinsic parameters, because this numerical maximization is not template based, i.e., the overlaps between $Q^I(t)$ and the detector output are not affected by it. Moreover, we find physical arguments and evidence in our simulations that an unconstrained maximization over P_I works fairly well, and we can use the unconstrained maximization result as an initial condition to trigger the constrained maximization. This two-stage search scheme is suggested and tested (for efficiency) in Section 3.5. In that section, we also investigate the unconstrained and constrained false-alarm statistics by simulations, assuming stationary Gaussian detector noise. These simulations should be repeated with real LIGO noise when designing the two-stage search scheme for real data analysis.

For the physical templates, we do not need to test the signal-matching efficiency (which is always perfect by definition, though there remains the issue of the accuracy of the 2PN approximation used to compute the physical waveform). Nor do we need to worry about the false-alarm rate, as it is determined by the physical properties of the signal and the noise. The key problems in building the physical template family are the template-placement strategy and the number of templates (i.e., the computational cost).

In Section 3.6, we describe in detail the definition of, and the method to compute, the full metric (in the entire parameter space), the projected metric (in the intrinsic-parameter subspace but depending on extrinsic parameters), and the average metric (in the intrinsic-parameter subspace and independent of extrinsic parameters). The average metric we define has a direct connection with the loss of SNR due to template discreteness.

Our analysis in Sec. 3.6 reveals that the average metric is near singular for single-spin binaries. In other words, there is strong degeneracy in the intrinsic parameters, i.e., certain combinations of the parameters have almost no effect on the waveform. For instance, if we start with a central target signal with certain parameters, and follow the integral curve of the eigenvector that corresponds to the smallest eigenvalue of the metric to another point in the parameter space, the mismatch between the signal at this point and the central target signal will be small. We call such eigenvectors the *null parameter directions* and such curves the *null curves*. We did several tests starting from points somewhere in the middle of the parameter space, and followed the null curves until the match (FF) between the waveforms with parameters of the point on the null curve and of the starting point droped down to 0.99. We found that the 0.99 match is reached near the boundary of the parameter space in the χ-κ section (these two parameters are clearly bounded between 0 to 1 and -1 to 1). This means that in template placement, where we usually require a minimum 0.97 match (FF) between neighboring templates, we can ignore the *null dimension* along the null curve, i.e., we need to place only one template along this null dimension. We call this fact *dimensional reduction*. Since we have four intrinsic parameters in the physical template family, after dimensional reduction, in principle, we need to place templates to cover only a three-dimensional parameter space, which greatly simplifies the problem.

In previous template-placement tasks with DTFs (or physical template families for low-mass binaries), the LSC has met metrics that are either constants in the parameter space (e.g., the BCV DTF metric), or at worst depend only on one parameter (e.g., the BCV2 DTF metric depending on $\mathcal{B}$); so the LSC has no mature method for dealing with the template-placement problem in two parameter dimensions or higher with a general metric. In a two-dimensional space, it in principle is possible to get a constant metric in the entire space by a clever transformation of parameters, while in three or higher dimensions, this is possible only locally.

The actual placement of the physical templates is under investigation now, with a focus on two issues:

(i) What is the null dimension (which depends on all intrinsic parameters), in the parameter space?

(ii) How should we place templates in the 3-dimensional space after dimensional reduction?

Finally, in Sec. 3.6, assuming successful dimensional reduction, and successful template placement on local cubic lattices that cover the entire parameter space, we estimate the number of templates needed for the PTF family. For BH-BH or NS-BH binaries with component masses $(m_1, m_2) \in [7, 12]M_\odot \times [1, 3]M_\odot$, we estimate that the number of physical templates needed is ~76,000, with minimum match between neighboring templates 0.98 (assuming dimensional reduction costs 0.01 of the match). About 90% of the templates come from the parameter region with $m_2 = 1M_\odot$, i.e., the small-η region. For each template, we need to take five overlaps between the $Q^I(t)$ factors and the detector output, and thus the computational cost is roughly 5 times the cost of a nonspinning template. As a result, the computational cost corresponds to roughly the cost for a bank of $\sim 10^5$ nonspinning templates, which is at the limit of the LSC's currently available computational power.

Instead of using the physical templates directly and along for detection and parameter estimation, it

is widely expected, in the LSC, to use the physical templates as the second step in a hierarchical search, following a first-stage BCV2 DTF search. This will reduce the BCV2 false-alarm rate and produce good estimates of physical parameters, while saving computational cost.

In the next section, I introduce our work to generalize this PTF from single-spin binary inspirals to general precessing binary inspirals.

1.1.4 Detecting general precessing, compact binaries with a quasi-physical template family [Chapter 4]

In Sec. 1.1.1, we defined two ACST configurations for spinning binaries: single-spin binaries and equal-mass binaries with the 2PN spin-spin coupling ignored. In fact, at 2PN order, an equal-mass binary (no spin-spin coupling) has effectively the same dynamics as a single-spin binary with the same masses and single spin equal to the total spin of the equal-mass binary [14] (for this effective single-spin binary, the dimensionless spin parameter $\chi \equiv$ spin angular momentum/mass^2 could take a nonphysical value between 1 and 2, which does not affect the data analysis). For binaries with mass ranges of interest to ground-based interferometers, the spin-spin effects contribute only mildly to the binary dynamics, even close to the last stable orbit. Therefore the PTF we proposed for single-spin binaries can also be used as the PTF for equal-mass binaries.

Since the single-spin PTF works well for both asymmetric-mass-ratio binaries (approximately single-spin configuration) and comparable-mass-ratio binaries (approximately equal-mass configuration), we conjecture that it works also for binaries with an intermediate mass ratio, as a *quasi-physical template family*, which we will also loosely abbreviate as "PTF."

In Sec. 4.3.2, we test the efficiency of the PTF on binaries with component masses $(m_1, m_2) \in [3, 15]M_\odot \times [3, 15]M_\odot$, and find satisfactory performance (see Table 4.1 and Figure 4.1). These test results verify that the spin-spin effects can be safely ignored. They also show that the worst performance of the PTF is on low mass binaries with an intermediate mass ratio, such as $(6 + 3)M_\odot$ binaries, for which the average fit is still higher than 0.98. Since the PTF is not exactly physical for such systems, we study the projection of the target signal into the physical parameter space of the PTF. We find that the physical parameters that maximize the overlap spread moderately in the parameter space, around the true signal parameters. We propose a range of parameters to do template-based searches.

In Section 4.3.4, we study the precessional dynamics of double-spin binaries, for the purpose of better understanding the matching performance of the quasi-physical template family. In Ref. [22], Apostolatos investigated the effects of spin-spin coupling on the dynamical evolution of equal-mass, equal-spin BH-BH binaries, and found that the spin-spin interaction, besides slightly changing the precession frequency and orbital inclination, causes a *nutation*, i.e., an oscillation of the orbital inclination angle. We also study the effect of mass-difference perturbations on equal-mass binaries, and find, at the leading order, that the

change in the evolution equations is similar to that caused by spin-spin effects, and the mass difference causes also a nutation. When the mass difference is intermediate, although the perturbation treatment is not valid quantitatively, there is still the same qualitative feature of nutation, but it is much larger than the one caused by spin-spin interaction for the binary mass ranges considered. Based on the relative size of the nutation angle and the initial orbital inclination angle, we gain a rough intuition as to which configurations of double-spin, intermediate-mass-ratio binaries can be well matched by the quasi-physical template family.

In Sec. 4.4, we estimate the number of templates needed for these binaries in the same way as that for single-spin binaries, and get ~320,000. Again, most templates come from the small-η region and about 70% of them come from the unphysical region $\chi \in [1, 2]$.

Compared with the BCV2 DTF, among other advantages, this quasi-physical template family has the possibility of estimating the signal parameters. Although this template family is parameterized by physical parameters (not always in physical ranges), since it is not exactly physical, systematic bias and error in parameter estimation are introduced. We investigate these systematic effects in Section 4.5. The *chirp mass* $\mathcal{M} \equiv M\eta^{3/5}$ that determines the leading-order radiation-reaction timescale is always estimated much better than other parameters; its systematic bias and error are 0.01% and 1%. For the mass ratio η, they are both around 5%. We also suggest parameter combinations containing the spin parameters (magnitude and direction) that may be estimated with less systematic bias and error than the individual spin parameters χ_1 and χ_2 themselves. However, since the metric is near singular and the null directions have large components along the spin-parameter dimensions, we expect that (at least for moderate signal-to-noise ratio) the statistical errors will always dominate over systematic effects.

1.2 Analysis and design of nondegenerate signal-recycling cavity in Advanced LIGO [Chapter 5]

The upgrading of the initial LIGO interferometers to the next-generation Advanced LIGO interferometers is planned to begin in early 2011 (though procurement and fabrication of components will begin three years earlier in 2008). Advanced LIGO targets a design sensitivity 15 times better than initial LIGO, at which it is probable to detect a rich variety of GWs [10] (See Table 1.1 for estimated binary-inspiral event rates).

The Advanced LIGO improvements include, among others, major improvements in seismic isolation, test mass suspension, core optics, circulating laser power in the arm cavities (ACs), and most important for Chapter 5: a new "signal-recycling" mirror (SRM) at the dark output port of the interferometer (see Figure 5.1).

The position (distance from the input test mass) and reflectivity of the SRM strongly influence the resonant properties of the interferometer's coupled cavities. With different choices of these parameters, the interferometer can operate in either a *broadband*, *resonant-sideband-extraction* (RSE) configuration [23] or

a *narrowband* configuration. The Advanced LIGO baseline design [8] adopts the RSE broadband configuration, with the possibility, later, of changing the SRM parameters so as to alter the detector noise spectrum, optimizing its detection of GWs with specific frequency features.

Signal recycling is also able to circumvent the standard quantum limit (SQL) for free test masses by altering the test-mass dynamics [24].

In Chapter 5 of this thesis, I investigate a serious potential problem in the current design of the signal-recycling cavity (SRC) formed by the SRM and the input test-mass (ITM). The current SRC design has a cavity length $l \simeq 10$m, and therefore a transverse diffraction length scale $b \simeq \sqrt{\lambda L} \simeq 3$mm, which is far smaller than the 6cm light beam size in the cavity, and the SRC is consequently very degenerate (see Sec. 5.2.2 for a quantitative analysis). A degenerate cavity does not distinguish between transverse optical modes; they resonate in the cavity just as easily as the desired TEM00 mode, therefore the power in the fundamental TEM00 optical mode will be transferred, in significant amounts, to higher-order modes (HOMs) when there is mode coupling caused by perturbations in the SRC, e.g., by figure error and thermal aberration of the mirrors. Since the signal-to-noise ratio (SNR) of the detector, loosely speaking, is proportional to the amplitude of the signal light in the fundamental mode, in order to avoid serious loss of SNR, we must pose serious constraints on the deformations of the mirrors, constraints that are difficult to achieve with current technology.

In fact, the power-recycling cavity (PRC) in the initial LIGO interferometers has shown this problem severely for the local oscillator light circulating in the PRC, and this in turn reduced the signal strength. This problem was so severe that the interferometers were forced to operate with lower laser power to reduce thermal aberration of the ITMs. This problem in initial LIGO has been cured by introducing a thermal compensation system (TCS) [25] that actively corrects the surface shape of the ITMs. However, in Advanced LIGO, with much higher circulating light power, there is a worry that the TCS cannot completely correct the mirror deformation.

The effect of SRC degeneracy, in contrast to PRC degeneracy, had not been clearly investigated before this thesis. Since the GW signal light entering the SRC has different resonance conditions from the control signal light, the two have to be investigated individually. In Sec. IV J of Ref. [26], Thorne estimated using a geometrical optics approximation, that the peak-to-valley mirror surface deformations must be smaller than $\sim$1nm for the Advanced-LIGO baseline design parameters of the SRM, in order to have less than 1% loss in SNR. This is a very serious constraint for current technology.

In Chapter 5, I investigate this SRC degeneracy problem more carefully, using a numerical simulation of the light propagation in the interferometer. In particular, I describe how the simulation is set up, the numerical results, and the consequent conclusions. I deduce a constraint on the mirror deformation that is consistent with Thorne's estimate [26]. I also deduce a level of degeneracy for a near nondegenerate SRC that is optimal for reducing the loss of SNR due to mirror deformations. Finally, I discuss quantitatively two possible modifications to the current design that can achieve the optimal level of degeneracy: a mode-

matching telescope (MMT) design proposed originally for the PRC by Müller and Wise [27], and a kilometer-long SRC design.

1.3 Bibliography

[1] A. Abramovici et al., Science **256**, 325 (1992).

[2] B. Caron et al., Class. Quantum Grav. **14**, 1461 (1997).

[3] H. Lück et al., Class. Quantum Grav. **14**, 1471 (1997); B. Willke et al., Class. Quantum Grav. **19**, 1377 (2002).

[4] M. Ando et al., Phys. Rev. Lett. **86**, 3950 (2001).

[5] LIGO Scientific Collaboration, `http://www.ligo.org/` .

[6] See, e.g., LIGO Scientific Collaboration, Phys. Rev. D **69**, 082004 (2004); **69**, 102001 (2004); **69**, 122001 (2004); **69**, 122004 (2004);

[7] B.J. Owen, Phys. Rev. Lett. **95**, 211101 (2005).

[8] P. Fritshel, Proc. SPIE **4856-39**, 282 (2002).

[9] T. Damour, *300 Years of Gravitation*, S. W. Hawking and W. Isreal, eds. (Cambridge University Press, Cambridge, England, 1987); L. Blanchet, *Living Reviews in Relativity*, 2002-3 (2002), `http://www.livingreviews.org/Articles/Volume5/2002-3blanchet`.

[10] C. Cutler and K.S. Thorne, *An overview of gravitational-wave sources*, gr-qc/0204090

[11] C.W. Lincoln and C.M. Will, Phys. Rev. D **42** 1123 (1990).

[12] L.A. Wainstein and L.D. Zubakov, *Extraction of signals from noise* (Prentice-Hall, Englewood Cliffs, NJ, 1962).

[13] J.B. Hartle and K.S. Thorne, Phys. Rev. D **31**, 1815 (1984).

[14] T.A. Apostolatos, C. Cutler, G.J. Sussman and K.S. Thorne, Phys. Rev. D **49**, 6274 (1994).

[15] L.E. Kidder, Phys. Rev. D **52**, 821 (1995).

[16] F. Pretorius, Phys. Rev. Lett. **95**, 121101 (2005).

[17] T.A. Apostolatos, Phys. Rev. D **54**, 2421 (1996).

[18] Y.C. Chen *Topics of LIGO physics: Quantum noise in advanced interferometers and template banks for compact-binary inspirals*, Ph.D. thesis, California Institute of Technology, Pasadena, California, USA (2003).

[19] A. Buonanno, Y. Chen, and M. Vallisneri, Phys. Rev. D **67**, 024016 (2003).

[20] A. Buonanno, Y. Chen, and M. Vallisneri, Phys. Rev. D **67**, 104025 (2003).

[21] B.J. Owen, Phys. Rev. D **53**, 6749 (1996); B.J. Owen and B. Sathyaprakash, Phys. Rev. D **60**, 022002 (1999).

[22] T.A. Apostolatos, Phys. Rev. D **54**, 2438 (1996).

[23] J. Mizuno, K. A. Strain, P. G. Nelson, J. M. Chen, R. Schilling, A. Rüdiger, W. Winkler, and K. Danzmann, Phys. Lett. A **175**, 273 (1993).

[24] A. Buonanno, Y. Chen, Phys. Rev. D **64**, 042006 (2001).

[25] R. Lawrence, *Active wavefront correction in Laser Interferometric Gravitational Wave Detectors*, Ph.D. thesis, Massachusetts Institute of Technology, Cambridge, Massachusetts, USA (2003).

[26] E. D'Ambrosio, R. O'Shaughnessy, S. Strigin, K. S. Thorne and S. Vyatchanin, gr-qc/0409075, Submitted to Phys. Rev. D.

[27] G. Müller and S. Wise, "Mode matching in Advanced LIGO," LIGO Document Number T020026-00-D, `http://www.ligo.caltech.edu/docs/T/T020026-00.pdf`.

Chapter 2

Detecting gravitational waves from precessing binaries of spinning compact objects. II. Search implementation for low-mass binaries

Detection template families (DTFs) are built to capture the essential features of true gravitational waveforms using a small set of phenomenological waveform parameters. Buonanno, Chen, and Vallisneri [Phys. Rev. D **67**, 104025 (2003)] proposed the "BCV2" DTF to perform computationally efficient searches for signals from precessing binaries of compact stellar objects. Here we test the signal-matching performance of the BCV2 DTF for asymmetric-mass-ratio binaries, and specifically for double–black hole binaries with component masses $(m_1, m_2) \in [6, 12]M_\odot \times [1, 3]M_\odot$, and for black hole–neutron star binaries with component masses $(m_1, m_2) = (10M_\odot, 1.4M_\odot)$; we take all black holes to be maximally spinning. We find a satisfactory signal-matching performance, with fitting factors averaging between 0.94 and 0.98. We also scope out the region of BCV2 parameters needed for a template-based search, we evaluate the template-match metric, we discuss a template-placement strategy, and we estimate the number of templates needed for searches at the LIGO design sensitivity. In addition, after gaining more insight in the dynamics of spin-orbit precession, we propose a modification of the BCV2 DTF that is parametrized by *physical* (rather than phenomenological) parameters. We test this modified "BCV2P" DTF for the $(10M_\odot, 1.4M_\odot)$ black hole–neutron star system, finding a signal-matching performance comparable to the BCV2 DTF, and a reliable parameter-estimation capability for target-binary quantities such as the chirp mass and the opening angle (the angle between the black hole spin and the orbital angular momentum).

Originally published as A. Buonanno, Y. Chen, Y. Pan, H. Tagoshi, and M. Vallisneri, Phys. Rev. D **72**, 084027 (2005).

2.1 Introduction

As ground-based gravitational-wave (GW) detectors based on laser interferometry [1] approach their design sensitivities, the emphasis in data analysis is shifting from upper-limit studies [2] to proper detection searches.

In addition, the length of data-taking runs is stretching to several months, with typical duty cycles approaching unity, substantiating the need for *online* (or at least *real-time*) searches to be performed as data become available. It is then crucial to develop search algorithms that maximize the number of detections while making efficient use of computational resources.

Inspiraling binaries of black holes (BHs) and/or neutron stars (NSs) are among the most promising [3] and best-understood sources for GW interferometers, which can observe the waveforms emitted during the adiabatic phase of these inspirals, well described by post-Newtonian (PN) calculations [4]. For these signals, the search algorithms of choice are based on *matched filtering* [5], whereby the detector output is compared (*i.e.*, correlated, after noise weighting) with a *bank* of theoretically derived signal *templates*, which encompass the GW signals expected from systems with a prescribed range of physical parameters.

Reference [6] introduced the phrase "detection template families" (DTFs) to denote families of signals that capture the essential features of the true waveforms, but depend on a smaller number of parameters, either physical or phenomenological (*i.e.*, describing the waveforms rather than the sources). At their best, DTFs can reduce computational requirements while achieving essentially the same detection performance as exact templates; however, they are less adequate for upper-limit studies, because they may include non-physical signal shapes that result in increased noise-induced triggers, and for parameter estimation, because the mapping between template and binary parameters may not be one-to-one, or may magnify errors. In Ref. [6], the "BCV1" DTF was designed to span the families of nominally exact (but partially inconsistent inspiraling-binary waveforms obtained using different resummation schemes to integrate the PN equations.

A reduction in the number of waveform parameters is especially necessary when the binary components carry significant spins not aligned with the orbital angular momentum; spin-orbit and spin-spin couplings can then induce a strong precession of the orbital plane, and therefore a substantial modulation of GW amplitude and phase [7]. Detection-efficient search templates must account for these effects of spin, but a straightforward parametrization of search templates by the physical parameters that can affect precession results in intractably large template banks.

To solve this problem, several DTFs for precessing compact binaries have been proposed in the past decade [7, 8, 9, 10, 11, 12, 13]. A DTF based on the *Apostolatos ansatz* for the evolution of precession frequency was amply investigated in Refs. [11, 13], and an improved version was proposed in Ref. [12]. However, the computational resources required by the Apostolatos-type families are still prohibitive; more important, their signal-matching performance (*i.e.*, the fitting-factor FF) is not very satisfactory.

In Ref. [14], Buonanno, Chen, and Vallisneri analyzed the physics of spinning-binary precession and waveform generation, and showed that the modulational effects can be isolated in the evolution of the GW polarization tensors, which are combined with the detector's *antenna patterns* to yield its response. As a result, the response of the detector can be written as the product of a carrier signal and a complex modulation factor; the latter can be viewed an extension of the Apostolatos formula. In Ref. [14], the precessing waveforms were cast into a mathematical form (the linear combination of three simpler signals, with complex

coefficients) that allows searching automatically and economically over all the precession-related parameters, except for a single parameter $\mathcal{B}$ that describes the timescale of modulation. Henceforth, we shall refer to the template family proposed in Ref. [14] as the "BCV2" DTF.

In Ref. [14], the BCV2 DTF was tested for precessing BH-BH binaries with high total mass ($12M_\odot < M < 30M_\odot$) and comparable component masses, and for the single mass configuration $(10+1.4)M_\odot$, representative of NS–BH systems. In all cases, the signal-matching performance was good (FF > 0.9), with consistent improvements over search templates that do not include precessional effects (for instance, in the NS–BH system the FF increases from ~ 0.78 to ~ 0.93). Signals from precessing binaries with asymmetric component masses are harder to match, because they have more orbital and precessional cycles (*i.e.*, more complex waveforms) in the band of good interferometer sensitivity.

In this chapter, we extend the BCV2 performance analysis of Ref. [14] to asymmetric mass ratios, taking into consideration systems with component masses $(m_1, m_2) \in [6, 12]M_\odot \times [1, 3]M_\odot$, for which we expect a large number of precession cycles (see Fig. 2.9 below). In addition, we estimate the region of the DTF parameter space that must be included in a search for such systems; we calculate the template-match metric [15, 16, 17]; we provide a strategy for template placement; last, we estimate the number of templates required for the search. After reconsidering the Apostolatos ansatz, we are also able to shed new light on the phenomenological parameter $\mathcal{B}$ that describes the timescale of modulation; indeed, we derive an explicit formula for the evolution of the precession angle in terms of the physical parameters of the binary, and we use this formula to propose a modification of the BCV2 DTF that dispenses with $\mathcal{B}$.

While this chapter is concerned with DTFs for precessing binaries, we note that a *physical* template family for *single-spin* precessing compact binaries was proposed in Ref. [14], and thoroughly tested in Ref. [18]. The attribute "physical" is warranted because the family is obtained by integrating the PN equations [4] in the time domain, and the templates are labeled by the physical parameters of the binary. Furthermore, Ref. [19] showed that the single-spin physical family has a satisfactory signal-matching performance also for the waveforms emitted by *double-spin* precessing compact binaries, at least for component masses $(m_1, m_2) \in [3, 15]M_\odot \times [3, 15]M_\odot$; moreover, the parameters of the best-fit single-spin templates can be used to estimate the parameters of the double-spin target systems [19]. However, this physical template family may be more complicated to implement and more computationally expensive (and therefore less attractive for use in online searches) than the frequency-domain DTFs such as BCV2.

This chapter is organized as follows. In Sec. 2.2, we briefly review the BCV2 DTF and the Apostolatos ansatz, and we discuss how the phenomenological parameter $\mathcal{B}$, which describes the timescale of precession, can be related to the physical parameters of the binary. In Sec. 2.3.1, we discuss the signal-matching performance of the BCV2 DTF over a range of binary component masses. In Sec. 2.3.2, we introduce a version of the BCV2 DTF modified to include the physical evolution of the precession angle in single-spin binaries, and we test its performance for NS–BH inspirals. In Sec. 2.4.1, we compute the template-match metric for the BCV2 DTF. In Sec. 2.4.2, we provide a strategy for template placement, and we estimate the number of

templates required in a search. Last, in Sec. 2.5 we summarize our conclusions.

In the following, the binary component masses are denoted by m_1 and m_2 (with $m_1 > m_2$); the symmetric mass ratio and the total mass by $\eta = m_1 m_2/M^2$ and $M = m_1 + m_2$; the binary component spins by $\mathbf{S}_1 = \chi_1 m_1^2$ and $\mathbf{S}_2 = \chi_2 m_2^2$. For single-spin binaries, we assume $\mathbf{S}_1 = \chi m_1^2$ and $\mathbf{S}_2 = 0$. Throughout the chapter, the signal-matching performance of DTFs is evaluated against a target model for precessing binaries governed by Eqs. (6)–(32) of Ref. [18]; this target model is valid in the adiabatic phase of the inspiral, when dynamics are correctly described by PN equations. We use an analytic fit to the LIGO-I design noise spectrum (given, *e.g.*, by Eq. (28) of Ref. [6]); we adopt the standard formalism of matched-filtering GW detection; we follow the conventions of Ref. [19], which contains a useful glossary of matched-filtering notions and quantities; last, we always set $G = c = 1$.

2.2 Features of precession dynamics in single-spin binaries

2.2.1 Review of the Apostolatos ansatz and of the BCV2 DTF

Apostolatos, Cutler, Sussman, and Thorne (ACST) [7] investigated orbital precession in binaries of spinning compact objects in two special cases: (i) equal-mass binaries ($m_1 = m_2$), where the spin-spin coupling is switched off, and (ii) single-spin binaries ($S_2 = 0$). In these cases, precessional dynamics can always be categorized as *simple precession* or *transitional precession*. In simple precession, the direction of the total angular momentum $\hat{\mathbf{J}}$ is roughly constant, while the orbital angular momentum $\mathbf{L}$ and the total spin $\mathbf{S} = \mathbf{S}_1 + \mathbf{S}_2$ precess around it. ACST were able to derive an analytical solution for the evolution of simple precession (see Sec. IV of Ref. [7]). Transitional precession occurs when, during evolution, $\mathbf{L}$ and $\mathbf{S}$ have roughly the same amplitude and become nearly antialigned. When this happens, $|\mathbf{J}|$ is almost zero and $\hat{\mathbf{J}}$ can change suddenly and dramatically. Although transitional precession is too complicated for analytical treatment, it occurs rarely [14, 7], so we will ignore it in this chapter.

GW signals from generic precessing binaries are well approximated by simple-precession waveforms when the ACST assumptions are valid, which happens for two classes of binaries: (i) BH-BH binaries with comparable component masses where the spin-spin interaction can be neglected, which are equivalent to systems where a single object carries the total spin of the system; (ii) BH-NS or BH-BH binaries with very asymmetric mass ratios, which can be approximated as single-spin systems because the spin of the lighter object is necessarily small. It is not guaranteed *a priori* that simple-precession waveforms can describe also signals emitted by BH-BH binaries with intermediate mass ratios and/or important spin-spin effects. However, it was recently shown [19] that simple-precession waveforms are adequate also for these classes of binaries, although the dynamical evolution of $\mathbf{L}$ and $\mathbf{S}$ can exhibit rather different features [9].

In simple precession, $\hat{\mathbf{L}}$ and $\hat{\mathbf{S}}$ precess around $\hat{\mathbf{J}}$ (which is roughly fixed) with the precession frequency

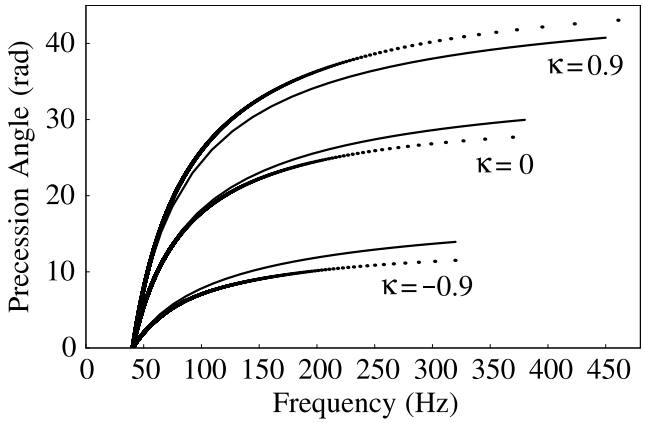

Figure 2.1: Evolution of precession angle (radians) as a function of GW frequency, for $(10+1.4)M_\odot$ binaries with opening angles $\kappa = 0.9, 0$ and -0.9. The dotted curves show the numerical evolution of our target systems, while the continuous curves follow the analytical expression (2.5).

given by Eq. (42) of Ref. [7],

$$\Omega_p \equiv \frac{d\alpha_p}{dt} = \left(2 + \frac{3m_2}{2m_1}\right)\frac{J}{r^3}\,. \tag{2.1}$$

ACST found that the evolution of the precession angle α_p can be approximated by power laws in two extreme cases. When $L \gg S$ and $J \simeq L$, using leading-order Newtonian expressions, we find

$$L = \eta M^2 (M\omega)^{-1/3}\,, \qquad r = \left(\frac{M}{\omega^2}\right)^{1/3}\,, \qquad \frac{\dot\omega}{\omega^2} = \frac{96}{5}\eta\,(M\omega)^{5/3}\,, \tag{2.2}$$

where ω is the orbital angular frequency, and r is the orbital separation, so it is straightforward to get $\alpha_p = \mathcal{B}_1 f^{-1}$; this regime corresponds to comparable-mass binaries, or to binaries at large separations (*i.e.*, in the early stages of the inspiral). When $L \ll S$ and $J \simeq S$, we have $\alpha_p = \mathcal{B}_2 f^{-2/3}$; this regime corresponds to binaries with large mass asymmetry, or to binaries at small separations (*i.e.*, in the late stages of the inspiral). The analytical expressions for the coefficients $\mathcal{B}_1$ and $\mathcal{B}_2$ are given by Eq. (45) of Ref. [7], and depend only on the masses and on the total spin of the binary, but *not* on the opening angle between the spin and the orbital angular momentum. Although the power laws were derived for simple precession under the ACST assumptions, it turns out that they can model the dynamics of more general configurations, as shown in Refs. [14, 19].

On the basis of the ACST analysis, Apostolatos [9] reasoned that GWs from precessing binaries should be modulated by the orbital precession frequency Ω_p, and suggested adding an Ω_p-dependent modulation term to the nonspinning waveform phasing,

$$\psi_{\rm spinning} \to \psi_{\rm nonspinning} + C\cos(\delta + \mathcal{B} f^{-2/3}) \tag{2.3}$$

(this is the Apostolatos ansatz). Although the resulting DTF has higher fitting factors with precessing-binary

waveforms than nonspinning DTFs, it is not completely satisfactory [9, 11], especially because of the huge computational cost implicit in adding the three parameters $C, \delta, \mathcal{B}$, which are *intrinsic* (*i.e.*, they increase the dimensionality of search template banks).

In Ref. [14], Buonanno, Chen, and Vallisneri proposed a DTF (BCV2) based on a modification of Eq. (2.3),

$$h(\psi_0, \psi_{3/2}, \mathcal{B}, f_{\rm cut}, C_k; f) = \\ f^{-7/6}\left[(C_1 + iC_2) + (C_3 + iC_4)\cos(\mathcal{B}f^{-2/3}) + (C_5 + iC_6)\sin(\mathcal{B}f^{-2/3})\right]\theta(f_{\rm cut} - f)e^{2\pi i f t_0} \times e^{i[\psi_0 f^{-5/3} + \psi_{3/2} f^{-2/3}]}\,; \tag{2.4}$$

here t_0 is the signal's time of arrival, and $f_{\rm cut}$ is the cutoff frequency; precessional effects are modeled by the modulation terms $\cos(\mathcal{B}f^{-2/3})$ and $\sin(\mathcal{B}f^{-2/3})$ in the complex amplitude, separately from the nonspinning evolution of phase. Possible modulation morphologies are enriched by the presence of the complex linear-combination coefficients $C_3 + iC_4$ and $C_5 + iC_6$, improving the efficiency of matching to target waveforms. Indeed the complex modulation terms modulate both amplitude and phase of the nonspinning signal. An important feature of the BCV2 DTF is that little computational cost is added by the search over the parameters $C_{1,\ldots,6}$, which are *extrinsic* (*i.e.*, the detection statistic can be maximized analytically over them).

Although the $f^{-2/3}$ power law adopted in the BCV2 DTF (2.4) is expected to be valid only for $S \gg L$, (*i.e.*, for binaries with asymmetric mass ratios, or in the late stages of inspiral), the DTF yields high fitting factors also for comparable-mass binaries, as verified in Ref. [14] by Monte Carlo simulation. The reason is probably to be found in the broad variety of modulation morphologies parametrized by the $\mathcal{B}$ and $C_{1,\ldots,6}$ parameters.

2.2.2 Analysis of the DTF parameter $\mathcal{B}$

In this section we relate the phenomenological precession parameter $\mathcal{B}$ to the physical parameters of the binary (the two masses, m_1, m_2, the cosine between the directions of the total spin and the orbital angular momentum, $\kappa \equiv \hat{\mathbf{L}} \cdot \hat{\mathbf{S}}$, and the magnitude of the spin, $\chi \equiv S_1/m_1^2$). In doing so, we clarify why the BCV2 DTF is capable of mimicking the precessional effects in the target signal.

In Fig. 16 of Ref. [14], the distribution of the best-fit DTF $\mathcal{B}$ is plotted against the target-system parameter κ. The target waveforms were generated at 2PN order, for BH-NS binaries of component masses $(10+1.4)M_\odot$ with maximally spinning BHs. The spread of the data points corresponds to uniform distributions of the initial spin and angular-momentum orientations. The points seem to cluster around three lines, but no explanation is offered for this interesting feature. We are now able to explain this behavior; what we learn in the process will enable us to construct an improved DTF (BCV2P) parametrized by physical parameters (see Sec. 2.3.2).

Although the best-fit DTF parameter $\mathcal{B}$ is not, strictly speaking, physical, it is clearly related to the evolution of the precession angle α_p in the target system. Moreover, we expect the best-fit $\mathcal{B}$ to be a function

of the target-system opening angle κ (as seen in Fig. 16 of Ref. [14]), except in the limits $L \gg S$ and $L \ll S$, where the power laws $\alpha_p = \mathcal{B}_1 f^{-1,-2/3}$ do not include κ. Let us see what function we should expect. From Eq. (49) of [7], we have

$$\Omega_p = \left(2 + \frac{3m_2}{2m_1}\right)\sqrt{1 + 2\kappa\gamma + \gamma^2}\,\frac{L}{r^3}\,, \tag{2.5}$$

which was obtained by expressing the total angular momentum J in Eq. (2.1) in terms of the orbital angular momentum L. In Eq. (2.5), $\gamma(t)$ denotes the quantity $S/L(t)$; the dependence of Ω_p on κ vanishes with $\gamma \gg 1$ (*i.e.*, with $L \ll S$) or $\gamma \ll 1$ (*i.e.*, with $L \gg S$). Using the leading-order Newtonian expressions for L and r given in Eq. (2.2), we can integrate Ω_p analytically and obtain α_p as a function of m_1, m_2, κ, and χ:

$$\begin{aligned}\alpha_p^N(f) \;=\; & \frac{5}{384}\frac{4m_1 + 3m_2}{m_1} \\ & \times\Big\{-A\left[(2 - 3\kappa^2)\chi_M^2 + \kappa\chi_M\, v^{-1} + 2\, v^{-2}\right] + 3\,\kappa\,(1 - \kappa^2)\chi_M^3\,\log\left[\kappa\chi_M + v^{-1} + A\right]\Big\} + \text{const.},\end{aligned} \tag{2.6}$$

where

$$v = (\pi M f)^{1/3}\,, \qquad \chi_M = \frac{m_1}{m_2}\chi\,, \qquad A = \sqrt{\chi_M^2 + 2\,\kappa\chi_M\, v^{-1} + v^{-2}}\,, \tag{2.7}$$

and where $f = \omega/\pi$. The "N" in α_p^N stands for "Newtonian." These expressions are equivalent to Eqs. (63a) and (63b) of Ref. [7]. Note that an analytical expression including higher PN corrections could also be given. However, for simplicity we prefer to restrict ourselves to the lowest order. In Fig. 2.1, for a binary of mass $(10 + 1.4)M_\odot$ and for several values of κ, we compare the analytical precession angles $\alpha_p^N(f)$ with numerical values obtained from our target models by projecting $\hat{\mathbf{L}}(f)$ onto the plane perpendicular to the vector $\hat{\mathbf{J}}$ (which is constant because we only consider simple precession), and recording the cumulative angle swept by the projected image. We see that our leading-order formula reproduces the shape of the numerically obtained curve, although the quantitative difference is appreciable. This is due to the fact that we write α_p^N at the Newtonian order; the agreement would otherwise be perfect.

We can now try to explain the dependence of the DTF parameter $\mathcal{B}$ on the parameters of the binary, and the clustering seen in Fig. 16 of Ref. [14]. Since the power laws $\mathcal{B}f^{-2/3,1}$ cannot match $\alpha_p(f)$ exactly, we establish a correspondence by requiring that the instantaneous rate of change of the two precession angles be equal at the approximate frequency of best detector sensitivity, $\sim 150\,\text{Hz}$ (appropriate for initial LIGO):

$$\frac{d}{dt}\mathcal{B}f^{-2/3} \equiv \Omega_p^t = \Omega_p^s \equiv \frac{d}{dt}\alpha_p(t)\,, \quad f = 150\,\text{Hz}\,, \tag{2.8}$$

and therefore

$$\mathcal{B} = -\frac{3}{2}f^{5/3}\left.\frac{d\alpha_p(f)}{df}\right|_{f=150Hz}\,. \tag{2.9}$$

Here Ω_p^t denotes the template's equivalent precession frequency, while Ω_p^s denotes the target's orbital precession frequency at 150 Hz. Figure 2.2 shows a test of the correspondence, performed for $(10 + 1.4)M_\odot$

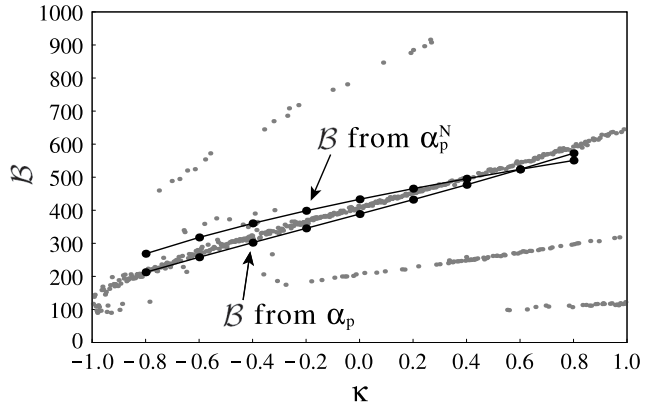

Figure 2.2: Best-fit values of the BCV2 DTF parameter $\mathcal{B}$ as a function of the target-system opening angle κ, for $(10 + 1.4)M_\odot$ binaries with uniformly distributed initial orientations of spin and angular momentum. The larger connected dots show the equivalent $\mathcal{B}$ as evaluated from Eq. (2.9) using the numerical $\alpha_p(f)$ and the analytical $\alpha_p^N(f)$, respectively.

binaries with uniformly distributed values of κ and of the initial orientations of total spin and orbital angular momentum. The small dots indicate the best-fit values of $\mathcal{B}$, similarly to Fig. 16 of Ref. [14]. The larger dots mark the pairs $(\kappa, \mathcal{B}(\kappa))$ obtained from Eq. (2.9) using the analytical $\alpha_p^N(f)$ and the numerical $\alpha_p(f)$, respectively. The pairs line up quite well with the linear cluster in the middle of Fig. 2.2, which includes the majority of data points. Thus, it is correct to state that the value of $\mathcal{B}$ represents the rate of change $\Omega_p^t = \Omega_p^s$ of the precession angle in the middle of the frequency band of good detectory sensitivity. Similar conclusions hold also for binaries with masses $(m_1, m_2) \in [6, 12]M_\odot \times [1, 3]M_\odot$. The other linear clusters seen in Fig. 2.2 correspond roughly to $2\Omega_p^t = \Omega_p^s$ and $\Omega_p^t = 2\Omega_p^s$, for reasons explained in the next section (the clusters in the lower corners, on the other hand, correspond to systems where the effects of precession on the waveforms are negligible).

[Note that there are some differences between Fig. 2.2 and Fig. 16 of Ref. [14].[1] The linear cluster identified with $\Omega_p^t = \Omega_p^s$ in Fig. 2.2 corresponds in fact to the top linear cluster in Fig. 16 of Ref. [14], and the fraction of points in this cluster is significantly larger here than there. Moreover, the top linear cluster corresponding to $\Omega_p^t = 2\Omega_p^s$ cannot be seen clearly in Fig. 16 of Ref. [14]. These differences are due to the adoption, for this chapter, of a better numerical overlap-maximization scheme, which has a better chance of finding the true global maximum overlap. We shall discuss the maximization scheme in detail in Sec. 2.3.1.]

2.2.3 Higher harmonics in templates and signals

We shall now consider why multiple clusters appear in Fig. 2.2. We shall see that the precession frequencies Ω_p^t and Ω_p^s defined in Eq. (2.8) are not usually the only modulation frequencies to appear in the spectra of the template and signal waveforms—indeed, they may not even be the dominant frequencies. It is then conceiv-

[1] In Fig. 16 of [14], the x axis refers to $\kappa_{\rm eff}/\kappa_{\rm eff}^{\rm max}$, where $\kappa_{\rm eff} = \hat{\mathbf{L}} \cdot \mathbf{S}_{\rm eff}/M^2$, with $\mathbf{S}_{\rm eff}$ defined by Eq. (7) of Ref. [14]. In the limit in which only one of the two bodies carries spin, the quantity κ used in this chapter equals $\kappa_{\rm eff}/\kappa_{\rm eff}^{\rm max}$.

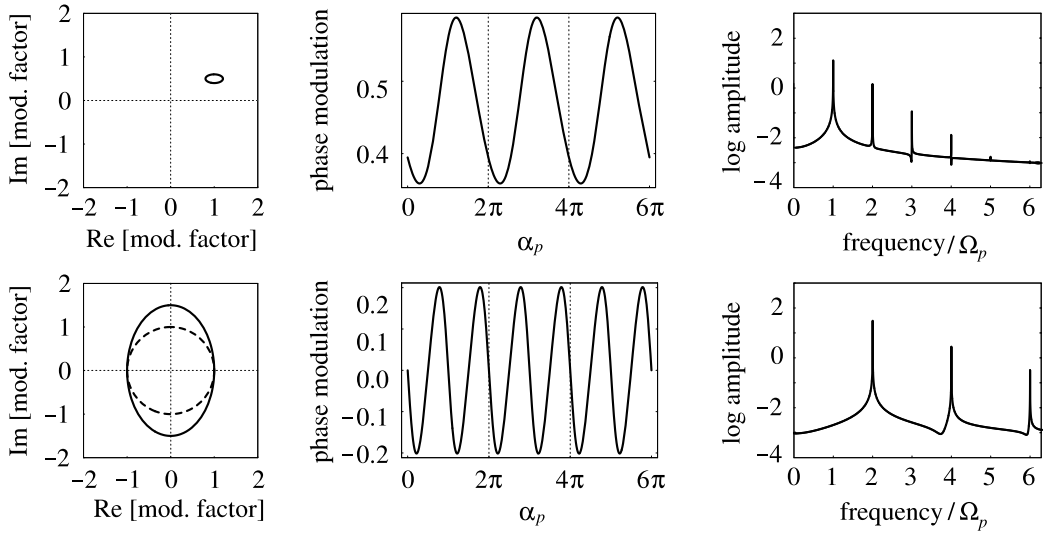

Figure 2.3: BCV2 DTF complex modulation factor, as given by Eq. (2.11). The top (bottom) row refers to a $C_{1,2}$-dominated ($\mathcal{A}_{r,i}$-dominated) choice of the modulation parameters. The left column shows the complex-plane trajectory of the modulation factor when the precession angle α_p varies between 0 and 2π; the middle column shows the oscillatory part of phase as function of α_p; the right column shows the log-amplitude of the Fourier transform of phase.

able that if different harmonics of the precession frequency dominate in the template and signal waveforms, the maximum overlaps may occur when Ω_p^t and Ω_p^s are not equal, but instead related by integer factors.

We first consider the frequency content of the BCV2 template phase modulations. As discussed above, their precession angle is $\alpha_p \equiv \mathcal{B}f^{-2/3}$, and the precession frequency Ω_p^t is given by the time derivative of α_p. Modulation effects are included by way of the complex factor

$$(C_1 + iC_2) + (C_3 + iC_4)\cos(\mathcal{B}f^{-2/3}) + (C_5 + iC_6)\sin(\mathcal{B}f^{-2/3}) \tag{2.10}$$

(with $C_{1,\ldots,6} \in \mathbb{R}$), which is clearly a periodic function of α_p, but is obviously far from a simple sinusoid with a single frequency. Recasting the factor as

$$(C_1 + iC_2) + \mathcal{A}_r\cos(\mathcal{B}f^{-2/3} + \varphi_r) + i\mathcal{A}_i\cos(\mathcal{B}f^{-2/3} + \varphi_i) \tag{2.11}$$

(with $C_{1,2}, \mathcal{A}_{r,i}, \varphi_{r,i} \in \mathbb{R}$), we see that it traces an ellipse in the complex plane as α_p varies from 0 to 2π. The shape of the ellipse is determined by $\mathcal{A}_{r,i}$ and $\varphi_{r,i}$, and the displacement of its center from the origin by $C_1 + iC_2$.

For two choices of the modulation parameters $C_{1,2}$, $\mathcal{A}_{r,i}$, and $\varphi_{r,i}$, Fig. 2.3 shows the complex-plane trajectory of the modulation factor (left panels), the oscillatory part[2] of the phase as a function of $\alpha_p \equiv \mathcal{B}f^{-2/3}$ (middle panels), and the amplitude of its Fourier transform. In the first example, we choose $C_{1,2}$ to dominate,

[2]That is, the residual obtained after fitting the total phase to the nonspinning phase $\phi_0 + 2\pi t_0 f + \psi_0 f^{-5/3} + \psi_{3/2} f^{-2/3}$.

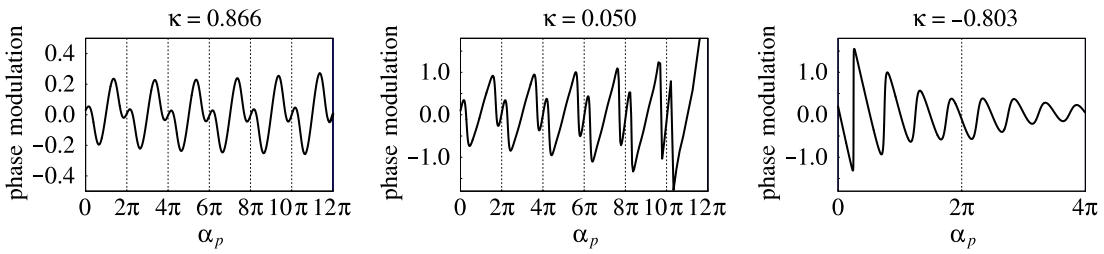

Figure 2.4: Oscillatory part of phase modulation in target waveforms for BH-NS binaries with $(m_1, m_2, \chi) = (10M_\odot, 1.4M_\odot, 1)$, and with directional parameters such that the detector line of sight is perpendicular to the initial **L**-**S** plane and to the detector plane, and that the detector is oriented along the "+" GW polarization. The three panels correspond to $\kappa = 0.866$ (for which **L** is close to $\mathbf{\Omega}_L$), $\kappa = 0.050$, and $\kappa = -0.803$ (for which **L** is perpendicular to $\mathbf{\Omega}_L$ at $f = 30$ Hz). The sharp turns observed in the second and third panels are not singularities of the phase, but happen when the projections of $\mathbf{e}_+$ and $\mathbf{e}_\times$ on the detector frame (and therefore the real and imaginary components in Eq. (2.12)) are both small, so that the phase can change very rapidly.

setting $C_1 = 1$, $C_2 = 0.5$, $\mathcal{A}_r = 0.2$, $\mathcal{A}_i = 0.1$, $\varphi_r = 0$, and $\varphi_i = \pi/2$. The phase is periodic in α_p with period 2π, and it is rather close to a single sinusoid (upper middle panel). The Fourier spectrum (upper right panel) shows that the dominant template modulation frequency Ω^t_m is the precession frequency Ω^t_p, and that the contributions from higher harmonics are at least an order of magnitude smaller.

In the second example, we choose $\mathcal{A}_{r,i}$ to dominate, setting $C_1 = 0$, $C_2 = 0$, $\mathcal{A}_r = 1$, $\mathcal{A}_i = 1.5$, $\varphi_r = 0$, and $\varphi_i = \pi/2$. In this case the modulation ellipse encloses the origin, so the phase contains a monotonic component that grows by 2π each time the modulation factor completes an orbit around the origin. It is easy to see that this monotonic component is simply α_p. The oscillatory part of the phase can be obtained from Fig. 2.3 (lower left panel) by taking the phase difference between points with the same real parts on the ellipse and on the unit circle. In this case, the phase is (almost) periodic in α_p with period π, as shown in the lower middle panel. The Fourier spectrum (lower right panel) shows clearly that the dominant frequency is $\Omega^t_m = 2\Omega^t_p$, and that there is no component at Ω^t_p or at any other odd harmonic.

Investigating other choices of the modulation parameters, we find that the Fourier spectra of the phase modulations have always their highest peaks at either Ω^t_p or $2\Omega^t_p$, depending on whether the modulation ellipse encloses the origin or not. Most of the differences between the various cases lie in the structure of harmonics above the second. For instance, if the trajectory of the complex amplitude has very large ellipticity, higher-order harmonics can become comparable to the lowest harmonic (*i.e.*, the fundamental or the second harmonic).

We now consider the frequency content of the target-waveform phase modulations. Under the *precession convention* introduced in Ref. [14], the frequency-domain expression for the waveforms, at the leading order in the stationary-phase approximation, are given by Eq. (83) of Ref. [14], or namely

$$\tilde{h}_{\rm resp}(f) = -\tilde{h}_C(f)\left\{\left[\mathbf{e}_+(t_f)\right]^{jk} + i\left[\mathbf{e}_\times(t_f)\right]^{jk}\right\} \times \left(\left[\mathbf{T}_+(t_f)\right]_{jk} F_+ + \left[\mathbf{T}_\times(t_f)\right]_{jk} F_\times\right) \quad \text{for } f > 0\,, \tag{2.12}$$

where $\tilde{h}_C(f)$ is the unmodulated carrier signal, the $\mathbf{T}_{+,\times}(t_f)$ are the detector polarization tensors in the radiation frame [see Eq.(25) of BCV2], and all precessional effects are isolated in the evolving GW polarization tensors $\mathbf{e}_{+,\times}(t_f)$. These are defined as

$$\begin{aligned} \mathbf{e}_+ &= \mathbf{e}_1 \otimes \mathbf{e}_1 - \mathbf{e}_2 \otimes \mathbf{e}_2 \,, \\ \mathbf{e}_\times &= \mathbf{e}_1 \otimes \mathbf{e}_2 + \mathbf{e}_2 \otimes \mathbf{e}_1 \,, \end{aligned} \tag{2.13}$$

where $\mathbf{e}_1$ and $\mathbf{e}_2$ form a basis in the instantaneous orbital plane. The time dependence of these polarization tensors enters the waveform through terms of the form

$$\left[\mathbf{e}_{+,\times}(t_f)\right]^{ij} \left[\mathbf{T}_{+,\times}(t_f)\right]_{ij} \,, \tag{2.14}$$

which can be approximated by $C_{+,\times}\cos(\mathcal{B}f^{2/3} + \delta_{+,\times})$, adopting the Apostolatos ansatz. However, this is only an approximation, in two distinct ways. First, the components of the polarization tensors depend quadratically on the components of the basis vectors $\mathbf{e}_{1,2}$; as a consequence, even if the basis vectors contained only oscillations with frequency Ω_p^s, the waveform would still end up with both Ω_p and $2\Omega_p$ modulations. Second, under the precession convention, the basis vectors $\mathbf{e}_{1,2}$ [and thus the quantities in Eq. (2.14)] do not really precess together with the orbital plane around $\hat{\mathbf{J}}$ with angular velocity $\mathbf{\Omega}_L = \Omega_p^s \hat{\mathbf{J}}$; instead, they precess around the component of $\mathbf{\Omega}_L$ that is orthogonal to the orbital angular momentum $\mathbf{L}$ [Eq.(72) of BCV2],

$$\mathbf{\Omega}_e(t) = \mathbf{\Omega}_L(t) - \left[\mathbf{\Omega}_L(t) \cdot \hat{\mathbf{L}}_N(t)\right] \hat{\mathbf{L}}_N(t) \,, \tag{2.15}$$

which in turn precesses together with $\mathbf{L}_N(t)$ around $\mathbf{\Omega}_L(t)$. For this reason, the oscillations in $\mathbf{e}_{1,2}$ are more complicated than simple sinusoids of frequency Ω_p^s. ACST had already observed this fact, noticing that the phase modulations are certainly due to the precessional evolution of the orbital plane, but arise also from the so-called *Thomas precession* term (see Eq. (29) of Ref. [7] and the discussion around it).

In Fig. 2.4, we show the modulation of the target-waveform phase as a functions of α_p for three binary configurations. As for the discussion of template waveforms, we consider only the oscillatory part of phase modulation. This is done here by fitting the total phase to a nonspinning phase $\phi_0 + 2\pi t_0 f + \psi_0 f^{-5/3} + \psi_{3/2} f^{-2/3}$, and taking the residual. In the first example on the left of Fig. 2.4, the phase modulation is periodic in α_p with period 2π, and it is not very different from a single sinusoid. So in this case the dominant modulation frequency is the precession frequency Ω_p^s. In the second example in the middle of Fig. 2.4, the dominant frequency is still Ω_p^s, but the $2\Omega_p^s$ component is also quite significant. In the third example on the right of Fig. 2.4, the dominant frequency is $4\Omega_p^s$. Other systems with values of κ between those used for Fig. 2.4 show similar features, sometimes with a larger number of frequency components.

So far, this discussion suggests that the phase-modulation frequencies Ω_m^t and Ω_m^s of the template and target waveforms are not always the precession frequencies Ω_p^t and Ω_p^s (which depend on $\mathcal{B}$ and on the

physical parameters of the target system, respectively), but can also be their integer multiples. In light of this, how can we understand the multiple clustering seen in Fig. 2.2? The answer is that, for a given target signal, there can be several templates whose overlap with the target is a local maximum, corresponding to different combinations of the Ω^t_p and Ω^s_p harmonics.

Suppose for example that the target waveform contains the first and second harmonics of the precession frequency, Ω^s_p and $2\Omega^s_p$; then a template with $\Omega^t_p = \Omega^s_p/2$ could match these two components with its second and fourth harmonics, a template with $\Omega^t_p = \Omega^s_p$ could match them with its first and second harmonics, while a template with $\Omega^t_p = 2\Omega^s_p$ could match only the $\Omega^s_m = 2\Omega^s_p$ component with its first harmonic. Using this reasoning, we can easily understand the existence of clusters of local maxima with $\Omega^t_p = \Omega^s_p, 2\Omega^s_p, 3\Omega^s_p, \ldots,$ and $\Omega^t_p = \Omega^s_p/2, \Omega^s_p/3, \Omega^s_p/4, \ldots$. However, if the DTF is able to reproduce the entire harmonic structure of the signal, then the local maximum with $\Omega^t_p = \Omega^s_p$ must also be the global maximum. The fact that in Fig. 2.2 we have clusters at $\Omega^t_p = \Omega^s_p/2$ and $\Omega^t_p = 2\Omega^s_p$ suggests that the BCV2 DTF cannot do this perfectly. The analysis of the best-fit template modulation parameters for the points in the $\Omega^t_p = \Omega^s_p/2$ cluster of Fig. 2.2 (extending from $\kappa \simeq -0.2$ to $\kappa \simeq 1.0$) confirms the template frequency-doubling scenario discussed in this section.

2.3 Signal-matching performance of the BCV2 and BCV2P DTFs

2.3.1 Performance of the BCV2 detection template family

The basic diagnostic of DTF signal-matching performance is the *fitting factor* FF ($0 \leq \mathrm{FF} \leq 1$), defined as the match between a given template in the target family and the templates in the DTF, *maximized* over all the parameters of the DTF. The maximization of the match induces a many-to-one *projection* between the target-signal parameters and the best-fitting DTF parameters. The way in which the maximization is carried out informs the distinction between intrinsic and extrinsic DTF parameters: Full templates must be recomputed for each value of the intrinsic parameters to be explored, while the maximum over the extrinsic parameters can be computed analytically, given a choice of the intrinsic parameters. For the BCV2 DTF, the intrinsic parameters are ψ_0, $\psi_{3/2}$, $\mathcal{B}$, and f_{cut}, and the extrinsic parameters are $\mathcal{C}_{1,\ldots,6}$ and the time of arrival t_0.

In our tests, the maximization of the match is performed by way of a *simplex*-based search [20] in the continuous space of intrinsic parameters (as opposed to the lattice-based searches used in bank-efficiency Monte Carlos): *simplex* methods have shown good efficiency in finding extrema in spaces of moderate dimensionality. In the light of the discussion of Fig. 2.2 in Sec. 2.2.2, we understand that several values of the parameter $\mathcal{B}$ may yield local maxima of the match, corresponding to multiples $\Omega^s_p/2$, Ω^s_p, and $2\Omega^s_p$ of the target-signal precession frequency. To improve the robustness of our search, we run it repeatedly, starting with different initial values of $\mathcal{B}$ (100, 200, 300, 400, 500, and 600, covering the likely range of $\mathcal{B}$), so the final FF is usually picked out from the best of a few local maxima. In addition, after each run we *restart* the

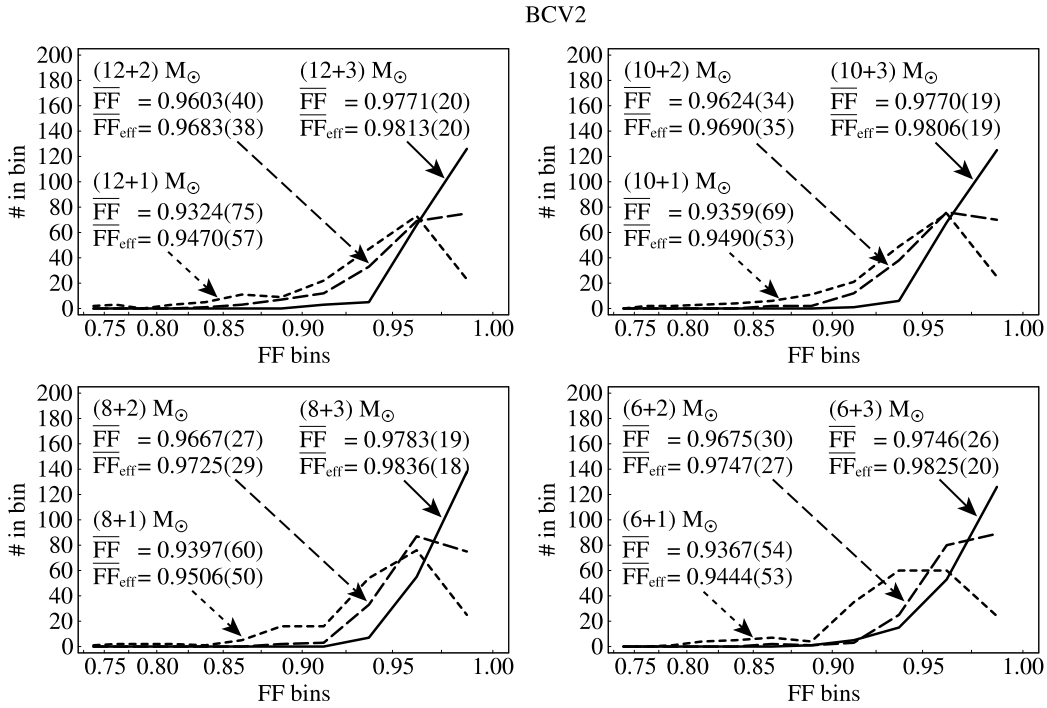

Figure 2.5: Distribution of BCV2 DTF fitting factors for populations of target systems with component masses $(m_1, m_2) = \{6, 8, 10, 12\}M_\odot \times \{1, 2, 3\}M_\odot$, and with uniformly sampled directional and local angular parameters. For each pair of masses, we include 200 target systems. The curves show the number of samples falling within each bin marked on the abscissa; the bins have equal width, but are plotted logarithmically to emphasize FFs close to unity. The figures show also the average fitting factor $\overline{\text{FF}}$ and the effective average fitting factor $\overline{\text{FF}}_{\text{eff}}$ (as defined by Eq. (119) of Ref. [14]), with their estimated Monte Carlo error in parentheses.

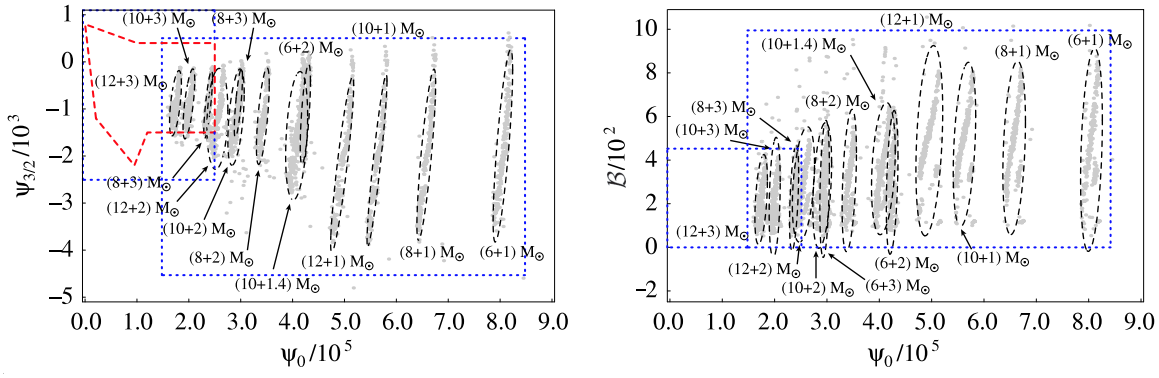

Figure 2.6: FF projection maps onto the BCV2 intrinsic parameter space for target systems with component masses $(m_1, m_2) = \{6, 8, 10, 12\}M_\odot \times \{1, 2, 3\}M_\odot$ and for $(10 + 1.4)M_\odot$ BH-NS systems, with uniformly sampled directional and local angular parameters. The left panel shows the $(\psi_0,\psi_{3/2})$ section of the map, while the right panel shows the $(\psi_0, \mathcal{B})$ section. The dots mark the values of the BCV2 parameters that achieve the maximum match for each target system. For each pair of masses, we draw an ellipse centered at the baricenter of the corresponding dot cloud, sized to include 90% of the dots; the axes of the ellipse follow the quadratic moments of the dots. The dotted rectangles show the regions used in Sec. 2.4.2 to estimate the number of BCV2 templates needed to search for the systems with component masses $(m_1, m_2) \in [6, 12]M_\odot \times [1, 3]M_\odot$ and $(m_1, m_2) \in [5, 20]M_\odot \times [5, 20]M_\odot$. In the left panel, the dashed lines enclose the region that was prescribed in Ref. [14] for the heavier systems.

search from the current best-fit $\mathcal{B}$, creating one more chance to escape a local maximum. (By contrast, in Ref. [14] we always started simplex-based maximization at $\mathcal{B} = 20$, too small compared to the values that we now see to correspond to the physical precession frequency. Because of this choice, Fig. 16 of Ref. [14] shows more points clustered around what are likely to be values of $\mathcal{B}$ corresponding to $\Omega_p^s/2$.)

We test the performance of the BCV2 DTF for BH-BH target systems with component masses

$$(m_1, m_2) = \left\{ \begin{array}{c} 12M_\odot \\ 10M_\odot \\ 8M_\odot \\ 6M_\odot \end{array} \right\} \times \left\{ \begin{array}{c} 3M_\odot \\ 2M_\odot \\ 1M_\odot \end{array} \right\}, \tag{2.16}$$

as well as for BH-NS systems with $(m_1, m_2) = (10M_\odot, 1.4M_\odot)$. We always take BHs to have maximal spins and NSs to be nonspinning. Without loss of generality, we fix the directional parameters describing GW propagation and detector orientation, while we randomly generate 200 configurations of the other directional parameters and of the local parameters of the binary (see Table I and the discussion around it in Ref. [14] for the definition of directional and local parameters).

The FFs obtained are generally high, as seen by the plots of their distributions in Fig. 2.5. That figure shows also the average fitting factor $\overline{\text{FF}}$ and the effective average fitting factor $\overline{\text{FF}}_{\text{eff}}$, as defined by Eq. (119) of Ref. [14]. The FFs have a strong dependence on the mass ratio of the target binary. The more asymmetric the masses, the harder it is to get high FFs, probably because the number of precessional cycles is larger.

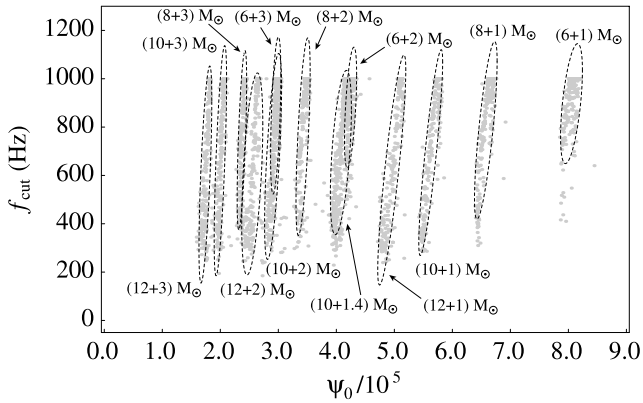

Figure 2.7: FF projection maps onto the BCV2 $(\psi_0, f_{\rm cut})$ parameter subspace. See Fig. 2.6 for details. The cutoff seen at 1000 Hz is due to a hard constraint arbitrarily imposed on the $f_{\rm cut}$ search range.

Due to the improved search procedure, we find slightly better FFs for $(10 + 1.4)M_\odot$ BH-NS binaries than the values obtained in Ref. [14] (see Fig. 2.10). Moreover, we see that in Fig. 2.2 the relative number of points in the cluster corresponding to $\Omega_p^t = \Omega_p^s$ is increased with respect to Fig. 16 of Ref. [14].

An important question is what ranges of DTF parameters should be included in a template bank to be used in a search for a given class of target systems. Since all the BCV2 parameters are phenomenological, the straightforward approach is to include templates corresponding to the range of the FF projection maps (*i.e.*, to include the regions in the DTF parameter space where the maximum matches were achieved, for a representative set of target systems). Figure 2.6 shows the $(\psi_0, \psi_{3/2})$ and $(\psi_0, \mathcal{B})$ sections of the FF projection. The clusters of maxima are labeled by the mass parameters of the target system; the spread in each cluster corresponds to different choices of the directional and local parameters of the binary. The dotted rectangles show the regions used in Sec. 2.4.2 to estimate the number of BCV2 templates needed to search for the systems analyzed in this chapter (with component masses $(m_1, m_2) \in [6, 12]M_\odot \times [1, 3]M_\odot$) and for heavier systems (with component masses $(m_1, m_2) \in [5, 20]M_\odot \times [5, 20]M_\odot$). For comparison, the dashed polygon shows the $(\psi_0, \psi_{3/2})$ region suggested in Ref. [14] for the heavier systems.

Figure 2.7 shows the $(\psi_0, f_{\rm cut})$ section of the projection map. The range of $f_{\rm cut}$ has a weak dependence on the masses of the target system, very probably because the target signals end their evolution at the margin of the frequency band of good interferometer sensitivity (for LIGO-I), where little signal power is lost by excluding higher frequencies. Throughout this chapter, we define the target-signal ending frequency as the instantaneous GW frequency at the minimum energy circular orbit (MECO), as given by Eqs. (11)–(12) of Ref. [14], and plotted in Figs. 5 and 6 of Ref. [14], and in Fig. 1 of Ref. [18]. This frequency is inversely proportional to the total mass of the binary, and it is smaller for antialigned spin and orbital angular momentum (*i.e.*, negative κ).

In fact, it seems that the $f_{\rm cut}$ parameter can be dropped altogether, as suggested by the following test: using the BCV2 DTF but *fixing* $f_{\rm cut} = 400$ Hz, we evaluate FFs for $(6 + 1)M_\odot$ and $(12 + 3)M_\odot$ systems. The

first mass configuration was chosen because, although it corresponds to the largest ending frequency (*i.e.*, the smallest total mass) among the systems studied in this chapter, it shows the largest distribution of $\psi_{3/2}$ in Fig. 2.6; thus, by removing $f_{\rm cut}$ from the maximization of the overlap, we could expect a very mild dependence on $f_{\rm cut}$, but a noticeable change in the FF projection. The second mass configuration was chosen because it corresponds to the smallest ending frequency (*i.e*, the largest total mass) among our systems. For both classes of systems the FF drops by *only* 0.5% with respect to searches that include $f_{\rm cut}$, with insignificant changes in the FF projection ranges.

Although the analytic maximization over the entire ranges of the extrinsic parameters carries little computational burden, it is useful to constrain their ranges as tightly as possible to reduce the rate of false alarms. By constraining the ranges, we are in effect reducing the range of candidate signals that are compared against the detector output, and that have a (small) chance of being triggered by detector noise alone. In Fig. 2.8 we show the (C_1, C_2), (C_3, C_4), and (C_5, C_6) section of the FF projection. The absolute magnitude of the C_k ranges is application-dependent, since it is determined by the overall normalization of the waveforms.[3] However, we notice that the $C_{3,\ldots,6}$ coefficients (which govern the amplitude of modulations) have magnitude comparable to the $C_{1,2}$ coefficients (which multiply the unmodulated waveform), and that the area occupied by the points shrinks slightly with decreasing total mass and more asymmetric mass ratios (corresponding to higher ending frequencies, and therefore greater signal power to be normalized).

Asymmetric-mass-ratio binaries are not the only systems to have a large number of precession cycles. In Fig. 2.9, we show the number of precession cycles between 40 Hz and the GW frequency of the test-mass ISCO, as evaluated from Eq. (2.6). In the left panel, we consider asymmetric-mass-ratio binaries with $m_2 = 1M_\odot$ and m_1 ranging between $1M_\odot$ and $15M_\odot$; in the right panel, we consider equal-mass binaries. We take two values of the opening angle; only the first object ("m_1") is spinning (maximally). We notice that the number of precession cycles is larger for binaries with asymmetric mass ratios than for equal-mass binaries, but that the largest number of precession cycles occurs for binaries with small, comparable masses. For these, the BCV2 DTF has good performance: for instance, we find an average FF ~ 0.965 for $(2 + 2)M_\odot$ systems (in the search, we fix $f_{\rm cut} = 1000$ Hz).

2.3.2 Performance of the BCV2P detection template family

As we just saw, the BCV2 DTF offers good performance in matching the target waveforms. Its simple form allows the formulation of a simple prescription for template-bank placement (as we shall see in Sec. 2.4.1), and the computational requirements are arguably economical. However, it is not straightforward to extract physical information from the BCV2 DTF parameters, which are phenomenological. In this section, we discuss a modification of the BCV2 DTF for single-spin target systems, which is also written in the frequency domain, where the phenomenological intrinsic parameters ψ_0, $\psi_{3/2}$, and $\mathcal{B}$ are replaced by the physical pa-

[3] We normalize all target signals and templates by assuming arbitrary luminosity distances: This has no effect on the computation of FFs and template-match metrics, which always involve normalized waveforms.

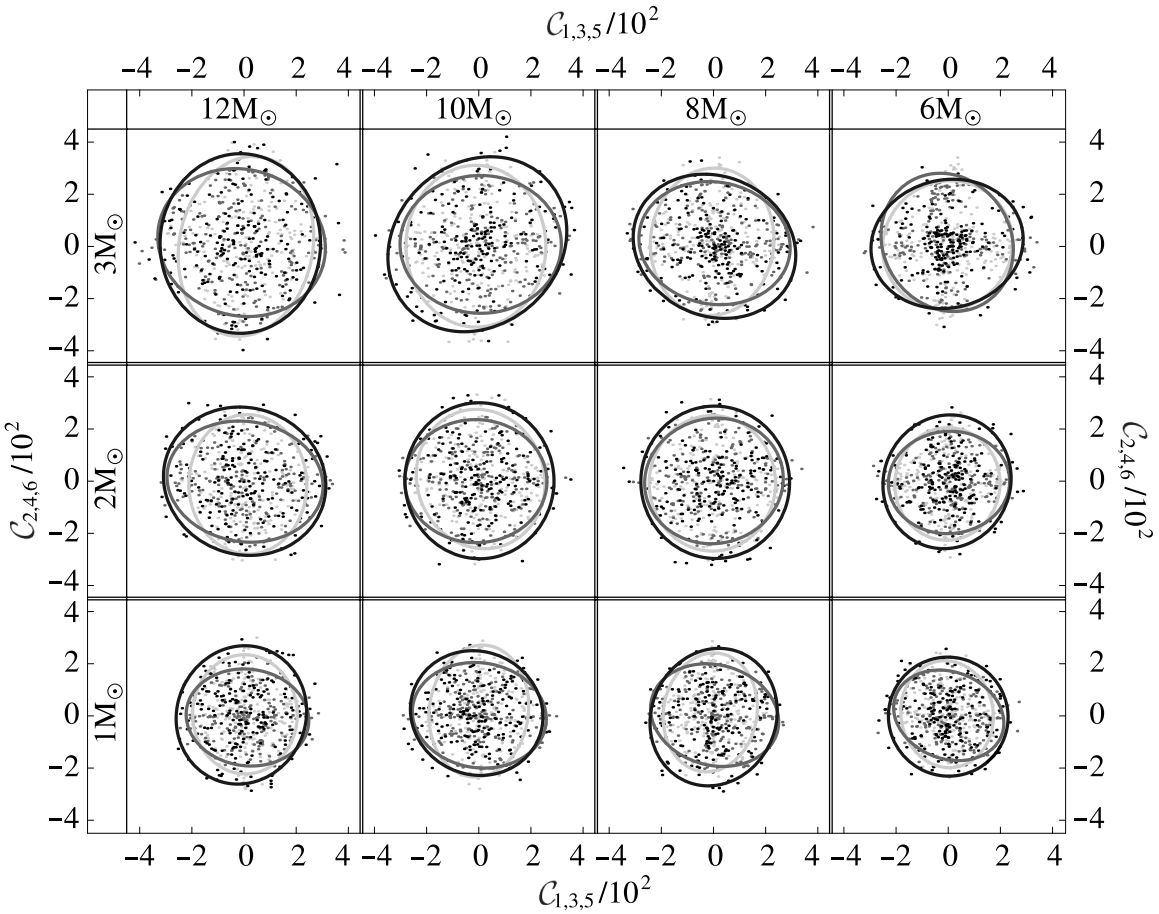

Figure 2.8: FF projection maps onto the BCV2 extrinsic parameter space, for the same target systems considered in Figs. 2.6 and 2.7. Dots of different darkness mark the best-fit values of (C_1, C_4), (C_2, C_5), (C_3, C_6). The ellipses are drawn as in Fig. 2.6.

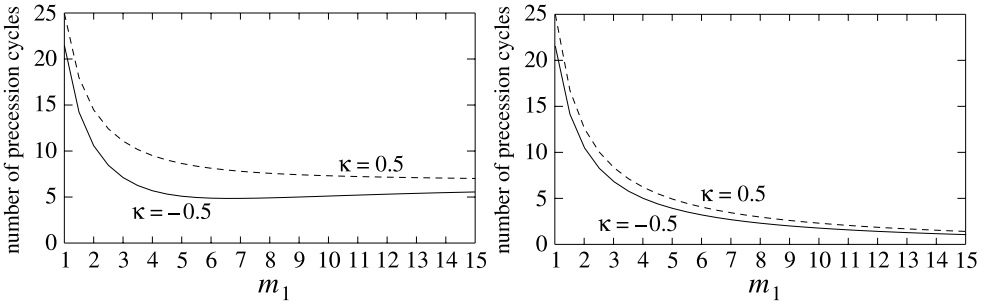

Figure 2.9: Number of precession cycles for asymmetric-mass-ratio binaries (left panel) with $m_2 = 1M_\odot$, and for equal-mass binaries (right panel), as functions of m_1, for two values of the opening angle κ.

rameters m_1, m_2, χ, and κ.

The first natural step toward a more physical parametrization is to replace the unmodulated phasing, $\psi_0 f^{-5/3} + \psi_{3/2} f^{-2/3}$, with the standard 2PN SPA phasing (as given, for instance, by Eq. (94) of Ref. [14]), which is a function of m_1, m_2, χ, and κ. The second step is to replace the power-law precession angle $\alpha_p = \mathcal{B} f^{-2/3}$ with the analytic expression derived at Newtonian level Eq. (2.6), which is valid for single-spin systems, and which matches the numerical evolution of α_p quite well [see Fig. (2.1)]. In addition, since we expect this template family to be used in searches for asymmetric-mass-ratio binaries, for which the ending frequency falls at the margin of the band of good interferometer sensitivity, we do not include $f_{\rm cut}$ among the intrinsic parameter, but instead we fix it to the GW frequency of the ISCO, as evaluated in the test mass limit. We denote this modified frequency-domain DTF as BCV2P (where the P in BCV2P stands for both "Pan" and "physical").

We emphasize that, although physically parametrized, the BCV2P DTF is not on the average much closer to the target waveforms than the BCV2 DTF. Both DTFs suffer from the limitation emphasized in Sec. 2.2.3: namely, that the frequency components that appear in the modulated GW phasing because of the evolution of the polarization tensors do not simply occur at the precession frequency Ω_p, but also at its multiples (see Fig. 2.4). Thus, the structure of the precession-frequency harmonics and the amplitude modulations are not reproduced perfectly in either the BCV2 or the BCV2P DTFs. Truly exact physical templates for adiabatic spinning waveforms are so far available only in the time domain (where they are computed by solving the equations of motion) for single-spin binaries [18].

We test the signal-matching performance of the BCV2P DTF only for $(10 + 1.4)M_\odot$ BH-NS binaries. The BCV2P DTF is as effective as the BCV2 DTF, and much better than the standard unmodulated stationary phase–approximated templates (SPA). We plot the distributions of FFs for these three families in Fig. 2.10, which shows also the average and effective average FF. In Fig. 2.11, we plot FF as a function of the target-system parameter κ.

In Tab. 2.1, we examine the parameter-estimation capabilities of M, η, $\mathcal{M}$, χ and κ, by giving three characteristic quantities for each parameter:

- the bias, defined as the average systematic error of the FF projection (it might be possible to remove the bias partially by careful characterization of the projection map);
- the rms systematic error, caused by the spread in the FF projection due to the presence of unmodeled target-system parameters;
- the Gaussianity of the distribution, as characterized by the percentage of estimators falling in the 1-σ and 3-σ intervals (for a Gaussian distribution, these should be $\sim 69\%$ and $\sim 100\%$, respectively).

These systematic errors are distinct from statistical error due to detection in noise, which is roughly inversely proportional to source strength (*i.e.*, S/N). We see that chirp mass is the parameter that can be estimated most precisely, with $\sim 1\%$ bias and rms deviation. Interestingly, κ can also be estimated rather well.

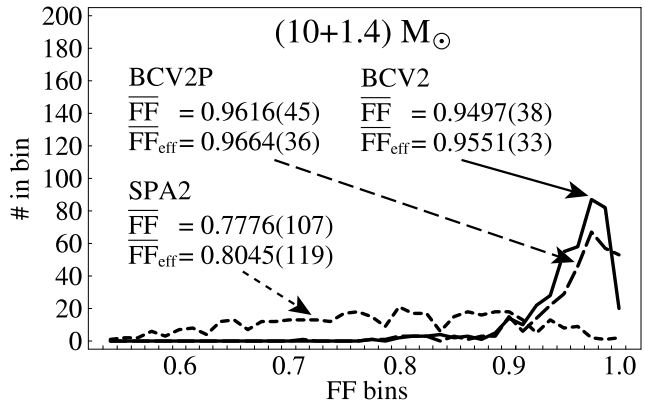

Figure 2.10: Distribution of BCV2, BCV2P, and 2PN SPA fitting factors for $(10 + 1.4)M_\odot$ BH-NS target systems with uniformly sampled directional and local angular parameters (400 sets). See Fig. 2.5 for details, but note that here FF bins are shown on a linear scale.

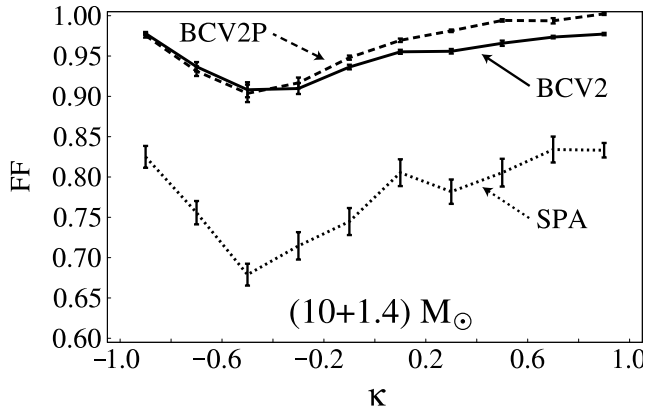

Figure 2.11: Average fitting factors achieved by the BCV2, BCV2P, and 2PN SPA DTFs for $(10 + 1.4)M_\odot$ BH-NS target systems with uniformly sampled directional and local angular parameters (400 sets), plotted against κ. The vertices of the segmented curves show the FFs averaged on the sets of target systems with κ in the bins $[-1.0, -0.8), [-0.8, -0.6), \ldots, [0.8, 1.0]$. The bars show the sampling error on the bin averages.

parameter	bias	rms	% within 1-σ/3-σ
M	10.4%	13.9%	82%/98%
η	−0.104 (abs)	0.187 (abs)	78%/98%
$\mathcal{M}$	1.2%	1.3%	60%/100%
χ	−20.0%	15.1%	80%/96%
κ	0.020 (abs)	0.153 (abs)	80%/98%

Table 2.1: Bias, systematic rms error, and percentage of estimators falling in the 1-σ and 3-σ intervals for the BCV2P DTF parameters M, η, $\mathcal{M} = M\eta^{3/5}$ (the *chirp mass*), χ and κ. The rms errors for M, $\mathcal{M}$, and χ are given as percentages of the target-system value of those parameters.

Despite its fine parameter-estimation performance, the BCV2P DTF has some disadvantages with respect to the BCV2 DTF and to the time-domain physical templates of Ref. [18]. For example, it will be more complex to build the template-match metric and to place down templates for BCV2P than for BCV2 (see Sec. 2.4.1 below). From the point of view of FF, false-alarm rate, and parameter estimation, the BCV2P DTF is less attractive than the physical templates of Ref. [19]. However, these might well be too computationally burdensome to be implemented for online searches; in that case, the BCV2P DTF could be use as an efficient first stage in a hierarchical search strategy.

2.4 A procedure for template placement using the template-match metric

In this section we show how to place the BCV2 templates within a certain DTF parameter region, while guaranteeing a chosen *minimum match* MM [21, 22] defined by

$$\begin{aligned} \mathrm{MM} &= \min_{\lambda} \max_{\lambda' \in \mathrm{bank}} \rho(\lambda, \lambda') \\ &\equiv \min_{\lambda} \max_{\lambda' \in \mathrm{bank}} \frac{\langle h(\lambda), h(\lambda') \rangle}{\sqrt{\langle h(\lambda), h(\lambda) \rangle \langle h(\lambda'), h(\lambda') \rangle}} \end{aligned} \tag{2.17}$$

(where ρ is the *match*) in terms of the noise inner product

$$\langle g, h \rangle \equiv 4\,\mathrm{Re} \int_0^{+\infty} \frac{\tilde{g}^*(f)\tilde{h}(f)}{S_n(f)} df\,, \tag{2.18}$$

with $S_n(f)$ the one-sided noise spectral density (given for this chapter by Eq. (68) of Ref. [6]). Although the maximization over the extrinsic DTF parameters can be carried out analytically, the existence of extrinsic parameters still influences the placement of templates, as discussed, *e.g.*, in Sec. VI of Ref. [18].

2.4.1 Template metric of the BCV2 DTF

The match between templates with close parameter values can be approximated using a *metric* in parameter space [15, 16, 17],

$$\rho(\lambda, \lambda + \Delta\lambda) = 1 - g_{CD} \Delta\lambda^C \Delta\lambda^D\,. \tag{2.19}$$

The components of the metric can be expressed in terms of first derivatives of the template waveforms,

$$g_{CD} = \frac{1}{2}\left[\frac{1}{\langle h, h \rangle} \left\langle \frac{\partial h}{\partial \lambda^C}, \frac{\partial h}{\partial \lambda^D} \right\rangle - \frac{1}{\langle h | h \rangle^2} \left\langle \frac{\partial h}{\partial \lambda^C}, h \right\rangle \left\langle h, \frac{\partial h}{\partial \lambda^D} \right\rangle \right]. \tag{2.20}$$

It should be noted that the match between nearby templates with different cutoff frequencies cannot be described by the metric of Eq. (2.20); in this chapter, we shall consider only the problem of placing templates

that share the same cutoff frequency $f_{\rm cut}$. For binaries with low masses, the waveforms end at relatively high frequencies compared to the band of good interferometer sensitivity, so $f_{\rm cut}$ does not play an important role. (For instance, adopting the language of Sec. VI of Ref. [6], $f_{\rm cut}$ can be set by requesting that $\langle h(f_{\rm cut}), h(+\infty)\rangle \simeq 0.99$, which yields $f_{\rm cut} \simeq 400$ Hz using the Newtonian amplitude evolution $f^{-7/6}$.)

To evaluate the metric g_{CD}, we project $h(\psi_0, \psi_{3/2}, \mathcal{B}, f_{\rm cut}, C_k; f)$ [Eq. (2.4)] onto an orthonormal basis $e_i(f)$ ($j = 1, \ldots, 6$), writing

$$h = A^i e_i(f), \qquad \langle e_i, e_j\rangle = \delta_{ij}\,; \tag{2.21}$$

the template is then normalized if

$$\langle h, h\rangle = A_j A^j = 1\,. \tag{2.22}$$

A convenient choice of the basis functions $e_i(f)$ is the following: obtain the functions $\widehat{e}_{1,3,5}(f)$ from the Schmidt orthonormalization procedure,

$$\begin{bmatrix} \widehat{e}_1 \\ \widehat{e}_3 \\ \widehat{e}_5 \end{bmatrix} = \begin{bmatrix} a_{11} & & \\ a_{31} & a_{33} & \\ a_{51} & a_{53} & a_{55} \end{bmatrix} \begin{bmatrix} 1 \\ \cos(\mathcal{B} f^{-2/3}) \\ \sin(\mathcal{B} f^{-2/3}) \end{bmatrix} f^{-7/6} \tag{2.23}$$

(note that the a_{ij} are functions of $\mathcal{B}$); define $\widehat{e}_{2,4,6}(f)$ from

$$\widehat{e}_{n+1}(f) \equiv i\,\widehat{e}_n(f)\,, \qquad n = 1, 3, 5\,; \tag{2.24}$$

(for $f > 0$); finally, define

$$e_n(f) = \widehat{e}_n(f) e^{i\Psi(f) + 2\pi i f t_c}\,. \tag{2.25}$$

Our parameter set is now $\lambda^C \equiv \{A^i; x^\alpha\} \equiv \{A^i; t_c, \mathcal{B}, \psi_0, \psi_{3/2}\}$, with $i = 1, \ldots, 6$ and $\alpha = 0, 1, 2, 3$. The A^i, along with $x^0 \equiv t_c$, are extrinsic parameters, while the $x^{\hat\alpha}$ (for $\hat\alpha = 1, 2, 3$), are intrinsic parameters.

Equation (2.22) is complemented by the useful relations

$$\left\langle \frac{\partial h}{\partial A^i}, h \right\rangle = A_i\,, \tag{2.26}$$

$$\left\langle \frac{\partial h}{\partial x^\alpha}, h \right\rangle = 0\,, \tag{2.27}$$

$$\left\langle \frac{\partial h}{\partial A^i}, \frac{\partial h}{\partial A^j} \right\rangle = \delta_{ij}\,, \tag{2.28}$$

$$\left\langle \frac{\partial h}{\partial A^i}, \frac{\partial h}{\partial x^\alpha} \right\rangle = A^j \left\langle e_i, \frac{\partial e_j}{\partial x^\alpha} \right\rangle, \tag{2.29}$$

$$\left\langle \frac{\partial h}{\partial x^\alpha}, \frac{\partial h}{\partial x^\beta} \right\rangle = A_i A_j \left\langle \frac{\partial e_i}{\partial x^\alpha}, \frac{\partial e_j}{\partial x^\beta} \right\rangle; \tag{2.30}$$

also, the first derivatives of $e_n(f)$ with respect to the x^α can be summarized in the differential expression

$$\mathrm{d}e_n = \left[2\pi i f \widehat{e_n}\,\mathrm{d}t_c + i f^{-5/3}\widehat{e_n}\,\mathrm{d}\psi_0 + i f^{-2/3}\widehat{e_n}\,\mathrm{d}\psi_{3/2} + \frac{\partial \widehat{e_n}(f)}{\partial \mathcal{B}}\,\mathrm{d}\mathcal{B}\right] e^{i\Psi(f)+2\pi i f t_c}\,. \tag{2.31}$$

Assuming $A_i A^i = 1$, we write the match between nearby templates as

$$\rho(\lambda, \lambda+\Delta\lambda) = 1 - g_{CD}(A^i,\mathcal{B})\Delta\lambda^C\Delta\lambda^D = 1 - \frac{1}{2}\begin{bmatrix} \Delta A^i & \Delta x^\alpha \end{bmatrix}\left[\begin{array}{c|c} \delta_{ij} - A_i A_j & A^l\Big\langle e_i, \dfrac{\partial e_l}{\partial x^\beta}\Big\rangle \\ \hline A^l\Big\langle \dfrac{\partial e_l}{\partial x^\alpha}, e_j\Big\rangle & A_l A_m\Big\langle \dfrac{\partial e_l}{\partial x^\alpha}, \dfrac{\partial e_m}{\partial x^\beta}\Big\rangle \end{array}\right]\begin{bmatrix} \Delta A^j \\ \\ \Delta x^\beta \end{bmatrix}. \tag{2.32}$$

In the language of Ref. [18], g_{CD} is the *full* metric, which describes the match between nearby templates in terms of differences between *all* their parameters. In general, g_{CD} can depend on all intrinsic and extrinsic parameters, but in our case it depends only on A^i and $\mathcal{B}$, but not on $\psi_{0,3/2}$ and t_c [as a consequence of Eq. (2.25)].

To determine the spacing of bank templates along the intrinsic-parameter directions, we work in terms of the extrinsic parameter–maximized match

$$\rho_{\max}(A^j, x^\gamma; x^{\hat\gamma} + \Delta x^{\hat\gamma}) \equiv \max_{\Delta A^j, \Delta t_c} \rho_{\max}(A^j, x^\gamma; A^j + \Delta A^j, t_c + \Delta t_c, x^{\hat\gamma} + \Delta x^{\hat\gamma})\,, \tag{2.33}$$

which is approximated by the *projected* metric $g^{\mathrm{proj}}_{\hat\alpha\hat\beta}$, calculated by maximizing Eq. (2.32) over ΔA^j and Δt_c, while fixing $\Delta x^{\hat\alpha}$ (see Eq. (65) of Ref. [18]). Maximizing first over ΔA^j, we notice that the submatrix $\delta_{ij} - A_i A_j$ is degenerate, with the single null eigenvector A^i [this degeneracy occurs because the match (2.32) remains constant when ΔA^i moves parallel to A^i—it must then be broken when we impose, without loss of generality, $A_k \Delta A^k = 0$]. We find the maximum

$$1 - \frac{1}{2}\left[A^i A^j G_{ij\alpha\beta}(\mathcal{B})\right]\Delta x^\alpha \Delta x^\beta \tag{2.34}$$

at the location

$$\Delta A^k = -A^j\Big\langle e^k, \frac{\partial e_j}{\partial x^\beta}\Big\rangle \Delta x^\beta \tag{2.35}$$

[note that $A_k \Delta A^k = 0$ due to Eq. (2.26)]. The tensor $G_{ij\alpha\beta}$ of Eq. (2.34) is given by

$$G_{ij\alpha\beta}(\mathcal{B}) \equiv \Big\langle \frac{\partial e_i}{\partial x^\alpha}, \frac{\partial e_j}{\partial x^\beta}\Big\rangle - \Big\langle \frac{\partial e_i}{\partial x^\alpha}, e_k\Big\rangle\Big\langle e^k, \frac{\partial e_j}{\partial x^\beta}\Big\rangle\,. \tag{2.36}$$

Further maximizing (2.34) over Δt_c, we find the maximum

$$\rho_{\max}(A^j, x^\gamma; x^{\hat\gamma} + \Delta x^{\hat\gamma}) = 1 - g^{\mathrm{proj}}_{\hat\alpha\hat\beta}(A^j, \mathcal{B})\,\Delta x^{\hat\alpha}\Delta x^{\hat\beta}\,, \tag{2.37}$$

where $g^{\rm proj}_{\hat\alpha\hat\beta}$ is the *three-dimensional* projected metric

$$g^{\rm proj}_{\hat\alpha\hat\beta}(A^j,\mathcal{B}) = \frac{1}{2}\left[A^iA^jG_{ij\hat\alpha\hat\beta} - \frac{A^iA^jA^lA^mG_{ij0\hat\alpha}G_{lm0\hat\beta}}{A^iA^jG_{ij00}}\right].$$

In general, the projected metric can depend on all the parameters, but in our case it depends only on A^i and $\mathcal{B}$.

We can now go back to the problem of template placement. Within the metric approximation, if we choose a target template [the $h(\lambda)$ of Eq. (2.17)] with parameters $\lambda^C \equiv (A^j, x^\gamma)$, the nearby templates with (extrinsic parameter–maximized) match greater than MM must have intrinsic parameters $x^{\hat\gamma} + \Delta x^{\hat\gamma}$ that lie within the ellipse $\mathcal{E}(A^j,\mathcal{B},{\rm MM})$ specified by

$$\mathcal{E}(A^j,\mathcal{B},{\rm MM}):\ g^{\rm proj}_{\hat\alpha\hat\beta}(A^j,\mathcal{B})\,\Delta x^{\hat\alpha}\Delta x^{\hat\beta} \le 1-{\rm MM}\,. \tag{2.38}$$

The shape of this ellipse depends on the target-template extrinsic parameters A^j, which is not appropriate for the placement procedure that we are seeking, which should be formulated in terms of the intrinsic parameters only.

To that purpose, Ref. [18] suggested adopting the *average* shape of the match ellipse, as obtained by averaging the maximized match [and hence the left-hand side of Eq. (2.38)] over the extrinsic parameters. In Ref. [18], the averaging weights were determined from the prior distribution of the target-signal physical extrinsic parameters, in such a way that a template-placement procedure guided by the average match contour would guarantee a certain *expected* detection efficiency.

In our case, however, the extrinsic parameters are not physical, and do not have obvious prior distributions. We take a conservative approach, and we require that for every value of the intrinsic parameters $x^{\hat\gamma}$ in the bank *and* for every possible value of the extrinsic parameters A^j, there exists a nearby bank template with $\Delta x^{\hat\gamma}$ within the ellipse $\mathcal{E}(A^j,\mathcal{B},{\rm MM})$. In principle, the neighboring template that satisfies the criterion could be different for different A^j, as illustrated at the top of Fig. 2.12. For simplicity, however, we adopt a suboptimal strategy, requiring the existence of a nearby template within the *intersection* of all the ellipses centered at $x^{\hat\gamma}$ (the gray region at the top of Fig. 2.12),

$$\mathcal{E}_{\rm minmax}(\mathcal{B},{\rm MM}) \equiv \bigcap_{A^j}\mathcal{E}(A^j,\mathcal{B},{\rm MM})\,. \tag{2.39}$$

In analogy to the usage of Ref. [21], we denote $\mathcal{E}_{\rm minmax}(\mathcal{B},{\rm MM})$ as the *minmax* region, because it corresponds to considering the contours of the match maximized over the extrinsic parameters of search templates, and minimized over the extrinsic parameters of the prospective target signals,

$$\min_{A^j}\left[1 - g^{\rm proj}_{\hat\alpha\hat\beta}(A^j,\mathcal{B})\,\Delta x^{\hat\alpha}\Delta x^{\hat\beta}\right] \ge {\rm MM}\,. \tag{2.40}$$

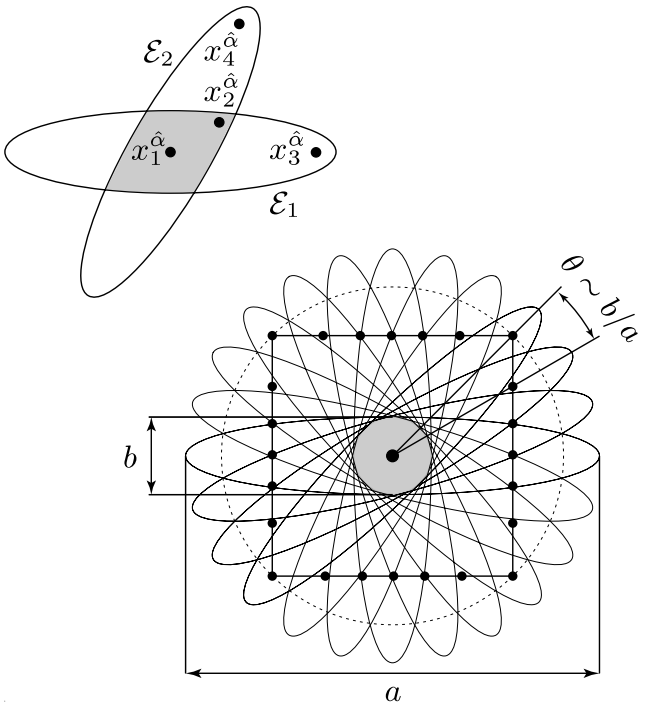

Figure 2.12: Strategies to place templates in the space of BCV2 intrinsic parameters. *Top.* Suppose we have already placed a template at $x_1^{\hat{\alpha}}$, and consider only two sets of target-template extrinsic parameters, associated with which are two different match ellipses, $\mathcal{E}_1$ and $\mathcal{E}_2$. In order for the bank to guarantee the MM for both sets of extrinsic parameters, each of $\mathcal{E}_1$ and $\mathcal{E}_2$ must contain at least another template at a location different from $x_1^{\hat{\alpha}}$. This can be achieved with two templates ($x_3^{\hat{\alpha}}$ and $x_4^{\hat{\alpha}}$ in the figure), or more easily (but less optimally) with a single template ($x_2^{\hat{\alpha}}$ in the figure) in the intersection of $\mathcal{E}_1$ and $\mathcal{E}_2$. *Bottom.* In the idealized situation where all ellipses have the same elongated shape, but take all possible orientations, placing templates along a *multilattice* (black dots) can be much more efficient than tiling on the basis of the minmax region (gray). To obtain the multilattice, we construct a set of maximized-match ellipses evenly separated by angles $\theta \sim b/a$, so that the circle (dashed) through the intersections of the ellipses has radius $\sim a$. The unit cell of the multilattice is then given by the intersections of the semi-major axes of the ellipses with the square inscribed in the dashed circle.

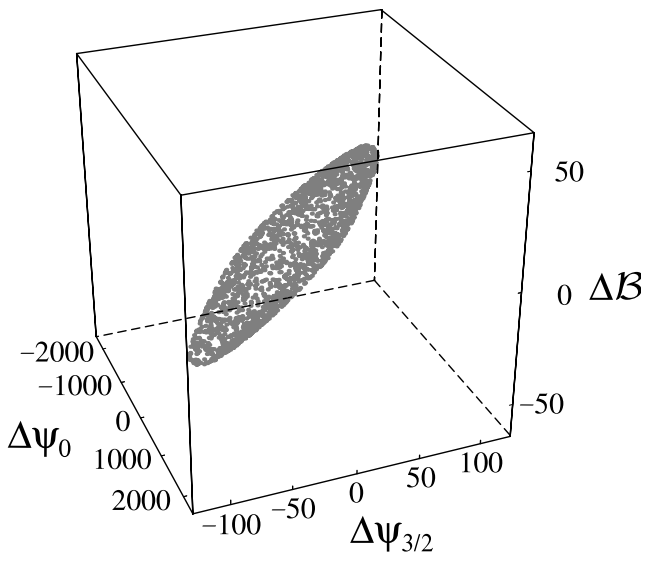

Figure 2.13: The BCV2 DTF minmax region for $\mathcal{B} = 60$, $f_{\rm cut} = 400$ Hz (and any ψ_0, $\psi_{3/2}$), obtained by sampling Eq. (2.40) with a random distribution of A^i.

The minmax regions $\mathcal{E}_{\rm minmax}(\mathcal{B}, {\rm MM})$ may no longer be elliptical in shape, but their linear dimensions still scale linearly with $\sqrt{1-{\rm MM}}$, as it happened for the ellipses $\mathcal{E}(A^j, \mathcal{B}, {\rm MM})$.

It is worth pointing out that if the orientations of the ellipses $\mathcal{E}(A^j, \mathcal{B}, {\rm MM})$ vary substantially when A^j is changed, relying on different nearby templates to achieve the MM for different extrinsic parameters can be much more efficient than relying on the minmax region. As a simple example, consider a situation in which all the ellipses $\mathcal{E}(A^j, \mathcal{B}, {\rm MM})$ have the same shape, with semi-major and semi-minor axes a and b (with $a \gg b$), but assume all possible orientations, as shown at the bottom of Fig. 2.12. In this case, the minmax region has area $\sim b^2$. If we place templates according to the minmax prescription, the template density becomes $\sim 1/b^2$, much larger than the density $\sim 1/(ab)$ associated with each individual ellipse.

On the other hand, we could place templates on the sides of squares with size $\sim a$, separated by a parameter distance $\sim b$, as shown at the bottom of Fig. 2.12. In this *multilattice*, the average area occupied by each template is $\sim a^2/(a/b) \sim ab$, corresponding to a density $\sim 1/(ab)$, much better than obtained with the minmax prescription. Unfortunately, generating the appropriate multilattice is definitely more complicated than using the minmax prescription; it is also not clear whether for the BCV2 DTF we have in fact elongated ellipses with dramatically different orientations. Thus, we will adopt the minmax prescription in the rest of this chapter.

We can approximate the minmax regions for the BCV2 DTF by sampling the A^i randomly. In Fig. 2.13, we plot an example minmax region for $\mathcal{B} = 60$, $f_{\rm cut} = 400$ Hz. This figure is typical in the sense that the minmax regions in the $(x^{\hat{1}}, x^{\hat{2}}, x^{\hat{3}}) = (\psi_0, \psi_{3/2}, \mathcal{B})$ space can be approximated rather well by ellipses. As a consequence, we can rely on (yet another) metric $\hat{g}_{\hat{\alpha}\hat{\beta}}(\mathcal{B})$ in the space of intrinsic parameters, whose match ellipses lie *within* the corresponding minmax regions, but have similar volumes. Once we are equipped with

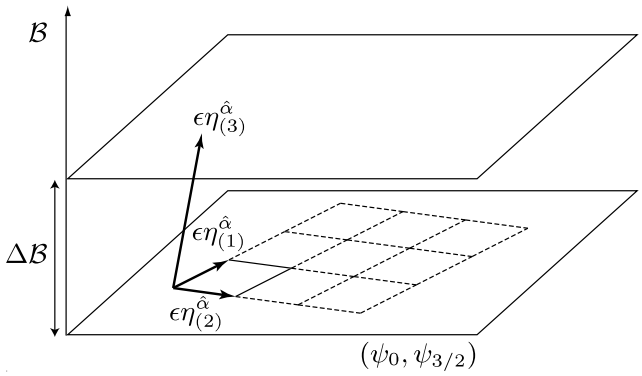

Figure 2.14: Template placement in the BCV2 intrinsic-parameter space $(\psi_0, \psi_{3/2}, \mathcal{B})$. The orthonormal basis $(\eta^{\hat{\alpha}}_{(1)}, \eta^{\hat{\alpha}}_{(2)}, \eta^{\hat{\alpha}}_{(3)})$ is constructed in such a way that $\eta^{\hat{\alpha}}_{(1)}$ and $\eta^{\hat{\alpha}}_{(2)}$ both lie in the $(\psi_0, \psi_{3/2})$ plane, along which the projected metric is constant. Unit cells constructed along these basis vectors, as shown in the figure, can be extended to the entire intrinsic-parameter space consistently. The coefficient ϵ is $\sqrt{4(1 - \mathrm{MM})/3}$.

$\hat{g}_{\hat{\alpha}\hat{\beta}}(\mathcal{B})$, the placement of the BCV2 templates can be performed along the lines of conventional template-placement procedures.

2.4.2 Template placement

The standard *local* prescription for template placement is to follow a cubic lattice[4] constructed with three orthonormal basis vectors $\{\eta^{\hat{\alpha}}_{(1)}, \eta^{\hat{\alpha}}_{(2)}, \eta^{\hat{\alpha}}_{(3)}\}$, setting the side length [as measured with the metric $\hat{g}_{\hat{\alpha}\hat{\beta}}(\mathcal{B})$] of the unit cell equal to $\sqrt{4(1 - \mathrm{MM})/3}$ [16]. For general metrics that depend on location in parameter space, such a local lattice cannot usually be extended consistently to cover the entire space. Luckily, this is possible in our case because of the translational invariance of $\hat{g}_{\hat{\alpha}\hat{\beta}}(\mathcal{B})$ along the ψ_0 and $\psi_{3/2}$ directions.

We first identify a set of orthogonal basis vectors $\{\eta^{\hat{\alpha}}_{(1)}, \eta^{\hat{\alpha}}_{(2)}, \eta^{\hat{\alpha}}_{(3)}\}$ at each point $x^{\hat{\alpha}}$, with the property that both $\eta^{\hat{\alpha}}_{(1)}$ and $\eta^{\hat{\alpha}}_{(2)}$ lie within the $(\psi_0, \psi_{3/2})$ plane. One such set follows from defining

$$\eta^{\hat{\alpha}}_{(3)} \equiv \frac{1}{\sqrt{\hat{g}^{\hat{3}\hat{3}}}} g^{\hat{\alpha}\hat{3}}\,; \tag{2.41}$$

this $\eta^{\hat{\alpha}}_{(3)}$ is orthogonal to all tangent vectors that lie within the $(\psi_0, \psi_{3/2})$ plane. We can complete the basis with any pair of $\hat{g}$-orthonormal vectors $\{\eta^{\hat{\alpha}}_{(1)}, \eta^{\hat{\alpha}}_{(2)}\}$ in that plane. Due to translational invariance, the cubic lattice constructed with this basis can be extended consistently along the ψ_0 and $\psi_{3/2}$ directions, covering a thin slice of parameter space parallel to the $(\psi_0, \psi_{3/2})$ plane, with coordinate thickness

$$\Delta\mathcal{B} = \sqrt{\frac{4(1 - \mathrm{MM})}{3}}\eta^{\hat{3}}_{(3)} = \sqrt{\frac{4(1 - \mathrm{MM})}{3}}\sqrt{\hat{g}^{\hat{3}\hat{3}}} \tag{2.42}$$

[4]Under some circumstances, other lattices can provide better packing: For the BCV2 DTF, preliminary tests suggest that a tetrahedral lattice could reduce the number of templates by one-fourth with respect to a cubic lattice.

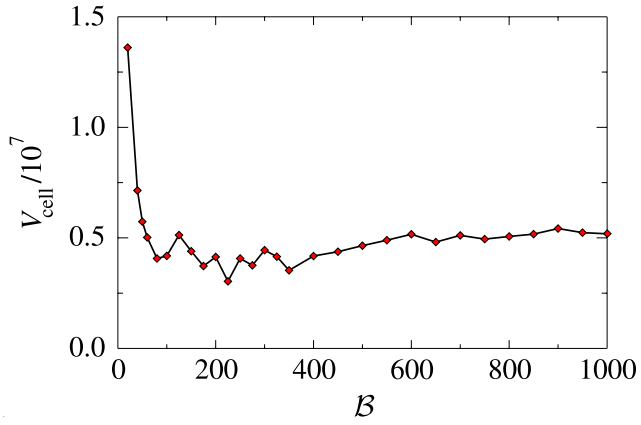

Figure 2.15: Effective parameter volume of a single-template cell as a function of $\mathcal{B}$, assuming a cubic lattice with MM = 0.97. We fix $f_{\rm cut}$ = 400 Hz.

along the $\mathcal{B}$ direction. We can stack these slices to cover the entire tridimensional parameter space (see Fig. 2.14). In Fig. 2.15, we plot the parameter volume of the cube inscribed in the MM=0.97 minmax regions (*i.e.*, the effective volume around each template in the cubic lattice) as a function of $\mathcal{B}$.

We are now ready to give a rough estimate of the number of templates required for a matched-filtering search for BH-NS and BH-BH target systems. We assume a single value (400 Hz) for $f_{\rm cut}$. For BH-BH and BH-NS systems with component masses $(m_1, m_2) \in [6, 12]M_\odot \times [1, 3]M_\odot$, we select (following Fig. 2.6) the BCV2 DTF parameter region

$$\left[\frac{\psi_0}{10^5}, \frac{\psi_{3/2}}{10^3}, \frac{\mathcal{B}}{10^2}\right] \in [1.5, 8.5] \times [-4.5, 0.5] \times [0, 10]\,; \tag{2.43}$$

our estimate for the number of templates is $\mathcal{N}_{\rm BH\text{-}NS} \simeq 7 \times 10^5$ for MM=0.97. By contrast, for BH-BH systems with component masses $(m_1, m_2) \in [5, 20]M_\odot \times [5, 20]M_\odot$, we select the BCV2 DTF parameter region

$$\left[\frac{\psi_0}{10^5}, \frac{\psi_{3/2}}{10^3}, \frac{\mathcal{B}}{10^2}\right] \in [0, 2.5] \times [-2.5, 1] \times [0, 4.5]\,; \tag{2.44}$$

out estimate for the number of templates is $\mathcal{N}_{\rm BH\text{-}BH} \simeq 8 \times 10^4$ for MM=0.97. However, it is not clear that precessing-binary templates are needed for this entire region: for binaries with relatively high component masses, "BCV1" (unmodulated) templates can already yield high FFs.

2.5 Conclusions

Reference [14] introduced the BCV2 DTF for use in precessing-binary searches; the BCV2 templates are written directly in the frequency domain, and depend on ten phenomenological parameters (the intrinsic parameters ψ_0, $\psi_{3/2}$, $\mathcal{B}$, and $f_{\rm cut}$, and the extrinsic parameters $C_{1,\ldots,6}$). The modulational effects of precession

in the target systems are modeled by the $C_{1,\ldots,6}$ and by the single intrinsic parameter $\mathcal{B}$; this marks a definite improvement over previous attempts at spinning-binary templates [7, 8, 9, 10, 11, 12, 13], which require several intrinsic parameters to model precession, leading to larger and more computationally expensive search template banks.

In this chapter, we have tested the signal-matching performance of the BCV2 DTF against target signals from asymmetric-mass-ratio binaries with component masses $(m_1, m_2) \in [6, 12]M_\odot \times [1, 3]M_\odot$ (with both components maximally spinning), and from $(10 + 1.4)M_\odot$ BH-NS binaries (with maximally spinning BHs and nonspinning NSs). The waveforms were computed at the 2PN order in the adiabatic approximation [4]. We found very good fitting factors, averaging between 0.94 and 0.98; our results are summarized in Fig. 2.5. By means of the FF projection map (see Sec. 2.3.1) we also identified the region in BCV2 DTF parameter space that must be included in a template bank–based search for these systems; our results are shown in Figs. 2.6 and 2.7.

Because all the asymmetric-mass-ratio binaries considered in this chapter generate waveforms with ending frequencies (*i.e.*, MECO frequencies, see Eqs. (11)–(12) of Ref. [14]) at the margin of the band of good interferometer sensitivity, we are free to fix $f_{\rm cut}$ to a reasonable value (see, for instance, the discussion below Eq. (2.20)), reducing the dimensionality of template space without a corresponding degradation in the FFs.

In addition, by a closer study of precessional dynamics and GW generation in single-spin binaries, we were able to relate the BCV2 phenomenological parameter $\mathcal{B}$ to the physical parameters of the target binary (see Sec. 2.2.2). In the process of doing so, we realized that waveform modulations occur at the fundamental *and* at higher and lower harmonics of the precession frequency Ω_p (for our target systems, the frequency at which the orbital angular momentum and the spin precess around the total angular momentum; for the BCV2 templates, the equivalent precession frequency corresponding to a choice of $\mathcal{B}$). In the target signals, the higher harmonics arise because modulation is caused by oscillations in the components of the polarization tensor [see Eq. (2.14)], and not directly by the precession of the orbital angular momentum and spins. In the BCV2 templates, the higher harmonics follow naturally from Eq. (2.4), and can even be made dominant by an appropriate choice of the phenomenological coefficients $C_{1,\ldots,6}$ (see Fig. 2.3).

These considerations allowed us to understand certain features in the distribution of best-fit $\mathcal{B}$ against the target-system opening angle κ that had remained unexplained in Ref. [14]. The analysis performed in this chapter suggests also a modification of the BCV2 DTF, whereby the three phenomenological parameters ψ_0, $\psi_{3/2}$, and $\mathcal{B}$ are replaced by the four physical parameters M, η, κ and χ. This modified DTF (BCV2P) has a signal-matching performance comparable to (or slightly better than) the BCV2 DTF, for $(10+1.4)M_\odot$ BH-NS binaries (see Figs. 2.10 and 2.11); we expect that we would find slightly higher FFs if we were to include higher-order PN corrections in α_p. The BCV2P DTF has the advantage of providing the straightforward and reliable estimation of certain parameters of the target system, such as $\mathcal{M}$ and κ (see Table 2.1); it has the drawback of depending on four rather than three intrinsic parameters, and its template-match metric would be even more complicated than the BCV2 metric described in Sec. 2.4.1. Therefore, we suggest that the BCV2P

DTF could be used for follow-up searches on a reduced set of BCV2 triggers, or to estimate target-system parameters, if it turns out that we cannot computationally afford the physical template family of Ref. [18], which is also written in terms of the physical parameters of the target system, and which yields FFs very close to unity.

Last, we computed the full ten-dimensional template-match metric in the (ψ_0, $\psi_{3/2}$, t_c, $\mathcal{B}$, $C_1, \ldots, C_6$) parameter space, and the tridimensional projected metric in the (ψ_0, $\psi_{3/2}$, $\mathcal{B}$) subspace, obtained by projecting out the seven extrinsic parameters. The projected metric does not depend on ψ_0 and $\psi_{3/2}$, but only on $\mathcal{B}$ (and $f_{\rm cut}$). We described a prescription to place BCV2 templates in a search bank using *minmax regions*, and exploiting the (ψ_0, $\psi_{3/2}$) translation invariance of the metric. Fixing $f_{\rm cut} = 400$ Hz and adopting a cubic lattice, we find that the estimated number of templates required for MM = 0.97 is $\sim 7 \times 10^5$ for target systems with component masses $(m_1, m_2) \in [6, 12]M_\odot \times [1, 3]M_\odot$, and $\sim 8 \times 10^4$ for target systems with component masses $(m_1, m_2) \in [5, 20]M_\odot \times [5, 20]M_\odot$. These numbers make it unlikely that a straightforward BCV2 search could be performed *online*, with the current computational resources, for these full parameter ranges. Workarounds might include carefully isolating (by extensive Monte Carlo runs) the subregions of parameter space where spin effects are weaker, so that nonspinning templates (such as the BCV1 DTF [6]) can be substituted effectively for BCV2 templates, or employing the BCV1 and BCV2 DTFs sequentially in a hierarchical search.

2.6 Bibliography

[1] LIGO: `http://www.ligo.caltech.edu`;
VIRGO: `http://www.virgo.infn.it`;
GEO: `http://www.geo600.uni-hannover.de`;
TAMA: `http://tamago.mtk.nao.ac.jp`.

[2] See, *e.g.*, LIGO Scientific Collaboration, Phys. Rev. D **69**, 082004 (2004); **69**, 102001 (2004); **69**, 122001 (2004); **69**, 122004 (2004).

[3] M. Burgay et al., Nature **426**, 531 (2003).

[4] L.E. Kidder, C.M. Will, and A.G. Wiseman, Phys. Rev. D **47**, R4183 (1993); L.E. Kidder, *ibid.* **52**, 821 (1995); L. Blanchet, T. Damour, B.R. Iyer, C.M. Will, and A.G. Wiseman, Phys. Rev. Lett. **74**, 3515 (1995); C.M. Will and A.G. Wiseman, Phys. Rev. D **54**, 4813 (1996).

[5] See Refs. [6, 14, 18] for extensive references.

[6] A. Buonanno, Y. Chen, and M. Vallisneri, Phys. Rev. D **67**, 024016 (2003).

[7] T.A. Apostolatos, C. Cutler, G.J. Sussman, and K.S. Thorne, Phys. Rev. D **49**, 6274 (1994).

[8] T.A. Apostolatos, Phys. Rev. D **52**, 605 (1995).

[9] T.A. Apostolatos, Phys. Rev. D **54**, 2421 (1996).

[10] T.A. Apostolatos, Phys. Rev. D **54**, 2438 (1996).

[11] P. Grandclément, V. Kalogera, and A. Vecchio, Phys. Rev. D **67**, 042003 (2003).

[12] P. Grandclément and V. Kalogera, Phys. Rev. D **67**, 082002 (2003).

[13] P. Grandclément, M. Ihm, V. Kalogera, and K. Belczynski, Phys. Rev. D **69**, 102002 (2004).

[14] A. Buonanno, Y. Chen, and M. Vallisneri, Phys. Rev. D **67**, 104025 (2003).

[15] R. Balasubramanian, B.S. Sathyaprakash, and S.V. Dhurandhar, Phys. Rev. D **53**, 3033 (1996).

[16] B.J. Owen, Phys. Rev. D **53**, 6749 (1996).

[17] B.J. Owen and B.S. Sathyaprakash, Phys. Rev. D **60**, 022002 (1999).

[18] Y. Pan, A. Buonanno, Y. Chen, and M. Vallisneri, Phys. Rev. D **69**, 104017 (2004).

[19] A. Buonanno, Y. Chen, Y. Pan, and M. Vallisneri, Phys. Rev. D **70**, 104003 (2004).

[20] J.A. Nelder and R. Mead, Comp. J. **7**, 308 (1965); W.H. Press, B.P. Flannery, S.A. Teukolsky, and W.T. Vetterling, *Numerical Recipes in C* (Cambridge University Press, 1988)

[21] T. Damour, B.R. Iyer, and B.S. Sathyaprakash, Phys. Rev. D **57**, 885 (1998).

[22] B.S. Sathyaprakash and S.V. Dhurandhar, Phys. Rev. D **44**, 3819 (1991).

Chapter 3

A physical template family for gravitational waves from precessing binaries of spinning compact objects: Application to single-spin binaries

The detection of the gravitational waves (GWs) emitted by precessing binaries of spinning compact objects is complicated by the large number of parameters (such as the magnitudes and initial directions of the spins, and the position and orientation of the binary with respect to the detector) that are required to model accurately the precession-induced modulations of the GW signal. In this chapter we describe a fast matched-filtering search scheme for precessing binaries, and we adopt the physical template family proposed by Buonanno, Chen, and Vallisneri [*Phys. Rev. D* **67**, 104025 (2003)] for ground-based interferometers. This family provides essentially exact waveforms, written directly in terms of the physical parameters, for binaries with a single significant spin, and for which the observed GW signal is emitted during the phase of adiabatic inspiral (for LIGO-I and VIRGO, this corresponds to a total mass $M \lesssim 15 M_{\odot}$). We show how the detection statistic can be maximized automatically over all the parameters (including the position and orientation of the binary with respect to the detector), except four (the two masses, the magnitude of the single spin, and the opening angle between the spin and the orbital angular momentum), so the template bank used in the search is only four-dimensional; this technique is relevant also to the searches for GW from extreme-mass-ratio inspirals and supermassive black hole inspirals to be performed using the space-borne detector LISA. Using the LIGO-I design sensitivity, we compute the detection threshold ($\sim$ 10) required for a false-alarm probability of 10^{-3}/year, and the number of templates ($\sim$ 76,000) required for a minimum match of 0.97, for the mass range $(m_1, m_2) = [7, 12] M_{\odot} \times [1, 3] M_{\odot}$.

Originally published as Y. Pan, A. Buonanno, Y. Chen, and M. Vallisneri, Phys. Rev. D **69**, 104017 (2004).

3.1 Introduction

Binaries consisting of a black hole (BH) in combination with another BH or with a neutron star (NS) are among the most promising gravitational-wave (GW) sources for first-generation laser-interferometer GW detectors such as LIGO [1, 2], VIRGO [3], GEO 600 [2, 4], and TAMA 300 [5]. For LIGO-I and VIRGO, and for binaries with total mass $M \lesssim 15 M_\odot$, the observed GW signal is emitted during the adiabatic-inspiral regime, where post-Newtonian (PN) calculations can be used to describe the dynamics of the binary and predict the gravitational waveforms emitted [6, 7, 8, 9].

Very little is known about the statistical distribution of BH spin magnitudes in binaries: the spins could very well be large, with a significant impact on both binary dynamics and gravitational waveforms. On the contrary, it is generally believed that NS spins will be small in the NS–BH and NS–NS binaries that are likely to be observed with first-generation GW detectors. For example, the observed NS–NS binary pulsars have rather small spin, $S_{\rm NS}/m_{\rm NS}^2 \sim 10^{-3}$ [6]. One reason the NSs in binaries of interest for GW detectors should carry small spin is that they are old enough to have spun down considerably (even if they once had spins comparable to the theoretical upper limits, $S_{\rm NS}/m_{\rm NS}^2 \simeq 0.6$–$0.7$ [10], where $m_{\rm NS}$ is the NS mass, and where we set $G = c = 1$), and because dynamical evolution cannot spin them up significantly (even during the final phase of inspiral when tidal torques become important [11]).

Population-synthesis studies [12, 13] suggest that in NS–BH binaries there is a possibility for the BH spin to be substantially misaligned with the orbital angular momentum of the binary. Early investigations [14, 15] showed that when this is the case and the BH spin is large, the evolution of the GW phase and amplitude during the adiabatic inspiral is significantly affected by spin-induced modulations. While reliable templates for precessing binaries should include these modulational effects, performing GW searches with template families that include all the *prima facie* relevant parameters (the masses, the spins, the angles that describe the relative orientations of detector and binary, and the direction of propagation of GWs to the detector) is extremely computationally intensive.

Several authors have explored this issue, and they have proposed *detection template families* (DTFs) that depend on fewer parameters and that can still reproduce the expected physical signals well. An interesting suggestion, built on the results obtained in Ref. [14], came from Apostolatos [15], who introduced a modulational sinusoidal term (the *Apostolatos ansatz*) in the frequency-domain phase of the templates to capture the effects of precession. This suggestion was tested further by Grandclément, Kalogera, and Vecchio [16]. The resulting template family has significantly fewer parameters, but its computational requirements are still very high, and its signal-fitting performance is not very satisfactory; Grandclément and Kalogera [17] subsequently suggested a modified family of *spiky* templates that fit the signals better.

After investigating the dynamics of precessing binaries, Buonanno, Chen, and Vallisneri [18, henceforth BCV2] proposed a new convention for quadrupolar GW emission in such binaries, whereby the oscillatory effects of precession are isolated in the evolution of the GW polarization tensors. As a result, the response of

the detector to the GWs can be written as the product of a carrier signal and a modulational correction, which can be handled using an extension of the Apostolatos ansatz. On the basis of these observations, BCV2 built a modulated frequency-domain DTF that, for maximal spins, yields average fitting factors ($\overline{\mathrm{FF}}$, see Sec. VIB of BCV2) of $\simeq 0.97$ for $(7+5)M_\odot$ BH–BH binaries, and $\simeq 0.93$ for $(10+1.4)M_\odot$ NS–BH binaries (see also Tab. VIII, Tab. IX, and Fig. 14 of BCV2). Note that the stationary-phase-approximation (SPA) templates developed for nonspinning binaries give much lower $\overline{\mathrm{FF}}$s of $\simeq 0.90$ for $(7+5)M_\odot$ BH–BH binaries, and $\simeq 0.78$ for $(10+1.4)M_\odot$ NS–BH binaries, while according to our computations the Apostolatos templates give $\overline{\mathrm{FF}} \simeq 0.81$ for $(10+1.4)M_\odot$ NS–BH binaries [19].

An important feature of the BCV2 templates is that their mathematical structure allows an automatic search over several of the modulational parameters (in strict analogy to the automatic search over initial orbital phase in GW searches for nonspinning binaries), reducing significantly the number of templates in the search banks, and therefore the computational cost. However, since many more signal shapes are effectively (if implicitly) tested against the detector output, the detection threshold for this DTF should be set higher than those for simpler families (for the same false-alarm probability). According to simple false-alarm computations performed with Gaussian, stationary detector noise (see BCV2) for a single template, the gain in FF is larger than the increase in the threshold only for binaries (such as NS–BH binaries) with low symmetric mass ratios $m_1 m_2/(m_1+m_2)^2$; while the opposite is true for high mass ratios. [Ultimately, the issue of FF gain versus threshold increase will be settled only after constructing the mismatch metric for this template family and performing Monte Carlo analyses of false-alarm statistics for the entire template bank under realistic detector noise.] Although the improvement in FF with the BCV2 DTF is relevant, it is still not completely satisfactory, because it translates to a loss of $\sim 20\%$ in detection rate (for the maximal-spin case) with respect to a perfect template bank (the loss will be higher if the higher required threshold is taken into account). Current estimates of binary-inspiral event rates within the distance accessible to first-generation GW interferometers hovers around one event per year, so a reduction of $\sim 20\%$ in the detection rate may not be acceptable.

BCV2 also proposed, but did not test, a promising new family of *physical* templates (i.e., templates that are exact within the approximations made to write the PN equations) for binaries where only one of the two compact bodies carries a significant spin. This family has two remarkable advantages: (i) it consists only of the physical waveforms predicted by the PN equations in the adiabatic limit, so it does not raise the detection threshold unnecessarily by including unphysical templates, as the BCV2 DTF did; (ii) all the template parameters except four are *extrinsic*: that is, they can be searched over semi-algebraically without having to compute all of the corresponding waveforms.

In this chapter we describe a data-analysis scheme that employs this family, and we estimate the number of templates required for a NS–BH search with LIGO-I: we assume $1M_\odot < m_{\mathrm{NS}} < 3M_\odot$, and $7M_\odot < m_{\mathrm{BH}} < 12M_\odot$ (see Sec. 3.3.4). In a companion paper [20], we show how a simple extension of this template family can be used to search for the GWs emitted by binaries when both compact bodies have significant spins (and where of course the adiabatic limit of the PN equations is still valid). The problem of estimating the

parameters of the binaries is examined in a forthcoming paper [21].

This chapter is organized as follows. In Sec. 3.2 we review the formalism of matched-filtering GW detection, and we establish some notation. In Sec. 3.3 we review the PN dynamics and GW generation in single-spin binaries, and we discuss the accuracy of the resulting waveforms, indicating the range of masses to which our physical template family can be applied. In Sec. 3.4 we describe the parametrization of the templates, and we discuss the semi-algebraic maximization of signal–template correlations with respect to the extrinsic parameters. In Sec. 3.5 we describe and test a fast two-stage detection scheme that employs the templates, and we discuss its false-alarm statistics. In Sec. 3.6 we build the template mismatch metric, and we evaluate the number of templates required for an actual GW search. Finally, in Sec. 3.7 we summarize our conclusions.

3.2 A brief refresher on matched-filtering GW detection

We refer the reader to Ref. [22] (henceforth BCV1), for a self-contained discussion of matched-filtering techniques for GW detection, which includes all relevant bibliographic references. In this section we mainly establish our notation and conventions; the experienced reader may therefore want to jump ahead to Sec. III.

Matched filtering [36, 31, 30, 26, 33, 32, 23, 35, 27, 29, 25, 28, 34, 24] is the standard method to detect GW signals of known shape, whereby we compare the detector output with *templates* that closely approximate the signals expected from a given class of sources, for a variety of source parameters. The goodness of fit between the template $h(\lambda^A)$ (where λ^A denotes all the source parameters) and the real GW signal s is quantified by the *overlap*

$$\rho[s, h(\lambda^A)] = \frac{\langle s, h(\lambda^A)\rangle}{\sqrt{\langle h(\lambda^A), h(\lambda^A)\rangle}} \tag{3.1}$$

[also known as the *signal-to-noise ratio* after filtering s by $h(\lambda^A)$], where the inner product $\langle g(t), h(t)\rangle$ of two real signals with Fourier transforms $\tilde{g}(f)$, $\tilde{h}(f)$ is given by [33]

$$\langle g, h\rangle = 2\int_{-\infty}^{+\infty} \frac{\tilde{g}^*(f)\tilde{h}(f)}{S_n(|f|)}df = 4\,\mathrm{Re}\int_0^{+\infty} \frac{\tilde{g}^*(f)\tilde{h}(f)}{S_n(f)}df; \tag{3.2}$$

throughout this chapter we adopt the LIGO-I one-sided noise power spectral density S_n given by Eq. (28) of BCV1. Except where otherwise noted, we shall always consider normalized templates $\hat{h}$ (where the hat denotes normalization), for which $\langle \hat{h}(\lambda^A), \hat{h}(\lambda^A)\rangle = 1$, so we can drop the denominator of Eq. (3.1).

A large overlap between a given stretch of detector output and a particular template implies that there is a high probability that a GW signal similar to the template is actually present in the output, and is not being merely simulated by noise alone. Therefore the overlap can be used as a *detection statistic*: We may claim a detection if the overlap rises above a *detection threshold* ρ^*, which is set, on the basis of a characterization of the noise, in such a way that false alarms are sufficiently unlikely.

The maximum (*optimal*) overlap that can be achieved for the signal s is $\sqrt{\langle s, s\rangle}$ (the *optimal signal-to-*

noise ratio), which is achieved by a perfect (normalized) template $\hat{h} \equiv s/\sqrt{\langle s, s\rangle}$. In practice, however, this value will not be reached, for two distinct reasons. First, the template family $\{\hat{h}(\lambda^A)\}$ might not contain a faithful representation of the physical signal w. The fraction of the theoretical maximum overlap that is recovered by the template family is quantified by the *fitting factor* [35]

$$\mathrm{FF} = \frac{\max_{\lambda^A}\langle w, \hat{h}(\lambda^A)\rangle}{\sqrt{\langle w, w\rangle}}. \tag{3.3}$$

Second, in practice we will usually not be able to use a *continuous* template family $\{\hat{h}(\lambda^A)\}$, but instead we will have to settle with a discretized template bank $\{\hat{h}(\lambda^A_{(k)})\}$, where (k) indexes a finite lattice in parameter space; so the best template to match a given physical signal will have to be replaced by a nearby template in the bank. [As we shall see in Sec. 3.4, there is a partial exception to this rule: We can take into account all possible values of certain parameters, known as *extrinsic parameters* [23, 27], without actually laying down templates in the bank along that parameter direction.] The fraction of the optimal overlap that is recovered by the template bank, in the worst possible case, is quantified by the *minimum match* [31, 27]. Assuming that the physical signal belongs to the continuous template family $\{\hat{h}(\lambda^A)\}$, the minimum match is equal to

$$\mathrm{MM} = \min_{\lambda'^A} \max_{(k)} \langle \hat{h}(\lambda'^A), \hat{h}(\lambda^A_{(k)})\rangle. \tag{3.4}$$

The required minimum match MM sets the allowable coarseness of the template bank [31, 32, 23]: the closer to one the MM, the closer to one another the templates will need to be laid down. In Sec. 3.6 we shall use a notion of *metric* [29, 27, 34] in parameter space to characterize the size and the geometry of the template bank corresponding to a given MM.

3.3 Adiabatic post-Newtonian model for single-spin binary inspirals

In this section we discuss PN adiabatic dynamics and GW generation for NS–BH and BH–BH binaries. Specifically, in Secs. 3.3.1–3.3.3 we review the relevant PN equations and the GW emission formalism developed in BCV2. In Sec. 3.3.4 we study the accuracy of the waveforms, and determine the mass range where the waveforms produced by adiabatic models can be considered accurate for the purpose of GW detection. The discussion of this section is continued in App. 3.8, where we investigate the effects of quadrupole-monopole interactions (tidal torques) on the waveforms, which have been so far neglected in studies of precessing-binary waveforms, and in fact turn out to be only marginally important for NS–BH binaries. The time-pressed reader may want to skip Secs. 3.3.1 and 3.3.2 (which review BCV2 material), move on to Sec. 3.3.3 (which introduces the template bank examined in this chapter), and then jump to the last two paragraphs of Sec. 3.3.4 (which summarize the comparisons between PN orders).

In this chapter, we restrict ourselves to binaries in which only one body has significant spin, leaving a similar study of generic binaries to a companion paper [21]. As a further restriction, we consider only binaries

in circular orbits, assuming that they have already been circularized by radiation reaction as they enter the frequency band of ground-based GW detectors. For all binaries, we denote the total mass by $M = m_1 + m_2$ and the symmetric mass ratio by $\eta = m_1 m_2/M^2$; we also assume that the heavier body (with mass $m_1 \geq m_2$) carries the spin $S_1 = \chi_1 m_1^2$, with $0 \leq \chi_1 \leq 1$ (here and throughout this chapter we set $G = c = 1$).

3.3.1 The PN dynamical evolution

In the adiabatic approach [6, 37, 38] to the evolution of spinning binaries, one builds a sequence of precessing (due to spin effects) and shrinking (due to radiation reaction) circular orbits. The orbital frequency increases as the orbit shrinks. The timescales of the precession and shrinkage are both long compared to the orbital period (this is the *adiabatic condition*), until the very late stage of binary evolution. (Such orbits are also called *spherical orbits*, since they reside on a sphere with slowly shrinking radius.)

The radiation reaction–induced evolution of frequency can be calculated by using the energy-balance equation, $\dot{\omega} = -\mathcal{F}/(d\mathcal{E}/d\omega)$, where $\mathcal{E}$ is the orbital-energy function, and $\mathcal{F}$ the GW energy-flux (or luminosity) function. Both have been calculated as functions of the orbital frequency using PN-expansion techniques, and are determined up to 3.5PN order [7, 8, 9]; however, spin effects have been calculated only up to 2PN order [37]. The resulting evolution equation for ω, obtained by inserting the PN expansions of $\mathcal{E}$ and $\mathcal{F}$ into the balance equation and reexpanding is

$$\begin{aligned}\frac{\dot{\omega}}{\omega^2} = \frac{96}{5}\,\eta\,(M\omega)^{5/3}\,\Bigg\{1 - \frac{743+924\,\eta}{336}\,(M\omega)^{2/3} - \left(\frac{1}{12}\left[\chi_1(\hat{\mathbf{L}}_N\cdot\hat{\mathbf{S}}_1)\left(113\frac{m_1^2}{M^2}+75\eta\right)\right] - 4\pi\right)(M\omega) \\ + \left(\frac{34\,103}{18\,144} + \frac{13\,661}{2\,016}\,\eta + \frac{59}{18}\,\eta^2\right)(M\omega)^{4/3} - \frac{1}{672}\,(4\,159 + 14\,532\,\eta)\,\pi\,(M\omega)^{5/3} \\ + \Bigg[\left(\frac{16\,447\,322\,263}{139\,708\,800} - \frac{1\,712}{105}\gamma_E + \frac{16}{3}\pi^2\right) + \left(-\frac{273\,811\,877}{1\,088\,640} + \frac{451}{48}\pi^2 - \frac{88}{3}\hat{\theta}\right)\eta \\ + \frac{541}{896}\eta^2 - \frac{5\,605}{2\,592}\eta^3 - \frac{856}{105}\log\left[16(M\omega)^{2/3}\right]\Bigg](M\omega)^2 + \left(-\frac{4\,415}{4\,032} + \frac{661\,775}{12\,096}\,\eta + \frac{149\,789}{3\,024}\,\eta^2\right)\pi\,(M\omega)^{7/3}\Bigg\}\,,\end{aligned} \tag{3.5}$$

where $\gamma_E = 0.577\ldots$ is Euler's constant. We denote by $\hat{\mathbf{L}}_N \propto \mathbf{r}\times\mathbf{v}$ the unit vector along the orbital angular momentum, where $\mathbf{r}$ and $\mathbf{v}$ are the two-body center-of-mass radial separation and relative velocity, respectively. $\hat{\mathbf{L}}_N$ is also the unit normal vector to the orbital plane. [Throughout this chapter we shall always add hats to vectors to denote the corresponding unit vectors.] The (scalar) quantity $\hat{\theta}$ is an undetermined regularization parameter that enters the GW flux at 3PN order [8]. As in Ref. [18], we do not include the (partial) spin contributions to $\dot{\omega}$ at 2.5PN, 3PN, and 3.5PN orders, which arise from known 1.5PN and 2PN spin terms of $\mathcal{E}$ and $\mathcal{F}$. (To be fully consistent one should know the spin terms of $\mathcal{E}$ and $\mathcal{F}$ at 2.5PN, 3PN and 3.5PN orders.) In Sec. 3.3.4 we shall briefly comment on the effect of these terms. We ignore also the quadrupole-monopole interaction, which we discuss in Sec. 3.8.

The precession equation for the spin is [38, 14]

$$\dot{\mathbf{S}}_1 = \frac{\eta}{2M}(M\omega)^{5/3}\left(4+3\frac{m_2}{m_1}\right)\hat{\mathbf{L}}_N \times \mathbf{S}_1\,, \tag{3.6}$$

where we have replaced $r \equiv \mathbf{r}$ and $|\mathbf{L}_N|$ by their leading-order Newtonian expressions in ω. The precession of the orbital plane (defined by its normal vector $\hat{\mathbf{L}}_N$) can be computed following Eqs. (5)–(8) of BCV2, and it reads

$$\dot{\hat{\mathbf{L}}}_N = \frac{\omega^2}{2M}\left(4+3\frac{m_2}{m_1}\right)\mathbf{S}_1 \times \hat{\mathbf{L}}_N \equiv \mathbf{\Omega}_L \times \hat{\mathbf{L}}_N\,. \tag{3.7}$$

Equations (3.5)–(3.7) describe the adiabatic evolution of the three variables ω, $\mathbf{S}_1$, and $\hat{\mathbf{L}}_N$. It can be easily deduced that the magnitude of the spin, $S_1 = |\mathbf{S}_1|$, and the angle between the spin and the orbital angular momentum, $\kappa_1 \equiv \hat{\mathbf{L}}_N \cdot \widehat{\mathbf{S}}_1$, are conserved during the evolution.

The integration of Eqs. (3.5)–(3.7) should be stopped at the point where the adiabatic approximation breaks down. This point is usually reached (e.g., for 2PN and 3PN orders) when the orbital energy $\mathcal{E}_{n\mathrm{PN}}$ reaches a minimum, as found by solving $d\mathcal{E}_{n\mathrm{PN}}/d\omega = 0$ (exceptions occur at Newtonian, 1 PN, and 2.5 PN orders, as we shall explain in more detail in Sec. 3.3.4). We shall call the corresponding orbit the Minimum Energy Circular Orbit, or MECO. Up to 3PN order, and including spin-orbit effects up to 1.5PN order, the orbital energy $\mathcal{E}(\omega)$ reads [6, 37, 40]

$$\begin{aligned}\mathcal{E}(\omega) = -\frac{\mu}{2}(M\omega)^{2/3}\Bigg\{1 - \frac{(9+\eta)}{12}(M\omega)^{2/3} + \frac{8}{3}\left(1+\frac{3}{4}\frac{m_2}{m_1}\right)\frac{\hat{\mathbf{L}}_N\cdot\mathbf{S}_1}{M^2}(M\omega) - \frac{1}{24}(81-57\eta+\eta^2)(M\omega)^{4/3} \\ + \left[-\frac{675}{64} + \left(\frac{34445}{576} - \frac{205}{96}\pi^2 + \frac{10}{3}\omega_s\right)\eta - \frac{155}{96}\eta^2 - \frac{35}{5184}\eta^3\right](M\omega)^2\Bigg\}\,.\end{aligned} \tag{3.8}$$

Henceforth, we assume the regularization parameter ω_s to be zero, as computed in Ref. [7, 9, 39].

3.3.2 The precessing convention

BCV2 introduced a new convention to express the leading-order mass-quadrupole gravitational waveform generated by binaries of spinning compact objects; here we review it briefly. At this order, the radiative gravitational field emitted by the quasi-circular binary motion reads

$$h^{ij} = \frac{2\mu}{D}\left(\frac{M}{r}\right)Q_c^{ij}\,, \tag{3.9}$$

where D is the distance between the source and the Earth, and $Q_c^{ij} = 2\left[\hat{\lambda}^i\hat{\lambda}^j - \hat{n}^i\hat{n}^j\right]$, with $\hat{\mathbf{n}}$ and $\hat{\lambda}$ the unit vectors along the separation vector $\mathbf{r}$, and the relative velocity $\mathbf{v}$ of the binary. In general, $\hat{\mathbf{n}}(t)$ and $\hat{\lambda}(t)$ can be

written as

$$\hat{\mathbf{n}}(t) = \mathbf{e}_1(t)\,\cos\Phi(t) + \mathbf{e}_2(t)\,\sin\Phi(t)\,, \tag{3.10}$$

$$\hat{\lambda}(t) = -\mathbf{e}_1(t)\,\sin\Phi(t) + \mathbf{e}_2(t)\,\cos\Phi(t)\,, \tag{3.11}$$

where $\mathbf{e}_1(t)$, $\mathbf{e}_2(t)$, and $\mathbf{e}_3(t) \equiv \hat{\mathbf{L}}_N(t)$ are orthonormal vectors, and $\mathbf{e}_{1,2}(t)$ forms a basis for the instantaneous orbital plane. Now Q_c^{ij} can be written as

$$Q_c^{ij} = -2\Big\{[\mathbf{e}_+]^{ij}\cos 2(\Phi+\Phi_0) + [\mathbf{e}_\times]^{ij}\sin 2(\Phi+\Phi_0)\Big\}\,, \tag{3.12}$$

with $\mathbf{e}_+ = \mathbf{e}_1\otimes\mathbf{e}_1 - \mathbf{e}_2\otimes\mathbf{e}_2$ and $\mathbf{e}_\times = \mathbf{e}_1\otimes\mathbf{e}_2 + \mathbf{e}_2\otimes\mathbf{e}_1$, and Φ_0 an arbitrary initial phase. For quasi-circular orbits, we have $\dot{\hat{\mathbf{n}}} = \omega\hat{\lambda}$, but in general $\dot{\Phi}\neq\omega$, because of the time dependence of $\mathbf{e}_{1,2}(t)$. BCV2 defined the *precessing convention* by requiring that

$$\dot{\mathbf{e}}_i(t) = \boldsymbol{\Omega}_e(t)\times\mathbf{e}_i(t)\,,\quad i=1,2\,, \tag{3.13}$$

$$\boldsymbol{\Omega}_e(t) = \boldsymbol{\Omega}_L - (\boldsymbol{\Omega}_L\cdot\hat{\mathbf{L}}_N)\hat{\mathbf{L}}_N\,. \tag{3.14}$$

[See Eq. (3.7) for the definition of $\boldsymbol{\Omega}_L$]. In this convention, we do have $\dot{\Phi}=\omega$.

3.3.3 The detector response

The response of a ground-based interferometric detector to the GW signal of Eq. (3.9) is given by

$$h = \underbrace{-\frac{2\mu}{D}\frac{M}{r}\Big([\mathbf{e}_+]^{ij}\,\cos 2(\Phi+\Phi_0) + [\mathbf{e}_\times]^{ij}\,\sin 2(\Phi+\Phi_0)\Big)}_{\text{factor Q: wave generation}}\underbrace{\Big([\mathbf{T}_+]_{ij}\,F_+ + [\mathbf{T}_\times]_{ij}\,F_\times\Big)}_{\text{factor P: detector projection}}\,; \tag{3.15}$$

the tensors $[\mathbf{T}_{+,\times}]_{ij}$ are defined by $\mathbf{T}_+ \equiv \mathbf{e}_x^R\otimes\mathbf{e}_x^R - \mathbf{e}_y^R\otimes\mathbf{e}_y^R$ and $\mathbf{T}_\times \equiv \mathbf{e}_x^R\otimes\mathbf{e}_y^R + \mathbf{e}_y^R\otimes\mathbf{e}_x^R$, after we introduce the *radiation frame*

$$\mathbf{e}_x^R = -\mathbf{e}_x^S\,\sin\varphi + \mathbf{e}_y^S\,\cos\varphi\,, \tag{3.16}$$

$$\mathbf{e}_y^R = -\mathbf{e}_x^S\,\cos\Theta\cos\varphi - \mathbf{e}_y^S\,\cos\Theta\sin\varphi + \mathbf{e}_z^S\,\sin\Theta\,, \tag{3.17}$$

$$\mathbf{e}_z^R = +\mathbf{e}_x^S\,\sin\Theta\cos\varphi + \mathbf{e}_y^S\,\sin\Theta\sin\varphi + \mathbf{e}_z^S\,\cos\Theta = \hat{\mathbf{N}}\,, \tag{3.18}$$

with $\hat{\mathbf{N}}$ the direction of wave propagation and Θ, φ the corresponding angles in an arbitrarily chosen *source frame*, $\{\mathbf{e}_x^S, \mathbf{e}_y^S, \mathbf{e}_z^S\}$ [see Fig. 1 of BCV2]. For the antenna patterns $F_{+,\times}$ we have

$$F_{+,\times} = \frac{1}{2}[\bar{\mathbf{e}}_x\otimes\bar{\mathbf{e}}_x - \bar{\mathbf{e}}_y\otimes\bar{\mathbf{e}}_y]^{ij}[\mathbf{T}_{+,\times}]_{ij}\,, \tag{3.19}$$

where $\bar{\mathbf{e}}_{x,y}$ are the unit vectors along the orthogonal interferometer arms. More explicitly [26],

$$F_+ = \frac{1}{2}(1+\cos^2\theta)\,\cos 2\phi\,\cos 2\psi - \cos\theta\,\sin 2\phi\,\sin 2\psi, \tag{3.20}$$

$$F_\times = \frac{1}{2}(1+\cos^2\theta)\,\cos 2\phi\,\sin 2\psi + \cos\theta\,\sin 2\phi\,\cos 2\psi. \tag{3.21}$$

Here ϕ, θ, and ψ are the orientation angles of the detector, as defined by Fig. 2 of BCV2.

Mathematically, we see that the factor P of Eq. (3.15), which is independent of time, collects only terms that depend on the position and orientation of the detector, and that describe the *reception* of GWs; while factor Q collects only terms that depend on the dynamical evolution of the binary, and that describe the *generation* of GWs (at least if the vectors $\mathbf{e}_{1,2,3}$ are defined without reference to the detector, as we will do soon). Using the language of BCV2, in the precessing convention the *directional* parameters Θ, φ, ϕ, θ, and ψ are isolated in factor P, while the *basic* and *local* parameters of the binary are isolated in factor Q.

Physically, we see that factor Q evolves along three different timescales: (i) the orbital period, which sets the GW *carrier* frequency $2\dot{\Phi} = 2\omega$; (ii) the precession timescale at which the $\mathbf{e}_{+,\times}$ change their orientation in space, which modulates the GWs; (iii) the radiation-reaction timescale, characterized by $\omega/\dot{\omega}$, which drives the evolution of frequency. In the adiabatic regime, the orbital period is the shortest of the three: so for convenience we shall define the (leading-order) *instantaneous GW frequency* $f_{\rm GW}$ directly from the instantaneous orbital frequency ω, $f_{\rm GW} \equiv (2\omega)/(2\pi) = \omega/\pi$.

Thus, what parameters are needed to specify Q completely? Equation (3.5) for $\omega(t)$ can be integrated numerically, starting from an arbitrary $\omega(0)$ [41] once we specify the basic parameters M, η, and χ_1, and the local parameter $\kappa_1 \equiv \hat{\mathbf{L}}_N \cdot \hat{\mathbf{S}}_1$ (conserved through evolution). With the resulting $\omega(t)$ we can integrate Eqs. (3.6) and (3.7), and then Eq. (3.13). For these we need initial conditions for $\hat{\mathbf{S}}_1$, $\hat{\mathbf{L}}_N$, and for the $\mathbf{e}_i$: without loss of generality, we can introduce a (fixed) source frame attached to the configuration of the binary at $t = 0$:

$$\begin{aligned} \mathbf{e}_x^S &\propto \mathbf{S}_1(0) - [\mathbf{S}_1(0)\cdot\hat{\mathbf{L}}_N(0)]\,\hat{\mathbf{L}}_N(0)\,, \\ \mathbf{e}_y^S &= \hat{\mathbf{L}}_N(0)\times\mathbf{e}_x^S\,, \quad \mathbf{e}_z^S = \hat{\mathbf{L}}_N(0)\,, \end{aligned} \tag{3.22}$$

and then take

$$\mathbf{e}_1(0) = \mathbf{e}_x^S\,, \quad \mathbf{e}_2(0) = \mathbf{e}_y^S\,, \quad \mathbf{e}_3(0) = \mathbf{e}_z^S\,. \tag{3.23}$$

[If $\mathbf{S}_1(0)$ and $\hat{\mathbf{L}}_N(0)$ are parallel, $\mathbf{e}_x^S$ can be chosen to lie in any direction orthogonal to $\hat{\mathbf{L}}_N(0)$.] The initial orbital phase Φ_0 that enters the expression of Q is defined by

$$\hat{\mathbf{n}}(0) = \mathbf{e}_1(0)\cos\Phi_0 + \mathbf{e}_2(0)\sin\Phi_0\,, \tag{3.24}$$

while the initial conditions for $\hat{\mathbf{S}}_1$ and $\hat{\mathbf{L}}_N$, as expressed by their components with respect to the source frame,

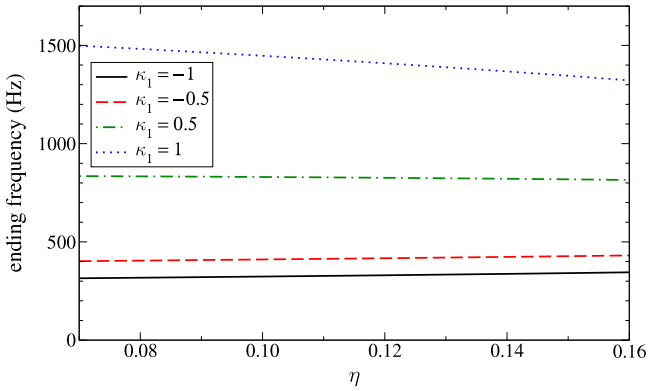

Figure 3.1: Ending frequency (instantaneous GW frequency at the MECO) as a function of η, evaluated from Eq. (3.8) at 2PN order for $M = 15M_\odot, \chi_1 = 1$, and for different values of κ_1.

are

$$\hat{\mathbf{L}}_N(0) = (0, 0, 1)\,, \tag{3.25}$$

$$\hat{\mathbf{S}}_1(0) = \left(\sqrt{1-\kappa_1^2}, 0, \kappa_1\right). \tag{3.26}$$

BCV2 proposed to use the family of waveforms (detector responses) defined by Eqs. (3.5)–(3.7) and (3.13)–(3.15) as a family of *physical templates* for compact binaries with a single spin. Depending on the maximum PN order N up to which the terms of Eq. (3.5) are retained, we shall denote this class of template families ST_N. The ST_N templates deserve to be called *physical* because they are derived from a physical model, namely the adiabatic PN dynamics plus quadrupole GW emission. Each ST_N template family is indexed by *eleven* parameters: M, η, χ_1 (basic), κ_1 (local), Θ, φ, θ, ϕ, ψ (directional), plus the time t_0 at which the instantaneous GW frequency passes through the fiducial value $\omega(0)/\pi$, and the corresponding initial phase Φ_0. Of these, using the distinction between intrinsic and extrinsic parameters introduced in Ref. [27, 42] and further discussed in BCV2, the first four are intrinsic parameters: that is, when we search for GWs using ST_N templates, we need to lay down a discrete template bank along the relevant ranges of the intrinsic dimensions. The other seven are extrinsic parameters: that is, their optimal values can be found semi-algebraically without generating multiple templates along the extrinsic dimensions (another way of saying this is that the maximization of the overlap over the extrinsic parameters can be incorporated in the detection statistic, which then becomes a function only of the intrinsic parameters). In Sec. 3.4 we shall describe how this maximization over the extrinsic parameters can be achieved in practice.

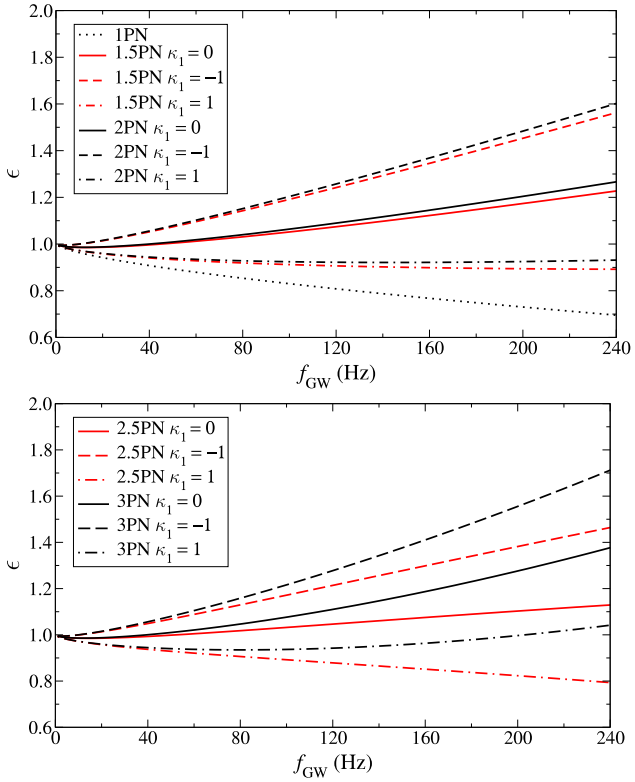

Figure 3.2: Plot of $\epsilon \equiv (\dot{\omega}/\omega^2)/(96/5\eta(M\,\omega)^{5/3})$ as a function of $f_{\rm GW} = \omega/\pi$, evaluated from Eq. (3.5) at different PN orders for a $(10 + 1.4)\,M_\odot$ binary. We do not show the 3.5PN curves, which are very close to the 3PN curves.

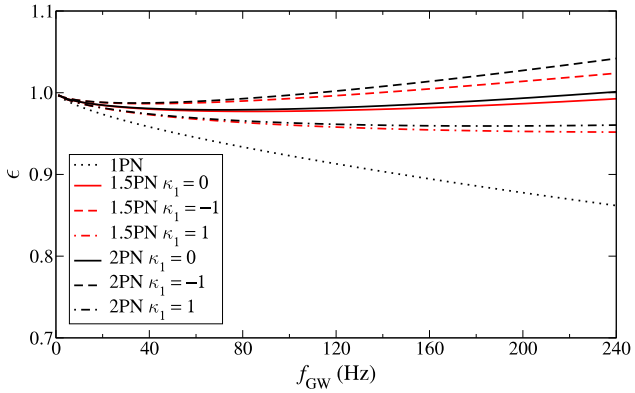

Figure 3.3: Plot of $\epsilon \equiv (\dot{\omega}/\omega^2)/(96/5\eta(M\,\omega)^{5/3})$ as a function of $f_{\rm GW} = \omega/\pi$, evaluated from Eq. (3.5) at different PN orders for a $(1.4 + 1.4)\,M_\odot$ NS–NS binary. We do not show the 2.5PN, 3PN ($\widehat{\theta} = 0$), and 3.5PN curves, which are very close to the 2PN curves. Note the change in scale with respect to Fig. 3.2.

3.3.4 Comparison between different post-Newtonian orders and the choice of mass range

In this section we investigate the range of masses m_1 and m_2 for which the PN-expanded evolution equations (3.5)–(3.7) [and therefore the template family (3.15)] can be considered reliable. As a rule of thumb, we fix the largest acceptable value of the total mass by requiring that the *GW ending frequency* (in our case, the instantaneous GW frequency at the MECO) should not lie in the frequency band of good detector sensitivity for LIGO-I. Considering the results obtained by comparing various nonspinning PN models [24, 22], and considering the variation of the ending frequency when spin effects are taken into account [BCV2], we require $M \leq 15M_\odot$. In keeping with the focus of this chapter on binaries with a single significant spin, we also impose $m_2/m_1 \leq 0.5$, which constrains the spin of the less massive body to be relatively small (of course, this condition is always satisfied for NS–BH binaries). Population-synthesis calculations [43] suggest that the more massive of the two compact bodies will have the larger spin, since usually it will have been formed first, and it will have been spun up through accretion from the progenitor of its companion. For definiteness, we assume $m_1 = 1$–$3M_\odot$ and $m_2 = 7$–$12M_\odot$; the corresponding range of η is 0.07–0.16.

In Fig. 3.1 we plot the GW ending frequency as a function of η, evaluated from Eq. (3.8) at 2PN order for $M = 15M_\odot$ and $\chi_1 = 1$. The various curves refer to different values of κ_1. The minimum of the GW ending frequency is $\sim$ 300 Hz, and it corresponds to a $(12 + 1)M_\odot$ binary with spin antialigned with the orbital angular momentum. In Fig. 3.2 we plot $\dot{\omega}/\omega^2$, normalized to its leading (Newtonian) term $96/5\eta(M\,\omega)^{5/3}$, as a function of the instantaneous GW frequency; $\dot{\omega}/\omega^2$ is evaluated from Eq. (3.5) at different PN orders, for a $(10 + 1.4)\,M_\odot$ binary with $\chi_1 = 1$. We see that the effects of the spin-orbit interaction (evident for different κ_1 within the same PN order) are comparable to, or even larger than, the effect of increasing the PN order. We see also that the different PN curves spread out more and more as we increase M and η. For comparison, in Fig. 3.3 we show the same plot for a $(1.4 + 1.4)M_\odot$ NS–NS binary; note the different scale on the vertical axis. In this case the various curves remain rather close over the entire frequency band.

	$(10+1.4)M_\odot$	$(12+3)M_\odot$	$(7+3)M_\odot$
Newtonian	3577.0	1522.3	2283.8
1PN	213.1	114.3	139.0
1.5PN	$-181.3 + 114.2\kappa_1\chi_1$	$-99.7 + 55.7\kappa_1\chi_1$	$-102.3 + 48.2\kappa_1\chi_1$
2PN	9.8	6.3	6.4
2.5PN	$-20.4 + (21.1\kappa_1\chi_1)$	$-12.7 + (12.1\kappa_1\chi_1)$	$-10.9 + (9.0\kappa_1\chi_1)$
3PN	$2.2 + (-17.0\kappa_1\chi_1 + 2.4\kappa_1^2\chi_1^2) + 0.42\,\hat{\theta}$	$2.2 + (-9.7\kappa_1\chi_1 + 1.2\kappa_1^2\chi_1^2) + 0.40\,\hat{\theta}$	$2.3 + (-6.6\kappa_1\chi_1 + 0.7\kappa_1^2\chi_1^2) + 0.43\,\hat{\theta}$
3.5PN	$-1.9 + (6.4\kappa_1\chi_1)$	$-1.3 + (3.8\kappa_1\chi_1)$	$-1.1 + (2.6\kappa_1\chi_1)$

Table 3.1: PN contributions to the number $\mathcal{N}_{\rm GW}$ of GW cycles accumulated from $\omega_{\rm min} = \pi \times 10\,{\rm Hz}$ to $\omega_{\rm max} = \omega_{\rm ISCO} = 1/(6^{3/2}\,\pi\,M)$. The contributions in parentheses, "(...)", are partial spin terms present at 2.5PN, 3PN and 3.5PN orders and due to known 1.5PN spin terms in the orbital energy and luminosity.

$(N+k,N)$	$\langle \mathrm{ST}_{N+k}, \mathrm{ST}_N \rangle$ for $(10+1.4)M_\odot$ binary, $\chi_1 = 1$							
	$\kappa_1 = 0.9$		$\kappa_1 = 0.5$		$\kappa_1 = -0.5$		$\kappa_1 = -0.9$	
(1,0)	0.1976	(0.7392) [24.5,0.02,0.00,0.00]	0.1976	(0.7392)	0.1976	(0.7392) [24.5,0.02,0.00,−0.00]	0.1976	(0.7392)
(1.5,1)	0.2686	(0.7848) [4.53,0.54,0.00,0.00]	0.2696	(0.7008)	0.2065	(0.6040) [6.58,0.36,0.00,−0.00]	0.1800	(0.6255)
(2,1.5)	0.4876	(≥ 0.99) [9.56,0.14,0.83,0.93]	0.5627	(≥ 0.99)	0.6623	(≥ 0.99) [11.7,0.10,0.97,−0.50]	0.7728	(0.9760)
(2.5,2)	0.1587	(0.9578) [10.5,0.13,1.56,0.95]	0.2011	(0.9887)	0.2902	(0.9398) [10.2,0.13,2.00,−0.19]	0.3460	(≥ 0.99)
(3,2)	0.4395	(0.9848) [11.5,0.10,0.84,0.81]	0.5057	(0.9881)	0.5575	(0.9712) [12.0,0.10,0.92,−0.48]	0.6606	(≥ 0.99)
(3,2.5)	0.1268	(0.9758) [12.8,0.08,0.05,0.98]	0.1539	(≥ 0.99)	0.2520	(0.9744) [25.6,0.03,0.35,−0.21]	0.2488	(≥ 0.99)
(3.5,3)	0.9614	(≥ 0.99) [11.7,0.10,1.00,0.90]	0.9738	(≥ 0.99)	0.9907	(≥ 0.99) [11.3,0.11,1.02,−0.49]	0.9939	(≥ 0.99)

$(N+k,N)$	$\langle \mathrm{ST}_{N+k}, \mathrm{ST}_N \rangle$ for $(12+3)M_\odot$ binary, $\chi_1 = 1$							
	$\kappa_1 = 0.9$		$\kappa_1 = 0.5$		$\kappa_1 = -0.5$		$\kappa_1 = -0.9$	
(1,0)	0.2506	(0.7066) [10.5,0.22,0.00,0.00]	0.2506	(0.7066)	0.2506	(0.7066) [10.5,0.22,0.00,−0.00]	0.2506	(0.7066)
(1.5,1)	0.3002	(0.7788) [8.22,0.50,0.00,0.00]	0.2597	(0.7381)	0.2124	(0.6934) [11.6,0.44,0.00,−0.00]	0.2017	(0.5427)
(2,1.5)	0.6379	(≥ 0.99) [16.0,0.14,1.14,0.92]	0.7089	(≥ 0.99)	0.8528	(≥ 0.99) [14.2,0.18,1.14,−0.59]	0.8620	(≥ 0.99)
(2.5,2)	0.2039	(0.9397) [15.4,0.17,1.95,0.87]	0.2800	(0.9863)	0.4696	(0.9756) [13.5,0.18,1.22,−0.51]	0.4219	(≥ 0.99)
(3,2)	0.6679	(0.9851) [11.0,0.25,0.72,0.84]	0.7267	(≥ 0.99)	0.9052	(≥ 0.99) [13.1,0.21,1.50,−0.70]	0.8868	(≥ 0.99)
(3,2.5)	0.1603	(≥ 0.99) [18.5,0.10,0.05,0.99]	0.2272	(≥ 0.99)	0.3804	(0.9759) [15.8,0.15,0.94,−0.49]	0.3060	(≥ 0.99)
(3.5,3)	0.9517	(≥ 0.99) [15.2,0.15,0.84,0.86]	0.9694	(≥ 0.99)	0.9932	(≥ 0.99) [15.3,0.16,1.00,−0.49]	0.9900	(≥ 0.99)

$(N+k,N)$	$\langle \mathrm{ST}_{N+k}, \mathrm{ST}_N \rangle$ for $\chi_1 = 0$			
	$(10+1.4)M_\odot$		$(12+3)M_\odot$	
(1,0)	0.1976	(0.7392) [24.5,0.02]	0.2506	(0.7066) [10.5,0.22]
(1.5,1)	0.1721	(0.6427) [5.22,0.51]	0.2153	(0.6749) [9.22,0.51]
(2,1.5)	0.7954	(0.9991) [12.7,0.09]	0.8924	(0.9981) [16.2,0.14]
(2.5,2)	0.4872	(0.9961) [6.94,0.25]	0.5921	(0.9977) [8.05,0.48]
(3,2)	0.7471	(0.9970) [15.3,0.06]	0.8982	(0.9994) [19.3,0.10]
(3,2.5)	0.4127	(0.9826) [26.5,0.02]	0.5282	(0.9783) [29.0,0.05]
(3.5,3)	0.9931	(≥ 0.99) [11.6,0.11]	0.9924	(≥ 0.99) [15.4,0.15]

Table 3.2: Test of Cauchy convergence of the adiabatic templates ST_N at increasing PN orders, for $(10+1.4)M_\odot$ and $(12+3)M_\odot$ binaries, and for maximally spinning BHs ($\chi_1 = 1$, upper and middle panels) and nonspinning BHs ($\chi_1 = 0$, lower panel). The overlaps quoted at the beginning of each column are maximized only with respect to the extrinsic parameters t_0 and Φ_0. In parentheses, "(...)", we give the overlaps maximized over all the parameters of the lower-order family (i.e., the fitting factors FF for the target family ST_{N+k} as matched by the search family ST_N, evaluated at the target masses shown); the fitting factors are obtained by extending the search into the unphysical template region where $\eta > 0.25$ and $\chi_1 > 1$. In brackets, "[...]", we show the parameters $M, \eta, \chi_1, \kappa_1$ (or M, η when $\chi_1 = 0$) at which the maximum overlap is achieved. The detector is perpendicular to the initial orbital plane, and at 3PN order we set $\hat{\theta} = 0$; in all cases the integration of the equations is started at a GW frequency of 60 Hz. The maximization procedure was stopped whenever an overlap ≥ 0.99 was achieved.

Another procedure (often used in the literature) to characterize the effects of spin and PN order on the evolution of the GW frequency is to count the number of GW cycles accumulated within a certain frequency band: $\mathcal{N}_{\rm GW} \equiv (1/\pi)\int_{\omega_{\rm min}}^{\omega_{\rm max}} (\omega/\dot{\omega})\, d\omega$. Here we take $\omega_{\rm min} = \pi \times 10\,{\rm Hz}$ and $\omega_{\rm max} = \omega_{\rm ISCO} = (6^{3/2}\pi M)^{-1}$, corresponding to the orbital frequency at the innermost stable circular orbit (ISCO) of a Schwarzchild black hole with mass M. In Table 3.1 we show $\mathcal{N}_{\rm GW}$ at increasing PN orders, for $(10 + 1.4)M_\odot$, $(12 + 3)M_\odot$, and $(7 + 3)M_\odot$ binaries. The contributions in parentheses are partial spin terms present at 2.5PN, 3PN, and 3.5PN orders, and due to known 1.5PN spin terms in the orbital energy and luminosity. These terms were neglected in Eq. (3.5) to be consistent in including PN terms of the same order, and we list them here only to give their order of magnitude. Unless there are cancellations, the large number of cycles suggests that it is worthwhile to compute spin effects up to the 3.5PN order.

The number of accumulated GW cycles $\mathcal{N}_{\rm GW}$ can be a useful diagnostic, but taken alone it provides incomplete and sometimes even misleading information. There are three reasons for this. First, $\mathcal{N}_{\rm GW}$ is related only to the number of orbital cycles of the binary *within* the orbital plane, but it does not reflect the precession of the plane, which modulates the detector response in both amplitude and phase. These modulations are very important effects, as witnessed by the fact that neither the standard nonspinning-binary templates (which do not have built-in modulations) nor the original Apostolatos templates (which add only modulations to the phase) can reproduce satisfactorily the detector response to the GWs emitted by precessing binaries. Second, even if two signals have values of $\mathcal{N}_{\rm GW}$ that differ by $\sim$ one when $\omega_{\rm max}$ equals the GW ending frequency (which apparently represents a total loss of coherence, and hence a significant decrease in overlap), one can always shift their arrival times to obtain higher overlaps. Third, in the context of GW searches the differences in $\mathcal{N}_{\rm GW}$ should be minimized with respect to the search parameters, as done with the fitting factor.

The Cauchy criterion [28] states that the sequence ST_N converges if and only if for every k, $\langle \mathrm{ST}_{N+k}, \mathrm{ST}_N\rangle \to 1$ as $N \to \infty$. In Table 3.2, we test the specific case of $k = 0.5$, for maximally spinning and nonspinning $(10 + 1.4)M_\odot$ and $(12 + 3)M_\odot$ binaries. The overlaps quoted at the beginning of each column are maximized over the extrinsic parameters t_0 and Φ_0, but not over the five extrinsic directional parameters φ, Θ, θ, ϕ and ψ or the intrinsic parameters m_1, m_2, χ_1 and κ_1 (we call this the *nonmaximized* overlap). For comparison, we show in parentheses the overlaps maximized over all the parameters of the lower-order family [i.e., the *fitting factors* (FF) for the target family ST_{N+k} as matched by the search family ST_N]; we show in brackets the parameters at which the maximum overlaps are achieved. [The overlaps are especially bad when 1PN and 2.5PN waveforms are used. These two orders are rather peculiar: The flux function $\mathcal{F}$ can be a decreasing function of ω, and even assume negative values (which is obviously not physical); correspondingly, $\dot{\omega}$ can become negative. Furthermore, the MECO criterion used to set the ending frequency can also fail, because for some configurations the MECO does not exist, or occurs after $\dot{\omega}$ has become negative. To avoid these problems, we stop the numerical integration of the equations of motion when $\dot{\omega}$ decreases to one-tenth of its Newtonian value, or at a GW frequency of 1 kHz, whichever comes first. For comparison, in Table 3.2 we show also the overlaps between ST_2 and ST_3, which are much higher than those between ST_2 and $\mathrm{ST}_{2.5}$, and

than those between $ST_{2.5}$ and ST_3.]

While the nonmaximized overlaps can be very low, the FFs are consistently high (note that this requires extending the search into the unphysical template region where $\eta > 0.25$ and $\chi_1 > 1$); however, the best-fit search parameters can be rather different from the target parameters. This suggests that higher-order PN effects can be reabsorbed by a change of parameters, so the ST_N templates can be considered rather reliable for the purpose of detecting GWs from precessing binaries in the mass range examined; however, the estimation of binary parameters can suffer from systematic errors. In the rest of this chapter we shall describe and analyze a search scheme that uses the ST_2 template family.

A more thorough analysis of the differences between the various PN orders would be obtained by comparing the PN-expanded adiabatic model used in this chapter with PN-resummed adiabatic models (*à la* Padé [28]) and nonadiabatic models (*à la* effective-one-body [44]). A similar comparison was carried out for the nonspinning case in Refs. [24, 22]. Unfortunately, waveforms that include precessional effects are not yet available for the PN-resummed adiabatic and nonadiabatic models.

3.4 A new physical template family for NS–BH and BH–BH precessing binaries

In this section we discuss the detection of GWs from single-spin precessing binaries using the template family first suggested in BCV2, and further discussed in Sec. 3.3. The proposed detection scheme involves the deployment of a discrete template bank along the relevant range of the intrinsic parameters M, η, χ_1, and κ_1, and the use of a detection statistic that incorporates the maximization of the overlap over all the extrinsic parameters: the directional angles Θ, φ, θ, ϕ, and ψ, the time of arrival t_0, and the initial phase Φ_0. In Sec. 3.4.1 we describe the reparametrization of the templates used for the formulation of the maximized statistic, which is then discussed in Sec. 3.4.2, where we also present an approximated but computationally cheaper version. The exact and approximated statistics are discussed together in Sec. 3.5 in the context of an optimized two-stage detection scheme.

3.4.1 Reparametrization of the waveforms

We recall from Eqs. (3.15)–(3.21) that the generic functional form of our precessing templates is

$$h[\lambda^A] = Q^{ij}[M, \eta, \chi_1, \kappa_1; \Phi_0, t_0; t] P_{ij}[\Theta, \varphi; \theta, \phi, \psi]. \tag{3.27}$$

[Please note that for the rest of this chapter we shall use coupled raised and lowered indices to denote contraction; however, the implicit metric is always Euclidian, so covariant and contravariant components are equal. This will be true also for the symmetric trace-free (STF) components introduced later, which are denoted by uppercase roman indices.]

The factor $Q^{ij}(t)$ (which describes the time-evolving dynamics of the precessing binary) is given by

$$Q^{ij} = -\frac{2\mu}{D}\frac{M}{r}\Big[[\mathbf{e}_+]^{ij}\cos 2(\Phi+\Phi_0) + [\mathbf{e}_\times]^{ij}\sin 2(\Phi+\Phi_0)\Big], \tag{3.28}$$

where the GW phase $\Phi(t)$ and the GW polarization tensors $\mathbf{e}_{+,\times}(t)$ evolve according to the equations (3.5), (3.13), and (3.14). This factor depends on the intrinsic parameters M, η, χ_1, and κ_1, and on two extrinsic parameters: the initial phase Φ_0, and the time of arrival t_0 of the waveform, referred to a fiducial GW frequency. We can factor out the initial phase Φ_0 by defining

$$Q^{ij}_0 \equiv Q^{ij}(\Phi_0 = 0)\,, \tag{3.29}$$

$$Q^{ij}_{\pi/2} \equiv Q^{ij}(\Phi_0 = \pi/4)\,; \tag{3.30}$$

we then have

$$Q^{ij} = Q^{ij}_0\cos(2\Phi_0) + Q^{ij}_{\pi/2}\sin(2\Phi_0). \tag{3.31}$$

The factor P_{ij} (which describes the static relative position and orientation of the detector with respect to the axes initially defined by the binary) is given by

$$P_{ij} = [\mathbf{T}_+]_{ij}F_+ + [\mathbf{T}_\times]_{ij}F_\times, \tag{3.32}$$

where the detector antenna patterns $F_{+,\times}(\theta,\phi,\psi)$ and the detector polarization tensors $\mathbf{T}_{+,\times}(\Theta,\varphi)$ depend on the orientation angles θ, ϕ, and ψ, and on the position angles Θ and φ, all of them extrinsic parameters. The antenna patterns can be rewritten as

$$\left\{\begin{array}{c} F_+ \\ F_\times \end{array}\right\} = \sqrt{F_+^2 + F_\times^2}\left\{\begin{array}{c} \cos\alpha \\ \sin\alpha \end{array}\right\}; \tag{3.33}$$

the factor $F \equiv \sqrt{F_+^2 + F_\times^2}$ then enters h as an overall multiplicative constant [45]. In what follows we shall be considering normalized signals and templates, where F drops out, so we set $F = 1$. We then have

$$P_{ij} = [\mathbf{T}_+]_{ij}\cos\alpha + [\mathbf{T}_\times]_{ij}\sin\alpha. \tag{3.34}$$

Both $Q^{ij}(t)$ and P_{ij} are three-dimensional STF tensors, with five independent components each. Using an orthonormal STF basis M^I_{ij}, $I = 1,\ldots,5$, with $(M^I)_{ij}(M^J)^{ij} = \delta^{IJ}$, we can conveniently express P_{ij} and Q^{ij} in terms of their components on this basis,

$$Q^{ij} = Q^I(M^I)^{ij}\,, \quad P_{ij} = P^I(M^I)_{ij}\,, \tag{3.35}$$

where

$$Q^I = Q^{ij}(M^I)_{ij}\,, \quad P^I = P_{ij}(M^I)^{ij}\,. \tag{3.36}$$

In this chapter, we shall adopt a particular orthonormal basis,

$$\begin{aligned}
(M^1)_{ij} &= \sqrt{\frac{4\pi}{15}}(\mathcal{Y}^{22}_{ij} + \mathcal{Y}^{2-2}_{ij}),\\
(M^2)_{ij} &= -i\sqrt{\frac{4\pi}{15}}(\mathcal{Y}^{22}_{ij} - \mathcal{Y}^{2-2}_{ij}),\\
(M^3)_{ij} &= -\sqrt{\frac{4\pi}{15}}(\mathcal{Y}^{21}_{ij} - \mathcal{Y}^{2-1}_{ij}),\\
(M^4)_{ij} &= i\sqrt{\frac{4\pi}{15}}(\mathcal{Y}^{21}_{ij} + \mathcal{Y}^{2-1}_{ij}),\\
(M^5)_{ij} &= -\sqrt{\frac{8\pi}{15}}\mathcal{Y}^{20}_{ij},
\end{aligned} \tag{3.37}$$

with $\mathcal{Y}^{2m}_{ij}$ defined by

$$\mathcal{Y}^{2m}_{ij} q^i q^j \equiv Y^{2m}(\hat{\mathbf{q}}), \tag{3.38}$$

where $Y^{2m}(\hat{\mathbf{q}})$, $m = -2, \ldots, 2$ are the usual $l = 2$ spherical harmonics, and $\hat{\mathbf{q}}$ is any unit vector. We bring together this result with Eqs. (3.31) and (3.34) to write the final expression

$$h = P_I\Big(Q^I_0 \cos(2\Phi_0) + Q^I_{\pi/2} \sin(2\Phi_0)\Big), \tag{3.39}$$

where

$$P_I(\Theta, \varphi, \alpha) = \Big([\mathbf{T}_+(\Theta, \varphi)]_I \cos\alpha + [\mathbf{T}_\times(\Theta, \varphi)]_I \sin\alpha\Big). \tag{3.40}$$

Henceforth, we shall denote the surviving extrinsic parameters collectively as $\Xi^\alpha \equiv (t_0, \Phi_0, \alpha, \Theta, \varphi)$, and the intrinsic parameters as $X^i \equiv (M, \eta, \chi_1, \kappa_1)$.

3.4.2 Maximization of the overlap over the extrinsic parameters

As we have anticipated, it is possible to maximize the overlap $\rho = \langle s, \hat{h}\rangle$ *semialgebraically* over the extrinsic directional parameters Θ, φ, θ, ϕ, and ψ, without computing the full representation of $\hat{h}$ for each of their configurations. In addition, it is possible to maximize efficiently also over t_0 and Φ_0, which are routinely treated as extrinsic parameters in nonspinning-binary GW searches.

For a given stretch of detector output s, and for a particular set of template intrinsic parameters X^i =

$(M, \eta, \chi_1, \kappa_1)$, we denote the fully maximized overlap as

$$\rho_{\Xi^\alpha} \equiv \max_{\Xi^\alpha} \langle s, \hat{h}(X^i, \Xi^\alpha)\rangle = \max_{t_0,\Phi_0,\Theta,\varphi,\alpha} \underbrace{\left[\frac{P_I\left[\langle s, Q^I_0\rangle_{t_0}\cos 2\Phi_0 + \langle s, Q^I_{\pi/2}\rangle_{t_0}\sin 2\Phi_0\right]}{\sqrt{P_I P_J \langle Q^I_0 \cos 2\Phi_0 + Q^I_{\pi/2}\sin 2\Phi_0, Q^J_0\cos 2\Phi_0 + Q^J_{\pi/2}\sin 2\Phi_0\rangle}}\right]}_{\rho}, \tag{3.41}$$

where the subscript t_0 denotes the dependence of the signal-template inner products on the time-of-arrival parameter of the templates. In fact, each of these inner products can be computed simultaneously for all t_0 with a single FFT; in this sense, t_0 is an extrinsic parameter [46].

Let us now see how to deal with Φ_0. We start by making an approximation that will be used throughout this chapter. We notice that the template components $P_I Q^I_0$ and $P_I Q^I_{\pi/2}$ [Eqs. (3.29) and (3.30)] are nearly orthogonal, and have approximately the same signal power,

$$\langle P_I Q^I_0, P_J Q^J_{\pi/2}\rangle \simeq 0\,, \tag{3.42}$$

$$\langle P_I Q^I_0, P_J Q^J_0\rangle \simeq \langle P_I Q^I_{\pi/2}, P_J Q^J_{\pi/2}\rangle\,; \tag{3.43}$$

this is accurate as long as the timescales for the radiation reaction–induced evolution of frequency and for the precession-induced evolution of phase and amplitude modulations are both much longer than the orbital period. More precisely, Eqs. (3.42) and (3.43) are valid up to the leading-order stationary-phase approximation. Under this hypothesis Eq. (3.41) simplifies, and its maximum over Φ_0 is found easily:

$$\begin{aligned}\rho_{\Xi^\alpha} &= \max_{t_0,\Phi_0,\Theta,\varphi,\alpha} \frac{P_I\left[\langle s, Q^I_0\rangle\cos 2\Phi_0 + \langle s, Q^I_{\pi/2}\rangle\sin 2\Phi_0\right]}{\sqrt{P_I P_J\langle Q^I_0, Q^J_0\rangle}} \\ &= \max_{t_0,\Theta,\varphi,\alpha}\sqrt{\frac{P_I P_J A^{IJ}}{P_I P_J B^{IJ}}} \equiv \max_{t_0,\Theta,\varphi,\alpha}\rho_{\Phi_0}\,,\end{aligned} \tag{3.44}$$

where we have defined the two matrices

$$\begin{aligned}A^{IJ} &\equiv \langle s, Q^I_0\rangle_{t_0}\langle s, Q^J_0\rangle_{t_0} + \langle s, Q^I_{\pi/2}\rangle_{t_0}\langle s, Q^J_{\pi/2}\rangle_{t_0}\,, \\ B^{IJ} &\equiv \langle Q^I_0, Q^J_0\rangle\,,\end{aligned} \tag{3.45}$$

which are functions only of the intrinsic parameters (and, for A^{IJ}, of t_0). We have tested the approximations (3.42) and (3.43) by comparing the maximized overlaps obtained from Eq. (3.44) with the results of full numerical maximization without approximations; both the values and the locations of the maxima agree to one part in a thousand, even for systems with substantial amplitude and phase modulations, where the approximations are expected to be least accurate.

Although Eq. (3.44) looks innocent enough, the maximization of ρ_{Φ_0} is not a trivial operation. The

five components of P_I in Eq. (3.44) are not all independent, but they are specific functions of only three parameters, Θ, φ, and α [see the discussion leading to Eqs. (3.34) and (3.40).] We can therefore think of ρ_{Ξ^α} as the result of maximizing ρ_{Φ_0} with respect to the five-dimensional vector P_I, *constrained to the three-dimensional physical submanifold* $P_I(\Theta, \varphi, \alpha)$. We shall then refer to ρ_{Ξ^α} as the *constrained* maximized overlap.

What is the nature of the constraint surface? We can easily find the two constraint equations that define it. First, we notice from Eqs. (3.41) and (3.44) that the magnitude of the vector P_I does not affect the overlap: so we may rescale P_I and set one of the constraints as $P_I P^I = 1$; even better, we may require that the denominator of Eq. (3.44) be unity, $P_I P_J B^{IJ} = 1$. Second, we remember that P_{ij} [Eq. (3.32)] is the polarization tensor for a plane GW propagating along the direction vector

$$\hat{N}^i = (\sin\Theta\cos\varphi,\ \sin\Theta\sin\varphi,\ \cos\Theta). \tag{3.46}$$

Because GWs are transverse, P_{ij} must admit $\hat{N}^i$ as an eigenvector with null eigenvalue; it follows that

$$\det P_{ij} = 0. \tag{3.47}$$

This equation can be turned into the second constraint for the P_I [see Eq. (3.87) of App. 3.9].

Armed with the two constraint equations, we can reformulate our maximization problem using the method of Lagrangian multipliers [Eq. (3.88) in App. 3.9]. However, the resulting system of cubic algebraic equations does not appear to have closed-form analytic solutions. In App. 3.9 we develop an iterative algebraic procedure to solve the system, obtaining the constrained maximum and the corresponding P_I. In practice, we have found it operationally more robust to use a closed-form expression for the partial maximum over Φ_0 and α (which seems to be the farthest we can go analytically), and then feed it into a numerical maximum-finding routine (such as the well-known `amoeba` [47]) to explore the (Θ, φ) sphere, repeating this procedure for all t_0 to obtain the full maximum.

To maximize ρ_{Φ_0} over α, we use Eq. (3.40) to factor out the dependence of the P_I on α, and write

$$\sqrt{\frac{P_I P_J A^{IJ}}{P_I P_J B^{IJ}}} = \sqrt{\frac{\mathbf{u}\mathbf{A}_\alpha\mathbf{u}^T}{\mathbf{u}\mathbf{B}_\alpha\mathbf{u}^T}}\,, \tag{3.48}$$

where $\mathbf{u}$ is the two-dimensional row vector $(\cos\alpha, \sin\alpha)$, and where $\mathbf{A}_\alpha$ and $\mathbf{B}_\alpha$ are the two-by-two matrices

$$\mathbf{A}_\alpha = A^{IJ}\begin{pmatrix} [\mathbf{T}_+]_I[\mathbf{T}_+]_J & [\mathbf{T}_+]_I[\mathbf{T}_\times]_J \\ [\mathbf{T}_+]_I[\mathbf{T}_\times]_J & [\mathbf{T}_\times]_I[\mathbf{T}_\times]_J \end{pmatrix}, \tag{3.49}$$

$$\mathbf{B}_\alpha = B^{IJ}\begin{pmatrix} [\mathbf{T}_+]_I[\mathbf{T}_+]_J & [\mathbf{T}_+]_I[\mathbf{T}_\times]_J \\ [\mathbf{T}_+]_I[\mathbf{T}_\times]_J & [\mathbf{T}_\times]_I[\mathbf{T}_\times]_J \end{pmatrix}; \tag{3.50}$$

in these definitions we sum over the indices I and J. The matrices $\mathbf{A}_\alpha$ and $\mathbf{B}_\alpha$ are implicitly functions of the angles Θ and φ through the polarization tensors $\mathbf{T}_+$ and $\mathbf{T}_\times$. It is straightforward to maximize Eq. (3.48) over α, yielding [48]

$$\rho_{\Xi^\alpha} = \max_{t_0,\Theta,\varphi} \sqrt{\max \operatorname{eigv} [\mathbf{A}_\alpha \, \mathbf{B}_\alpha^{-1}]} \equiv \max_{t_0,\Theta,\varphi} \rho_{\Phi_0,\alpha} \,. \tag{3.51}$$

The overlap $\rho_{\Phi_0,\alpha}$ is essentially equivalent to the $\mathcal{F}$ statistic used in the search of GWs from pulsars [49].

The last step in obtaining ρ_{Ξ^α} is to maximize $\rho_{\Phi_0,\alpha}$ numerically over the (Θ, φ) sphere, repeating this procedure for all t_0 to obtain the full maximum. Now, t_0 enters Eq. (3.51) only through the ten signal-template inner products $\langle s, Q^I_{0,\pi/2} \rangle$ contained in $\mathbf{A}_\alpha$, and each such product can be computed for all t_0 with a single FFT. Even then, the semialgebraic maximization procedure outlined above can still be very computationally expensive if the search over Θ and φ has to be performed for each individual t_0. We have been able to reduce computational costs further by identifying a rapidly computed, fully algebraic statistic ρ'_{Ξ^α} that approximates ρ_{Ξ^α} from above. We then economize by performing the semialgebraic maximization procedure only for the values of t_0 for which ρ'_{Ξ^α} rises above a certain threshold; furthermore, the location of the approximated maximum provides good initial guesses for Θ and φ, needed to kickstart their numerical maximization.

Quite simply, our fast approximation consists in neglecting the functional dependence of the P_I on the directional parameters, computing instead the maximum of ρ_{Φ_0} [Eq. (3.44)] as if the five P_I were free parameters. Using the method of Lagrangian multipliers outlined in the beginning of App. 3.9 [Eqs. (3.84)–(3.86)], we get

$$\rho'_{\Xi^\alpha} = \max_{P_I} \sqrt{\frac{P_I P_J A^{IJ}}{P_I P_J B^{IJ}}} = \sqrt{\max \operatorname{eigv} [\mathbf{A} \, \mathbf{B}^{-1}]} \,, \tag{3.52}$$

with

$$(A^{IJ} - \lambda B^{IJ}) P_J = 0 \,, \qquad \lambda = \max \operatorname{eigv}[\mathbf{A} \, \mathbf{B}^{-1}] \,. \tag{3.53}$$

Here the prime stands for *unconstrained* maximization over P_I. We shall henceforth refer to ρ'_{Ξ^α} as the *unconstrained maximum*.

Note that the value of the P_I at the unconstrained maximum will not in general correspond to a physical set of directional parameters, so P_{ij} will not admit any direction vector $\hat{N}^i$ [Eq. (3.46)] as a null eigenvector. However, we can still get approximate values of Θ and φ by using instead the eigenvector of P_{ij} with the smallest eigenvalue (in absolute value).

3.5 Description and test of a two-stage search scheme

In Sec. 3.4 we have described a robust computational procedure to find the maximum overlap ρ_{Ξ^α} (which is maximized over the extrinsic parameters Φ_0, t_0, and P_I, where the allowed values of the P_I are constrained by their functional dependence on the directional angles). We have also established a convenient analytic approximation for ρ_{Ξ^α}, the unconstrained maximized overlap ρ'_{Ξ^α} (which is maximized over the extrinsic

parameters Φ_0, t_0, and P_I, but where the P_I are treated as five independent and unconstrained coefficients). Because the unconstrained maximization has access to a larger set of P_I, it is clear that $\rho'_{\Xi^\alpha} > \rho_{\Xi^\alpha}$. Still, at least when the target signal s is very close to the template $h(X_i)$, we expect ρ'_{Ξ^α} to be a very good approximation for ρ_{Ξ^α}.

A quick look at the procedures outlined in Sec. 3.4 shows that, for the filtering of experimental data against a discrete bank of templates $\{h(X^i_{(k)})\}$, the computation of ρ'_{Ξ^α} is going to be much faster than the computation of ρ_{Ξ^α}. Under these conditions, it makes sense to implement a two-stage search scheme where the discrete bank $\{h(X^i_{(k)})\}$ is first reduced by selecting the templates that have high ρ'_{Ξ^α} against the experimental data; at this stage we identify also the promising times of arrival t_0. The exact ρ_{Ξ^α} is computed only for these first-stage triggers, and compared with the detection threshold ρ^* to identify detection candidates (one would use the same threshold ρ^* in the first stage to guarantee that all the detection candidates will make it into the second stage) [50].

To prove the viability of such a search scheme, we shall first establish that ρ'_{Ξ^α} is a good approximation for ρ_{Ξ^α} for target signals and templates computed using the adiabatic model of Sec. 3.3. We will take slightly displaced intrinsic parameters for target signals and templates, to reproduce the experimental situation where we are trying to detect a signal of arbitrary physical parameters with the closest template belonging to a discrete bank. This first test is described in Sec. 3.5.1. We shall then study the false-alarm statistics of ρ_{Ξ^α} and ρ'_{Ξ^α}, and we shall show that, for a given detection threshold, the number of first-stage triggers caused by pure noise is only a few times larger than the number of *bona fide* second-stage false alarms. Such a condition is necessary because the two-stage detection scheme is computationally efficient only if few templates need ever be examined in the expensive second stage. The false-alarm statistics (in Gaussian stationary noise) are obtained in Sec. 3.5.2, and the second test is described in Sec. 3.5.3.

3.5.1 Numerical comparison of constrained and unconstrained maximized overlaps

In this section we describe a set of Monte Carlo runs designed to test how well ρ'_{Ξ^α} can approximate ρ_{Ξ^α}, for the target signals and templates computed using the adiabatic model of Sec. 3.3, for typical signal parameters, and for signal–template parameter displacements characteristic of an actual search. We choose target signals with 20 different sets of intrinsic parameters given by

$$(m_1, m_2, \chi_1, \kappa_1) = \left\{ \begin{array}{c} (10, 1.4) M_\odot \\ (7, 3) M_\odot \end{array} \right\} \times \left\{ \begin{array}{c} 0.5 \\ 1 \end{array} \right\} \times \left\{ \begin{array}{c} -0.9 \\ -0.5 \\ 0.0 \\ 0.5 \\ 0.9 \end{array} \right\}. \tag{3.54}$$

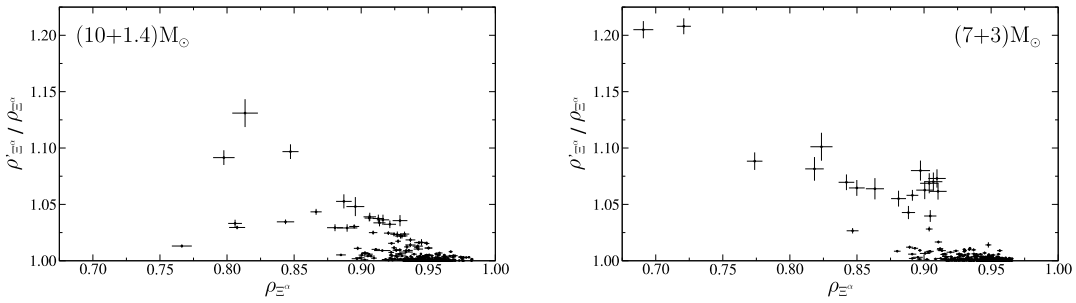

Figure 3.4: Ratio between the unconstrained (ρ'_{Ξ^α}) and constrained (ρ_{Ξ^α}) maximized overlaps, as a function of ρ_{Ξ^α}. Each point corresponds to one out of 20×50 sets of intrinsic parameters for target signal and template, and is averaged over 100 sets of extrinsic parameters for the target signal. The error bars show the standard deviations of the sample means (the standard deviations of the samples themselves will be 10 times larger, since we sample 100 sets of extrinsic parameters). The two panels show results separately for $(10 + 1.4)M_\odot$ (left) and $(7 + 3)M_\odot$ target systems (right). The few points scattered toward higher ratios and lower ρ_{Ξ^α} are obtained when the first set of extrinsic parameters happens to yield a high ρ'_{Ξ^α} that is not representative of most other values of the extrinsic parameters; then the magnitude of the intrinsic-parameter deviation is set too high, and the comparison between ρ'_{Ξ^α} and ρ_{Ξ^α} is done at low ρ_{Ξ^α}, where the unconstrained maximized overlap is a poor approximation for its constrained version.

For each set of target-signal intrinsic parameters, we choose 100 random sets of extrinsic parameters $(\Theta, \varphi, \alpha, \Phi_0)$, where the combination (Θ, φ) is distributed uniformly on the solid angle, and where α and Φ_0 are distributed uniformly in the $[0, 2\pi]$ interval. The target signals are normalized, so the allowed range for ρ_{Ξ^α} and ρ'_{Ξ^α} is $[0, 1]$.

For each target signal, we test 50 (normalized) templates displaced in the intrinsic-parameter space $(M, \eta, \chi_1, \kappa_1)$ (the optimal extrinsic parameters will be determined by the optimization of ρ_{Ξ^α} and ρ'_{Ξ^α}, so we do not need to set them). The direction of the displacement is chosen randomly in the $(M, \eta, \chi_1, \kappa_1)$ space. For simplicity, the magnitude of the displacement is chosen so that, for each set of target-signal intrinsic parameters and for the *first set* of target-signal extrinsic parameters, the overlap ρ'_{Ξ^α} is about 0.95; the magnitude is then kept fixed for the other 99 extrinsic-parameter sets, so ρ'_{Ξ^α} can be very different in those cases.

Figure 3.4 shows the ratio $\rho'_{\Xi^\alpha}/\rho_{\Xi^\alpha}$, for each pair (20×50 in total) of target and template intrinsic-parameter points, averaged over the 100 target extrinsic-parameter points, as a function of the averaged ρ_{Ξ^α}. The ρ'_{Ξ^α} get closer to the ρ_{Ξ^α} as the latter get higher; most important, the difference is within $\sim 2\%$ when $\rho_{\Xi^\alpha} > 0.95$, which one would almost certainly want to achieve in an actual search for signals. We conclude that ρ'_{Ξ^α} can indeed be used as an approximation for ρ_{Ξ^α} in the first stage of a two-stage search. The second stage is still necessary, because the false-alarm statistics are worse for the unconstrained maximized overlap (where more degrees of freedom are available) than for its constrained version. We will come back to this in the next two sections.

It is also interesting to compare the set of extrinsic parameters of the target signal with the set of extrinsic parameters that maximize ρ_{Ξ^α}, as characterized by the corresponding source direction vectors, $\hat{\mathbf{N}}_{\rm true}$ and $\hat{\mathbf{N}}_{\rm max}$

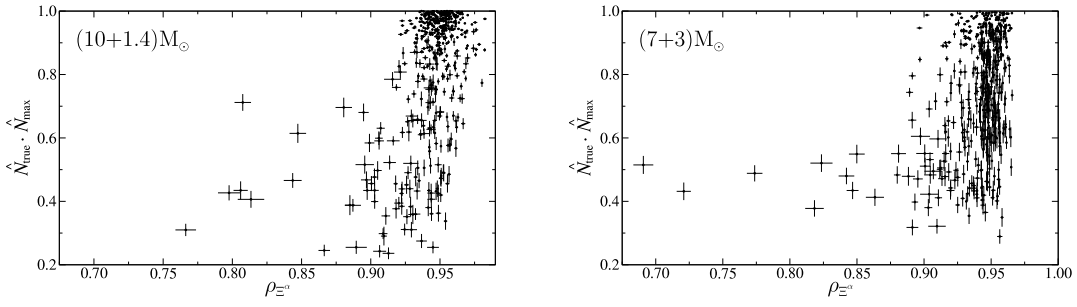

Figure 3.5: Inner product between target-signal source direction $\hat{\mathbf{N}}_{\rm true}$ and ρ_{Ξ^α}-maximizing source direction $\hat{\mathbf{N}}_{\rm max}$, as a function of ρ_{Ξ^α}. Each point corresponds to one out of 20×50 sets of intrinsic parameters for target signal and template, and is averaged over 100 sets of extrinsic parameters for the target signal. Standard deviations of the sample means are shown as error bars, as in Fig. 3.4. The two panels show separately $(10 + 1.4)M_\odot$ target systems (left) and $(7 + 3)M_\odot$ target systems (right).

respectively. Figure 3.5 shows the inner product $\hat{\mathbf{N}}_{\rm true}\cdot\hat{\mathbf{N}}_{\rm max}$, averaged over the 100 target extrinsic-parameter points, as a function of the averaged ρ_{Ξ^α}. The difference between the vectors can be very large, even when $\rho_{\Xi^\alpha} > 0.95$: This happens because the intrinsic-parameter displacement between target signal and template can be compensated by a change in the extrinsic parameters of template (in other words, the effects of the intrinsic and extrinsic parameters on the waveforms are highly correlated).

3.5.2 False-alarm statistics for the constrained and unconstrained maximized overlaps

In this section we derive and compare the false-alarm statistics of ρ_{Ξ^α} and ρ'_{Ξ^α}. Our purpose is to estimate the number of additional triggers that are caused by replacing the detection statistic ρ_{Ξ^α} by the first-stage statistic ρ'_{Ξ^α}. Our two-stage detection scheme, which employs the rapidly computed ρ'_{Ξ^α} to choose candidates for the more computationally expensive ρ_{Ξ^α}, will be viable only if the number of those candidates is small enough.

By definition, a false alarm happens when, with interferometer output consisting of pure noise, the detection statistic computed for a given template happens to rise above the detection threshold. Although the detection statistics ρ_{Ξ^α} and ρ'_{Ξ^α} include maximization over the time of arrival t_0, we find it convenient to exclude t_0 from this computation, and to include it later when we evaluate the total false-alarm probability for all the templates in the bank.

Recall that ρ_{Ξ^α} [Eq. (3.44)] and ρ'_{Ξ^α} [Eq. (3.52)] are functions of the matrices $\mathbf{A}$ and $\mathbf{B}$, which contain the inner products $\langle s, Q^I_{0,\pi/2}\rangle$ and $\langle Q^I_{0,\pi/2}, Q^J_{0,\pi/2}\rangle$, respectively. In this case the signal s is a realization of the noise, n. We combine the vectors Q^I_0 and $Q^I_{\pi/2}$ together as $Q^{\mathcal{I}}$ with $\mathcal{I} = 1,\ldots,10$; under the assumption of Gaussian stationary noise, $Y^{\mathcal{I}} \equiv \langle n, Q^{\mathcal{I}}\rangle$ is a ten-dimensional Gaussian random vector with zero mean and covariance matrix [36]

$$C^{\mathcal{I}\mathcal{J}} = \overline{\langle n, Q^{\mathcal{I}}\rangle\langle n, Q^{\mathcal{J}}\rangle} = \langle Q^{\mathcal{I}}, Q^{\mathcal{J}}\rangle\,. \tag{3.55}$$

The covariance matrix $C^{\mathcal{I}\mathcal{J}}$ completely specifies the statistical properties of the random vector $Y^{\mathcal{I}}$, and it is a function only of $\mathbf{B}$, and therefore only of the intrinsic parameters of the template. We can also combine $P_I \cos 2\Phi_0$ and $P_I \sin 2\Phi_0$ together as $P_{\mathcal{I}}$, and then write the maximized overlaps ρ_{Ξ^α} and ρ'_{Ξ^α} as

$$\max_{P_{\mathcal{I}}} \frac{P_{\mathcal{I}}\langle n, Q^{\mathcal{I}}\rangle}{\sqrt{P_{\mathcal{I}}P_{\mathcal{J}}\langle Q^{\mathcal{I}}, Q^{\mathcal{J}}\rangle}} = \max_{P_{\mathcal{I}}} \frac{P_{\mathcal{I}}Y^{\mathcal{I}}}{\sqrt{P_{\mathcal{I}}P_{\mathcal{J}}C^{\mathcal{I}\mathcal{J}}}}\,, \tag{3.56}$$

where maximization is performed over the appropriate range of the $P_{\mathcal{I}}$. In the rest of this section we shall use the shorthand ρ to denote both ρ_{Ξ^α} and ρ'_{Ξ^α}.

Equation (3.56) is very general: It describes ρ_{Ξ^α} and ρ'_{Ξ^α}, but it can also incorporate other maximization ranges over the $P_{\mathcal{I}}$, and it can even treat different template families. In fact, the maximized detection statistic for the $(\psi_0\psi_{3/2}\mathcal{B})_6$ DTF of BCV2 can be put into the same form, with $P_{\mathcal{I}} \equiv \alpha_{\mathcal{I}}$, for $\mathcal{I} = 1, \ldots, 6$, and with completely unconstrained maximization.

We can now generate a distribution of the detection statistic ρ for a given set of intrinsic parameters by generating a distribution of the Gaussian random vector $Y^{\mathcal{I}}$, and then computing ρ from Eq. (3.56). The first step is performed easily by starting from ten independent Gaussian random variables $Z^{\mathcal{I}}$ of zero mean and unit variance, and then setting $Y^{\mathcal{I}} = [\sqrt{C}]^{\mathcal{I}\mathcal{J}} Z_{\mathcal{J}}$ [51]. Thus, there is no need to generate actual realizations of the noise as time series, and no need to compute the inner products $\langle n, Q^{\mathcal{I}}\rangle$ explicitly.

The statistics ρ [Eq. (3.56)] are homogeneous with respect to the vector $Z^{\mathcal{I}}$: that is, if we define $Z^{\mathcal{I}} = r\hat{Z}^{\mathcal{I}}$ (where $r \equiv \sqrt{Z^{\mathcal{I}}Z_{\mathcal{I}}}$ and $\hat{Z}^{\mathcal{I}}\hat{Z}_{\mathcal{I}} = 1$) we have

$$\rho[Y^{\mathcal{I}}(Z^{\mathcal{I}})] = r\rho[Y^{\mathcal{I}}(\hat{Z}^{\mathcal{I}})] \equiv r\rho_1(\Omega)\,; \tag{3.57}$$

here Ω represents the direction of $\hat{Z}^{\mathcal{I}}$ in its ten-dimensional Euclidian space. The random variable r has the marginal probability density

$$p_r(r) = \frac{r^{\nu-1}\exp(-r^2/2)}{2^{\nu/2-1}\Gamma(\nu/2)}\,, \tag{3.58}$$

where the direction Ω is distributed uniformly over a ten-sphere. (For the rest of this section we shall write equations in the general ν-dimensional case; the special case of our template family is recovered by setting $\nu = 10$.] The random variables r and Ω [and therefore $\rho_1(\Omega)$) are statistically independent, so the cumulative distribution function for the statistic ρ is given by the integral

$$P(\rho < \rho^*) = \int d\Omega \int_0^{\rho^*/\rho_1(\Omega)} p_r(r)\, dr \Big/ \int d\Omega = 1 - \int \frac{\Gamma\left[\frac{\nu}{2}, \frac{\left(\rho^*/\rho_1(\Omega)\right)^2}{2}\right]}{\Gamma\left[\frac{\nu}{2}\right]} d\Omega \Big/ \int d\Omega\,, \tag{3.59}$$

where $\Gamma[k, z] = \int_z^{+\infty} t^{k-1}e^{-t}dt$ is the *incomplete gamma function*.

The false-alarm probability for a single set of intrinsic parameters and for a single time of arrival is then $1 - P(\rho < \rho^*)$. The final integral over the ν-dimensional solid angle can be performed by Monte Carlo

integration, averaging the integrand over randomly chosen directions Ω. Each sample of the integrand is obtained by generating a normalized $\hat{Z}^I$ (that is, a direction Ω), obtaining the corresponding Y^I, computing $\rho_1(\Omega)$ from Eq. (3.56), and finally plugging $\rho_1(\Omega)$ into the Γ function.

Equation (3.59) shows that if we set $\rho_1(\Omega) = 1$, the random variable ρ follows the $\chi_{(\nu)}$ distribution; this is obvious because in that case $\rho = r = \sqrt{Z^I Z_I}$ [see Eq. (3.57)], where the Z^I are ν independent Gaussian random variables. In fact, $\rho_1(\Omega)$ can be written as

$$\rho_1(\Omega) = \max_{P^I} \frac{R_I \hat{Z}^I}{\sqrt{R_I R_{\mathcal{J}} \delta^{I\mathcal{J}}}}, \quad \text{where } R_I = [\sqrt{C}]_{I\mathcal{J}} P^{\mathcal{J}}; \tag{3.60}$$

which shows that $\rho_1(\Omega) = 1$ uniformly for every Ω if and only if the range of maximization for P_I is the *entire* ν-dimensional linear space generated by the basis $\{Q^I\}$; however, once we start using the entire linear space, the particular basis used to generate it ceases to be important, so the covariance matrix $C^{I\mathcal{J}}$ drops out of the equations for the false-alarm probabilities. That is the case, for instance, for the $(\psi_0\psi_{3/2}\mathcal{B})_6$ DTF (see Sec. V B of BCV2), whose false-alarm probability is described by the $\chi_{(\nu=6)}$ distribution. For our template family $\nu = 10$, but both ρ_{Ξ^α} and ρ'_{Ξ^α} have very restrictive maximization ranges for P_I (because $P_{I=1,\dots,5}$ and $P_{I=6,\dots,10}$ are strongly connected): so both ρ_{Ξ^α} and ρ'_{Ξ^α} will have much lower false-alarm probability, for the same threshold ρ^*, than suggested by the $\chi_{(\nu=10)}$ distribution. In fact, in the next section we shall see that the effective ν for the detection statistic ρ'_{Ξ^α} is about 6; while the effective ν for ρ_{Ξ^α} is even lower.

3.5.3 Numerical investigation of false-alarm statistics

The total false-alarm probability for the filtering of experimental data by a template bank over a time T is

$$P_{\text{tot}}(\rho > \rho^*) = 1 - \left[P(\rho < \rho^*)\right]^{\mathcal{N}_{\text{shapes}}\mathcal{N}_{\text{times}}} \tag{3.61}$$

(see for instance BCV1), where the exponent $\mathcal{N}_{\text{shapes}}\mathcal{N}_{\text{times}}$ is an estimate of the number of effective independent statistical tests. The number of independent signal shapes $\mathcal{N}_{\text{shapes}}$ is related to (and smaller than) the number of templates in the bank [52]; the number of independent times of arrival $\mathcal{N}_{\text{times}}$ is roughly $T/\delta t_0$, where δt_0 is the mismatch in the time of arrival needed for two nearby templates to have, on average, very small overlap. In our tests we set $\mathcal{N}_{\text{shapes}} = 10^6$ and $\mathcal{N}_{\text{times}} = 3 \times 10^{10}$ (or equivalently $\delta t_0 \simeq 1$ ms), as suggested by the results of Sec. 3.6 for template counts and for the full mismatch metric; in fact, both numbers represent rather conservative choices.

We compute single-test false-alarm probabilities from Eq. (3.59), averaging the integrand over 10^5 randomly chosen values of Ω to perform the integration over Ω. Our convergence tests indicate that this many samples are enough to obtain the required precision [53]. In Fig. 3.6 we show the thresholds ρ^* required to achieve a total false-alarm rate of 10^{-3}/year; the figure suggests that a threshold close to 10 is adequate. The thresholds are only marginally higher for the unconstrained statistic, so the number of first-stage false alarms

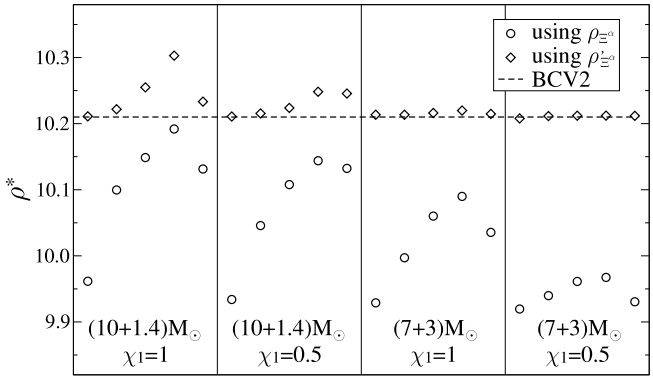

Figure 3.6: Detection thresholds ρ^* for a false-alarm rate of 10^{-3}/year, using the constrained statistic ρ_{Ξ^α} (circles), the approximated (unconstrained) statistic ρ'_{Ξ^α} (diamonds), and the detection statistic for the $(\psi_0\psi_{3/2}\mathcal{B})_6$ DTF from BCV2 (dashed line). The four windows correspond to the masses and χ_1 shown; the points in each window correspond to $\kappa_1 = 0.9, 0.5, 0, -0.5, -0.9$.

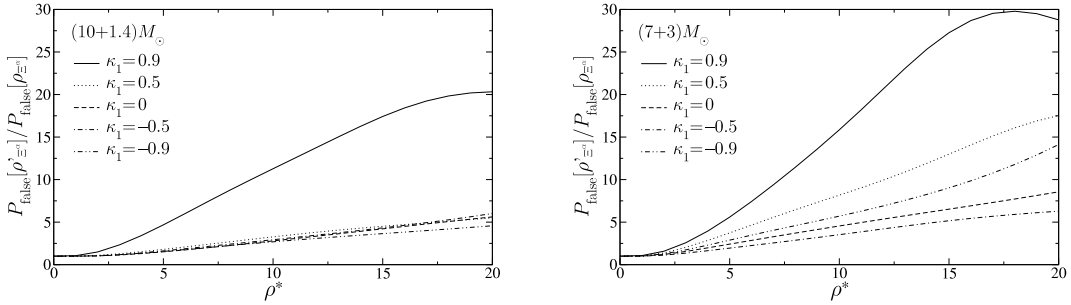

Figure 3.7: Ratio $(1 - P[\rho'_{\Xi^\alpha} < \rho^*])/(1 - P[\rho_{\Xi^\alpha} < \rho^*])$ between single-test false-alarm probabilities for the unconstrained and constrained detection statistics, as a function of threshold ρ^*. The two panels represent systems with masses equal to $(10+1.4)M_\odot$ (left) and to $(7+3)M_\odot$ (right). The five curves in each plot correspond to different κ_1.

that are dismissed in the second stage is limited. We show also the threshold required to achieve the same false-alarm rate with the $(\psi_0\psi_{3/2}\mathcal{B})_6$ DTF of BCV2: This threshold is very close to the values found for ρ'_{Ξ^α}, indicating that ρ'_{Ξ^α} has roughly six effective degrees of freedom (as it seems reasonable from counting the five P^I plus Φ_0). The BCV2 threshold is consistently higher than the ρ_{Ξ^α} threshold for the same single-test false-alarm rate; this suggests that the detection scheme discussed in this chapter is less wasteful (with respect to the available signal power) than the BCV2 scheme, assuming of course that the number of templates used in the two banks is similar.

In Fig. 3.7 we show the ratio between the single-test false-alarm probabilities for ρ_{Ξ^α} and ρ'_{Ξ^α}: for a common threshold around 10, we can expect about 5 times more false alarms using ρ'_{Ξ^α} than using ρ_{Ξ^α}, for most values of the intrinsic parameters (for some of them, this number could be as high as $\sim$ 15). These

results corroborate our suggestion of using ρ'_{Ξ^α} in the first-stage of a two-stage detection scheme, to weed out most of the detection candidates before computing the more computationally expensive ρ_{Ξ^α}.

We need to remember that our assumption of Gaussian stationary noise is usually not realized in practice. For non-Gaussian noise, the probability density function [the counterpart of $p_r(r)$ defined in Eq. (3.58), now a function of both r and Ω] drops more slowly for larger r, so more high-ρ events will appear than are expected for the Gaussian case. These events will cause false alarms for both the unconstrained and constrained statistics, but we expect the ratio of the ρ'_{Ξ^α} and ρ_{Ξ^α} false-alarm probabilities at a common threshold (shown in Fig. 3.7 for Gaussian noise) *to be reduced*, at least if the threshold is high enough; so our proposed two-stage scheme should still be relevant in reducing computational costs. This expectation is justified by the following argument. For a common threshold ρ^* and a given direction $\hat{Z}^I$, constrained-statistic triggers require $r = |Z^I|$ larger by a certain factor $N_r > 1$ than unconstrained-statistic triggers; this factor N_r is independent of ρ^* and of the probability distribution for r. Now, the ratio $P[r > N_r r_0]/P[r > r_0]$ drops much more quickly for a Gaussian distribution (or rather, for a χ^2 distribution with several degrees of freedom) than for a distribution with larger tails; thus, our Gaussian-noise estimates undercount the ρ_{Ξ^α} triggers with respect to the ρ'_{Ξ^α} triggers. As for nonstationarity, real-world data-analysis protocols try to cope by introducing vetoing schemes and by requesting coincident triggers between between two or more detectors [54]. It is hard to predict how these additional elements might play into our proposed search scheme; a full statistical analysis including non-Gaussianity and nonstationarity is beyond the scope of this chapter, and it will probably need to be quite empirical in nature.

3.6 Template counting and placement

The last aspect to examine before we can recommend the template family of Sec. 3.4 for actual use with the two-stage search scheme of Sec. 3.5 is the total number of templates that are needed in practice. As mentioned in Sec. 3.2, the template-bank size and geometry required to achieve a certain minimum match can be studied using the *mismatch metric* [29, 27, 34], which describes, to quadratic order, the degrading overlap between nearby elements in a template bank:

$$1 - \langle \hat{h}(\lambda^A), \hat{h}(\lambda^A + \Delta\lambda^A) \rangle \equiv \delta[\lambda^A, \lambda^A + \Delta\lambda^A] = g_{BC} \Delta\lambda^B \Delta\lambda^C, \tag{3.62}$$

where δ denotes the mismatch, and where

$$g_{BC} = -\frac{1}{2} \frac{\partial^2 \langle \hat{h}(\lambda^A), \hat{h}(\lambda^A + \Delta\lambda^A) \rangle}{\partial(\Delta\lambda^B)\partial(\Delta\lambda^C)}. \tag{3.63}$$

No zeroth- or first-order terms are needed in the expansion (3.62), because the overlap has a maximum of 1 (for normalized templates) at $\Delta\lambda^A = 0$. The metric is positive definite, because $\delta > 0$. Note that, according to this definition, the mismatch δ is the *square* of the *metric distance* between λ^A and $\lambda^A + \Delta\lambda^A$. It is also *half*

the square of the *inner-product distance* $\sqrt{\langle \Delta\hat{h}, \Delta\hat{h}\rangle}$, where $\Delta\hat{h} \equiv \hat{h}(\lambda^A) - \hat{h}(\lambda^A + \Delta\lambda^A)$ [55].

Ideally, for a given continuous template family, one could find a reparametrization in which the metric is a Kronecker delta, and then lay down a template bank as a uniform hypercubic lattice in these coordinates, with the appropriate density to yield the required MM. For a hypercubic lattice in n dimensions [56], the (metric) side δl of the lattice cell is given by the relation $1 - \mathrm{MM} = n(\delta l/2)^2$ [27, 22]; we then get the total number of templates in the bank by dividing the total (metric) volume of parameter space by the volume of each cell:

$$\mathcal{N}_{\text{templates}} = \int \sqrt{|\det g_{BC}|}\, d^n\lambda^A \Big/ \left[2\sqrt{(1-\mathrm{MM})/n}\right]^n . \tag{3.64}$$

In practice, this expression will usually underestimate the total number of templates, for two reasons: first, for more than two dimensions it is usually impossible to find coordinates where the metric is diagonalized everywhere at once; second, the fact that the actual parameter space is bounded will also introduce corrections to Eq. (3.64). (The presence of null parameter directions, discussed in Sec. 3.6.2, can also be seen as an extreme case of boundary effects.)

As we showed in Secs. 3.4 and 3.5, the overlap of the detector output with one of the ST_N templates can be maximized automatically over all the extrinsic parameters Ξ^α; it follows that a discrete template bank will need to extend only along the four intrinsic parameters X^i. So the estimate (3.64) for the number of templates should be computed on the *projected* metric g^{proj}_{ij} that satisfies

$$1 - \rho_{\Xi^\alpha}\left[\hat{h}(X^i, \Xi^\alpha), \hat{h}(X^i + \Delta X^i)\right] \equiv 1 - \max_{\Xi'^\alpha} \langle \hat{h}(X^i, \Xi^\alpha), \hat{h}(X^i + \Delta X^i, \Xi'^\alpha)\rangle = g^{\text{proj}}_{ij} \Delta X^i \Delta X^j .$$

Note that g^{proj}_{ij} is still a function of *all* the parameters. In Sec. 3.6.1 we compute g^{proj}_{ij} from the full metric g_{BC}; we then proceed to construct an *average* metric, $\overline{g^{\text{proj}}_{ij}}$, which is connected closely to detection rates, and does not depend on the extrinsic parameters.

In fact, it turns out that *not all four intrinsic parameters are needed to set up a template bank that achieves a reasonable* MM: we can do almost as well by replacing a 4D bank with a 3D bank where (for instance) we set $\kappa_1 = 0$. As a geometrical counterpart to this fact, the projected metric must allow a quasinull direction: that is, it must be possible to move along a certain direction in parameter space while accumulating almost no mismatch. The correct template counting for the 3D bank is then described by a *reduced* metric, which we discuss in Sec. 3.6.2. Finally, we give our results for the total number of templates in Sec. 3.6.3.

3.6.1 Computation of the full, projected, and average metric

According to Eq. (3.63), the full metric g_{BC} can be computed numerically by fitting the quadratic decrease of the overlap $\langle \hat{h}(\lambda^A), \hat{h}(\lambda^A + \Delta\lambda^A)\rangle$ around $\Delta\lambda^A = 0$. It is also possible to rewrite g_{BC} in terms of first-order

derivatives of the waveforms: since $\langle \hat{h}(\lambda^A), \hat{h}(\lambda^A)\rangle = 1$ for all λ^A,

$$\frac{\partial}{\partial\lambda^B}\langle \hat{h}, \hat{h}\rangle = 2\left\langle \hat{h}, \frac{\partial \hat{h}}{\partial\lambda^B}\right\rangle = 0 \tag{3.65}$$

[in this equation and in the following, we omit the parametric dependence $\hat{h}(\lambda^A)$ for ease of notation]; taking one more derivative with respect to λ^C, we get

$$\left\langle \frac{\partial \hat{h}}{\partial\lambda^C}, \frac{\partial \hat{h}}{\partial\lambda^B}\right\rangle + \left\langle \hat{h}, \frac{\partial^2 \hat{h}}{\partial\lambda^C\partial\lambda^B}\right\rangle = 0, \tag{3.66}$$

which implies [by Eq. (3.63)]

$$g_{BC} = \frac{1}{2}\left\langle \frac{\partial \hat{h}}{\partial\lambda^B}, \frac{\partial \hat{h}}{\partial\lambda^C}\right\rangle. \tag{3.67}$$

The inner product in the right-hand side of Eq. (3.67) expresses the *Fisher information matrix* for the normalized waveforms $\hat{h}(\lambda^A)$ (see for instance Ref. [30]); for nonnormalized waveforms $h(\lambda^A)$ we can write

$$g_{BC} = \frac{1}{2\langle h, h\rangle}\left\langle \frac{\partial h}{\partial\lambda^B}, \frac{\partial h}{\partial\lambda^C}\right\rangle - \frac{1}{2\langle h, h\rangle^2}\left\langle \frac{\partial h}{\partial\lambda^B}, h\right\rangle\left\langle h, \frac{\partial h}{\partial\lambda^C}\right\rangle. \tag{3.68}$$

It is much easier to compute the mismatch metric from Eq. (3.67) rather than from Eq. (3.63), for two reasons. First, we know the analytic dependence of the templates on all the extrinsic parameters (except t_0), so we can compute the derivatives $\partial\hat{h}/\partial\Xi^\alpha$ analytically (the derivative with respect to t_0 can be handled by means of the Fourier-transform time-shift property $\mathcal{F}[h(t + t_0)] = \mathcal{F}[h(t)]\exp[2\pi i f t_0]$). Second, although the derivatives $\partial\hat{h}/\partial X^i$ have to be computed numerically with finite-difference expressions such as $[\hat{h}(X^i + \Delta X^i, \Xi^a) - \hat{h}(X^i, \Xi^a)]/\Delta X^i$, this is still easier than fitting the second-order derivatives of the mismatch numerically [57].

To obtain the projected metric $g_{ij}^{\rm proj}$, we rewrite the mismatch $\delta(\lambda^A, \lambda^A + \Delta\lambda^A)$ by separating intrinsic and extrinsic parameters,

$$\delta(X^i, \Xi^\alpha; X^i + \Delta X^i, \Xi^\alpha + \Delta\Xi^\alpha) = \begin{pmatrix} \Delta X^i & \Delta\Xi^\alpha \end{pmatrix}\begin{pmatrix} G_{ij} & C_{i\beta} \\ C_{\alpha j} & \gamma_{\alpha\beta}\end{pmatrix}\begin{pmatrix} \Delta X^j \\ \Delta\Xi^\beta\end{pmatrix}; \tag{3.69}$$

here we have split the full metric g_{BC} into four sections corresponding to intrinsic-intrinsic (G_{ij}), extrinsic-extrinsic ($\gamma_{\alpha\beta}$), and mixed ($C_{\alpha j} = C_{j\alpha}$) components. Maximizing the overlap over the extrinsic parameters is then equivalent to minimizing Eq. (3.69) over the $\Delta\Xi^\alpha$ for a given ΔX^i, which is achieved when

$$\gamma_{\alpha\beta}\Delta\Xi^\beta + C_{\alpha j}\Delta X^j = 0\,, \tag{3.70}$$

while the resulting mismatch is

$$\min_{\Delta\Xi^\alpha} \delta(X^i, \Xi^\alpha; X^i + \Delta X^i, \Xi^\alpha + \Delta\Xi^\alpha) = = \left[G_{ij} - C_{i\alpha}(\gamma^{-1})^{\alpha\beta} C_{\beta j}\right] \Delta X^i \Delta X^j \equiv g^{\rm proj}_{ij} \Delta X^i \Delta X^j. \tag{3.71}$$

Here $(\gamma^{-1})^{\alpha\beta}$ is the matrix inverse of $\gamma_{\alpha\beta}$. For each point (X^i, Ξ^α) in the *full* parameter space, the *projected metric* $g^{\rm proj}_{ij}$ describes a set of concentric ellipsoids of constant ρ_{Ξ^α} in the intrinsic-parameter subspace. We emphasize that the projected metric has tensor indices corresponding to the intrinsic parameters, but it is a function of both the intrinsic and the extrinsic parameters, and so are the constant-ρ_{Ξ^α} ellipsoids.

Therefore, to build a template bank that covers all the signals (for all X^i and Ξ^α) with a guaranteed MM, we must use the projected metric at each X^i to construct the constant-mismatch ellipsoids for all possible Ξ^α, and then take the intersection of these ellipsoids to determine the size of the unit template-bank cell. This is a *minimax* prescription [28], because we are maximizing the overlap over the extrinsic parameters of the templates, and then setting the template-bank spacing according to the least favorable extrinsic parameters of the signal. In general, the intersection of constant-mismatch ellipsoids is not an ellipsoid, even in the limit $\delta \to 0$, so it is impossible to find a single intrinsic-parameter metric that can be used to enforce the minimax prescription. There is an exception: the projected metric is not a function of t_0 or Φ_0 [58], so it can be used directly to lay down banks of nonspinning-binary templates [29, 27], for which t_0 and Φ_0 are the only extrinsic parameters.

Returning to the generic case, we can still use the projected metric to guide the placement of a template bank if we relax the minimax prescription and request that the minimum match be guaranteed *on the average* for a distribution of signal extrinsic parameters []. It turns out that this *average-mismatch* prescription is closely related to the expected detection rates. Let us see how. The matched-filtering detection rate for a signal $s \equiv \mathrm{SA} \times \hat{h}(X^i, \Xi^\alpha)$, where $\mathrm{SA} = \langle s, s\rangle^{1/2}$ is the *signal amplitude* at a fiducial luminosity distance, is proportional to $\mathrm{SA}^3 \rho^3_{\Xi^\alpha}[\hat{s}, \hat{h}_{\rm near}]$, where $\hat{h}_{\rm near} \equiv \hat{h}(X^i + \Delta X^i, \Xi'^\alpha)$ is the closest template in the bank, and where we assume that sources are uniformly distributed throughout the volume accessible to the detector (see, for instance, BCV1). The minimax prescription is given by

$$\rho_{\Xi^\alpha}[\hat{s}, \hat{h}_{\rm near}] \simeq 1 - g^{\rm proj}_{ij}(X^i, \Xi^\alpha) \Delta X^i \Delta X^j \geq \mathrm{MM} \tag{3.72}$$

for all Ξ^α, which ensures that the detection rate is reduced at most by a factor MM^3 for every combination of signal extrinsic and intrinsic parameters.

Averaging over a uniform distribution of signal extrinsic parameters [60], we get a detection rate propor-

tional to

$$\begin{aligned}\int d\Xi^\alpha \mathrm{SA}^3 \rho^3_{\Xi^\alpha} &\simeq \int d\Xi^\alpha \mathrm{SA}^3 \left(1 - g^{\mathrm{proj}}_{ij}\Delta X^i \Delta X^j\right)^3 \\ &\simeq \overline{\mathrm{SA}^3} - 3\left[\int d\Xi^\alpha \mathrm{SA}^3 g^{\mathrm{proj}}_{ij}\right]\Delta X^i \Delta X^j \\ &\simeq \overline{\mathrm{SA}^3}\left(1 - \overline{g^{\mathrm{proj}}_{ij}}\Delta X^i \Delta X^j\right)^3,\end{aligned} \tag{3.73}$$

where $\overline{\mathrm{SA}^3} = \int d\Xi^\alpha \mathrm{SA}^3$, and where the *average metric* $\overline{g^{\mathrm{proj}}_{ij}}$, now a function only of X^i, is defined as

$$\overline{g^{\mathrm{proj}}_{ij}} = \int d\Xi^\alpha \mathrm{SA}^3 g^{\mathrm{proj}}_{ij} \Big/ \overline{\mathrm{SA}^3}. \tag{3.74}$$

[To derive Eq. (3.73) we assume that $1 - \rho_{\Xi^\alpha}[\hat{s}, \hat{h}_{\mathrm{near}}] \ll 1$ for all Ξ^α.] We can now state the new average-mismatch prescription as

$$1 - \overline{g^{\mathrm{proj}}_{ij}}(X^i)\Delta X^i \Delta X^j \geq \overline{\mathrm{MM}}, \tag{3.75}$$

which ensures that the detection rate, *averaged over the extrinsic parameters of the signal*, is reduced at most by the factor $\overline{\mathrm{MM}}^3$. We shall call $\overline{\mathrm{MM}}$ the *average minimum match*.

3.6.2 Null parameter directions and reduced metric

As discussed by Sathyaprakash and Schutz [61] and by Cutler [59], an extreme example of boundary effect occurs when one of the eigenvalues of g_{BC} at λ^A (say, $\Lambda_{(1)}$) becomes so small that it is possible to move away in parameter space along the corresponding eigendirection (say, $e^A_{(1)}$) and *reach the boundary of the allowed parameter region while keeping the mismatch* $\delta(\lambda^A, \lambda^A + \tau\, e^A_{(1)})$ *well below the required value* $\delta_{\mathrm{MM}} = 1 - \mathrm{MM}$. In other words, the ellipsoid of constant mismatch δ_{MM} extends far beyond the allowed parameter region in the quasinull-eigenvalue direction. In such a situation, Eq. (3.64) will underestimate the total number of templates, because the denominator should now express the volume of the intersection of each lattice cell with the allowed parameter region [62]. A simple-minded fix to Eq. (3.64) is the following: write $\det g_{BC} = \prod_{(k)} \Lambda_{(k)}$, where the $\Lambda_{(k)}$ are the n eigenvalues of g_{BC}; identify all the small eigenvalues, where *small* can be defined by $\Lambda_{(i)} \ll (1 - \mathrm{MM})/l^2_{(i)}$, with $l_{(i)}$ the coordinate diameter of the allowed parameter range along the eigenvector $e^A_{(i)}$; replace the small eigenvalues by the corresponding value of the expression $(1 - \mathrm{MM})/l^2_{(i)}$; use this modified determinant in Eq. (3.64).

Physically, the presence of k small eigenvectors suggests that the variety of waveform shapes spanned by an n-dimensional template family can be approximated with very high overlap by an $(n - k)$-dimensional. *reduced* family. A lower-dimensional template bank is certainly desirable for practical purposes, but it is necessary to exercise caution: because the metric g_{BC} is not homogeneous, the quasinull eigendirections rotate as we move in parameter space [63], so we need to show explicitly that any signal in the n-dimensional family can be reached from a given $(n - k)$-dimensional submanifold along a quasinull trajectory. For this to

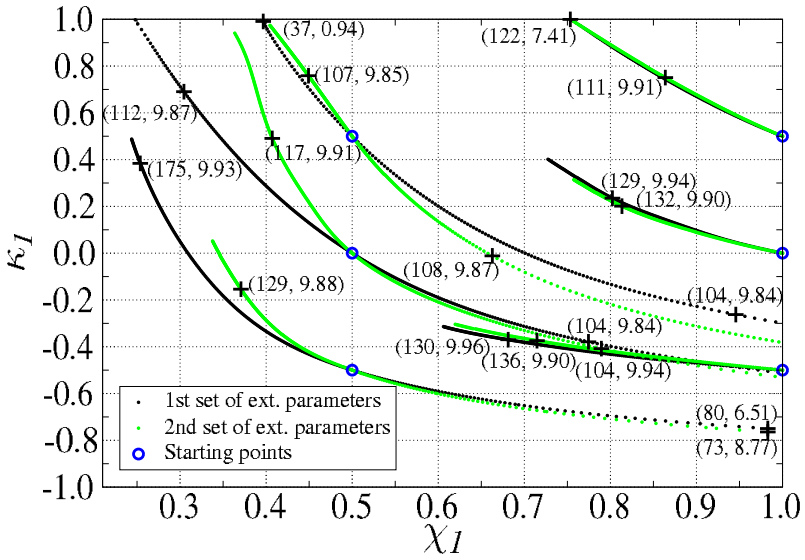

Figure 3.8: Plot of (χ_1, κ_1) reduction curves in the (χ_1, κ_1) plane. We show curves for two sets of starting extrinsic parameters, corresponding to detector directions perpendicular (dark dots) and parallel (light dots) to the initial orbital plane. The curves start at the points marked with circles, and proceed in steps of 10^{-6} for the nominal mismatch (i.e., the mismatch computed using the projected metric). For starting points at $\chi_1 = 0.5$, we follow the quasinull eigenvector for both positive and negative increments. The curves end at the (χ_1, κ_1) boundary, or (roughly) where the true mismatch (i.e., the exact mismatch between the local and the starting template) becomes greater than 0.01. The ending points are marked with crosses, and they are annotated with the number of steps taken since the starting point, and with the true mismatch in units of 10^{-3}.

happen, the small eigenvalues must exist throughout the entire n-dimensional parameter space, and the flow of the quasinull eigenvectors must map the submanifold into the entire space. To see that under these conditions the mismatch between the points on the submanifold and the points outside is indeed small, consider the following argument, due to Curt Cutler [59]. The triangle inequality for the inner-product distance guarantees that

$$\delta^{1/2}[\lambda^A(0), \lambda^A(1)] \leq \int_0^1 \sqrt{g_{BC} \frac{d\lambda^B}{d\nu} \frac{d\lambda^C}{d\nu}} d\nu \tag{3.76}$$

along *any* path $\lambda^A(\nu)$; for a path that follows the flow of the quasinull eigenvector $e^A_{(i)}$ (a *reduction curve*), the total mismatch is then bounded by the average of $\Lambda_{(i)}$ along the curve, times an integrated squared parameter length of order $l_{(i)}$ [64].

For the ST_N template bank and for the two-stage search scheme of Sec. 3.5, we find that the projected metric g^{proj}_{ij} admits a small eigenvalue for all values of the intrinsic and extrinsic parameters. Figures 3.8 and 3.9 show several examples of reduction curves that follow the quasinull eigendirections (the subtleties related to projected-metric reduction curves are discussed in App. 3.10). The curves shown [65] begin at the points

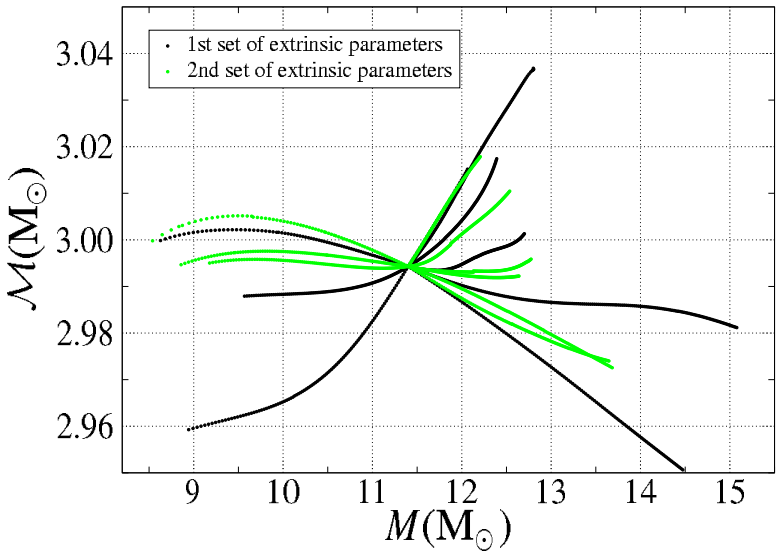

Figure 3.9: Plot of (χ_1, κ_1) reduction curves in the $(M, \mathcal{M})$ plane. The curves are the same as shown in Fig. 3.8, but we omit all markings.

marked with circles, where $(m_1 + m_2) = (10 + 1.4)M_\odot$ and

$$(\chi_1, \kappa_1) = \left\{ \begin{array}{c} 0.5 \\ 1.0 \end{array} \right\} \times \left\{ \begin{array}{c} -0.5 \\ 0.0 \\ 0.5 \end{array} \right\}; \tag{3.77}$$

the curves then proceed in steps of 10^{-6} for the *nominal* mismatch (i.e., the mismatch computed using the local projected metric) until they reach the (χ_1, κ_1) boundary, or (roughly) until the *true* mismatch (i.e., the exact mismatch between the local and the starting template) is greater than 0.01. We show curves for two sets of starting extrinsic parameters, corresponding to detector directions perpendicular (dark dots) and parallel (light dots) to the initial orbital plane. Figure 3.8 shows the projection of the reduction curves in the (χ_1, κ_1) plane; the ending points are marked with crosses, and they are annotated with the number of steps taken since the starting point, and with the true mismatch in units of 10^{-3}. Comparing the two numbers at each cross, we see that the triangle inequality is always respected: The true mismatch δ_N is always less than the accumulated nominal mismatch $10^{-6}N^2$ (where N is the number of steps); in fact, we see that the latter is a good approximation for the former. Figure 3.9 shows the projection of the same reduction curves in the $(M, \mathcal{M})$ plane. The chirp mass $\mathcal{M} \equiv M\eta^{3/5}$ varies by less than 2% along the curves: this is natural, since $\mathcal{M}$ dominates the evolution of the GW phase [see Eq. (3.5)].

Figure 3.8 suggests that we can reduce the dimensionality of our template bank by collapsing the (χ_1, κ_1)

plane into ~ three curves, while retaining the full (M, η) plane. Templates laid down on these 3D submanifolds with a required minimum match MM will then cover every signal in the full 4D family with mismatch no larger than $(1-\mathrm{MM})+\delta_{\mathrm{red}}$, where $\delta_{\mathrm{red}} \simeq 0.01$ is the *reduction mismatch* introduced by the reduction procedure. Further investigations will be needed to find the optimal choice of reduction curves in the (χ_1, κ_1) plane, and to investigate the reduction curves of the average metric $\overline{g_{ij}^{\mathrm{proj}}}$.

3.6.3 Template counting

While three or more reduction curves will probably be necessary to limit $\delta_{\mathrm{red}} \simeq 0.01$, for the sake of definiteness we select a 3D reduced template space corresponding to $(m_1, m_2) \in [7, 12] \times [1, 3]$, $\kappa_1 = 0$, and $\chi_1 \in (0, 1]$ [66]. We compute the total number of templates in this 3D template bank according to

$$\mathcal{N}_{\mathrm{templates}} = \frac{\int \sqrt{\left|\det \overline{g_{i'j'}^{\mathrm{proj}}}\right|}\, dM\, d\eta\, d\chi}{\left[2\sqrt{(1-\mathrm{MM})/3}\right]^3}, \tag{3.78}$$

where the primed indices i', j' run through M, η, and χ, and we set $X^4 \equiv \kappa_1 = 0$; furthermore, $\overline{g_{ij}^{\mathrm{proj}}}$ denotes the metric averaged over the extrinsic parameters Θ, φ, and α, as given by Eq. (3.74). The integral is carried out by evaluating the projected metric at the parameter sets

$$(m_1, m_2, \chi_1) = \left\{ \begin{array}{c} 7M_\odot \\ 12M_\odot \end{array} \right\} \times \left\{ \begin{array}{c} 1M_\odot \\ 2M_\odot \\ 3M_\odot \end{array} \right\} \times \left\{ \begin{array}{c} 0.1 \\ 0.3 \\ 0.5 \\ 0.7 \\ 1.0 \end{array} \right\}; \tag{3.79}$$

at each of the points the metric is averaged on 100 pseudorandom sets of extrinsic parameters. The integration then proceeds by interpolating across the parameter sets (3.79). The final result is $\mathcal{N}_{\mathrm{templates}} \simeq 76\,000$ for MM = 0.98 (not including the reduction mismatch). Given the uncertainties implicit in the numerical computation of the metric, in the interpolation, in the choice of the reduction curves, and in the actual placement of the templates in the bank, this number should be understood as an order-of-magnitude estimate. Most of the templates, by a factor of about 10 to 1, come from the parameter region near $m_2 = 1$ (that is, from the small-η region).

3.7 Summary

Buonanno, Chen, and Vallisneri recently proposed [BCV2] a family of physical templates that can be used to detect the GWs emitted by single-spin precessing binaries. The attribute *physical* refers to the fact that the

templates are exact within the approximations used to write the PN equations that rule the adiabatic evolution of the binary. In this chapter, after reviewing the definition of this template family (here denoted as ST_N), we discuss the range of binary masses for which the templates can be considered accurate, and examine the effects of higher-order PN corrections, including quadrupole-monopole interactions. We then describe an optimized two-stage detection scheme that employs the ST_N family, and investigate its false-alarm statistics. Finally, we estimate the number of templates needed in a GW search with LIGO-I. Our results can be summarized as follows.

We determine the range of binary masses where the ST_N templates can be considered accurate by imposing two conditions: First, for the orbital separations that correspond to GWs in the frequency band of good interferometer sensitivity, the dynamics of the binary must be described faithfully by an adiabatic sequence of quasi-spherical orbits; second, the nonspinning body must be light enough that its spin will be negligible for purely dimensional reasons. The selected mass range is $(m_1, m_2) \simeq [7, 12]M_\odot \times [1, 3]M_\odot$.

To evaluate the effect of higher-order PN corrections for binaries in this mass range, we compute the overlaps between templates computed at successive PN orders. When computed between templates with the same parameters, such overlaps can be rather low; however, they become very high when maximized over the parameters (both intrinsic and extrinsic) of the lower-order PN template [see Table 3.2]. This means that the ST_2 template family should be considered acceptable for the purpose of GW detection; but this means also that the estimation of certain combinations of binary parameters can be affected by large systematic errors [20]. [When precessing-binary gravitational waveforms computed within PN-resummed and nonadiabatic approaches [28, 44] become available, it will be interesting to compare them with the PN-expanded, adiabatic ST_N templates, to see if the maximized overlaps remain high. We do expect this to be the case, because the spin and directional parameters of the ST_N templates provide much leeway to compensate for nontrivial variations in the PN phasing.] Again by considering maximized overlaps, we establish that quadrupole-monopole effects [67, 68] can be safely neglected for the range of masses investigated [Table 3.3].

We describe a two-stage GW detection scheme that employs a discrete bank of ST_2 templates laid down along the intrinsic parameters $(M, \eta, \chi_1, \kappa_1)$ [although the (χ_1, κ_1) may be collapsed to one or few 1D curves, in light of the discussion of dimensional reduction of Sec. 3.6]. The detection statistic $\rho_{\Xi^\alpha}(M, \eta, \chi_1, \kappa_1)$ is the overlap between the template and the detector output, maximized over template extrinsic parameters: $(t_0, \Phi_0, P_I) \equiv (t_0, \Phi_0, \theta, \phi, \psi, \Theta, \varphi)$. This maximization is performed semialgebraically, in two stages. First, for all possible times of arrival t_0, we maximize the overlap over Φ_0 and over P_I without accounting for the constraints that express the functional dependence of the P_I on $(\theta, \phi, \psi, \Theta, \varphi)$: this step yields the approximated (unconstrained) maximum ρ'_{Ξ^α}, which can be computed very rapidly, and which sets an upper bound for ρ_{Ξ^α}. Second, only for the times of arrival t_0 at which ρ'_{Ξ^α} passes the detection threshold, we compute the fully constrained maximum ρ_{Ξ^α}, which is more expensive to compute. [Note that this scheme differs from traditional hierarchical schemes because we use the *same* threshold in the first and second stages.] We find that ρ'_{Ξ^α} is a good approximation to ρ_{Ξ^α}, so the number of first-stage triggers passed to the second stage is

small.

For a total false-alarm probability of 10^{-3}/year, and for a conservative estimate for the number of independent statistical tests, the detection threshold is around 10. For this value, between 5 and 15 first-stage triggers are passed to the second stage for each eventual detection. For the same threshold, the single-test false-alarm probability is lower for ST_2 templates than for the $(\psi_0\psi_{3/2}\mathcal{B})_6$ DTF of BCV2 [the total false-alarm probability depends on the number of independent statistical tests, which is not available at this time for the $(\psi_0\psi_{3/2}\mathcal{B})_6$ DTF].

The procedure of maximization over the extrinsic parameters outlined in this chapter can also be adapted for the task of detecting GWs from extreme-mass-ratio inspirals (i.e., the inspirals of solar-mass compact objects into the supermassive BHs at the center of galaxies [69]) and inspirals of two supermassive black holes with LISA [70]. This is possible under the simplifying assumptions of coherent matched filtering over times short enough that the LISA antenna patterns can be considered constant, and of GW emission described by the quadrupole formula. Furthermore, the formalism of projected and reduced mismatch metrics developed in Sec. 3.6 can treat GW sources, such as extreme-mass-ratio inspirals, where many physical parameters are present, but only a few of their combinations have significant effects on the emitted waveforms [61, 59]. In fact, this formalism is closely related to the procedures and approximations used in the ongoing effort (motivated by mission-design considerations) to count the templates needed to detect extreme-mass-ratio inspirals with LISA [71].

It should be possible to generalize the formalism beyond quadrupole GW emission, at least to some extent. When higher-multipole contributions are included, the detector response becomes much more complicated than Eq. (3.15) (see, e. g., Eqs. (3.22b)–(3.22h) of Ref. [38]). In particular, the response cannot be factorized into a factor that depends only on the dynamical evolution of the binary, and a factor that depends only on the position and orientation of the detector; it is instead a sum over a number of such terms, each containing different harmonics of the orbital and modulation frequencies. Despite these complications, it should still be possible to maximize the overlap over the extrinsic parameters, using a relatively small number of signal–template and template-template inner products. The constrained-maximization procedure would however be very complicated, and although the (fully algebraic) unconstrained maximum would still be easy to compute, the dimensionality of the unconstrained template space would now be so large that it may increase the false alarm probability too dramatically to make the two-stage scheme useful.

The last result of this chapter is an estimate of the number of ST_2 templates needed for a GW search in the mass range $[7, 12]M_\odot \times [1, 3]M_\odot$. To obtain this estimate, we first compute the full mismatch metric, which describes the mismatch for small displacements in the intrinsic and extrinsic parameters; we then obtain the projected metric, which reproduces the effect of maximizing the overlap over the extrinsic parameters. At this point we observe that the projected metric has an eigenvector corresponding to a very small eigenvalue; this indicates that we can choose one of the four intrinsic parameters to be a function of the other three, so the dimensionality of the ST_2 template bank can be reduced to three. For simplicity, we perform this reduction

view	$(10+1.4)M_\odot$ with $\chi_1 = 1$			
	$\kappa_1 = 0.9$		$\kappa_1 = 0.5$	
top	0.4796	(≥ 0.99) [10.3,0.13,1.21, 0.89]	0.9890	(≥ 0.99)
side	0.3503	(≥ 0.99) [10.0,0.13,0.77, 0.94]	0.8033	(≥ 0.99)
diagonal	0.3292	(≥ 0.99) [11.2,0.11,0.80, 0.94]	0.6669	(≥ 0.99)

view	$(10+1.4)M_\odot$ with $\chi_1 = 1$			
	$\kappa_1 = -0.5$		$\kappa_1 = -0.9$	
top	0.1873	(≥ 0.99) [11.3,0.11,1.08,−0.48]	0.7245	(0.9877)
side	0.8754	(≥ 0.99) [11.4,0.11,1.03,−0.39]	0.7598	(≥ 0.99)
diagonal	0.4546	(≥ 0.99) [11.3,0.11,1.08,−0.49]	0.8437	(0.9887)

Table 3.3: Effects of quadrupole-monopole terms, for $(10+1.4)M_\odot$ binaries with maximally spinning BH. At the beginning of each column we quote the overlaps between ST_2 templates and $\mathrm{ST}_2^{\mathrm{QM}}$ templates that include quadrupole-monopole effects. Just as in Table 3.2, these overlaps are maximizing only over the extrinsic parameters t_0 and Φ_0. In parentheses, "(...)", we show the fitting factors for the $\mathrm{ST}_2^{\mathrm{QM}}$ family as matched by the ST_2 family; in brackets, "[...]", we show the intrinsic parameters at which the fitting factors are achieved. The "view" column describes the position of the detector with respect to the initial orbital plane. In all cases the integration of the equations is started at a GW frequency of 60 Hz. The maximization procedure was stopped whenever an overlap ≥ 0.99 was achieved.

by setting $\kappa_1 = 0$. We then compute the reduced mismatch metric, and obtain a rough estimate of $\sim 76\,000$ as the number of templates required for an average MM of 0.98, or 0.97 including an estimated reduction mismatch of 0.01.

3.8 Appendix A: The quadrupole-monopole interaction

In this appendix we investigate the effect of the quadrupole-monopole interaction, which we have so far neglected in describing the dynamics of precessing binaries. It is well known [67] that the quadrupole moment of a compact body in a binary creates a distortion in its gravitational field, which affects orbital motion (both in the evolution of ω and in the precession of $\hat{\mathbf{L}}_N$), and therefore GW emission; the orbital motion, on the other hand, exerts a torque on the compact body, changing its angular momentum (i.e., it induces a *torqued precession*). Although the lowest-order quadrupole-monopole effect is Newtonian, it is smaller than spin-orbit effects and of the same order as spin-spin effects.

When the spinning body is a black hole, the equations for the orbital evolution and GW templates are modified as follows to include quadrupole-monopole effects. Eq. (3.5) gets the additional term [68]

$$\left(\frac{\dot{\omega}}{\omega^2}\right)_{\text{Q-M}} = \frac{96}{5}\,\eta\,(M\omega)^{5/3} \times \left[\frac{5}{2}\chi_1^2\,\frac{m_1^2}{M^2}\left(3\kappa_1^2 - 1\right)(M\omega)^{4/3}\right],$$

while the precession equations (3.6)–(3.7) become [68]

$$\dot{\mathbf{S}}_1 = \frac{\eta}{2M}\,(M\omega)^{5/3}\left[\left(4 + 3\frac{m_2}{m_1}\right) - 3\chi_1\kappa_1(M\omega)^{1/3}\right](\hat{\mathbf{L}}_N \times \mathbf{S}_1)\,, \tag{3.80}$$

and

$$\dot{\hat{\mathbf{L}}}_N = \frac{\omega^2}{2M}\left[\left(4+3\frac{m_2}{m_1}\right)-3\chi_1\kappa_1(M\omega)^{1/3}\right](\mathbf{S}_1\times\hat{\mathbf{L}}_N)\equiv\boldsymbol{\Omega}'_L\times\hat{\mathbf{L}}_N\,; \tag{3.81}$$

furthermore, the orbital energy (3.8) gets the additional term

$$\mathcal{E}_{\text{Q-M}}(\omega) = -\frac{\eta}{2}(M\omega)^{2/3}\quad\left[-\frac{1}{2}\chi_1^2\frac{m_1^2}{M^2}\left(3\kappa_1^2-1\right)(M\omega)^{4/3}\right];$$

finally, $\boldsymbol{\Omega}_e$ is again obtained from Eq. (3.14), using the modified $\boldsymbol{\Omega}'_L$ in Eq. (3.81). [Note that $\kappa_1\equiv\hat{\mathbf{L}}_N\cdot\hat{\mathbf{S}}_1$.]

The quadrupole-monopole interaction changes the number of GW cycles listed in Table 3.1 at 2PN order. The additional contributions are $5.2\,\chi_1^2-15.5\,\kappa_1^2\chi_1^2$ for a $(10+1.4)M_\odot$ binary, $2.5\,\chi_1^2-7.6\,\kappa_1^2\chi_1^2$ for a $(12+3)M_\odot$ binary, and $1.8\,\chi_1^2-5.4\,\kappa_1^2\chi_1^2$ for a $(7+3)M_\odot$ binary. To estimate more quantitatively the effect of the quadrupole-monopole terms, we evaluate the nonmaximized overlaps (in the sense of Sec. 3.3.4) between 2PN templates, computed with and without the new terms. The results for $(10+1.4)M_\odot$ binaries are summarized in Table 3.3. In parentheses we show the fitting factors, which are all very high; in brackets we show the intrinsic parameters at which the maximum overlaps are obtained. We conclude that for the purpose of GW searches, we can indeed neglect the effects of the quadrupole-monopole interaction on the dynamical evolution of the binary.

3.9 Appendix B: Algebraic maximization of the overlap over the P_I

In this section, we explore the algebraic maximization of ρ_{Φ_0} [see Eq. (3.44)], given by

$$\rho_{\Phi_0} = \sqrt{\frac{A^{IJ}P_IP_J}{B^{IJ}P_IP_J}}\,, \tag{3.82}$$

over the P_I. We recall that the five P_I are combinations of trigonometric functions of three angles, and therefore must satisfy two constraints: luckily, both of these can be formulated algebraically. In light of the discussion of Sec. 3.4.2, the overall normalization of the P_I does not affect the value of the overlap (3.44). As a consequence, we can rescale the P_I and replace the first constraint by

$$B^{IJ}P_IP_J = 1\,, \tag{3.83}$$

which enforces the normalization of the templates. This constraint is chosen only for convenience: The maximum, subject to this constraint, is exactly the same as the unconstrained maximum found by searching over the entire five-dimensional space. Let us work out its value, which will be useful later. Introducing the first Lagrangian multiplier λ, we impose

$$\frac{\partial}{\partial P_I}[A^{IJ}P_IP_J-\lambda(B^{IJ}P_IP_J-1)] = (A^{IJ}-\lambda B^{IJ})P_J = 0\,, \tag{3.84}$$

which has solutions only for λ corresponding to the eigenvalues of $\mathbf{A}\mathbf{B}^{-1}$. For those solutions, we multiply Eq. (3.84) by P_I to obtain

$$\lambda = A^{IJ} P_I P_J; \tag{3.85}$$

using Eqs. (3.82) and (3.83), we then see that λ is the square of the overlap, so it should be chosen as the largest eigenvalue of $\mathbf{A}\,\mathbf{B}^{-1}$. We then write the *unconstrained maximum* as

$$\rho'_{\Xi^\alpha} = \max_{t_0} \sqrt{\max \mathrm{eigv} \mathbf{A}\,\mathbf{B}^{-1}}\,. \tag{3.86}$$

By construction, ρ'_{Ξ^α} will always be larger than or equal to the constrained maximum, ρ_{Ξ^α}.

The second constraint comes from Eq. (3.47). Writing out the STF components, we get

$$\det P_{ij} \equiv \det \frac{1}{\sqrt{2}} \begin{pmatrix} P_1 + P_5/\sqrt{3} & P_2 & P_3 \\ P_2 & -P_1 + P_5/\sqrt{3} & P_4 \\ P_3 & P_4 & -2P_5/\sqrt{3} \end{pmatrix} \equiv D^{IJK} P_I P_J P_K = 0. \tag{3.87}$$

[The tensor D^{IJK} can be chosen to be symmetric since $D^{IJK} P_I P_J P_K = D^{(IJK)} P_I P_J P_K$.] The constrained maximum of ρ_{Φ_0} over the P_I, subject to the two constraints, can be obtained as the maximum of the function

$$A^{IJ} P_I P_J - \lambda (B^{IJ} P_I P_J - 1) - \mu (D^{IJK} P_I P_J P_K) \tag{3.88}$$

over P_I and over the two Lagrange multipliers λ and μ. After taking partial derivatives, we get a system of seven equations,

$$A^{IJ} P_J - \lambda B^{IJ} P_J - \frac{3}{2} \mu D^{IJK} P_J P_K = 0\,, \tag{3.89}$$

$$B^{IJ} P_I P_J - 1 = 0\,, \tag{3.90}$$

$$D^{IJK} P_I P_J P_K = 0\,, \tag{3.91}$$

where the last two equations come from the constraints (3.83) and (3.87). Multiplying the first equation by P_I and using the two constraints, we obtain Eq. (3.85) again. So the first Lagrange multiplier λ is still the square of the overlap. The second Lagrange multiplier μ is zero when the signal s belongs to ST_N template family, and has exactly the same intrinsic parameters as the template. In this case, the extrinsic parameters of the signal correspond to a vector P_I that satisfies Eq. (3.89) with $\mu = 0$ (the multiplier λ is still needed to enforce normalization of the template). When the intrinsic parameters are not exactly equal, but close, μ becomes finite, but small. Equations (3.89)–(3.91) can then be solved iteratively by expanding P_I in terms of μ,

$$P_I = \sum_{n=0}^{\infty} P_I^{(n)} \mu^n. \tag{3.92}$$

Inserting this expansion into Eqs. (3.89) and (3.91), we get the zeroth-order equation

$$A^{IJ}P^{(0)}_J - (A^{LM}P^{(0)}_L P^{(0)}_M)B^{IJ}P^{(0)}_J = 0, \tag{3.93}$$

where we have already used the zeroth-order version of Eq. (3.85) to eliminate λ.

Multiplying by $(B^{-1})^{KI}$, we see that the zeroth-order solution $P^{(0)}_J$ must lie along an eigenvector of $(B^{-1})^{KI}A^{IJ}$, and that the corresponding eigenvalue must be equal to $A^{LM}P^{(0)}_L P^{(0)}_M$, and therefore also to the square of the zeroth-order extremized overlap. To get the maximum overlap, we must therefore choose $P^{(0)}_I$ as the eigenvector corresponding to the largest eigenvalue. So the zeroth-order constrained maximum is exactly the unconstrained maximum obtained above [Eqs. (3.84)–(3.86)].

We can then proceed to nth-order equations:

$$\begin{aligned}
&[A^{IJ} - 2(A^{JM}P^{(0)}_M B^{IL}P^{(0)}_L) - (A^{LM}P^{(0)}_L P^{(0)}_M)B^{IJ}]P^{(n)}_J \\
&= \sum_{m_1=0}^{n-1}\sum_{m_2=0}^{n-1} A^{LM}P^{(m_1)}_L P^{(m_2)}_M B^{IJ}P^{(n-m_1-m_2)}_J + \sum_{m=0}^{n-1}\frac{3}{2}D^{IJK}P^{(m)}_J P^{(n-m-1)}_K.
\end{aligned} \tag{3.94}$$

At each order, we insert the nth-order expansion of P_I into Eq. (3.91), and select the real solution closest to zero as the nth-order approximation to μ (such a solution is guaranteed to exist for all odd n). We then obtain the nth-order approximation to λ (and therefore to ρ_{Ξ^α}) using Eq. (3.85). We proceed in this way, until λ and μ converge to our satisfaction.

This iterative procedure succeeds when the intrinsic parameters of signal and template are close; as their distance increases, the procedure becomes more and more unstable, and eventually fails to converge. The iteration fails often also when the overlap is optimized against pure noise. For these reasons, a practical implementation of the detection statistic ρ_{Ξ^α} must eventually rely on the semialgebraic maximization procedure discussed in Sec. 3.4.2. Indeed, we have used the semialgebraic procedure for all the tests discussed in Sec. 3.5.

3.10 Appendix C: Dimensional reduction with a nonuniform projected metric

In this appendix we extend the reasoning of Sec. 3.6.2 to study dimensional reduction under the projected metric $g^{\rm proj}_{ij}(\lambda^A)$, which lives in the intrinsic parameter space, but is a function of all parameters. For each point $\lambda^A = (X^i, \Xi^\alpha)$ in parameter space, we denote $\Lambda_{(1)}(\lambda^A)$ the smallest eigenvalue of $g^{\rm proj}_{ij}(\lambda^A)$, and $e^i_{(1)}(\lambda^A)$ the corresponding eigenvector in the intrinsic parameter space. Suppose we have

$$\Lambda_{(1)}(\lambda^A) \ll \frac{1-{\rm MM}}{l^2_{(1)}}, \tag{3.95}$$

for all values of λ^A in the allowed parameter region, where $l_{(1)}$ is the coordinate diameter of the allowed parameter range along the eigenvector $e^i_{(1)}$.

Now let us start from a generic point $\lambda^A_0 = (X^i_0, \Xi^\alpha_0)$ in parameter space and follow the normal eigenvector $e^i_{(1)}$ for a tiny parameter length ϵ, reaching $\lambda^A_1 = (X^i_1, \Xi^\alpha_1)$, according to

$$X^i_1 = X^i_0 + \epsilon\, e^i_{(1)}(\lambda^A_0), \tag{3.96}$$

$$\Xi^i_1 = \Xi^i_0 + \epsilon \left[\gamma^{-1}(\lambda^A_0)\right]^{\alpha\beta} \left[C(\lambda^A_0)\right]_{\beta j} e^j_{(1)}(\lambda^A_0); \tag{3.97}$$

this choice of $\Delta\Xi^\alpha$ makes Ξ^α_1 the extrinsic parameter that minimizes $\delta(X^i_0, \Xi^\alpha_0; X^i_1, \Xi^\alpha_1)$. Denoting the inner-product distance as $\mathrm{dist}(\lambda^A_0, \lambda^A_1) \equiv \sqrt{2\delta(\lambda^A_0, \lambda^A_1)}$, we can write

$$\mathrm{dist}(\lambda^A_0, \lambda^A_1) = \epsilon \sqrt{2\Lambda_{(1)}(\lambda^A_0)} + O(\epsilon^2); \tag{3.98}$$

from λ^A_1, we follow the eigenvector $e^i_{(1)}(\lambda^A_1)$ for another parameter length ϵ, and reach λ^A_2; then from λ^A_2 we reach λ^A_3, and so on. Up to the Nth step, we have traveled a cumulative parameter distance $l = N\epsilon$ in the intrinsic parameter space, and an inner-product distance

$$\begin{aligned} \mathrm{dist}(\lambda^A_0, \lambda^A_N) &\le \sum_{n=1}^{N} \mathrm{dist}(\lambda^A_{n-1}, \lambda^A_n) \\ &= \sum_{n=1}^{N} \left[\epsilon \sqrt{2\Lambda_{(1)}(\lambda^A_{n-1})} + O(\epsilon^2)\right] \\ &\le l \sqrt{2 \max_{\lambda^A} \Lambda_{(1)}(\lambda^A)} + O(N\epsilon^2), \end{aligned} \tag{3.99}$$

where in the first line we have used the triangle inequality for the inner-product distance. The term $O(N\epsilon^2)$ vanishes in the limit $\epsilon \to 0$, $N \to \infty$, keeping $l = N\epsilon$ finite (see Fig. 3.10). So we can take the continuous limit of Eqs. (3.96) and (3.97) and arrive at two differential equations that define the resulting trajectory:

$$\dot{X}^i(l) = e^i_{(1)}, \quad \dot{\Xi}^\alpha(l) = \left[\gamma^{-1}\right]^{\alpha\beta} C_{\beta j} e^j_{(1)}, \tag{3.100}$$

where X^i and Ξ^α are parametrized by the cumulative parameter length l, with

$$X^i(l = 0) = X^i_0\,, \qquad \Xi^\alpha(l = 0) = \Xi^\alpha_0\,. \tag{3.101}$$

We can allow l to be either positive or negative, in order to describe the two trajectories that initially propagate

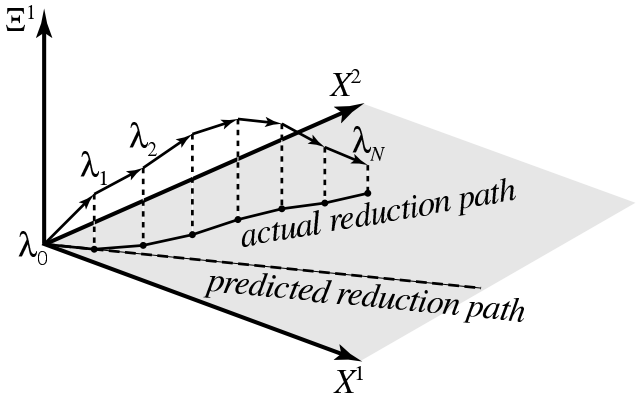

Figure 3.10: Illustration of dimensional reduction. Here we show a signal space with one extrinsic parameter (Ξ^1) and two intrinsic parameters ($X^{1,2}$), and we assume that the projected metric has one small eigenvalue all through parameter space. Starting from a generic point λ_0^A, we follow the flow of the quasinull eigenvector of g_{ij}^{proj} for an infinitesimal parameter distance to reach λ_1^A; we then repeat this process, each time adjusting the direction of the eigenvector according to the metric (hence the difference between the reduction path *predicted* at λ_0^A and the *actual* reduction path). In the end we reach λ_N^A after having accumulated a parameter length l in the *intrinsic* parameter space. The mismatch between λ_0 and λ_N will be smaller than $\delta_{\text{MM}} = 1 - \text{MM}$, if l is not much larger than $l_{(1)}$, the coordinate diameter of the intrinsic parameter space in the approximate direction of the quasinull eigenvector.

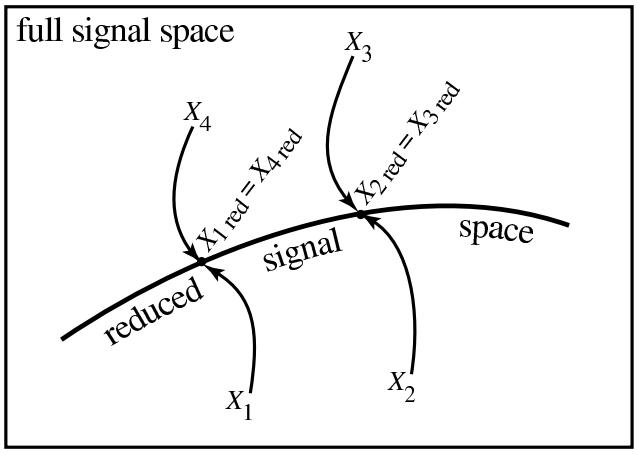

Figure 3.11: Illustration of reduced signal space as a hypersurface inside full signal space. Here we show only the directions along the intrinsic parameters. Starting from the points (X_1^i, Ξ_1^α), ..., (X_4^i, Ξ_4^α), we follow the trajectory (3.100) and reach the hypersurface at $(X_{1\,\text{red}}^i, \Xi_{1\,\text{red}}^\alpha)$, ..., $(X_{4\,\text{red}}^i, \Xi_{4\,\text{red}}^\alpha)$. For these particular initial points, $X_{1\,\text{red}}$ happens to coincide with $X_{4\,\text{red}}$, and $X_{2\,\text{red}}$ with $X_{3\,\text{red}}$. We can see that λ_1^A and λ_4^A (and indeed all points that reduce to $X_{1\,\text{red}}$, including the points along the reduction curve) will be indistinguishable upon detection with the reduced template bank. The same is true for λ_2^A, λ_3^A, and for all the points that reduce to $X_{1\,\text{red}}$.

along $\pm e^i_{(1)}(\lambda^A_0)$. Equation (3.99) then becomes

$$\begin{aligned} \mathrm{dist}\left[\lambda^A_0, \lambda^A(l)\right] &\leq \int_0^l dl' \sqrt{2\Lambda_{(1)}\left[\lambda^A(l')\right]} \\ &\leq |l| \sqrt{2 \max_{\lambda^A} \Lambda_{(1)}(\lambda^A)}. \end{aligned} \tag{3.102}$$

In terms of mismatch,

$$\begin{aligned} \min_{\Xi^\alpha} \delta\left[\lambda^A_0; X^i(l)\right] &= \frac{1}{2}\Big[\min_{\Xi^\alpha} \mathrm{dist}\left[\lambda^A_0; X^i(l)\right]\Big]^2 \\ &\leq \frac{1}{2}\Big[\mathrm{dist}\left[\lambda^A_0; \lambda^A(l)\right]\Big]^2 \\ &\leq \frac{1}{2}\left[\int_0^l dl' \sqrt{2\Lambda_{(1)}\left[\lambda^A(l')\right]}\right]^2 \\ &\leq l^2 \max_{\lambda^A} \Lambda_{(1)}(\lambda^A) \\ &\ll \left(\frac{l}{l_{(1)}}\right)^2 \delta_{\mathrm{MM}}, \end{aligned} \tag{3.103}$$

where the hybrid notation of the first line indicates the mismatch along the solution of (3.100), and where of course $\delta_{\mathrm{MM}} = 1 - \mathrm{MM}$. Here, although we evolve X^i and Ξ^α simultaneously, it is the trajectory $X^i(l)$ in the *intrinsic* parameter space that we are ultimately interested in. In the context of dimensional reduction for the projected metric, we shall call $X^i(l)$ the reduction curve.

If the reduction curves are reasonably straight, it should be easy to find a (dimensionally reduced) hypersurface with the property that any given point (X^i_0, Ξ^α_0) in the full parameter space admits a reduction curve that reaches the hypersurface at a parameter l_* not much larger than the coordinate diameter of parameter space (see Fig. 3.11). From Eq. (3.103), we then have $\min_{\Xi^\alpha} \delta[X^i_0, \Xi^\alpha_0; X^i(l_*), \Xi^\alpha] < \delta_{\mathrm{MM}}$. So any point in the full parameter space can be fit with a mismatch smaller than δ_{MM} by a point on the hypersurface.

3.11 Bibliography

[1] A. Abramovici et al., Science **256**, 325 (1992); `http://www.ligo.caltech.edu`.

[2] The LIGO Scientific Collaboration, "Detector Description and Performance for the First Coincidence Observations between LIGO and GEO," Nucl. Instr. and Meth. in Phys. Res. A, in print (2004).

[3] B. Caron et al., Class. Quantum Grav. **14**, 1461 (1997); `http://www.virgo.infn.it`.

[4] H. Lück et al., Class. Quantum Grav. **14**, 1471 (1997); `http://www.geo600.uni-hannover.de`.

[5] M. Ando et al., Phys. Rev. Lett. **86**, 3950 (2001); `http://tamago.mtk.nao.ac.jp`.

[6] L. Blanchet, T. Damour, B.R. Iyer, C.M. Will and A.G. Wiseman, Phys. Rev. Lett. **74**, 3515 (1995); L. Blanchet, T. Damour and B.R. Iyer, Phys. Rev. D **51**, 5360 (1995); C.M. Will and A.G. Wiseman, *ibid.* **54**, 4813 (1996).

[7] P. Jaranowski and G. Schäfer, Phys. Rev. D **57**, 7274 (1998); **60**, 124003 (1999); T. Damour, P. Jaranowski and G. Schäfer, *ibid.* **62**, 044024 (2000); 021501(R) (2000); **63**, 044021 (2001).

[8] L. Blanchet, G. Faye, B.R. Iyer, B. Joguet, Phys. Rev. D **65**, 061501 (2002).

[9] T. Damour, P. Jaranowski and G. Schäfer, Phys. Lett. B **513**, 147 (2001).

[10] M. Salgado, S. Bonazzola, E. Gourgoulhon and P. Haensel, Astrophys. J. **291**, 155 (1994); G.B. Cook, S.L. Shapiro and S.A. Teukolsky, *ibid.* **424**, 823 (1994); P. Haensel, M. Salgado, and S. Bonazzola, Astronomy and Astrophysics **296**, 745 (1995); W.G. Laarakkers and E. Poisson, Astrophys. J. **512**, 282L (1999).

[11] C.S. Kochanek, Astrophys. J. **398**, 234 (1992); L. Bildsten and C. Cutler, *ibid.* **400**, 175 (1992).

[12] V. Kalogera, Astrophys. J. **541**, 319 (2000).

[13] P. Grandclément, M. Ihm, V. Kalogera, and K. Belczynski, "Searching for gravitational waves from the inspiral of precessing binary systems: astrophysical expectations and detection efficiency of 'spiky' templates," gr-qc/0312084.

[14] T.A. Apostolatos, C. Cutler, G.J. Sussman and K.S. Thorne, Phys. Rev. D **49**, 6274 (1994).

[15] T.A. Apostolatos, Phys. Rev. D **54**, 2438 (1996).

[16] P. Grandclément, V. Kalogera and A. Vecchio, Phys. Rev. D **67**, 042003 (2003).

[17] P. Grandclément and V. Kalogera, Phys. Rev. D **67**, 082002 (2003).

[18] BCV2: A. Buonanno, Y. Chen, and M. Vallisneri, Phys. Rev. D **67**, 104025 (2003).

[19] The authors of Refs. [16, 17] did not include a Thomas precession term in the physical model used to test the templates; for this reason, the fitting factors quoted in Refs. [16, 17] are substantially lower than our result. We note that those authors have recently investigated the effect of that term and found agreement with our results [13].

[20] A. Buonanno, Y. Chen, Y. Pan and M. Vallisneri, "A physical family of gravity-wave templates for precessing binaries of spinning compact objects: III. Parameter estimation" (in preparation).

[21] A. Buonanno, Y. Chen, Y. Pan and M. Vallisneri, "A physical template family for gravitational waves from precessing binaries of spinning compact objects: II. Application to double-spin binaries" (in preparation).

[22] BCV1: A. Buonanno, Y. Chen, and M. Vallisneri, Phys. Rev. D **67**, 024016 (2003).

[23] B.S. Sathyaprakash, Phys. Rev. D **50**, R7111 (1994).

[24] T. Damour, B.R. Iyer, and B.S. Sathyaprakash, Phys. Rev. D **63**, 044023 (2001).

[25] É.É. Flanagan and S. A. Hughes, Phys. Rev. D **57**, 4535 (1998); **57** 4566 (1998).

[26] L.S. Finn and D.F. Chernoff, Phys. Rev. D **47**, 2198 (1993).

[27] B.J. Owen, Phys. Rev. D **53**, 6749 (1996).

[28] T. Damour, B.R. Iyer, and B.S. Sathyaprakash, Phys. Rev. D **57**, 885 (1998).

[29] R. Balasubramanian, B.S. Sathyaprakash, and S.V. Dhurandhar, Phys. Rev. D **53**, 3033 (1996).

[30] L.S. Finn, Phys. Rev. D **46**, 5236 (1992).

[31] B.S. Sathyaprakash and S.V. Dhurandhar, Phys. Rev. D **44**, 3819 (1991).

[32] S.V. Dhurandhar and B.S. Sathyaprakash, Phys. Rev. D **49**, 1707 (1994).

[33] C. Cutler and É.É. Flanagan, Phys. Rev. D **49**, 2658 (1994);

[34] B.J. Owen and B. Sathyaprakash, Phys. Rev. D **60**, 022002 (1999).

[35] T.A. Apostolatos, Phys. Rev. D **52**, 605 (1995).

[36] L.A. Wainstein and L.D. Zubakov, *Extraction of signals from noise* (Prentice-Hall, Englewood Cliffs NJ, 1962).

[37] L.E. Kidder, C.M. Will, and A.G. Wiseman, Phys. Rev. D **47**, 4183(R) (1993).

[38] L.E. Kidder, Phys. Rev. D **52**, 821 (1995).

[39] L. Blanchet, T. Damour, and G. Esposito-Farese, "Dimensional regularization of the third postnewtonian dynamics of point particles in harmonic coordinates," gr-qc/0311052; Y. Itoh and T. Futamesa, Phys. Rev. D **68**, 121501 (2003); Y. Itoh, Phys. Rev. D **69**, 064018 (2004).

[40] Equation (11) of BCV2 suffers from two misprints: the spin-orbit term should be divided by M^2, and the spin-spin term by M^4.

[41] When templates are used in actual GW searches, the initial orbital frequency $\omega(0)$ must be chosen so that most of the signal power (i.e., the square of the optimal signal to noise) is accumulated at GW frequencies higher than the corresponding $f_{\rm GW}(0) = \omega(0)/\pi$,

$$\int_{f_{\rm GW}(0)}^{+\infty} \frac{\tilde{h}^*(f)\tilde{h}(f)}{S_n(|f|)} df \simeq \int_0^{+\infty} \frac{\tilde{h}^*(f)\tilde{h}(f)}{S_n(|f|)} df.$$

For the range of binary masses considered in this chapter, and for the LIGO-I noise curve, such a $f_{\rm GW}(0)$ should be about 40 Hz. Most of the calculations performed in this chapter (for instance, the convergence tests and the calculation of the mismatch metric) set instead $f_{\rm GW}(0) = 60$ Hz to save on computational time; experience has proved that the results are quite stable with respect to this change.

[42] Note that the concept of extrinsic and intrinsic parameters had been present in the data-analysis literature for a long time (see, e.g., [36]). Sathyaprakash [23] draws the same distinction between *kinematical* and *dynamical* parameters.

[43] K. Belczynski, V. Kalogera and T. Bulik, Astrophys. J. **572**, 407 (2001).

[44] A. Buonanno and T. Damour, Phys. Rev. D **59**, 084006 (1999); **62**, 064015 (2000); T. Damour, P. Jaranowski and G. Schäfer, *ibid.*, 084011 (2000); T. Damour, *ibid.* **64**, 124013 (2001); T. Damour, B. R. Iyer, P. Jaranowski, and B.S. Sathyaprakash, *ibid.* **67**, 064028 (2003).

[45] In fact, multiple GW detectors are needed to disentangle this factor from the distance D to the source.

[46] B.F. Schutz, in *The Detection of Gravitational Radiation*, D. Blair, ed. (Cambridge University Press, Cambridge, England, 1989).

[47] W.H. Press, S.A. Teukolsky, W.T. Vetterling and B.P. Flannery, *Numerical Recipes in C: The Art of Scientific Computing* (Cambridge University Press, Cambridge, England, 1992).

[48] Just as it happens for the P_I, the magnitude of $\mathbf{u}$ does not affect the value of Eq. (3.48), so the maximization can be carried out equivalently over all the vectors $\mathbf{u}$ that satisfy $\mathbf{u}\mathbf{B}_\alpha\mathbf{u}^T = 1$. We can then use a Lagrangian-multiplier method to find the maximum, Eq. (3.51), and the corresponding $\mathbf{u}$, in a manner similar to the procedure used in App. 3.9.

[49] P. Jaranowski, A. Królak and B.F. Schutz Phys. Rev. D **58**, 063001 (1998); LIGO Scientific Collaboration, "Setting Upper Limits on the Strength of Periodic Gravitational Waves Using the First Science Data from the GEO 600 and LIGO Detectors," Phys. Rev. D, in print.

[50] This is not a conventional hierarchical scheme, at least not in the sense that there is a tradeoff between performance and accuracy.

[51] The square root of the matrix $[\sqrt{C}]^{\mathcal{I}\mathcal{J}}$ can be defined, for instance, by $\sqrt{\mathbf{C}}\,\sqrt{\mathbf{C}}^T = \mathbf{C}$, and it can always be found because the covariance matrix $C^{\mathcal{I}\mathcal{J}}$ is positive definite. It follows that $\overline{Y^{\mathcal{I}}Y^{\mathcal{J}}} = [\sqrt{C}]^{\mathcal{I}\mathcal{L}}[\sqrt{C}]^{\mathcal{J}\mathcal{M}}\overline{X_{\mathcal{L}}X_{\mathcal{M}}} = [\sqrt{C}]^{\mathcal{I}\mathcal{L}}[\sqrt{C}]^{\mathcal{J}\mathcal{M}}\delta_{\mathcal{L}\mathcal{M}} = C^{\mathcal{I}\mathcal{J}}$, as required.

[52] It is given, very roughly, by the number of templates when the minimum match is set to 0. See for instance BCV1.

[53] In fact, the average is dominated by the samples that yield the larger values of $\rho_1(\Omega)$, since the Γ function amplifies small changes in its argument. So the number of samples used in the Monte Carlo integration needs to be such that enough large $\rho_1(\Omega)$ do come up.

[54] LIGO Scientific Collaboration, "Analysis of LIGO data for gravitational waves from binary neutron stars," gr-qc/0308069.

[55] So g_{BC} is truly a metric, except for a factor of $1/2$.

[56] For specific dimensionalities, other regular packings might be more efficient: for instance, in two dimensions a lattice of equilateral triangles requires fewer templates than a lattice of squares.

[57] We have found that we can obtain a satisfactory precision for our metrics by taking several cautions: (i) reducing the parameter displacement ΔX^i along a sequence ${}^{(k)}\Delta X^i$ until the norm $\langle {}^{(k)}\Delta\hat{h} - {}^{(k-1)}\Delta\hat{h}, {}^{(k)}\Delta\hat{h} - {}^{(k-1)}\Delta\hat{h}\rangle$ of the kth correction becomes smaller than a certain tolerance, where ${}^{(k)}\Delta\hat{h} = \left[\hat{h}(X^i + {}^{(k)}\Delta X^i, \Xi^a) - \hat{h}(X^i, \Xi^a)\right] / {}^{(k)}\Delta X^i$ is the kth approximation to the numerical derivative; (ii) employing higher-order finite-difference expressions; (iii) aligning both the starting and ending times of the waveforms $\hat{h}(X^i, \Xi^a)$ and $\hat{h}(X^i + \Delta X^i, \Xi^a)$ by suitably modifying their lengths [by shifting the two waveforms in time, and by truncating or extending $\hat{h}(X^i + \Delta X^i, \Xi^a)$ at its starting point].

[58] The overlap $\langle \hat{h}(X^i, \Xi^\alpha), \hat{h}(X'^i, \Xi'^\alpha)\rangle$ depends only on $t_0 - t_0'$ and $\Phi_0 - \Phi_0'$: we have $\hat{h}(f) \sim \exp\{2\pi i f t_0 + i\Phi_0\}$ and $\hat{h}'(f) \sim \exp\{2\pi i f t_0' + i\Phi_0'\}$, so $\hat{h}'(f)\tilde{h}^*(f) \sim \exp\{2\pi i f(t_0' - t_0) + i(\Phi_0' - \Phi_0)\}$.

[59] C. Cutler, personal communication.

[60] All the expressions to follow can be adapted to the case of *a priori* known probability distribution for the extrinsic parameters. However, in our case it seems quite right to assume that the orientation angles Θ and φ are distributed uniformly over a sphere, and that α is distributed uniformly in the interval $[0, 2\pi]$.

[61] B.S. Sathyaprakash and B.F. Schutz, Class. Quant. Grav. **20**, S209-S218 (2003).

[62] Pictorially, the error that we make with Eq. (3.64) is to let the template bank be thinner than a single template in the direction $e^A_{(1)}$.

[63] In fact, in the context of our templates this rotation is such that Eq. (3.62) ceases to be true in the quasinull eigendirections for $\delta \gtrsim 0.01$. As soon as we move away from the point λ^A where the metric is computed, any rotation of the eigenvectors means that the original quasinull direction is no longer the path along which the mismatch grows most slowly. If the larger eigenvalues are several orders of magnitude larger than the smaller ones, as is true in our case, a tiny rotation is enough to mask the contribution from the smallest eigenvalue.

[64] At least if the geometry of the reduction curve is not very convoluted.

[65] The curves of Figs. 3.8 and 3.9 are in fact obtained by following the quasinull eigenvectors of the *fully projected* (χ_1, κ_1) metric, which is a 2D metric on χ_1 and κ_1 obtained by projecting $g_{ij}^{\rm proj}$ again over M and η [using Eq. (3.71)], *as if they were extrinsic parameters.* The two projection steps are equivalent to projecting the 9D full metric into the 2D (χ_1, κ_1) plane in a single step. This procedure estimates correctly the *reduction mismatch* introduced by adopting the reduced template family created by first collapsing the 2D (χ_1, κ_1) plane into several 1D curves, and then including all the values of (M, η) for each point on the curves. We choose to collapse the (χ_1, κ_1) plane for empirical reasons: the χ_1 and κ_1 parameter bounds are simple, $(\chi_1, \kappa_1) \in [0, 1] \times [-1, 1]$, and the reduction curves have large parameter lengths.

[66] In fact, a second small eigenvector appears as we get close to $\chi_1 = 0$; this is because spin effects vanish in that limit, so a 2D family of nonspinning waveforms should be sufficient to fit all signals with small χ_1.

[67] See, e.g., H. Goldstein, *Classical Mechanics* (Addison-Wesley, Reading, MA, 1980), ch. 5.

[68] E. Poisson, Phys. Rev. D **57**, 5287 (1998).

[69] D. Hils and P.L. Bender, Astrophys. J. **445**, L7 (1995); S. Sigurdsson and M.J. Rees, Mon. Not. R. Astron. Soc. **284**, 318 (1996); L.S. Finn and K.S. Thorne, Phys. Rev. D, **62**, 124021 (2000); A. Ori and K.S. Thorne, *ibid.*, 124022 (2000). For the scientific payoffs of observing extreme-mass-ratio inspirals, see F.D. Ryan, Phys. Rev. D, **52**, 5707 (1995); **56**, 1845 (1997).

[70] P.L. Bender, K. Danzmann, and the LISA Study Team, *Laser Interferometer Space Antenna for the Detection of Gravitational Waves, Pre-Phase A Report*, doc. MPQ233 (Max-Planck-Institüt für Quantenoptik, Garching, July 1998).

[71] L. Barack and C. Cutler, "LISA capture sources: approximate waveforms, signal-to-noise ratios, and parameter estimation accuracy," gr-qc/0310125; T. Creighton and J. Gair, private communication.

Chapter 4

A quasi-physical family of gravity-wave templates for precessing binaries of spinning compact objects: II. Application to double-spin precessing binaries

The gravitational waveforms emitted during the adiabatic inspiral of precessing binaries with two spinning compact bodies of comparable masses, evaluated within the post-Newtonian approximation, can be reproduced rather accurately by the waveforms obtained by setting one of the two spins to zero, at least for the purpose of detection by ground-based gravitational-wave interferometers. Here we propose to use this quasi-physical family of single-spin templates to search for the signals emitted by double-spin precessing binaries, and we find that its signal-matching performance is satisfactory for source masses $(m_1, m_2) \in [3, 15]M_\odot \times [3, 15]M_\odot$. For this mass range, using the LIGO-I design sensitivity, we estimate that the number of templates required to yield a minimum match of 0.97 is $\sim 320,000$. We also discuss the accuracy to which the single-spin template family can be used to estimate the parameters of the original double-spin precessing binaries.

Originally published as A. Buonanno, Y. Chen, Y. Pan, and M. Vallisneri, Phys. Rev. D **70**, 104003 (2004).

4.1 Introduction

An international network of long-baseline laser-interferometric gravitational-wave detectors, consisting of the Laser-Interferometer Gravitational-wave Observatory (LIGO) [1], of VIRGO [2], of GEO 600 [3], and of TAMA 300 [4], has by now begun science operations. VIRGO is in its commissioning phase, while LIGO has already completed three science runs (S1 in August–September 2002 [5], S2 in February–April 2003, and S3 in October 2003–January 2004; S1 and S3 were in coincidence with GEO 600) with increasing sensitivity and stability. The analysis of S1 data has been completed, yielding new upper limits on event rates for various

classes of astrophysical sources [6]; the data from S2 and S3 are still being analyzed. LIGO reached its full design sensitivity in 2005.

Compact binaries consisting of black holes (BHs) and neutron stars (NSs) are among the most promising [7] and best-understood sources for such gravitational-wave (GW) interferometers, which can observe the waves emitted by the binaries in the adiabatic-inspiral regime, where post-Newtonian (PN) calculations [8, 9, 10, 11, 12, 13, 14, 15, 16, 17] are appropriate to describe the orbital dynamics and predict the gravitational waveforms.

Very little is known about the statistical distributions of BH spins in compact binaries: The spins could be large, and they need not be aligned with the orbital angular momentum. When this is the case, spin-orbit and spin-spin interactions can cause the rapid precession of the orbital plane of the binary, and thus significant modulations of the emitted GWs, as it was shown by Apostolatos, Cutler, Sussman, and Thorne (ACST) [18], and later by Apostolatos [19]. These modulational effects should be included in the theoretical waveform models (templates) used in matched-filtering GW searches. However, using template banks parametrized by all the relevant physical parameters (the masses, the spins, the angles that describe the relative orientations of detector and binary, and the direction of propagation of GWs to the detector) would make such searches extremely computationally intensive.

One possibility to reduce the computational cost is the adoption of smaller *detection template families* (DTFs), which capture the essential features of the true waveforms, but depend on a smaller number of parameters. A DTF for precessing binaries was first proposed by Apostolatos [20, 21], building on the analysis of precessional dynamics of Refs. [18, 19]. However, according to Apostolatos' own estimates and to Grandclément, Kalogera and Vecchio's later tests [22], the computational resources required by the Apostolatos DTF are still prohibitive, and its signal-matching performance is unsatisfactory. The latter is improved in a modified version of the DTF [23, 24], which adds δ-like *spikes* in the waveform phase.

Buonanno, Chen, and Vallisneri [25, henceforth BCV2] investigated the dynamics of precession further, and proposed a new convention to write the dominant quadrupolar contribution to GW emission. In this convention, the oscillatory effects of precession are isolated in the evolution of the GW polarization tensors, which are combined with the detector's *antenna patterns* to yield its response. As a result, the response can be written as the product of a carrier signal and a modulational correction, which can be handled using an extension of Apostolatos' treatment of precessional effects. BCV2 cast these waveforms into a mathematical structure that allows searching automatically and economically over all the parameters related to precessional modulations, except for a single parameter that describes the timescale of modulation. The BCV2 DTF has reasonable computational requirements and good signal-matching capabilities. However, especially for binaries with high, comparable masses, it has the shortcoming that a large number of unphysical waveforms are automatically included in GW searches (albeit at no extra computational cost), increasing the probability of false alarms triggered by noise. [This shortcoming is unfortunately but unavoidably characteristic of DTFs, which replace a description in terms of physical source parameters by one in terms of phenomenological

signal parameters.]

This chapter is the second in a series (begun with Chapter 3) written to investigate the possibility of searching for precessing binaries using a *physical* family of signal templates (a PTF) computed from the PN equations of motion. Although at first sight the number of physical parameters necessary to describe a waveform is large, we were able to reduce the effective dimensionality of the template family using the insight developed in the construction of DTFs. As mentioned above, BCV2 [25, Sec. VI D] established that it is possible to search easily over most of the parameters related to the kinematics of precession (such as the orientation of the detector and of the binary as a whole, the direction of GW propagation, and the initial orbital phase). In effect, these *extrinsic* parameters can be incorporated in the detection statistic, while single "templates" [27] remain functions only of the masses of the binary components, of the magnitudes of their spins, and of the relative angles between the spins and the orbital angular momentum at a fiducial frequency. Under the assumption of circular adiabatic inspiral [28], seven such *intrinsic* parameters are needed for a generic binary where both spins are important (henceforth, a *double-spin binary*); four are needed for a binary where only one body has significant spin (henceforth, a *single-spin binary*). (See Sec. 4.2 for the distinction between extrinsic and intrinsic parameters.)

In Chapter 3, we demonstrated the feasibility of a PTF search for single-spin binaries: We described a two-stage algorithm to search over the extrinsic parameters (the first stage emphasizes computational efficiency, but retains some unphysical waveforms; the second stage, applied only to first-stage triggers, restricts the possible search outcomes to physical configurations). Using this algorithm, we tested a four-parameter PTF for binaries with $(m_1, m_2) \in [7M_\odot, 12M_\odot] \times [1M_\odot, 3M_\odot]$, where the assumption of a single significant spin is justified. We found that $\sim 76,000$ templates are required for a search in this mass range, for a minimal match of 0.97 (see Sec. 4.2 for a definition of minimal match); under the assumption of Gaussian, stationary noise, we also found that the detection threshold required for a given false-alarm probability is lower in the PTF search than in a DTF search with the same number of intrinsic parameters.

In this chapter we examine PTF searches for the more general class of double-spin binaries. Although in this case we have seven intrinsic parameters, they are not all essential in determining the waveforms. This is strictly true in two limits. First, as it was realized by ACST [18], if the two binary masses are equal, and if spin-spin interactions are ignored, the same orbital evolution can be replicated by giving the total spin to one of the objects. Indeed, for the mass ranges of interest to ground-based interferometers, spin-spin effects contribute mildly to the binding energy and to the PN GW flux, even close to the last stable orbit. Second, if the mass ratio $\eta = m_1 m_2/(m_1 + m_2)^2$ is very low (as it was assumed in Paper I), the spin of the less massive object can be ignored. In addition, as investigated by BCV2 (and less systematically by Kidder [10]), the dynamics of double-spin binaries with generic mass ratios show features similar to those described by ACST for single-spin binaries.

These arguments have led us to conjecture that single-spin waveforms may always be sufficient to approximate double-spin waveforms, at least for the purpose of GW searches with ground-based interferometers.

Since the single-spin parameters that best reproduce a given double-spin signal might not be in the physical range for a true single-spin binary (for instance, because the spin of one of two objects must do the work of two, it might have to exceed the maximal spin allowed for BHs), the single-spin family should be called *quasi-physical*, but we shall continue to use "PTF" loosely. In the rest of this chapter, we present evidence that our conjecture is correct for the mass range $(m_1, m_2) \in [3M_\odot, 15M_\odot] \times [3M_\odot, 15M_\odot]$, and we examine the computational requirements and the parameter-estimation performance of a single-spin PTF search for double-spin binaries in this mass range.

This chapter is organized as follows. In Sec. 4.2, we provide a short glossary for the notions and quantities of matched-filtering GW searches (some standard, some developed in Paper I) that are needed later. In Sec. 4.3.1, we review the adiabatic PN dynamics of double-spin binaries; in Sec. 4.3.2, we describe our family of quasi-physical single-spin templates, and we evaluate their signal-matching capabilities against double-spin binaries with maximal spins (where precessional effects are expected to be strongest); in Sec. 4.3.3, we study the robustness of adiabatic PN waveforms for binaries with high, comparable masses; in Sec. 4.3.4, we discuss some features of double-spin binary dynamics that help to explain the good signal-matching performance of single-spin templates. In Sec. 4.4, we estimate the number of templates required in a single-spin PTF search in our mass range of interest. In Sec. 4.5, we investigate the extraction of the physical parameters of the double-spin binary using single-spin templates. Last, in Sec. 4.6 we summarize our main conclusions.

4.2 A glossary of matched-filtering GW detection

In this chapter we adopt the standard formalism of matched-filtering GW detection, as summarized in Ref. [17] (which includes an extensive bibliography), and as extended in Ref. [26] to a special treatment of extrinsic and intrinsic parameters. Here we provide a glossary of the notions used in this chapter, with pointers to their definitions in Refs. [17, 26].

Templates $h(\lambda^A)$: Theoretical models of GW signals, parametrized by one or more *template parameters* λ^A. A *continuous template family* $\{h(\lambda^A)\}$ defines a smooth submanifold in signal space.

Noise inner product $\langle f, g\rangle$: Eq. (1) of Ref. [17]. A measure of the closeness of two signal, as given by a correlation product weighted by the power spectral density of noise; throughout this chapter we adopt the LIGO-I one-sided noise power spectral density S_n given by Eq. (28) of Ref. [17]. A *normalized* template $\hat{h}(\lambda^A)$ has $\langle \hat{h}(\lambda^A), \hat{h}(\lambda^A)\rangle = 1$.

Match: Inner product of two normalized signals. The *mismatch* is one minus the match.

Overlap $\rho(s, h(\lambda^A))$: Inner product of a signal s with the normalized template $\hat{h}(\lambda^A)$.

Detection statistic: Figure of merit compared with a *detection threshold* to decide whether the signal modeled by a template $h(\lambda^A)$ is present in the detector output o. For Gaussian, stationary noise, the overlap $\rho(o, h(\lambda^A))$ is the *optimal* statistic that minimizes the probability of false dismissal for a given probability of

false alarm (set by the detection threshold). In this context ρ is also known as the *signal-to-noise ratio* (S/N) of the detector output after filtering by the template $\hat{h}(\lambda^A)$. The corresponding detection statistic for an entire template family $\{h(\lambda^A)\}$ is the maximized overlap $\max_{\lambda^A} \rho(o, h(\lambda^A))$.

Fitting factor FF [29]: Eq. (20) of Ref. [17]. Match between a template in a *target* family (representing actual physical signals) and a template in a *search* family, *maximized over all the parameters of the search family*. The FF (a value between 0 and 1) characterizes the effectualness of the search family in reproducing signals modeled by the target family: Using an imperfect family means that only a fraction FF of the available S/N is recovered, reducing the number of true events that pass the detection threshold. The maximized match induces a (many-to-one) map between the space of target parameters and the space of search parameters (see Sec. V on the systematic errors in parameter estimation induced by this map).

Extrinsic (Θ^μ) *and intrinsic* (X^i) *template parameters*: Extrinsic parameters are those over which ρ can be maximized efficiently, without recomputing full search templates for each set of extrinsic parameters under consideration (but perhaps using a small number of subtemplates) [30]. By contrast, maximizing ρ over the intrinsic parameters requires computing a full template for each different set of intrinsic parameters in the search range. Searches for signals modeled by a template family $\{h(\lambda^A) \equiv h(X^i, \Theta^\mu)\}$ are usually implemented by obtaining $\max_{\Theta^\mu} \rho$ for each template in a discrete bank $\{h(X^i_{(k)}, \Theta^\mu)\}$, laid down only along the intrinsic-parameter directions.

Minimum match MM and mismatch metric [31]: Eqs. (21)–(24) of Ref. [17]. The spacing of discrete search banks is chosen so that at most a fraction MM is lost from the S/N that would be obtained with a continuous search bank; the corresponding loss in detection rate, for the same detection threshold, is a fraction MM^3. The choice of the spacing is helped by considering the (full) *mismatch metric* g_{AB}, which serves as a local quadratic expansion of the mismatch over all the search parameters. An approximation to the number of templates needed to achieve a given MM, computed using the metric, is given by Eq. (25) of Ref. [17].

Projected metric: Eqs. (65) and (72) of Ref. [26]. Given that the search template bank has no extension along the extrinsic-parameter directions, it is useful to consider a projected metric g^{proj}_{ij} that approximates the mismatch *already minimized over the extrinsic search parameters*. This g^{proj}_{ij} is still a function of the intrinsic and extrinsic *target* parameters. The *average projected metric* $\overline{g^{\mathrm{proj}}_{ij}}$ (Eq. (75) of Ref. [26]) is a weighted average over the extrinsic target parameters, which can be used to estimate the number of templates needed to achieve a given reduction in detection rate, for a uniform distribution of target extrinsic parameters (this reduction is proportional to $\overline{\mathrm{MM}}^3$, where $\overline{\mathrm{MM}}$ is the *average minimum match*).

Reduced search parameter space and reduction curves [32, 26]: It can happen that the variety of waveforms spanned by an n-dimensional (search) template family is approximated with very high FF by an $(n-k)$-dimensional subset of the family (a *reduced family*). This circumstance is signaled locally in the mismatch metric by the presence of k *quasi-null directions* (i.e., eigenvectors with very small eigenvalues). The integral curves of these directions (the *reduction curves*) correspond to sets of templates with very high match within

the set, and map a reduced family into another. In this case, it is advantageous to derive the discrete search bank from a reduced family: Ideally, one would reparametrize the full family using k parameters that run along the reduction curves, and then discard those parameters before laying down templates. See Ref. [26] for a thorough discussion.

4.3 Single-spin template family to match double-spin precessing binaries

This section contains the main results of this chapter. In Sec. 4.3.1 we describe the PN equations for the circular adiabatic inspiral of a double-spin binary; this *target model* is used throughout this chapter to represent physical signals. In Sec. 4.3.2 we describe our proposed single-spin *search template family*, and we evaluate its effectualness (which is excellent) in approximating the target waveforms. In Sec. 4.3.3 we compare single-spin signals obtained at different PN orders, to argue that the circular adiabatic model of inspirals used in this chapter gives robust predictions for the actual physical waveforms. Last, in Sec. 4.3.4 we study the precessional dynamics of double-spin binaries to understand which of their features can be represented accurately by single-spin systems, and which cannot.

4.3.1 Target model: Double-spin precessing binaries

Post-Newtonian calculations provide the following set of equations describing the adiabatic evolution of double-spin precessing binaries. The first derivative of the orbital (angular) frequency, up to 3.5PN order [33] reads [8, 9, 10, 11, 12, 13, 14, 15, 25]:

$$\frac{\dot{\omega}}{\omega^2} = \frac{96}{5}\,\eta\,(M\omega)^{5/3}\left(1 + \mathcal{P}_{1\mathrm{PN}} + \mathcal{P}_{1.5\mathrm{PN}} + \mathcal{P}_{2\mathrm{PN}} + \mathcal{P}_{2.5\mathrm{PN}} + \mathcal{P}_{3\mathrm{PN}} + \mathcal{P}_{3.5\mathrm{PN}}\right), \tag{4.1}$$

where

$$\mathcal{P}_{\rm 1PN} = -\frac{743+924\,\eta}{336}\,(M\omega)^{2/3}\,, \tag{4.2}$$

$$\mathcal{P}_{\rm 1.5PN} = -\left(\frac{1}{12}\sum_{i=1,2}\left[\chi_i\left(\hat{\mathbf{L}}_N\cdot\hat{\mathbf{S}}_i\right)\left(113\frac{m_i^2}{M^2}+75\eta\right)\right]-4\pi\right)(M\omega)\,, \tag{4.3}$$

$$\mathcal{P}_{\rm 2PN} = \left\{\left(\frac{34\,103}{18\,144}+\frac{13\,661}{2\,016}\,\eta+\frac{59}{18}\,\eta^2\right)-\frac{1}{48}\,\eta\chi_1\chi_2\left[247\,(\hat{\mathbf{S}}_1\cdot\hat{\mathbf{S}}_2)-721\,(\hat{\mathbf{L}}_N\cdot\hat{\mathbf{S}}_1)(\hat{\mathbf{L}}_N\cdot\hat{\mathbf{S}}_2)\right]\right\}(M\omega)^{4/3} \tag{4.4}$$

$$\mathcal{P}_{\rm 2.5PN} = -\frac{1}{672}\,(4\,159+14\,532\,\eta)\,\pi\,(M\omega)^{5/3}\,, \tag{4.5}$$

$$\mathcal{P}_{\rm 3PN} = \left[\left(\frac{16\,447\,322\,263}{139\,708\,800}-\frac{1\,712}{105}\,\gamma_E+\frac{16}{3}\pi^2\right)+\left(-\frac{273\,811\,877}{1\,088\,640}+\frac{451}{48}\pi^2-\frac{88}{3}\hat{\theta}\right)\eta\right.$$
$$\left.+\frac{541}{896}\,\eta^2-\frac{5\,605}{2\,592}\,\eta^3-\frac{856}{105}\log\left[16(M\omega)^{2/3}\right]\right](M\omega)^2\,, \tag{4.6}$$

$$\mathcal{P}_{\rm 3.5PN} = \left(-\frac{4\,415}{4\,032}+\frac{661\,775}{12\,096}\,\eta+\frac{149\,789}{3\,024}\,\eta^2\right)\pi\,(M\omega)^{7/3}\,. \tag{4.7}$$

Here, m_1 and m_2 are the masses of the two bodies, with $m_1 \geq m_2$; $M = m_1 + m_2$ is the total mass, and $\eta = m_1 m_2/M^2$ is the symmetric mass ratio; $\mathbf{L}_N = \mu\,\mathbf{x}\times\mathbf{v}$ (with $\mu = m_1 m_2/M$) is the Newtonian angular momentum (with $\mathbf{x}$ and $\mathbf{v}$ the two-body center-of-mass radial separation and relative velocity), and $\hat{\mathbf{L}}_N = \mathbf{L}_N/|\mathbf{L}_N|$; $\mathbf{S}_1 = \chi_1\,m_1^2\,\hat{\mathbf{S}}_1$ and $\mathbf{S}_2 = \chi_2\,m_2^2\,\hat{\mathbf{S}}_2$ are the spins of the two bodies (with $\hat{\mathbf{S}}_{1,2}$ unit vectors, and $0 < \chi_{1,2} < 1$ for BHs); $\gamma_E = 0.577\ldots$ is Euler's constant; last, $\hat{\theta} = \theta + 1987/1320 + 7\omega_s/11$ (with θ an unknown arbitrary parameter that enters the GW flux at 3PN order [13], and $\omega_s = 0$ [12, 14, 15]).

In Eq. (4.1) we did not include the quadrupole-monopole terms [34], because we have already shown (see Sec. III E of Ref. [26]) that those terms do not significantly affect matches once these are maximized on binary parameters. The precession equations for the spins read [10, 18]

$$\dot{\mathbf{S}}_1 = \frac{(M\omega)^2}{2M}\left\{\eta\,(M\omega)^{-1/3}\left(4+3\frac{m_2}{m_1}\right)\hat{\mathbf{L}}_N+\frac{1}{M^2}\left[\mathbf{S}_2-3(\mathbf{S}_2\cdot\hat{\mathbf{L}}_N)\hat{\mathbf{L}}_N\right]\right\}\times\mathbf{S}_1\,, \tag{4.8}$$

$$\dot{\mathbf{S}}_2 = \frac{(M\omega)^2}{2M}\left\{\eta\,(M\omega)^{-1/3}\left(4+3\frac{m_1}{m_2}\right)\hat{\mathbf{L}}_N+\frac{1}{M^2}\left[\mathbf{S}_1-3(\mathbf{S}_1\cdot\hat{\mathbf{L}}_N)\hat{\mathbf{L}}_N\right]\right\}\times\mathbf{S}_2\,, \tag{4.9}$$

and the precession equation for $\hat{\mathbf{L}}_N$ is [10, 18]

$$\dot{\hat{\mathbf{L}}}_N = \frac{\omega^2}{2M}\left\{\left[\left(4+3\frac{m_2}{m_1}\right)\mathbf{S}_1+\left(4+3\frac{m_1}{m_2}\right)\mathbf{S}_2\right]\times\hat{\mathbf{L}}_N-\frac{3\,\omega^{1/3}}{\eta\,M^{5/3}}\left[(\mathbf{S}_2\cdot\hat{\mathbf{L}}_N)\,\mathbf{S}_1+(\mathbf{S}_1\cdot\hat{\mathbf{L}}_N)\,\mathbf{S}_2\right]\times\hat{\mathbf{L}}_N\right\}. \tag{4.10}$$

We stop the adiabatic evolution when the binary reaches the minimum energy circular orbit (MECO) defined by Eqs. (11)–(13) of Ref. [25]. The leading-order mass-quadrupole gravitational waveform can be obtained from Eqs. (65)–(78) of Ref. [25]. Those equations for the gravitational waveform, together with Eqs. (4.1)–(4.10), define our target model for precessing double-spin binaries.

Using the language of Ref. [25], precessing binaries of spinning BHs are described by the four *basic* (intrinsic) parameters m_1, m_2, $S_1 \equiv |\mathbf{S}_1|$, $S_2 \equiv |\mathbf{S}_2|$, by three *local* (intrinsic) parameters describing the relative

orientation of the spins with respect to the angular momentum at a fiducial frequency (see Table I and Fig. 4 of Ref. [25]), and by five *directional* (extrinsic) parameters describing the relative orientation of the binary and the detector (see Table I of Ref. [25]). The waveforms depend also (if trivially) on two other extrinsic parameters, the initial phase Φ_0 and the time of arrival t_0; depending on the context, we shall at times omit these when counting the number of extrinsic parameters.

4.3.2 Search template family: Single-spin binaries

As discussed in Sec. 4.1, the results of previous investigations [18, 35, 25, 26] suggest that the gravitational waveforms emitted by double-spin binaries with comparable component masses can be approximated (at least for the purpose of detection with ground-based interferometers) by waveforms computed by neglecting spin-spin effects, and by assigning the total spin of the binary to a single BH. Thus, in this chapter we examine the detection performance of the single-spin search family obtained from Eqs. (4.1)–(4.10) by setting $\mathbf{S}_2 = 0$. The simplified equations are

$$\begin{aligned}
\frac{\dot{\omega}}{\omega^2} &= \frac{96}{5}\,\eta_s\,(M_s\,\omega)^{5/3}\Big[1 + \text{PN corrections} \qquad (4.11)\\
&- \frac{1}{12}\Big(\hat{\mathbf{L}}_N\cdot\hat{\mathbf{S}}_{1s}\Big)\chi_{1s}\Big(113\,\frac{m_{1s}^2}{M_s^2} + 75\eta_s\Big)(M_s\,\omega)\Big],\\
\dot{\mathbf{S}}_{1s} &= \frac{\eta_s(M_s\,\omega)^{5/3}}{2M_s}\left(4 + 3\frac{m_{2s}}{m_{1s}}\right)\hat{\mathbf{L}}_N\times\mathbf{S}_{1s}\,, \qquad (4.12)\\
\dot{\hat{\mathbf{L}}}_N &= \frac{\omega^2}{2M_s}\left(4 + 3\frac{m_{2s}}{m_{1s}}\right)\mathbf{S}_{1s}\times\hat{\mathbf{L}}_N\,, \qquad (4.13)
\end{aligned}$$

where $M_s = m_{1s} + m_{2s}$, $\eta_s = m_{1s}\,m_{2s}/M_s^2$ and $\mathbf{S}_{1s} = \chi_{1s}\,m_{1s}^2\,\hat{\mathbf{S}}_{1s}$. The "$s$" subscript stands for *search* parameters. In Eq. (4.11), "PN corrections" denotes the terms in Eqs. (4.3)–(4.7) that do not depend on the spins. The leading-order mass-quadrupole gravitational waveform is given by Eqs. (65)–(78) and (11)–(13) of Ref. [25], after setting the spin of the lighter body to zero. This completes the definition of our single-spin search template family, which is parametrized by the four intrinsic parameters M_s, η_s, χ_{1s}, and $\kappa_{1s} = \hat{\mathbf{S}}_{1s}\cdot\hat{\mathbf{L}}_N$, and by five extrinsic parameters that describe the relative orientation of the detector and the binary (see Sec. III C of Ref. [26]). The maximization of the overlap with respect to the extrinsic parameters can be performed semi-algebraically, in two steps, as described in Sec. IV of Ref. [26].

We note that the simplified Eqs. (4.11)–(4.13) are exactly equivalent to the full Eqs. (4.1)–(4.10) in the two limits mentioned in Sec. I: for equal masses, if spin-spin effects are neglected; and for $m_1 \gg m_2$ (i.e., small η). To test the effectualness of the single-spin search templates in matching our target signals for binary configurations with both comparable and unequal masses, we computed the FF (i.e., the match, maximized over the intrinsic and intrinsic search parameters; see Sec. II) for target binaries with two maximal spins, and with masses $(m_1 + m_2) = (3+3)M_\odot$, $(6+3)M_\odot$, $(6+6)M_\odot$, $(9+3)M_\odot$, $(12+3)M_\odot$, $(10+10)M_\odot$, $(15+10)M_\odot$, and $(15+15)M_\odot$. In the $(12+3)M_\odot$ case we also considered a target binary with $\chi_1 = 1/16$ and $\chi_2 = 1$, i.e.

	$(3+3)M_\odot$		$(6+3)M_\odot$	$(6+6)M_\odot$		$(9+3)M_\odot$	$(12+3)M_\odot$	
templates:	with spin	no spin	with spin	with spin	no spin	with spin	with spin	(eq-spin)
FF ≥ 0.99	95%	31%	74%	98%	59%	90%	95%	84%
FF < 0.99	5%	69%	26%	2%	41%	10%	5%	16%
FF < 0.95	0%	38%	3%	0%	25%	1%	0%	0%
lowest FF	0.9085	0.7042	0.9119	0.7250	0.6391	0.8945	0.9734	0.9684
$\overline{\text{FF}}$	≥ 0.989	≥ 0.9376	≥ 0.986	≥ 0.987	≥ 0.9342	≥ 0.989	≥ 0.990	≥ 0.990

	$(10+10)M_\odot$		$(15+10)M_\odot$		$(15+15)M_\odot$	
templates:	with spin	no spin	with spin	no spin	with spin	no spin
FF ≥ 0.99	100%	29%	98%	22%	100%	30%
FF < 0.99	0%	71%	2%	78%	0%	70%
FF < 0.95	0%	34%	0%	46%	0%	31%
lowest FF	0.9754	0.7142	0.9691	0.7138	≥ 0.99	0.7546
$\overline{\text{FF}}$	≥ 0.990	≥ 0.945	≥ 0.990	≥ 0.936	≥ 0.990	≥ 0.957

Table 4.1: Summary of FFs between the single-spin search template family and the double-spin target model. The numerical maximization procedure is stopped whenever a FF ≥ 0.99 is achieved. The upper table shows results for lower-mass binaries ($M \leq 15M_\odot$); the lower table for higher-mass binaries ($M \geq 20M_\odot$). In the first three rows of each table, we list the percentage of systems yielding FFs ≥ 0.99, < 0.99 and < 0.95, in a population of 100 target systems [500 for $(m_1+m_2) = (6+3)M_\odot$ and $(9+3)M_\odot$ binaries] with maximal spins and random, uniform distributions of initial spin and detector orientations (local parameters). In the fourth row we list the lowest FFs found among the population; in the last row, we list the average FFs (when a FF ≥ 0.99, we use 0.99 in computing the average.) The distribution of the FFs for selected mass configurations is also histogrammed in Fig. 4.1. The target and search waveforms are computed by starting the integration of the equations of motion at an instantaneous GW frequency of is 60 Hz and 40 Hz for upper and lower tables, respectively. For some mass configurations we show also the FFs for nonspinning templates (i.e., single-spin templates where χ_{1s} was set to zero), and for $(12+3)M_\odot$ binaries, we show the FFs for a target configuration with $\chi_1 = 1/16$ and $\chi_2 = 1$ (i.e., the S_2 is maximal and $S_1 = S_2$), which is referred to as "(eq-spin)" in the table.

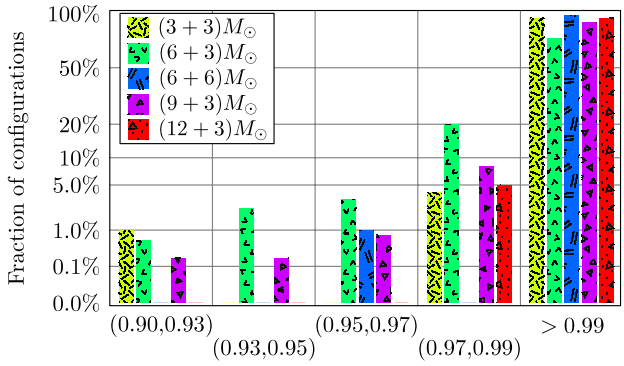

Figure 4.1: Distribution of FFs for lower-mass ($M \leq 15M_\odot$) binary configurations. See the caption to Table 4.1 for an explanation of how the FF distributions were obtained.

the two objects possess equal magnitude of spins, while the less massive one is maximally spinning. Search and target signals were always obtained at 2PN order, and the computation of the FF was repeated for 100 or 500 (for the lighter binaries) randomly generated configurations of the target-signal local parameters $\hat{\mathbf{L}}_N$, $\hat{\mathbf{S}}_1$ and $\hat{\mathbf{S}}_2$, assuming uniform and independent angular distributions. The directional parameters of the target signals were fixed to arbitrary values without loss of generality, since for the purpose of computing FFs they are degenerate with respect to the local parameters (see Sec. VI A of Ref. [25]).

The results of our tests are listed in Table 4.1, and plotted in Fig. 4.1. For comparison, in Table 4.1 we include also some FFs computed for the nonspinning search templates obtained by setting χ_{1s} to zero in Eqs. (4.11)–(4.13). Our numbers support our conjecture about the effectualness of the single-spin search family. More specifically:

- Spin-spin effects are not important for higher-mass binaries such as $(15 + 15)M_\odot$, $(15 + 10)M_\odot$ and $(10 + 10)M_\odot$, where FFs are consistently very high; however, spin-orbit effects cannot be neglected, as shown by the relatively low FFs achieved by the nonspinning search family.

- For lower-mass binaries such as $(3 + 3)M_\odot$ and $(6 + 6)M_\odot$, FFs are also very high, with few exceptions: thus, although in these binaries spin-spin effects can accumulate over many GW cycles within the band of good detector sensitivity, they rarely become comparable to spin-orbit effects.

- For low–mass-ratio binaries such as $(12 + 3)M_\odot$ ($\eta = 0.16$), FFs are high, since the spin of the heavier object dominates the precessional dynamics. If we reduce the magnitude of S_1 so that $S_1 = S_2$, the resulting FFs become lower, because the dynamics deviates farther from both the single-spin and equal-mass limits.

- The worst FFs are obtained for $(6 + 3)M_\odot$ and $(9 + 3)M_\odot$ binaries, which have rather low total masses, and intermediate mass ratios (thus, they sit halfway between the two single-spin equivalence limits). In this case, double-spin effects cannot be reproduced with accuracy by single-spin systems (in Sec. III D we shall examine in more detail what is happening there). Note however that this happens only for a limited number of angular configurations, so the average of the FF over the sampling is still very high.

The range of search-template parameters needed to yield the high FFs discussed above extends beyond values that would be physical for a real single-spin binary, with $\eta_s > 0.25$ and $\chi_{1s} > 1$. This is to be expected: Consider, for instance, that in the equal-mass case the equivalence between the simplified and the full equations implies values of χ_{1s} up to 2. In Fig. 4.2 we show the parameters of the best-fit search templates corresponding to target signals with the test masses examined above [augmented by $(15 + 3)M_\odot$, $(12 + 6)M_\odot$, and $(15 + 12)M_\odot$]. As shown in the top panel, the search-template images of target signals with the same masses but different local parameters are spread around the nominal (M_s, η_s) values (indicated by the end of the thin lines, and always enclosed within the dashed contour). The uncertainty in target parameter estimation induced by this spreading is discussed in Sec. 4.5. In the same panel, the dotted-dashed line

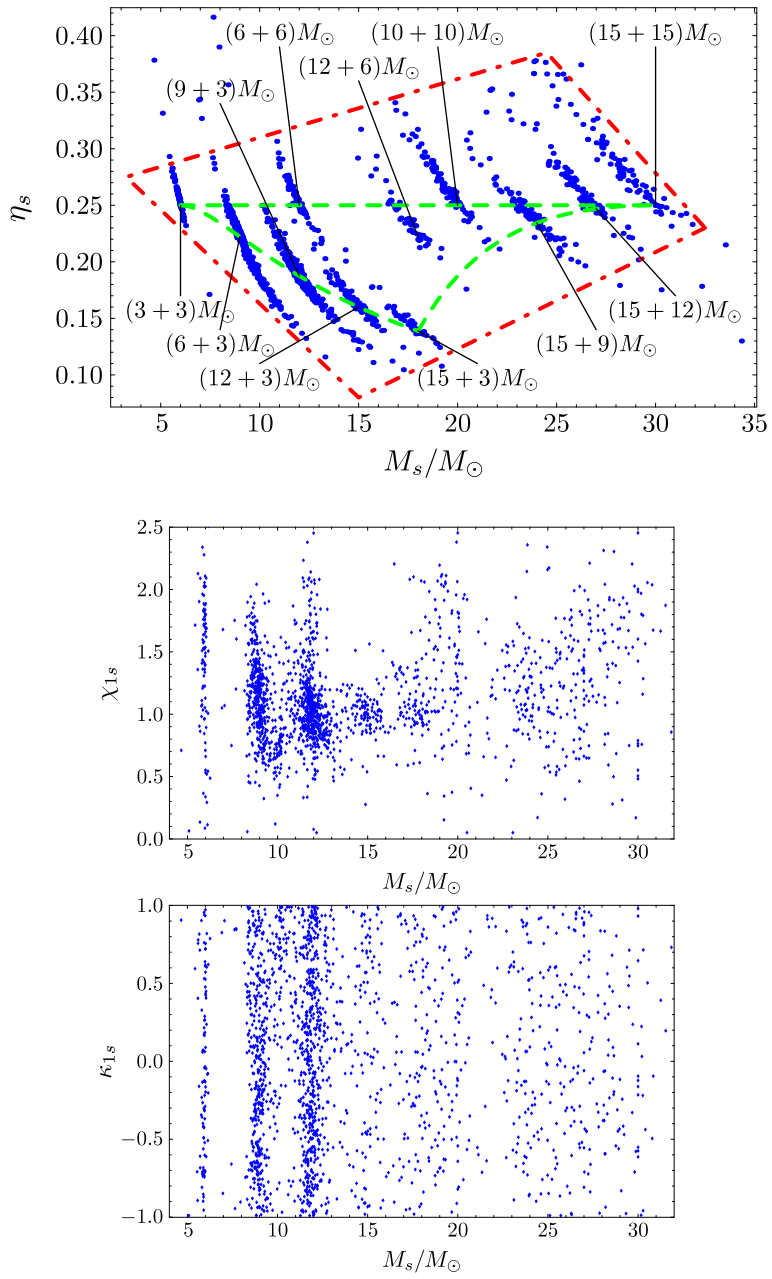

Figure 4.2: Location in the (intrinsic) search parameter space $(M_s, \eta_s, \chi_{1s}, \kappa_{1s})$ of the best-fit templates for target signals with $(m_1 + m_2) = (3 + 3)M_\odot$, $(6 + 3)M_\odot$, $(9 + 3)M_\odot$, $(12 + 3)M_\odot$, $(15 + 3)M_\odot$, $(6 + 6)M_\odot$, $(12+6)M_\odot$, $(10+10)M_\odot$, $(15+10)M_\odot$, $(15+12)M_\odot$, and $(15+15)M_\odot$, and with random angular distributions of the initial $\hat{\mathbf{L}}_N$, $\mathbf{S}_1$, $\mathbf{S}_2$. Dots are denser for the $(6 + 3)M_\odot$ and $(9 + 3)M_\odot$ configurations, for which more FF were computed. In the (M_s, η_s) scatter plot (on top), the dashed contour encloses the region obtained by setting $M_s = M$ and $\eta_s = \eta$, and by taking $(m_1, m_2) \in [3, 15]M_\odot \times [3, 15]M_\odot$. The dotted and dashed line, drawn somewhat arbitrarily, encloses a possible template-bank boundary, used in Sec. 4.4 to estimate the number of templates necessary to search for double-spin binaries in this mass range. The labels identify the search template clusters corresponding to each target mass configuration, and they are connected to the nominal projection point obtained by setting $M_s = M$ and $\eta_s = \eta$.

encloses the template-bank boundary used in Sec. 4.4 to estimate the number of templates necessary for a search of systems with masses $(m_1, m_2) \in [3, 15]M_\odot \times [3, 15]M_\odot$. The bottom panels show the range achieved by the search parameters χ_{1s} and κ_{1s}, which is comparable to the range of the analogous target parameters, $|\mathbf{S}_{\rm tot}|/M^2$ and $\kappa_{\rm tot} \equiv \hat{\mathbf{S}}_{\rm tot} \cdot \hat{\mathbf{L}}_N$.

4.3.3 On the robustness of waveforms across PN orders

In the previous section we have established that single-spin waveforms are good approximations for double-spin waveforms, at least within the mass range under consideration. However, whether double-spin waveforms are representative of actual physical signals is an entirely different question, which hinges on the validity of the circular adiabatic approximation, but also on the robustness of the waveforms under change of PN order: If the waveforms change substantially with increasing order, we should suspect that the description of the physics is incomplete without higher-order terms yet to be computed.

Studying the robustness of double-spin binaries is technically difficult, since it means computing the FF between two template families (of different PN order) with seven intrinsic parameters. This entails the delicate numerical maximization of a seven-parameter function whose evaluation is relatively costly. Instead, we choose to perform our study on single-spin waveforms, and then argue that the results should transfer to double-spin waveforms because the search and target families are close. Thus, our study is very similar to the Cauchy convergence test of Ref. [26], except for the choice of masses: Here we focus on binaries at the higher-mass end of our range, since these systems are expected to have stronger higher-order PN effects within the frequency band of good interferometer sensitivity.

For $(m_1 + m_2) = (10 + 10)M_\odot$, $(15 + 10)M_\odot$, and $(15 + 15)M_\odot$, we list in Table 4.2 the matches across PN orders, maximized only on t_0 and Φ_0; the numbers in parentheses, "(...)", give the FF for the higher-order family as matched by the lower-order family, and the numbers in brackets, "[...]", give the intrinsic parameters where the FF is attained. The tests are performed for $\chi_{1s} = 1$, for different values of κ_{1s}, and for a GW detector perpendicular to the initial orbital plane of the binary, which should be representative of the generic effects of precession. The high FFs obtained between the 2PN and the higher-order families suggest that the 2PN model is already representative of the variety of waveforms expected from actual sources; on the other hand, the lower direct matches (and the biased values of search parameters at the FF) suggest that the family of the highest available order should be used for source parameter estimation. It would be worthwhile to evaluate the FF between the double-spin (and indeed, single-spin) adiabatic model, and nonadiabatic models based on resummed PN equations [36, 16, 17, 37], especially when these predict the end of the inspirals within the band of good interferometer sensitivity.

$(N+k,N)$	$\langle \mathrm{ST}_{N+k}, \mathrm{ST}_N \rangle$ for $(10+10)M_\odot$ binary, $M = 20M_\odot$, $\eta = 0.250$							
	$\kappa_1 = 0.9$		$\kappa_1 = 0.5$		$\kappa_1 = -0.5$		$\kappa_1 = -0.9$	
(1,0)	0.3136	(0.6688) [16.1,0.25,0.00, 0.00]	0.3136	(0.6688)	0.3136	(0.6688) [16.1,0.25,0.00,−0.00]	0.3136	(0.6688)
(1.5,1)	0.3123	(0.5922) [23.7,0.25,0.00, 0.00]	0.2676	(0.5137)	0.2306	(0.4860) [29.2,0.25,0.00,−0.00]	0.2160	(0.4543)
(2,1.5)	0.7124	(0.9823) [19.2,0.25,1.00, 0.99]	0.7222	(0.9877)	0.8545	(0.9886) [19.3,0.25,1.00,−0.66]	0.8601	(≥0.99)
(2.5,2)	0.2851	(0.8702) [18.8,0.25,1.00, 0.91]	0.3099	(0.9206)	0.4166	(≥0.99) [20.4,0.25,1.00, 0.81]	0.4682	(≥0.99)
(3,2)	0.9604	(≥0.99) [20.2,0.25,0.88, 0.79]	0.9743	(≥0.99)	0.9915	(≥0.99) [19.7,0.24,0.88,−0.23]	0.9805	(≥0.99)
(3,2.5)	0.2848	(0.9846) [18,8,0.25,1.00,-0.31]	0.2898	(≥0.99)	0.4027	(0.9823) [20.4,0.25,1.00,−0.99]	0.4634	(0.9740)
(3.5,3)	0.9316	(≥0.99) [20.2,0.25,1.00, 0.90]	0.9475	(≥0.99)	0.9749	(≥0.99) [19.7,0.25,1.00,−0.99]	0.9744	(≥0.99)

$(N+k,N)$	$\langle \mathrm{ST}_{N+k}, \mathrm{ST}_N \rangle$ for $(15+10)M_\odot$ binary, $M = 25M_\odot$, $\eta = 0.247$							
	$\kappa_1 = 0.9$		$\kappa_1 = 0.5$		$\kappa_1 = -0.5$		$\kappa_1 = -0.9$	
(1,0)	0.3124	(0.6030) [19.1,0.25,0.00,0.00]	0.3124	(0.6030)	0.3124	(0.6030) [19.1,0.25,0.00,−0.00]	0.3124	(0.6030)
(1.5,1)	0.2784	(0.4994) [31.0,0.25,0.00,0.00]	0.2732	(0.4684)	0.2466	(0.3913) [41.9,0.25,0.00,−0.00]	0.1896	(0.3491)
(2,1.5)	0.5810	(≥0.99) [24.8,0.23,1.00,0.98]	0.8038	(≥0.99)	0.8644	(≥0.99) [25.4,0.24,1.00,−0.59]	0.9067	(≥0.99)
(2.5,2)	0.2558	(0.8525) [22.9,0.23,1.00,0.95]	0.3296	(0.9280)	0.5022	(≥0.99) [25.5,0.24,1.00, 0.80]	0.5921	(≥0.99)
(3,2)	0.9106	(≥0.99) [24.8,0.24,0.88,0.73]	0.9392	(≥0.99)	0.9858	(≥0.99) [25.1,0.23,0.89,−0.21]	0.9650	(≥0.99)
(3,2.5)	0.2520	(0.9148) [27.0,0.25,1.00,0.85]	0.2942	(≥0.99)	0.4552	(≥0.99) [25.7,0.24,1.00,−0.59]	0.5333	(≥0.99)
(3.5,3)	0.9264	(≥0.99) [24.9,0.24,1.00,0.90]	0.9528	(≥0.99)	0.9769	(≥0.99) [25.3,0.24,1.00,−0.36]	0.9839	(≥0.99)

$(N+k,N)$	$\langle \mathrm{ST}_{N+k}, \mathrm{ST}_N \rangle$ for $(15+15)M_\odot$ binary, $M = 30M_\odot$, $\eta = 0.250$							
	$\kappa_1 = 0.9$		$\kappa_1 = 0.5$		$\kappa_1 = -0.5$		$\kappa_1 = -0.9$	
(1,0)	0.2710	(0.5158) [22.5,0.25,0.00, 0.00]	0.2710	(0.5158)	0.2710	(0.5158) [22.5,0.25,0.00,−0.00]	0.2710	(0.5158)
(1.5,1)	0.2694	(0.4050) [38.3,0.25,0.00, 0.00]	0.2145	(0.3644)	0.2435	(0.3155) [49.6,0.25,0.00,−0.00]	0.1855	(0.2797)
(2,1.5)	0.7619	(≥0.99) [31.1,0.25,1.00, 0.89]	0.8613	(≥0.99)	0.9018	(≥0.99) [30.6,0.25,1.00,−0.43]	0.8946	(≥0.99)
(2.5,2)	0.3403	(0.9086) [28.0,0.24,0.92, 0.99]	0.3856	(0.9237)	0.5372	(≥0.99) [30.4,0.25,1.00, 0.95]	0.6216	(≥0.99)
(3,2)	0.9330	(≥0.99) [28.8,0.24,0.90, 0.82]	0.9360	(≥0.99)	0.9641	(≥0.99) [30.3,0.24,0.88, 0.17]	0.9612	(≥0.99)
(3,2.5)	0.2926	(≥0.99) [28.1,0.25,1.00,−0.58]	0.3549	(≥0.99)	0.4893	(≥0.99) [31.0,0.25,1.00,−0.67]	0.5498	(≥0.99)
(3.5,3)	0.9265	(≥0.99) [30.4,0.25,0.90, 0.71]	0.9456	(≥0.99)	0.9814	(≥0.99) [29.1,0.25,1.00,−0.30]	0.9831	(≥0.99)

Table 4.2: Test of robustness of the PN adiabatic waveforms ST_N (defined in Sec. 4.3.1) across PN orders, for $(m_1 + m_2) = (10 + 10)M_\odot$, $(15 + 10)M_\odot$ and $(15 + 15)M_\odot$. We set $\chi_1 = 1$, $\chi_2 = 0$, and $\kappa_1 = -0.9, -0.5, 0.5$, and 0.9. The matches quoted at the beginning of each column are maximized only with respect to the extrinsic parameters t_0 and Φ_0. In parentheses, "(...)", we give the matches maximized over all the parameters of the lower-order family (i.e., the fitting factors FF for the target family ST_{N+k} as matched by the search family ST_N, evaluated at the ST_{N+k} intrinsic parameters indicated). In brackets, "[...]", we give the parameters M, η, χ_1, and κ_1 (or M and η at 1PN and 1.5PN orders when spin terms are absent) at which the FF is achieved. The detector is set perpendicular to the initial orbital plane, and at 3PN and 3.5PN order we set $\hat{\theta} = 0$; in all cases the integration of the equations of motion starts at an instantaneous GW frequency of 40 Hz. [See Refs. [17, 25] for a discussion of why for some mass combinations the 2.5PN model differs so much from the other orders.]

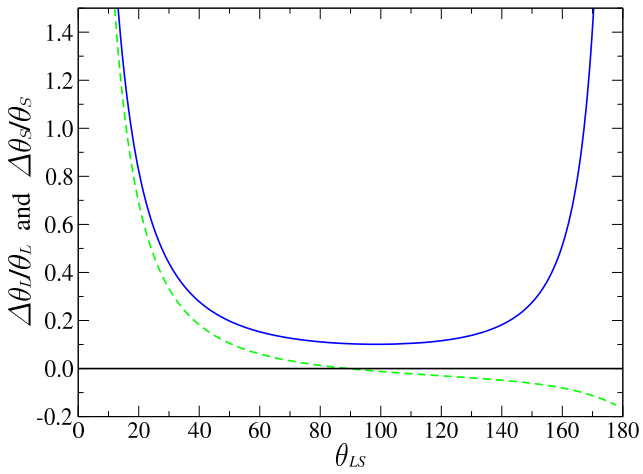

Figure 4.3: Relative change of the opening angles as function of θ_{LS} for a $(6+3)M_\odot$ binary, with $\chi_{\rm tot} = 0.4$, $|\mathbf{L}| = |\mathbf{L}_N| = \eta M^{5/3}\,\omega^{-1/3}$, and $\omega = 2\pi \times 30$ Hz. The change shown corresponds to a 10% increase in $|\mathbf{S}_{\rm tot}|$. The solid and dashed curves refer to θ_L and θ_S, respectively.

4.3.4 Some features of the dynamics of double-spin binaries

In this section we study the precessional dynamics of double-spin binaries, with the purpose of building a physical understanding of the matching performance of single-spin templates observed in Sec. 4.3.2; in particular, we wish to identify what features of double-spin dynamics, absent in single-spin systems, lead to the low FFs seen for lower-mass binary configurations.

From Eqs. (4.8)–(4.10), we see that the precession of double-spin binaries preserves both $\mathbf{J}$ and $|\mathbf{L}|$ at timescales shorter than the radiation-reaction timescale—at which $|\mathbf{L}|$ decreases steadily. Even at longer timescales, as recognized by ACST for single-spin binaries and further tested by BCV2 for generic double-spin binaries, for the vast majority of configurations the direction of the total angular momentum remains almost constant ($\dot{\hat{\mathbf{J}}} \simeq 0$); this behavior is known as *simple precession*.

For single-spin binaries, or for equal-mass binaries if we ignore the spin-spin interaction, the angle between $\mathbf{L}$ and $\mathbf{S}_{\rm tot}$ (θ_{LS}) remains fixed all through evolution [according to Eqs. (4.8)–(4.10)]; for simple precession, this implies that the angle between $\mathbf{L}$ and $\hat{\mathbf{J}}$ (θ_L) must increase, and that the angle between $\mathbf{S}_{\rm tot}$ and $\hat{\mathbf{J}}$ (θ_S) must decrease—both do so monotonically, at the radiation-reaction timescale. In summary, in these binaries the orbital plane precesses while its inclination decreases slowly and monotonically.

In Ref. [21], Apostolatos investigated the effect of spin-spin coupling on the dynamical evolution of *equal-mass, equal-spin* BBHs. He obtained analytical solutions for the opening-angle products $\hat{\mathbf{S}}_{1,2} \cdot \hat{\mathbf{J}}$ and $\hat{\mathbf{S}}_1 \cdot \hat{\mathbf{S}}_2$ to first order in S/L, where J is the total angular momentum, S is S_1 or S_2, and L is the orbital angular momentum (if $m_1 \sim m_2$, then throughout all the inspiral $S \ll L$ [18]). The main feature identified by Apostolatos was that the orbital plane not only becomes slowly less inclined (at the radiation-reaction timescale), but the spin-spin interaction also causes a *nutation*; namely, an oscillation of the orbital inclination

angle (θ_L) at the timescale of the spin-spin interaction.

In the following, we shall relax the assumption that the BH masses are equal, and we shall investigate what the consequences are on the evolution of $\hat{\mathbf{S}}_{1,2}\cdot\hat{\mathbf{J}}$ and $\hat{\mathbf{S}}_1\cdot\hat{\mathbf{S}}_2$. To simplify our notation we fix $m_1+m_2=1$, and we introduce the parameter $\delta\equiv m_1-m_2$, which describes the deviation from the equal-mass case. We keep only terms up to linear order in δ. We then have (assuming as always $m_1\geq m_2$)

$$m_1=\frac{1+\delta}{2}\,,\quad m_2=\frac{1-\delta}{2}\,, \tag{4.14}$$

$$S_1=m_1^2\chi_1\simeq\frac{1}{4}\,(1+2\delta)\chi_1\,, \tag{4.15}$$

$$S_2=m_2^2\chi_2\simeq\frac{1}{4}\,(1-2\delta)\chi_2\,. \tag{4.16}$$

Inserting these definitions into Eqs. (4.8) and (4.9) leads to

$$\frac{d}{dt}(\hat{\mathbf{S}}_1\cdot\hat{\mathbf{J}}) = \frac{\omega^2}{2}\,S_2\Big[\overbrace{(7-6\delta)}^{\text{spin-orbit}}-\overbrace{\Big(1+3\frac{\mathbf{J}\cdot\mathbf{S}_2}{L^2}\Big)}^{\text{spin-spin}}\Big]\hat{\mathbf{J}}\cdot(\hat{\mathbf{S}}_1\times\hat{\mathbf{S}}_2)\,, \tag{4.17}$$

$$\frac{d}{dt}(\hat{\mathbf{S}}_2\cdot\hat{\mathbf{J}}) = \frac{\omega^2}{2}\,S_1\Big[\overbrace{(7+6\delta)}^{\text{spin-orbit}}-\overbrace{\Big(1+3\frac{\mathbf{J}\cdot\mathbf{S}_1}{L^2}\Big)}^{\text{spin-spin}}\Big]\hat{\mathbf{J}}\cdot(\hat{\mathbf{S}}_2\times\hat{\mathbf{S}}_1)\,, \tag{4.18}$$

$$\frac{d}{dt}(\hat{\mathbf{S}}_1\cdot\hat{\mathbf{S}}_2) = \frac{\omega^2}{2}\Big[\overbrace{(-12\delta)}^{\text{spin-orbit}}+\overbrace{\Big(3\frac{\mathbf{J}\cdot(\mathbf{S}_1-\mathbf{S}_2)}{L^2}\Big)}^{\text{spin-spin}}\Big]\mathbf{J}\cdot(\hat{\mathbf{S}}_1\times\hat{\mathbf{S}}_2)\,; \tag{4.19}$$

following Apostolatos, in deriving these equations we have assumed that $S\ll L$, $L=J\,[1+O(S/L)]$, and that the direction of the total angular momentum remains almost constant during evolution. In Eqs. (4.17)–(4.19) we have separated the terms due to spin-orbit and spin-spin interactions.

According to Eq. (4.19), in the equal-mass case ($\delta=0$) without spin-spin effects, the angle between $\hat{\mathbf{S}}_1$ and $\hat{\mathbf{S}}_2$ is constant; generically, however, the spin-spin and even the spin-orbit interactions can cause that angle (and hence the magnitude of $\mathbf{S}_{\rm tot}$) to change. As first observed by ACST and further investigated by Apostolatos [21], this variation in $|\mathbf{S}_{\rm tot}|$ drives the nutation of the orbital plane: Oscillations are superimposed to the monotonic evolution of the angles between $\hat{\mathbf{L}}$ and $\hat{\mathbf{J}}$ (θ_L) and between $\hat{\mathbf{S}}_{\rm tot}$ and $\hat{\mathbf{J}}$ (θ_S) [21], as can be understood from the following simple argument. Recall that on timescales shorter than the radiation-reaction timescale, $|\mathbf{L}|$ and $\mathbf{J}$ are conserved; using δ to denote the change in the dynamical variables incurred during such a time, we write

$$\delta|\mathbf{J}|^2=0\,,\quad \delta|\mathbf{L}|^2=0 \tag{4.20}$$

to get

$$2\delta(\mathbf{L}\cdot\mathbf{S}_{\rm tot})=-\delta(|\mathbf{S}_{\rm tot}|^2)\,; \tag{4.21}$$

using $\delta\mathbf{J} = 0$ we then have

$$\delta\lambda_L = -\frac{1}{2LJ}\delta(|\mathbf{S}_{\rm tot}|^2) \quad \text{for} \quad \lambda_L = \frac{\mathbf{L}\cdot\mathbf{J}}{LJ}\,, \tag{4.22}$$

and

$$\delta\lambda_S = -\frac{\mathbf{L}\cdot\mathbf{S}_{\rm tot}}{2S_{\rm tot}^3 J}\delta(|\mathbf{S}_{\rm tot}|^2) \quad \text{for} \quad \lambda_S = \frac{\mathbf{S}_{\rm tot}\cdot\mathbf{J}}{LJ}\,. \tag{4.23}$$

Thus, when $|\mathbf{S}_{\rm tot}|$ oscillates, the opening angles θ_L and θ_S oscillate as well; in fact, we have

$$\delta\theta_L = \frac{1}{2|\mathbf{L}\times\mathbf{S}_{\rm tot}|}\delta(|\mathbf{S}_{\rm tot}|^2)\,, \tag{4.24}$$

$$\delta\theta_S = \frac{\mathbf{L}\cdot\mathbf{S}_{\rm tot}}{2|\mathbf{S}_{\rm tot}|^2|\mathbf{L}\times\mathbf{S}_{\rm tot}|}\delta(|\mathbf{S}_{\rm tot}|^2)\,, \tag{4.25}$$

which suggests that, for the same variation in $|\mathbf{S}_{\rm tot}|^2$, the nutation is most significant when $\mathbf{L}$ and $\mathbf{S}$ are either nearly aligned or antialigned. In Fig. 4.3, we plot the relative changes in θ_L and θ_S as functions of the angle between $\mathbf{L}$ and $\mathbf{S}$ ($\theta_{LS} = \theta_L + \theta_S$), choosing a fixed positive $\delta(|\mathbf{S}_{\rm tot}|)$. The change is always positive for θ_L, while it can be negative for θ_S, if $\theta_{LS} > 90^\circ$. In addition, the relative changes *diverge* near $\theta_{LS} \sim 0^\circ$ or 180°. These features follow straightforwardly from Eqs. (4.24) and (4.25).

Spin-spin effects. When spin-spin effects are included, the angle between $\hat{\mathbf{S}}_1$ and $\hat{\mathbf{S}}_2$ oscillates according to the second term on the right-hand side of Eq. (4.19). However, as evidenced by the FF results for equal-mass binaries given in Sec. III B, the amplitude of these oscillations does not seem to be very large, and the nutation of the orbital plane does not significantly complicate the waveforms, at least as evaluated at the leading mass-quadrupole order.

Spin-orbit effects. From the first term on the right-hand side of Eq. (4.19), we see that even in the absence of spin-spin effects, unequal masses (i.e., $\delta \neq 0$) can cause the evolution of $\hat{\mathbf{S}}_1\cdot\hat{\mathbf{S}}_2$, and therefore drive the nutation of the orbital plane. Spin-orbit effects, which come in at a lower PN order, can sometimes be more significant than spin-spin effects, especially for binaries with intermediate mass ratios, such as $(m_1 + m_2) = (6 + 3)M_\odot$ and $(9 + 3)M_\odot$ binaries; indeed, these effects could explain the lower FFs found in Sec. III B for those systems.

Examples of combined spin-spin and spin-orbit effects in double-spin binaries leading to oscillations in $|\mathbf{S}_{\rm tot}|$, and therefore θ_L and θ_S, are shown in Fig. 4.4 for systems with $(m_1 + m_2) = (6 + 3)M_\odot$ ($\delta = 1/3$), and with initial local parameters such that FF ≥ 0.99 (on the left) and FF ~ 0.94 (on the right). The nutation behavior evident in these figures is well described by the approximated equations (4.24) and (4.25). For comparison we show (as continuous lines) also the evolution of the analogous quantities in the best-fit single-spin configurations; for these, the opening angles θ_L and θ_S evolve monotonically. Lower overlaps seem to correspond to initial conditions for which nutation is rather significant and overwhelms the underlying monotonic evolution. In Fig. 4.5 we show the percentage of configurations with FF ≤ 0.99 (light pattern) and FF ≤ 0.97 (dark pattern) as a function of the initial $\lambda_{LS} \equiv \hat{\mathbf{L}}_N\cdot\hat{\mathbf{S}}_{\rm tot}$ (evaluated at the starting frequency [38]), for $(6 + 3)M_\odot$ and $(9 + 3)M_\odot$ binaries. The plot suggests that lower FFs are more likely to occur when

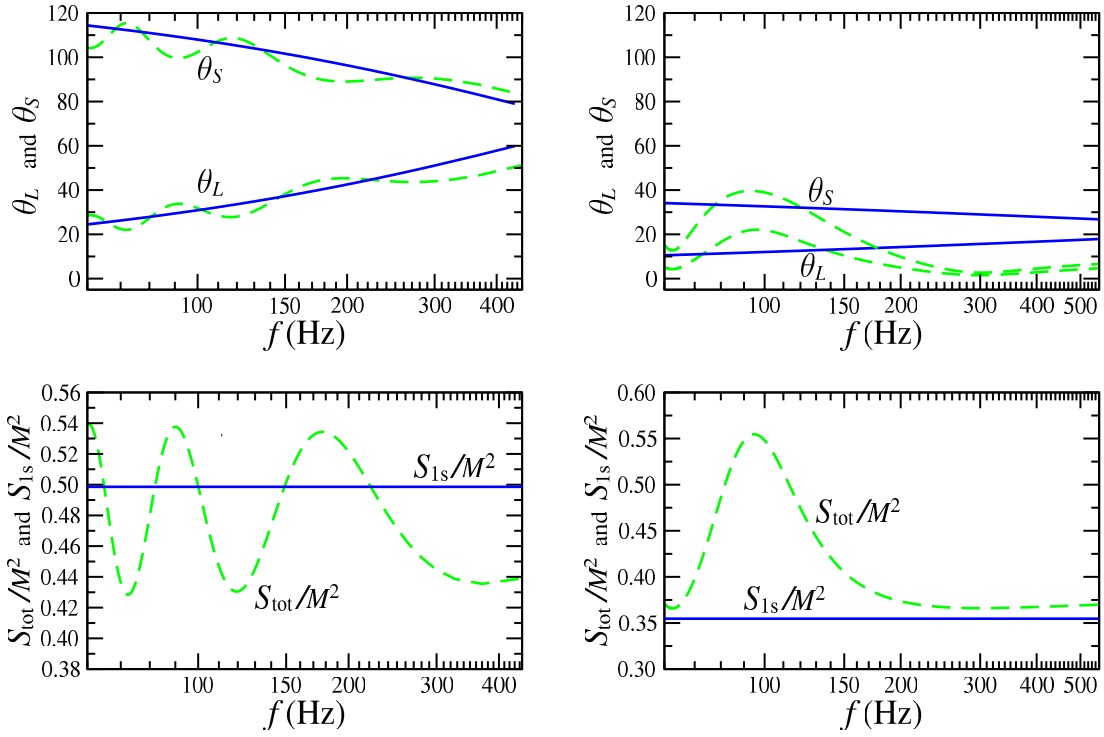

Figure 4.4: Evolution of the opening angles θ_L and θ_S, and of the total-spin magnitude $S_{\rm tot}$ (all plotted as dashed lines) for double-spin target systems yielding FF ≥ 0.99 (left column) and FF $\simeq 0.94$ (right column) when matched by single-spin templates; the target system has $(m_1 + m_2) = (6 + 3)M_\odot$. For comparison, the solid lines show the evolution of the analogous single-spin quantities [θ_L, $\theta_S = \arccos(\hat{\mathbf{S}}_{1s} \cdot \hat{\mathbf{J}})$, and S_{1s}] for the best-fit single-spin systems.

the initial $\hat{\mathbf{L}} \cdot \hat{\mathbf{S}}_{\rm tot} \simeq \pm 1$, which is consistent with the fact that nutation is most significant when $\theta_{LS} \sim 0^\circ$ or 180° [39].

Figure 4.5 shows also an asymmetry in the distribution of low FFs, which are denser when $\theta_{LS} < 90^\circ$. Currently we do not have a clear understanding of this behaviour [40]. It is worth pointing out that this asymmetry and, more in general, the low FFs observed could be due to other features of double-spin dynamics that cannot be reproduced by single-spin systems, but that are difficult to dig out by analysis or numerical experiment, in the absence of a full analytical solution to the precession equations. Moreover, some of the low FFs might be due to shortcomings in our numerical optimization procedure in cases where the match surface in the search parameter space has an especially convoluted geometry.

4.4 Template space and number of templates

In this section we estimate the number of single-spin templates necessary to search for double-spin signals with single masses in the $[3, 15]M_\odot$ range. To do this, we compute the average projected metric $\overline{g_{ij}^{\rm proj}}$ in the (M_s, η_s) region delimited by the dashed and dotted contour of Fig. 4.2, following the procedure de-

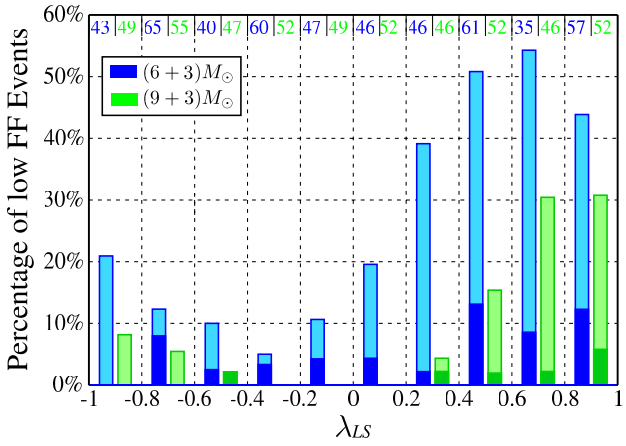

Figure 4.5: Percentage of initial spin configurations that yield FF ≤ 0.99 (light pattern) and FF ≤ 0.97 (dark pattern), as a function of the initial opening angle product $\lambda_{LS} = \hat{\mathbf{L}} \cdot \hat{\mathbf{S}}_{\rm tot}$, for $(m_1 + m_2) = (6 + 3)M_\odot$ and $(9 + 3)M_\odot$ binaries. The numbers on top show the total number of configurations (among 500) randomly extracted within each bin of $\Delta\lambda_{LS} = 0.2$.

scribed in Sec. VI of Ref. [26]. We notice the presence of reduction curves connecting (roughly) the segment $\chi_{1s} \in [0, 2], \kappa_{1s} = 0$ to the entire (χ_{1s}, κ_{1s}) plane in the search template space. Thus, we select a 3-D reduced template space corresponding to (M_s, η_s) within the quadrilateral with vertexes $(15M_\odot, 0.08)$, $(3.25M_\odot, 0.275)$, $(32.5M_\odot, 0.23)$, $(24.5M_\odot, 0.385)$, to $\chi_{1s} \in [0, 2]$, and to $\kappa_{1s} = 0$. Additional subfamilies might be needed to deal with certain singularities that we observe in the reduction curves as κ_{1s} gets close to ± 1, but our selection should already give us an acceptable idea of the number of necessary templates, which is computed according to

$$\mathcal{N}_{\rm templates} = \frac{\int \sqrt{\left|\det \overline{g^{\rm proj}_{i'j'}}\right|}\, dM_s\, d\eta_s\, d\chi_{1s}}{\left[2\sqrt{(1-{\rm MM})/3}\right]^3}, \tag{4.26}$$

where the primed indices i', j' run through M_s, η_s, and χ_{1s}; the metric is averaged over 1,000 sets of target extrinsic parameters. The integral is carried out by evaluating the projected metric (a computationally expensive operation) at 80 points within the integration region, and filling it by *natural neighbor interpolation* [41]. The final result is $\mathcal{N}_{\rm templates} \simeq 320{,}000$ for MM = 0.98 (not including a reduction mismatch of ~ 0.01 incurred along the reduction curves [26]). Given the uncertainties implicit in the numerical computation of the metric, in the interpolation, in the choice of the reduction curves, and in the actual placement of the templates in the bank, this number should be understood only as an order-of-magnitude estimate. Most of the templates, by a factor of many, come from the lower part of the integration region (i.e., from the lowest η_s for any given M_s); about 100,000 out of 320,000 come from the region with $\chi_{1s} < 1$.

4.5 Estimation of binary parameters

Since the single-spin template family contains only a subset (of lower dimensionality) of all possible double-spin waveforms, we cannot expect to obtain estimates of all the physical parameters of double-spin systems from a single-spin–template search. The most straightforward way to recover those parameters would be to perform a search using double-spin templates after single-spin templates have yielded a detection; such a follow-on search may be computationally feasible, since double-spin templates will then be applied only to the data stretches that have been established to contain signals. However, it is still meaningful to analyze the parameter-estimation performance of the single-spin template family, since any constraints on source parameters will decrease the size of the double-spin template bank necessary for the follow-on search, lowering the computational cost even further. In addition, this analysis can offer further useful insight into the FF map of double-spin into single-spin waveforms.

Double-spin target waveforms are parametrized by twelve parameters (seven intrinsic, and five extrinsic), while single-spin search templates are parametrized by nine (four intrinsic, M_s, η_s, χ_{1s}, and κ_{1s}; and five extrinsic). Thus, maximizing the match over the search parameters induces a map from the twelve-parameter target-signal space into the nine-parameter template space. The inverse map takes each point in the template space into a three-dimensional manifold in the target-signal space, whose size indicates the extent to which the physical parameters of the double-spin binary can be constrained. Unfortunately, evaluating the size of the inverse image requires computational resources well beyond what is currently available to us. Furthermore, such a procedure can only be meaningful after *statistical error* has also been taken into account: because the detector output contains also noise, the template parameters at which we obtain the maximal correlation between template and data (the *actual* projection point) will differ, by a random statistical error, from the parameters at which the correlation between template and *signal* is highest (the *theoretical* projection point) [42]. We leave the quantitative study of statistical errors to a forthcoming paper [43].

In this chapter we take a semi-quantitative approach. We ignore the extrinsic parameters, so we study the map of seven parameters into four; then, we identify a number of intrinsic parameters of the double-spin binary (our *target observables*), and we explore how well we can estimate their values using functions of the four intrinsic parameters of the best-fit single-spin template (our *estimators*). We use three general criteria in the choice of target observables and estimators:

Consistency. The target observables and estimators should coincide when the double-spin system is dynamically equivalent to a single-spin system (according to the criteria spelled out in Sec. I).

Robustness. The definitions of the target observables and of the estimators should be independent of the detector noise curve; equivalently, the target observables should be (almost) conserved quantities (we already know that the four template parameters, and hence the estimators, are conserved).

Strong influence. The target observables, and therefore the estimators, should have a strong influence to the

waveforms. Quantitatively, we can require the mismatch metric to have large components along the direction of change of the target observables and estimators; it follows that the target observables and estimators should remain essentially constant along eventual reduction curves.

This criterion is important for two reasons: first, the seven-to-four-dimensional FF map in unlikely to preserve unessential features of the target space; second, even if the map preserved these features, statistical error would inevitably spoil their estimation, because the associated mismatch-metric components are small. A third reason, contingent on our implementation of the FF search, is that we stop the maximization of the match whenever this reaches 0.99; this adds a dominant artificial fluctuation (roughly corresponding to the statistical error for a S/N of 100) to parameter estimation.

Since our search template family possesses a family of approximate reduction curves, it will be generally possible to estimate efficiently only three independent target observables, and four only for very high S/N. Our hope is then to find three target-parameter-estimators pairs that satisfy all three criteria, and four pairs that satisfy the consistency and robustness criteria.

		$(6+3)\,M_\odot$ (500 points)	$(9+3)\,M_\odot$ (500 points)	$(12+3)\,M_\odot$ (100 points)	$(10+10)\,M_\odot$ (500 points)	$(15+10)\,M_\odot$ (100 points)	$(15+15)\,M_\odot$ (100 points)
M	$(\overline{M}_s - M)/M$	+0.0232	+0.0021	−0.0066	−0.0351	−0.0206	−0.0579
	$\Delta M_s/M$	0.0817	0.0755	0.0631	0.0437	0.0603	0.0639
	1-σ/3-σ percentage	75.6%/98.0%	84.0%/97.4%	79.0%/97.0%	76.4%/98.6%	70.0%/99.0%	72.0%/100.0%
η	$\overline{\eta}_s - \eta$	−0.0057	+0.0022	+0.0038	+0.0191	+0.0122	+0.0362
	$\Delta\eta_s$	0.0268	0.0254	0.0178	0.0219	0.0283	0.0387
	1-σ/3-σ percentage	72.6%/99.0%	84.4%/98.8%	81.0%/98.0%	76.6%/98.6%	74.0%/99.0%	74.0%/100.0%
$\mathcal{M}$	$(\overline{\mathcal{M}}_s - \mathcal{M})/\mathcal{M}$	−0.0004	+0.0015	+0.0021	+0.0055	+0.0033	+0.0142
	$\Delta\mathcal{M}_s/\mathcal{M}$	0.0074	0.0106	0.0104	0.0092	0.0145	0.0192
	1-σ/3-σ percentage	71.6%/99.0%	69.6%/99.2%	66.0%/100.0%	71.2%/99.2%	70.0%/98.0%	80.0%/99.0%
$\frac{\mathbf{S}_{\rm eff}\cdot\hat{\mathbf{L}}_N}{M^2}$	$\overline{\left(\frac{\hat{\mathbf{L}}_N\cdot\mathbf{S}_{\rm eff}}{M^2}\right)_s - \frac{\hat{\mathbf{L}}_N\cdot\mathbf{S}_{\rm eff}}{M^2}}$	+0.0236	+0.0210	+0.0129	−0.0071	−0.0015	+0.0004
	$\Delta\left[\left(\frac{\hat{\mathbf{L}}_N\cdot\mathbf{S}_{\rm eff}}{M^2}\right)_s - \frac{\hat{\mathbf{L}}_N\cdot\mathbf{S}_{\rm eff}}{M^2}\right]$	0.1290	0.1130	0.1010	0.0747	0.0886	0.0917
	1-σ/3-σ percentage	79.4%/98.0%	73.4%/98.8%	68.0%/100.0%	75.8%/99.0%	66.0%/100.0%	73.0%/98.0%
$\frac{\mathbf{S}_{\rm eff}}{M}$	$\frac{1}{M}\overline{\left[\left(\frac{\mathbf{S}_{\rm eff}}{M}\right)_s - \frac{\mathbf{S}_{\rm eff}}{M}\right]}$	+0.0253	−0.0264	−0.0183	+0.0375	+0.0028	+0.0387
	$\frac{1}{M}\Delta\left[\left(\frac{\mathbf{S}_{\rm eff}}{M}\right)_s - \frac{\mathbf{S}_{\rm eff}}{M}\right]$	0.1920	0.1480	0.1050	0.1170	0.1860	0.1460
	1-σ/3-σ percentage	75.0%/98.6%	72.6%/98.6%	67.0%/99.0%	75.0%/98.8%	74.0%/100.0%	79.0%/99.0%
$\chi_{\rm tot}$	$\overline{(\chi_{\rm tot})_s - \chi_{\rm tot}}$	+0.0627	−0.0053	−0.0140	+0.0174	+0.0036	+0.0149
	$\Delta\left[(\chi_{\rm tot})_s - \chi_{\rm tot}\right]$	0.2040	0.1610	0.1190	0.0901	0.1450	0.1220
	1-σ/3-σ percentage	81.6%/98.2%	81.8%/97.8%	85.0%/97.0%	78.8%/98.0%	71.0%/99.0%	80.0%/98.0%

Table 4.3: Systematic biases, rms deviations, and percentage of samples within ±1 and 3 deviations of the average, for six target-observable-estimator pairs. The mass configurations are those studied in Sec. 4.3.2.

It is straightforward to see that using M_s to estimate M and η_s to estimate η (or in shorthand, $M_s \to M$ and $\eta_s \to \eta$) satisfies the consistency and robustness criteria. We shall pay a special attention to the estimation of chirp mass according to $\mathcal{M}_s \equiv M_s \eta_s^{3/5} \to \mathcal{M} \equiv M\eta^{3/5}$), which satisfies all three criteria (in particular, chirp mass is conserved very accurately along reduction curves). In the upper part of Table 4.3 we characterize the distribution of estimation error for M, η, and $\mathcal{M}$, for the same systems (with fixed masses and random local parameters) used in Sec. 4.3.2 to compute FFs. Each section shows the estimation bias (defined as the average of the error, and measuring a systematic displacement between observables and estimators that can in principle be removed), its rms deviation (measuring the intrinsic uncertainty in the estimation), and the percentage of estimators enclosed within 1-deviation and 3-deviation intervals (measuring the normality of the distribution). The chirp mass, which satisfies all three criteria, is indeed estimated with higher relative accuracy than both M and η. Even after statistical errors are taken into account, this accuracy should be retained for $\mathcal{M}$ better than for M and η. The distributions of M_s, η_s, and $\mathcal{M}_s$ are also histogrammed in Fig. 4.6, for $(m_1 + m_2) = (6 + 3)M_\odot$ and $(10 + 10)M_\odot$ binaries.

It is very hard to identify additional target-parameter-estimator pairs that satisfy all three criteria, mainly because double-spin binaries lack conserved quantities that clearly dominate the waveforms; so the two additional target observables that can be estimated efficiently may not have simple physical meanings. When spin-spin effects are negligible, the only truly conserved quantity that could be interesting for our purposes is $\mathbf{S}_{\rm eff} \cdot \hat{\mathbf{L}}_N$, with

$$\mathbf{S}_{\rm eff} \equiv \left(1 + \frac{3m_2}{4m_1}\right)\mathbf{S}_1 + \left(1 + \frac{3m_1}{4m_2}\right)\mathbf{S}_2 \,. \tag{4.27}$$

[The magnitudes of the individual spins do not satisfy the consistency criterion, since single-spin binaries (e.g., with m_1 spinning) require $|\mathbf{S}_{1s}| \to |\mathbf{S}_1|$, while double-spin, equal-mass binaries require $|\mathbf{S}_{1s}| \to |\mathbf{S}_1 + \mathbf{S}_2|$.] Therefore, we choose the target observable $\mathbf{S}_{\rm eff} \cdot \hat{\mathbf{L}}_N / M^2$, which is conserved and closely related to the opening angle between $\mathbf{S}_{\rm eff}$ and $\hat{\mathbf{L}}_N$, and hence to the depth of the modulation caused by orbital precession. The estimator is naturally

$$\left[\frac{\mathbf{S}_{\rm eff} \cdot \hat{\mathbf{L}}_N}{M^2}\right]_s \equiv \left(1 + \frac{3m_{2s}}{4m_{1s}}\right)\frac{m_{1s}^2}{M_s^2}\chi_{1s}\kappa_{1s} \,, \tag{4.28}$$

where $(m_{1,2})_s \equiv \mathrm{Re}\left[(1 \pm \sqrt{1 - 4\eta_s})/2\right] M_s$ (taking the real part becomes necessary when $\eta_s > 0.25$). As we see from Table 4.3, this observable can be estimated with bias within $[-0.01, +0.02]$, and with rms deviation 0.07–0.13. Although conserved, this observable is not quite constant along reduction curves. In the left panels of Fig. 4.7, we plot the distribution of the pairs $(\mathbf{S}_{\rm eff} \cdot \hat{\mathbf{L}}_N / M^2, [\mathbf{S}_{\rm eff} \cdot \hat{\mathbf{L}}_N / M^2]_s)$ for $(m_1 + m_2) = (6 + 3)M_\odot$ and $(10 + 10)M_\odot$ binaries. In each case we conclude that the target observable and the estimator are strongly correlated; however, the dispersion is noticeably smaller for $(10 + 10)M_\odot$ than for $(6 + 3)M_\odot$ binaries; this must be because for equal-mass binaries only spin-spin effects can cause differences between double-spin and single-spin waveforms.

In the light of Eq. (4.10), we choose the third target observable as $|\mathbf{S}_{\rm eff}|/M$, which measures the instantaneous angular precession frequency divided by ω^2. This quantity is conserved only for single-spin binaries

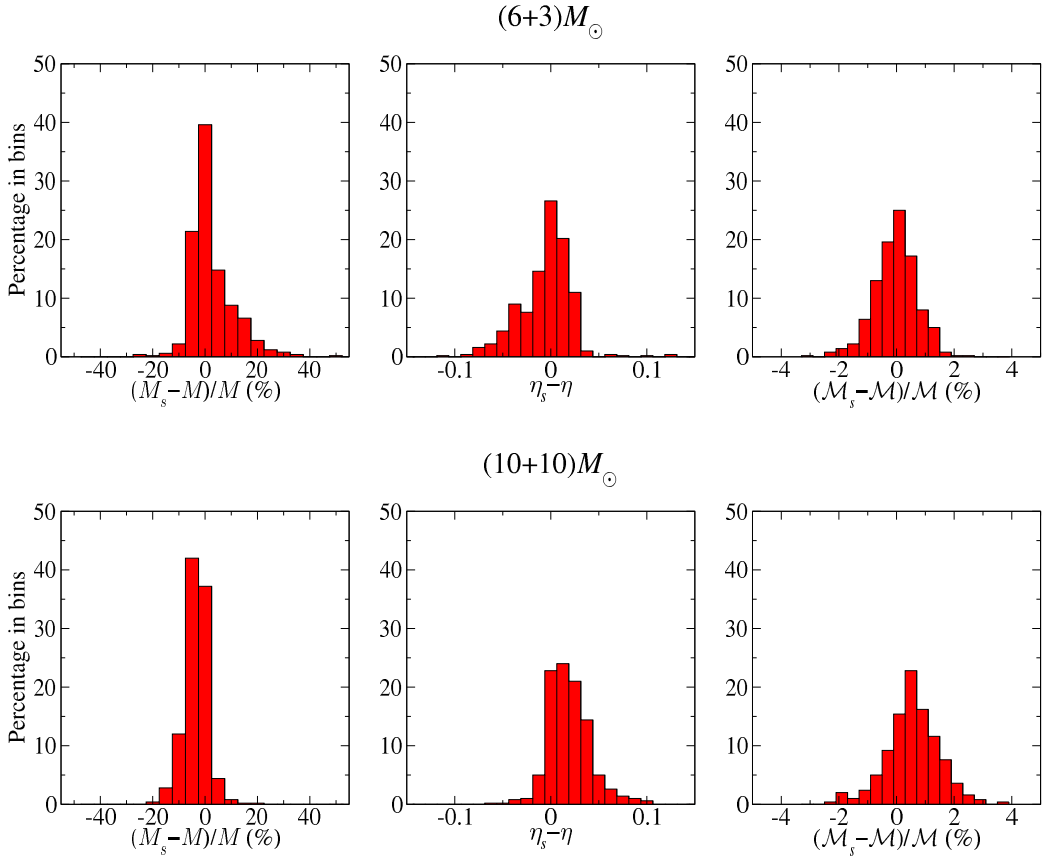

Figure 4.6: Distribution of errors for the target observables M, η, and $\mathcal{M}$, as estimated by M_s, η_s and $\mathcal{M}_s$, for 500 double-spin binaries with $(m_1 + m_2) = (6 + 3)M_\odot$ and $(10 + 10)M_\odot$, maximal spins, and uniform distributions of local parameters. The $\mathcal{M}_s$ distribution has the smallest bias and dispersion; the M_s and η_s distributions have much larger dispersion and are skewed in opposite directions (as needed to reduce the dispersion of $\mathcal{M}_s \equiv M_s \eta_s^{3/5}$).

and for equal-mass binaries with negligible spin-spin effects, so it does not completely satisfy the robustness criterion. In our study, we use the value of $|\mathbf{S}_{\rm eff}|/M$ at the initial frequency (40 or 60 Hz) from which the equations of motion are integrated. [However, it would be more reasonable to evaluate it at the frequency at which the detector is most sensitive, or to weight its values at different frequencies according to the detector noise spectrum.] The estimator is

$$\left[\frac{|\mathbf{S}_{\rm eff}|}{M}\right]_s = \left(1 + \frac{3m_{2s}}{4m_{1s}}\right)\frac{m_{1s}^2}{M}\chi_{1s}\,. \tag{4.29}$$

To make the observable and the estimator dimensionless, we divide both by M; Table 4.3 then shows that $|\mathbf{S}_{\rm eff}|/M^2$ can be estimated with bias within $[-0.03, +0.04]$, and rms deviation 0.11–0.19. Despite the apparent physical meaning of $[|\mathbf{S}_{\rm eff}|/M]_s$, this observable is also not conserved well along reduction curves. Thus, we might as well use a more familiar target observable, $\chi_{\rm tot} \equiv \mathbf{S}_{\rm tot}/M^2$, as estimated by $[\chi_{\rm tot}]_s = \chi_{1s}m_{1s}^2/M^2$. This pair satisfies the consistency criterion, and it changes through the inspiral at a level similar to $\mathbf{S}_{\rm eff}/M^2$. Table 4.3 shows that $\chi_{\rm tot}$ can be estimated with bias within $[-0.005, +0.06]$, and rms deviation 0.10–0.20. In the center and right panels of Fig. 4.7, we plot (target, estimator) distributions for these two spin observables, again for for $(m_1 + m_2) = (6 + 3)M_\odot$ and $(10 + 10)M_\odot$ binaries. It is clear from the plots that the accuracy of estimation is poorer than for $\mathbf{S}_{\rm eff}\cdot\hat{\mathbf{L}}_N/M^2 \rightarrow [\mathbf{S}_{\rm eff}\cdot\hat{\mathbf{L}}_N/M^2]_s$; again, the dispersion is smaller for the $(10 + 10)M_\odot$ binaries. For $(6 + 3)M_\odot$ binaries, the worse accuracy can be attributed in part to the fact that these two target observables are not as well conserved as $\mathbf{S}_{\rm eff}\cdot\hat{\mathbf{L}}_N/M^2$ during evolution.

4.6 Conclusions

As originally pointed out by ACST [18], the dynamics of double-spin precessing binaries become equivalent to the dynamics of single-spin binaries (at least for the purpose of computing gravitational waveforms at the leading mass-quadrupole order) in two limits: equal masses, when spin-spin effects can be neglected (then $\mathbf{S}_1 \rightarrow \mathbf{S}_{\rm tot}$), and very different masses (then $\mathbf{S}_1$ tends to the spin of the heavier body). Building on this observation, on the results of Refs. [10, 21, 25], and on the (justified) assumption that spin-spin effects contribute mildly to the PN binding energy and GW flux of the binary for mass configurations of interest to ground-based GW interferometers, we conjectured that single-spin templates (as defined in Sec. 4.3.2) can be used effectually to search for double-spin precessing binaries with such masses.

We tested our conjecture by evaluating the FF between the single-spin and double-spin families, and we found confirmation in the very high FF values [see Table 4.1 and Fig. 4.1] for equal-mass binaries of both low and high total masses. FFs were high also for unequal-mass binaries, except for few initial-spin configurations. As discussed in Sec. IIID, for those configurations the evolution of the opening angles between $\hat{\mathbf{J}}$ and $\hat{\mathbf{L}}_N$ and between $\hat{\mathbf{J}}$ and $\hat{\mathbf{S}}_{1,2}$ seem to contain large oscillations, induced by spin-spin and nonequal-mass effects, that cannot be reproduced sufficiently well by single-spin systems.

The region in the single-spin parameter space needed to match double-spin binaries with (m_1, m_2) =

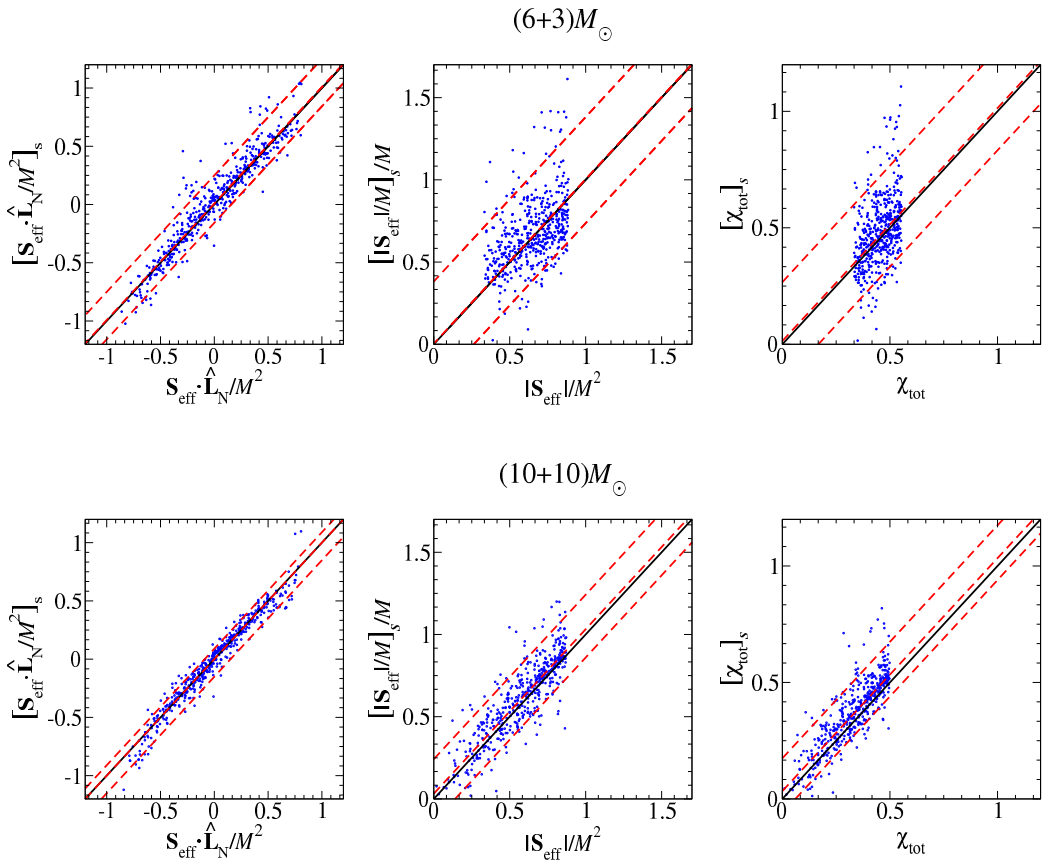

Figure 4.7: Estimation of spin-related parameters for 500 double-spin binaries with $(m_1 + m_2) = (6 + 3)M_\odot$ and $(10 + 10)M_\odot$, maximal spins, and uniform distributions of local parameters. The three columns display the correlations between the (target-observable, estimator) pairs $(\mathbf{S}_{\rm eff}\cdot\hat{\mathbf{L}}_N/M^2, [\mathbf{S}_{\rm eff}\cdot\hat{\mathbf{L}}_N/M^2]_s)$, $(|\mathbf{S}_{\rm eff}|/M^2, [|\mathbf{S}_{\rm eff}|/M]_s/M)$, and $(\chi_{\rm tot}, [\chi_{\rm tot}]_s)$. In each panel, three red dashed lines are used to indicate the median of the bias and the 90% percentiles above and below it. The black solid line marks the line of zero bias. Lower biases correspond to solid lines closer to the central dashed lines; lower dispersions correspond to closer outer dashed lines.

$[3, 15]M_\odot \times [3, 15]M_\odot$ is shown in Fig. 4.2. Using the LIGO-I design sensitivity, we counted (very roughly) as $\sim 320,000$ the number of templates required to yield a minimum match of 0.97. The number of BCV2 templates needed for a similar mass range is somewhat larger. More generally, with respect to the detection template families introduced in Refs. [20, 21, 22, 25, 23], the advantage of the quasi-physical single-spin family suggested in this chapter is the possibility of estimating the parameters of the source. In Sec. 4.5 we computed the systematic errors that would affect the measurement: The total mass M could be estimated with a fractional bias within $[-6\%, +3\%]$ and a fractional rms deviation of 5%–8%; the symmetric mass ratio η could be estimated with a bias within $[-0.06, +0.04]$ and an rms deviation of 0.02–0.04; the chirp mass $\mathcal{M}$ could be estimated with a fractional bias within $[-0.04\%, +0.01\%]$ and a fractional rms deviation of 0.7%–2%. We also proposed estimators for certain spin parameters of the double-spin system. For example, the parameter $(\mathbf{S}_{\rm eff} \cdot \hat{\mathbf{L}}_N)/M^2$ [where $\mathbf{S}_{\rm eff}$ is defined by Eq. (4.28)], which is conserved when spin-spin effects can be neglected, could be estimated with a bias within $[-0.01, +0.03]$ and an rms deviation of 0.07–0.13; the parameter $\chi_{\rm tot} \equiv \mathbf{S}_{\rm tot}/M^2$ could be estimated with a bias within $[-0.005, +0.06]$ and an rms deviation of 0.10–0.20. However, since the mismatch metric has small components along the directions of these spin estimators, we expect that (at least for moderate S/N) statistical errors will always be dominant over the systematic errors discussed here. We defer the study of statistical errors to a forthcoming paper [43].

In evaluating the performance of the quasi-physical single-spin template family, we have assumed a *uniform* distributions for the initial local parameters (spin and orientation angles) of the double-spin target model. It would be interesting in the future to redo our analyses assuming more realistic nonuniform distributions derived from astrophysical considerations. The only available results for spin distributions in BH–BH binaries (unfortunately, with a single spin) and in NS–BH binaries were obtained using population-synthesis techniques [44, 24]. For the case of binaries formed in globular clusters, there is no theoretical argument to suggest any particular spin distribution.

Last, recent studies of PN spin-spin effects [45] suggest that, for binaries with comparable masses, the two BH spins may have become roughly *locked* into a fixed relative configuration by the time the GWs enter the band of good interferometer sensitivity. If these results are confirmed, they could provide preferred initial spin conditions, and by reducing the variability of GW signals, they could help to explain the good performance of our single-spin template family. We must however note that we were motivated in proposing our single-spin templates by the assumption that spin-spin effects never dominate, while for locking to occur spin-spin effects seem to be crucial [45].

4.7 Bibliography

[1] A. Abramovici et al., Science **256**, 325 (1992); `http://www.ligo.caltech.edu`.

[2] B. Caron et al., Class. Quantum Grav. **14**, 1461 (1997); `http://www.virgo.infn.it`.

[3] H. Lück et al., Class. Quantum Grav. **14**, 1471 (1997); http://www.geo600.uni-hannover.de.

[4] M. Ando et al., Phys. Rev. Lett. **86**, 3950 (2001); http://tamago.mtk.nao.ac.jp.

[5] The LIGO Scientific Collaboration, Nucl. Instr. and Meth. in Phys. Res. A, **517**, 154 (2004).

[6] LIGO Scientific Collaboration, Phys. Rev. D **69**, 082004 (2004); "Analysis of LIGO data for gravitational waves from binary neutron stars," *ibid.*, in print (2004), gr-qc/0308069; "First upper limits from LIGO on gravitational wave bursts," *ibid.*, **69**, 102001 (2004), gr-qc/0312056; "Analysis of first LIGO science data for stochastic gravitational Waves," unpublished, gr-qc/0312088.

[7] M. Burgay et al., Nature **426**, 531 (2003).

[8] L. Blanchet, T. Damour, B.R. Iyer, C.M. Will, and A.G. Wiseman, Phys. Rev. Letters **74**, 3515 (1995); L. Blanchet, T. Damour, and B.R. Iyer, Phys. Rev. D **51**, 5360 (1995); erratum, **54**, 1860 (1996); C.M. Will and A.G. Wiseman, Phys. Rev. D **54**, 4813 (1996).

[9] L.E. Kidder, C.M. Will, and A.G. Wiseman, Phys. Rev. D **47**, 4183 (R) (1993).

[10] L.E. Kidder, Phys. Rev. D **52**, 821 (1995).

[11] P. Jaranowski and G. Schäfer, Phys. Rev. D **57**, 7274 (1998); *ibid.* **60**, 124003 (1999); T. Damour, P. Jaranowski and G. Schäfer, Phys. Rev. D **62**, 044024 (2000); *ibid.*, 021501(R) (2000); **63**, 044021 (2001).

[12] T. Damour, P. Jaranowski, and G. Schäfer, Phys. Lett. B **513**, 147 (2001).

[13] L. Blanchet, G. Faye, B.R. Iyer, and B. Joguet, Phys. Rev. D **65**, 061501 (2002).

[14] Y. Itoh and T. Futamase, Phys. Rev. D **68**, 121501 (2003); Y. Itoh, *ibid.*, bf 69, 064018 (2004).

[15] L. Blanchet, T. Damour, and G. Esposito-Farese, Phys. Rev. D, in print (2004). gr-qc/0311052

[16] T. Damour, B.R. Iyer, and B.S. Sathyaprakash, Phys. Rev. D **63**, 044023 (2001); Phys. Rev. D **66**, 027502 (2002).

[17] A. Buonanno, Y. Chen, and M. Vallisneri, Phys. Rev. D **67**, 024016 (2003).

[18] T.A. Apostolatos, C. Cutler, G.J. Sussman, and K.S. Thorne, Phys. Rev. D **49**, 6274 (1994).

[19] T.A. Apostolatos, Phys. Rev. D **52**, 605 (1995).

[20] T.A. Apostolatos, Phys. Rev. D **54**, 2421 (1996).

[21] T.A. Apostolatos, Phys. Rev. D **54**, 2438 (1996).

[22] P. Grandclément, V. Kalogera, and A. Vecchio, Phys. Rev. D **67**, 042003 (2003).

[23] P. Grandclément and V. Kalogera, Phys. Rev. D **67**, 082002 (2003).

[24] P. Grandclément, M. Ihm, V. Kalogera, and K. Belczynski, Phys. Rev. D **69**, 102002 (2004).

[25] BCV2: A. Buonanno, Y. Chen, and M. Vallisneri, Phys. Rev. D **67**, 104025 (2003).

[26] Y. Pan, A. Buonanno, Y. Chen, and M. Vallisneri, "A physical family of gravity-wave templates for precessing binaries of spinning compact objects: I. Application to single-spin precessing binaries," Phys. Rev. D, in print (2004). `gr-qc/0310034`

[27] In fact, such "templates" are not complete waveforms, but contain all the ingredients needed to construct the waveforms for any choice of the extrinsic parameters. Thus, they are perhaps better described as "multitemplates," or "pseudotemplates."

[28] C.W. Lincoln and C.M. Will, Phys. Rev. D **42**, 1123 (1990); L. Wen, Astrophys. J. **598**, 419 (2003).

[29] T.A. Apostolatos, Phys. Rev. D **52**, 605 (1995).

[30] One example is the initial phase Φ_0 in nonspinning-binary templates: fixing all the other parameters, the value of ρ for any Φ_0 (and indeed, the maximum ρ over all Φ_0) is obtained by combining $\rho(\Phi_0 = 0)$ and $\rho(\Phi_0 = \pi/2)$.

[31] B.S. Sathyaprakash and S.V. Dhurandhar, Phys. Rev. D **44**, 3819 (1991); S.V. Dhurandhar and B.S. Sathyaprakash, *ibid.*, **49**, 1707 (1994); B.S. Sathyaprakash, *ibid.*, **50**, R7111 (1994); R. Balasubramanian, B.S. Sathyaprakash and S.V. Dhurandhar, *ibid.*, **53**, 3033 (1996); B.J. Owen, *ibid.*, 6749 (1996); B.J. Owen and B.S. Sathyaprakash, *ibid.*, **60**, 022002 (1999).

[32] B.S. Sathyaprakash and B.F. Schutz, Class. Quant. Grav. **20**, S209 (2003); C. Cutler, private communication (on the existence of reduction curves given small metric eigenvalues); L. Barack and C. Cutler, Phys. Rev. D, in print (2004).

[33] To be fully consistent in using Eq. (4.1) up to 3.5PN order, we should include high-order spin-orbit and spin-spin terms that are not available at this time.

[34] E. Poisson, Phys. Rev. D **57**, 5287 (1998).

[35] C. Cutler and É.É. Flanagan, Phys. Rev. D **49**, 2658 (1994);

[36] T. Damour, B.R. Iyer, and B.S. Sathyaprakash, Phys. Rev. D **57**, 885 (1998); A. Buonanno and T. Damour, Phys. Rev. D **59**, 084006 (1999); A. Buonanno and T. Damour, Phys. Rev. D **62**, 064015 (2000); T. Damour, P. Jaranowski and G. Schäfer, Phys. Rev. D **62**, 084011 (2000); T. Damour, Phys. Rev. D **64**, 124013 (2001).

[37] T. Damour, B.R. Iyer, P. Jaranowski, and B.S. Sathyaprakash, Phys. Rev. D **67**, 064028 (2003).

[38] For double-spin binaries λ_{LS} is not constant, since the evolution of $|\mathbf{S}_{\rm tot}|$ can lead it to oscillate [see Eq. (4.21)]; however, these oscillations do not destroy the qualitative picture see in Fig. 4.5.

[39] When $\hat{\mathbf{L}}$ and $\hat{\mathbf{S}}_{\rm tot}$ are almost aligned or anti-aligned, the FF is again high, since the total waveform modulation induced by orbital procession is negligible. This effect competes with nutation in determining the eventual FF, but it dominates only for a small range of θ_{LS}.

[40] One conjecture is the following: In the single-spin case, θ_L always increases while θ_S decreases in time. In the double-spin case, oscillations are superimposed; if $\theta_{LS} > 90^\circ$, θ_L increases, and θ_S decreases (or viceversa); while if $\theta_{LS} < 90^\circ$, θ_L and θ_S either both increase or decrease in time. This difference might be the origin of the poor performance of single-spin templates $\theta_{LS} < 90^\circ$.

[41] R. Sibson, in *Interpreting Multivariate Data*, V. Barnett, ed. (Wiley, Chichester, 1981), p. 21–36.

[42] Qualitatively, for high-S/N events, the actual projection point lies within the template-space contour that has mismatch $\sim (\mathrm{S/N})^{-1}$ with the theoretical projection point.

[43] A. Buonanno, Y. Chen, Y. Pan, and M. Vallisneri, "Gravity-wave templates for precessing binaries of spinning compact objects: III. Parameter estimation," in preparation.

[44] V. Kalogera, Astrophysical Journal **541**, 319 (2000).

[45] J.D. Schnittman, private communication; "Spin-Orbit Resonance in Compact Binary LIGO Sources," talk given at LSC workshop, Hanford, August 2002.

Chapter 5

Optimal degeneracy for the signal-recycling cavity in advanced LIGO

As currently designed, the signal-recycling cavity (SRC) in the Advanced-LIGO interferometer is degenerate. In such a degenerate cavity, the phase fronts of optical fields become badly distorted when the mirror shapes are slightly deformed due to mirror figure error and/or thermal aberration, and this causes significant loss of the signal power and the signal-to-noise ratio (SNR) of a gravitational wave event. Through a numerical modal simulation of the optical fields in a simplified model of an Advanced-LIGO interferometer, We investigate the loss of the SNR and the behavior of both the carrier and signal optical fields, with the SRC at various levels of degeneracy. We show that the loss of the SNR is severe with a degenerate SRC, and a nondegenerate SRC can be used to solve this problem. We identify the optimal level of degeneracy for the SRC, which is achieved when the cavity Gouy phase is between 0.2 and 1.3 radians. We also discuss possible alternative designs of the SRC to achieve this optimal degeneracy.

5.1 Introduction and summary

Advanced LIGO [1] entails, among other upgrades from initial LIGO [2], introducing a signal-recycling mirror (SRM) at the dark port output of the interferometer (see Fig. 5.1).

The SRM forms the signal-recycling cavity (SRC) with the input test mass (ITM), and the SRC and the arm cavity (AC) form a coupled resonant cavity. The resonant property of this coupled cavity can be controlled by two parameters of the SRM (position and reflectivity) [3, 4]. With different choices of these parameters, the interferometer can operate in either a *broadband*, *resonant-sideband-extraction* (RSE) configuration [4, 6, 7] or a *narrowband* configuration. The Advanced-LIGO baseline design adopts the RSE broadband configuration, with the possibility, later, of changing the SRM parameters so as to alter the detector noise spectrum, optimizing its detection of GWs with specific frequency features [5].

Signal recycling can also circumvent the standard quantum limit (SQL) for free test masses by altering the test-mass dynamics [8].

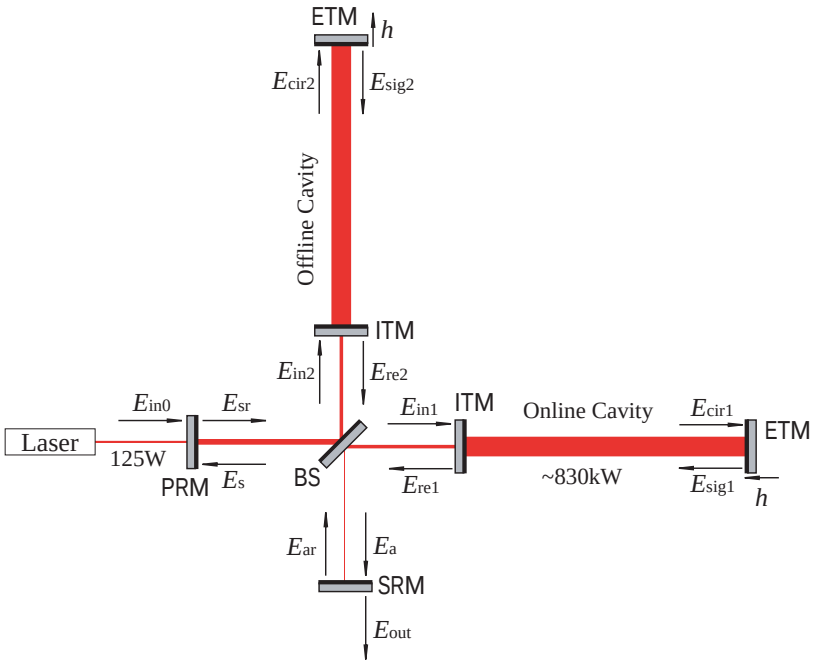

Figure 5.1: Illustration of an Advanced-LIGO interferometer. A signal-recycling mirror is placed at the dark output port of the LIGO interferometer, forming an SRC with the ITMs. In this plot we introduced symbols and abbreviations for the mirrors and the electric fields at various positions that will be used in this chapter. The two ACs are named "online" and "offline" for convenience.

However, there is a potential problem in the current design of the SRC.

The SRC and the power-recycling cavity (PRC) are both nearly degenerate, and it is well known that a degenerate cavity is not selective for transverse optical modes. As a result, perturbations of the cavity geometry will cause strong mode coupling [9]. Specifically, in initial-LIGO and Advanced-LIGO interferometers, figure error and thermal aberration of the mirrors (PRM, SRM and ITMs) will cause strong optical mode coupling, which transfers light power from the fundamental TEM00 mode to higher-order modes (HOMs) and reduces the amplitudes of the radio frequency (RF) sidebands (in both the PRC and SRC) and the signal sideband (in the SRC).

This consequence of the high PRC degeneracy is well known: strong mode mixing of the RF sideband has been observed in initial LIGO. This problem was so severe that the interferometer had to be operated with lower circulating power to reduce thermal aberration of the mirrors. Measures had been taken to fix the problem, including introducing a thermal compensation system (TCS) to actively correct the deformations of the mirrors [10] and replacing bad optical elements that had unexpectedly high absorption. However, there is a worry about Advanced LIGO, where much higher optical power in the AC will cause even worse thermal aberration on the ITMs that the TCS might not be able to correct. Müller and Wise have suggested reducing the PRC degeneracy by moving the mode-matching telescope (MMT) into the recycling cavities to reduce the beam waist size [11], and they are currently working on practical issues in implementing this modified

topology in Advanced LIGO [12].

The consequence of SRC degeneracy, by contrast with PRC degeneracy, have not been clearly investigated. Since the GW signal sideband light entering the SRC has different resonance conditions from the carrier light or the RF sideband light, the three must be investigated individually. Specifically, the signal sideband is resonant in the coupled two-cavity system formed by the AC and the SRC, while the carrier and the RF sideband, roughly speaking, are resonant only in the nondegenerate AC and the degenerate PRC respectively. It seems that mode mixing in the signal sideband is at a level somewhere between those of the carrier and the RF sideband.

In Section IV J of Ref. [13], Thorne estimated the strength of mode mixing in the signal sideband using the approximation that light propagation in the degenerate SRC is well described by geometric optics. (Because a very degenerate cavity accommodates most the optical eigenmodes up to very high orders, "light rays" with sharp edges are eigenmodes of the cavity as well). Thorne found (Eq. (4.54) of Ref. [13]) that for the signal-to-noise ratio (SNR) to be reduce by less than 1% due to mode mixing [1], the *peak-to-valley* mirror figure error in the central region (region enclosing 95% of the light power) in the SRC has to be less than 2 nm for the broadband Advanced-LIGO baseline design, and less than 1nm for a narrowband configuration. This is independent of whether a Gaussian beam or Mesa beam [13] is used, since a degenerate cavity does not distinguish optical modes. These are severe constraints that are difficult to achieve with current technology.

In this chapter, we investigate this SRC degeneracy problem using a mode-decomposition-based numerical simulation of light propagation, including both the carrier and the signal sidebands, in a simplified model of an Advanced-LIGO interferometer. In our simulations, we focus on the consequences of phase-front distortions of the light in recycling cavities with various levels of degeneracy. We make idealizations and approximations to simplify the analysis of the interferometer, so long as they do not make errors larger than a factor of order two. All assumptions and approximations are discussed in detail in this chapter and we give a full list of them in Appendix 5.8. Among the most important ones are the following:

(i) We consider only the five lowest-order HOMs and focus mostly on the two lowest-order modes, i.e., the modes excited by errors in mirror curvature radii.

(ii) We assume that the sizes of mirrors in the interferometers are all large enough for diffraction losses to be negligible.

(iii) We assume that the interferometer noise is dominated by photon shot noise, and we ignore radiation pressure noise.

(iv) We assume all degrees of freedom of the interferometer (cavity tuning, optical element alignment, etc.) are fixed to their ideal values as if there were no mirror deformation, except for the tuning of the PRC and the AC. The PRC and AC are tuned to maximize the total carrier light power (sum of power in all optical modes) in the AC, for fixed input light power.

We use our simulations to study the loss of the SNR due to phase-front distortions caused by mirror

[1] Assuming that shot noise is the dominant noise source

deformations, and reach the following conclusions:

(i) With the degenerate SRC in the current Advanced-LIGO baseline design, if we require the loss of the SNR due to mirror deformations to be smaller than 1%, then the constraint on mirror deformations is severe. In the broadband Advanced-LIGO design, if the only type of mirror deformation is curvature radius error, then this error must be smaller than 2.5m∼7m on the ITMs, which corresponds to a peak-to-vally figure error smaller than 1nm∼3nm in the central region of the mirrors. In reality, the mirror deformation is formed by the combination of many spatial modes, and when we consider the next lowest order spatial modes, as depicted in Eq. (5.27) and Fig. 5.2, we get a constraint $\sim$ 4nm on the SRM. In the narrowband design, the constraint on the ITMs is tightened to $\sim$ 0.4nm. These results are consistent with the estimates in Ref. [13].

(ii) When we change the degeneracy of the SRC while keeping tunings of other cavities the same, we find for Gaussian beams that the loss of the SNR due to mirror deformations is minimized when the one-way Guoy phase inside the SRC is in the range 0.2∼1.3 radians and is chosen to be away from *HOM resonant peaks* (see Sec 5.4).

(iii) We find that it is not practical to add a single lens into the SRC so as to focus the beam and reduce the cavity degeneracy to its optimal value, because the beam must be focused so strongly that the beam size on the SRM is of order 10^{-5}m, and the power density on it exceeds 10GW/m^2 (This fact was pointed out long ago by Bochner [14]).

(iv) We discuss two alternative designs of the SRC for achieving the optimal degeneracy. The first is the MMT design Müller and Wise suggested originally for reducing the degeneracy of the PRC [11]. In the MMT design, the beam size is brought down to $\sim 10^{-3}$m by two mirrors so as to achieve the optimal degeneracy. The second is a long SRC design, in which the beam size is kept at ∼6cm, while the SRC is extended to ∼4 kilometers to achieve the optimal degeneracy. The 4km long SRC design has been suggested for various reasons [6, 15], and in practice it is possible to fit the SRC into the existing LIGO AC beam tubes.

This chapter is organized as follows. In Sec. 5.2, we give a brief overview of the mode decomposition formalism and Hermite-Gaussian modes [16], and interpret the cavity degeneracy from a modal-space point of view. In Sec. 5.3, we describe the Advanced-LIGO interferometer model that is used in our simulations. In Sec. 5.4, we summarize the numerical results that come out of our simulations, including the constraints on mirror figure error and thermal aberration, and the optimal SRC degeneracy. In Sec. 5.5, we discuss the various designs for achieving the optimal SRC degeneracy. In Sec. 5.6, we summarize our conclusions.

5.2 Mode decomposition formalism

5.2.1 Modal decomposition in general

The mode decomposition formalism for calculating optical fields in a perturbed interferometer is discussed in detail by Hefetz *et al* in Sec. 2 of Ref.[17]. We will review the general idea briefly in this section.

One can generally expand the electromagnetic (EM) field of a light beam as a superposition of orthonormal optical modes:

$$E(x, y, z) = \sum_n a_n U_n(x, y, z) \,. \tag{5.1}$$

Though the basis modes $U_n(x, y, z)$ are arbitrary in principle, it is preferable to use the eigenmodes of the cavities of an ideal interferometer, e.g., (i) Hermite-Gaussian modes, which are eigenmodes of the cavities in the Advanced-LIGO baseline design, formed by spherical mirrors (assuming infinite mirror size); or (ii) Mesa-beam modes [13], which are eigenmodes suggested for Advanced LIGO to reduce thermal noise. The complex vector space formed by $U_n(x, y, z)$ is called the *modal space*, and the EM field in modal space is represented by a complex vector a_n. (In Sec. 5.3 and Appendix 5.9 we keep using E to denote this vector.) In the modal space, the optical fields of a perturbed interferometer can be calculated from the unperturbed fields using linear algebra only, without numerically solving the wave equation.

The propagation of the optical field can be described by matrices in this modal space. In Cartesian coordinates where the z-axis is along the optical axis and the x- and y-axis are transverse, an operator $M(x, y, z_2, z_1)$ transforms the EM field at position z_1 to the field at position z_2:

$$E(x_2, y_2, z_2) = M(x_2, y_2; x_1, y_1; z_2, z_1) \otimes E(x_1, y_1, z_1) \,. \tag{5.2}$$

The representation of M in the modal space is given by

$$M_{mn}(z_2, z_1) = \iiiint_{-\infty}^{\infty} U_m^*(x_2, y_2, z_2) M(x_2, y_2; x_1, y_1; z_2, z_1) U_n(x_1, y_1, z_1) dx_1 dy_1 dx_2 dy_2 \,. \tag{5.3}$$

It is convenient to separate these operators into propagation operators in free space and interaction operators describing how the EM fields transform when interacting with optical elements. The free-space propagator is given by:

$$P_{mn}(z_1, z_2) = \delta_{mn} e^{-ik(z_2 - z_1)} e^{i\eta_n} \,, \tag{5.4}$$

where k is the wave number and η_n is the diffraction phase associated with the nth optical mode (i.e., the extra phase accumulated during propagation besides $k(z_2 - z_1)$, due to diffraction effects, e.g., the Guoy phase of Gaussian beam).

To write out the interaction operator for an optical element, we choose, near the element's surfaces, reference surfaces that match the phase fronts of the unperturbed eigenmodes. The operator can then be written in the general form

$$M_{mn} = \langle m | M(x, y) | n \rangle = \langle m | e^{-ikZ(x,y)} | n \rangle \,, \tag{5.5}$$

where $Z(x, y)$ is the optical path light travels from the element's entrance reference surface to the element's exit reference surface. For ideal optical elements in our model, $Z(x, y) =$ constant, i.e., the mirrors or lens exactly match the optical modes and there is no coupling between optical modes when the light beam inter-

acts with the optical elements. For perturbed elements, e.g., slightly deformed mirrors due to figure error and/or thermal aberration, $Z(x, y)$ is not constant and the optical modes couple to each other. $Z(x, y)$ contains contributions from both the figure error and the change of refraction index in the material, and is referred to as the *distortion function*; it can be complex, when used to describe lossy optical elements. This interaction operator must be accompanied by the optical element's scalar reflectivity and transmissivity coefficients to give the true transform of the fields.

In writing the interaction operators, we adopted the short-distance approximation [18], where propagation inside optical elements between reference planes is approximated by a simple non-uniform phase factor $kZ(x, y)$. The spatially variable phase error caused by this approximation, in addition to a factor of the order unity determined by the geometry of the unperturbed cavity, is derived in Sec. 2 of Ref. [18]; its magnitude is

$$\Delta\Phi \sim \frac{1}{4\pi}\frac{\lambda}{L}\,, \tag{5.6}$$

where λ is the wavelength of the light and L is the length of the cavity. In initial LIGO or Advanced LIGO, L is at least $\simeq$ 10m, and the phase distortion error is thus smaller than 10^{-8}. Since a 1nm mirror figure error gives a phase distortion of 6×10^{-4}, $\Delta\Phi$ is always negligible.

5.2.2 Hermite-Gaussian modes

In this section, we review briefly the Hermite-Gaussian modes (see Chapters 16 and 17 of Ref. [16]) that are used as basis modes in our simulation.

A Hermite-Gaussian mode of beam waist size w_0 is given by

$$U_n(x, z) = \left(\frac{2}{\pi}\right)^{1/4}\left(\frac{1}{2^n n! w(z)}\right)^{1/2} H_n\left(\frac{\sqrt{2}x}{w(z)}\right)\exp\left(-x^2\left(\frac{1}{w(z)^2} + \frac{ik}{2R(z)}\right)\right)\exp\left(i\left(n + \frac{1}{2}\right)\eta(z)\right)\,, \tag{5.7}$$

where $H_n(x)$ is the Hermite polynomial and $R(z)$, $w(z)$, and $\eta(z)$ are the curvature radius of the phase front, the beam spot size and the Guoy phase, respectively, given in terms of the Rayleigh length $z_0 = \pi w_0^2/\lambda$ by

$$R(z) = z + \frac{z_0^2}{z}\,, \qquad w(z) = w_0\sqrt{1 + \frac{z^2}{z_0^2}}\,, \qquad \eta(z) = \tan^{-1}\left(\frac{z}{z_0}\right)\,. \tag{5.8}$$

These Hermite-Gaussian modes are exact solutions to the paraxial wave equation in one dimension, and they form a complete orthogonal basis in the solution space. We use Hermite-Gaussian modes as basis modes in the modal space

$$E(x, y, z) = \sum_{mn} a_{mn} U_m(x, z) U_n(y, z)\exp(-ikz)\,, \tag{5.9}$$

where each transverse mode is labeled by two integers (m, n) corresponding to the directions x and y. In this chapter, we consider only the five lowest-order symmetric HOMs, i.e., modes with even m and n, and $m+n \leq 4$. We omit the two $m+n = 1$ modes because they can be corrected by the tilt control system. We omit

modes with $m + n > 4$ to reduce computational cost, and because modes with higher orders are suppressed by stronger diffraction loss, their coupling to the fundamental mode is weaker when mirror deformations are smooth. Moreover, mode-coupling behaviors due to mirror deformations are qualitatively the same for all modes, and there is no need to include more modes with order $m + n > 4$ for an order of magnitude estimation. We also focus our attention on the second order ($m + n = 2$) modes since they are most likely to be the dominant deformations present in Advanced LIGO due to mirror figure error or thermal lensing, and thus are the lowest order perturbations of Hermite-Gaussian modes after mirror tilts have been suppressed by control systems.

The propagation operators for Hermite-Gaussian modes are given by Eq. (5.4), with the diffraction phases replaced by the Gouy phases of the (m, n) Hermite-Gaussian modes: $(m+n+1)\eta(z)$. The interaction operators defined in Eq. (5.5) are derived analytically for Hermite-Gaussian modes in Section 2 of Ref. [17], assuming that the mirror radius is much larger than the beam size. For the mirror deformations considered in this chapter, this approximation produces a few percent errors in the coupling strengths between optical modes (measured by components of the interaction operators). In fact, these errors are less than 10^{-3} for the coupling between the fundamental mode and the five HOMs we considered, which is the leading order effect we would like to investigate in this chapter. Only for coupling between HOMs, which is a higher-order effect in changing the SNR, does the error caused by the finite size of mirrors become as large as $1 \sim 10\%$. Also, because Gaussian modes are eigenmodes of cavities formed by spherical mirrors with infinite size, it is in fact self-consistent that we treat the mirrors as large when using Gaussian modes as eigenmodes. As long as we use eigenmodes consistent with mirror size, even if we use infinite-size mirrors, our estimates are valid up to fractional errors of order the difference between the Hermite-Gaussian modes and the true eigenmodes of the cavity with finite-size mirrors. Thus, we approximate the mirrors as having infinite sizes and use Gaussian modes throughout the chapter.

Gaussian beams have spherical phase fronts, and are thus eigenmodes of cavities formed by spherical mirrors. There are simple relations between the geometry of the cavity (measured by, e.g., cavity *g-factor*, and mirror radii of curvature) and the physical properties of the Gaussian eigenmodes (e.g., Guoy phase, beam waist size, waist position) that are available in Chapter 19 of Ref. [16].

A very useful formula relating a cavity's one-way Guoy phase η (the Guoy phase of the cavity's fundamental eigenmode) to the cavity g-factor is:

$$\eta = \arccos \sqrt{g}\,. \tag{5.10}$$

The cavity g-factor is the product of the two mirror g-factors. If the curvature radii of the two mirrors are R_1 and R_2, and the length of the cavity is L, then the mirror and cavity g-factors are defined as

$$g_i \equiv 1 - \frac{L}{R_i} \quad (i = 1, 2) \quad \text{and} \quad g \equiv g_1 g_2\,. \tag{5.11}$$

The cavity is stable (i.e., the cavity geometry supports Hermite-Gaussian modes as eigenmodes) if and only if $0 \le g \le 1$.

From Eq. (5.4), we see that it is the Guoy phase that distinguishes optical modes (modes with different $m + n$ for Hermite-Gaussian modes). If the one-way cavity Gouy phases are very close to 0 or π, the round trip phase shifts in the cavity are almost the same for all modes, so if one of the optical modes is tuned to be resonant, so are the others. Such a cavity is thus called degenerate. In terms of g-factor, a cavity is degenerate if g is very close to 0 or 1.

To conclude this section, we use the baseline design of the AC and the PRC in Advanced LIGO as examples to demonstrate quantitatively the degeneracy level of cavities. The baseline curvature radii of the PR mirror and the test masses are [11]

$$R_{\mathrm{ETM}} = R_{\mathrm{ITM}} = 2076.4\mathrm{m}\,, \qquad R_{\mathrm{ITM2}} = -1186.4\mathrm{m}\,, \qquad R_{\mathrm{PR}} = 1194.7\mathrm{m}\,, \tag{5.12}$$

where R_{ITM} and R_{ITM2} are curvature radii of the ITM seen from inside the AC and the PRC, respectively, and the ITM is convex as seen from the PRC. The cavity lengths are $d_{\mathrm{AC}} = 4000\mathrm{m}$ and $d_{\mathrm{PRC}} = 8.34\mathrm{m}$, and the Rayleigh lengths and Guoy phases are

$$z_{0\,\mathrm{AC}} = \quad 390.9\mathrm{m}\,, \qquad \eta_{\mathrm{AC}} = \quad 0.39\,, \tag{5.13}$$

$$z_{0\,\mathrm{PRC}} = \quad 82.1\mathrm{m}\,, \qquad \eta_{\mathrm{PRC}} = \quad 4.9 \times 10^{-4}\,. \tag{5.14}$$

In the AC, the Rayleigh length is clearly much shorter than the typical distance 4km that carrier light travels in the cavity, i.e., the light propagation is in the strong-diffraction zone, which indicates a nondegenerate cavity. More rigorously, the Guoy phase, corresponding to a frequency shift of

$$\Delta\nu = \frac{c}{2\pi d_{\mathrm{AC}}}\eta_{\mathrm{AC}} = 4.6\mathrm{kHz}\,, \tag{5.15}$$

is much larger than the bandwidth of the AC ($\sim 15\mathrm{Hz}$). This means, the Guoy phase breaks the degeneracy between the Gaussian modes with different orders (different $m + n$), i.e., when the cavity is tuned to have the fundamental mode in resonance, nearly all other HOMs are suppressed. Of course there are always HOMs with round trip Guoy phases (mode 2π) close to that of the fundamental mode by coincidence, but these HOMs that resonate with the fundamental mode generally have very high orders (except for very bad choices of the Guoy phase) and are thus strongly suppressed by diffraction losses.

In the PRC, the Rayleigh length is longer than the length of the cavity, but shorter than the typical distance RF sideband light travels inside the cavity after we take count of the number of round trips (~ 50). Therefore, the RF sideband propagation in the PRC is still in its strong diffraction zone. However, the frequency shift of $\Delta\nu = 2.8\mathrm{kHz}$ is much smaller than the bandwidth of the PRC ($\simeq 100\mathrm{kHz}$), and consequently the Guoy phases are close to 0 and π (mode 2π). The PRC, therefore, although not degenerate to the extreme level

that geometric optics becomes valid, accommodates tens of low-order HOMs together with the fundamental mode, and is thus highly degenerate.

Finally, through the example above, we can see that for Hermite-Gaussian modes, reducing the beam waist size w_0 (i.e., reducing Rayleigh length z_0) and/or increasing the cavity length will reduce the degeneracy of the cavity.

5.3 Advanced-LIGO interferometer modeling

In this section, we describe our simplified model of an Advanced-LIGO interferometer, and the way our simulations work.

In our simulations, we study an Advanced-LIGO interferometer in equilibrium with static optical fields. We use the standard Advanced-LIGO optical topology displayed in Fig. 5.1, and the input light is a pure (0,0) Hermite-Gaussian mode coming in from the PR mirror. We consider both broadband and narrowband interferometer designs. The interferometer parameters for the broadband detector are chosen as their values for the Advanced-LIGO baseline design. The parameters in the two designs are listed below [11, 13, 19], where we begin using the following subscripts to denote different mirrors and cavities throughout the whole chapter (see Appendix 5.7 for a list of symbols and subscripts): "bs," "i," "e," "p," and "s" stand for the beam splitter (BS), ITM, ETM, PRM, and SRM; "ac," "prc," and "src" stand for AC, PRC, and SRC.

(i) *Cavity macroscopic length*: The ACs both have $L = 4000$m; the lengths between the PRM and the two ITMs are denoted l_1 and l_2 and referred to as Michelson lengths; the lengths between the SRM and the two ITMs are denoted l_3 and l_4. It is convenient to define common and differential lengths:

$$l_{\rm prc} \equiv \frac{l_1 + l_2}{2} = 8.34{\rm m}\,, \qquad l_{\rm src} \equiv \frac{l_3 + l_4}{2} = 8.327{\rm m}\,, \tag{5.16}$$

and

$$d \equiv \frac{l_1 - l_2}{2} = \frac{l_3 - l_4}{2}\,. \tag{5.17}$$

In our model, there is no macroscopic asymmetry between the two Michelson arms. Therefore only a microscopic tuning value is assigned to d in the next paragraph.

(ii) *Cavity microscopic tuning*: The carrier light gets the following phase shifts during a single trip in the AC, PRC, and SRC:

$$\phi_{\rm ac} = \phi_{\rm pc} = 0\,, \qquad \phi^{\rm B}_{\rm src} = 0.06\,, \qquad \phi^{\rm N}_{\rm src} = \pi - 1.556\,, \tag{5.18}$$

where the superscripts on the SRC phasing denote broadband (B) and narrowband (N). An asymmetry in the Micheleson arm lengths is introduced because, among other reasons, we choose the homodyne readout scheme where a tiny amount of the carrier light power goes toward the dark port and beats with the resonant signal sideband to give the detector output. For this purpose solely, the asymmetry is specified at the micro-

scopic level as the phase difference the carrier accumulates in the two Micheleson arms: $\Delta\phi = \omega_0 d/c = 0.01$, so that about 1W of carrier power goes into the SRC.

(iii) *Mirror power transmissivity*:

$$\begin{aligned} t_{\rm i}^2 &= \quad 0.5\%\,, \qquad t_{\rm e}^2 = \quad 76\,{\rm ppm}\,, \qquad t_{\rm p}^2 = 5.9\%\,, \\ {t_{\rm s}^{\rm B}}^2 &= \quad 7\%\,, \qquad\quad {t_{\rm s}^{\rm N}}^2 = \quad 0.3\%\,. \end{aligned} \tag{5.19}$$

We assume lossless mirrors throughout our simulation, so the amplitude reflectivity and transmissivity are completely determined.

(iv) *Mirror curvature radii*: These are given in Eq. (5.12) except for the SRM. In this chapter, we will change the SRC degeneracy through the value of its Guoy phase, and assume that the geometry of the SRM always matches our choice of degeneracy. The corresponding SRM curvature radius is relevant to nothing but the SRC Guoy phase, so we do not specify it explicitly

The differences between the broadband and the narrowband designs are all in the choice of the SRM transmissivity and the SRC tuning, as we mentioned in Sec. 5.1. The complex optical-sideband resonant frequency in the coupled SRC and AC two-cavity system is given by Eq. (13) of Ref. [20]:

$$\tilde{\omega} = \frac{ic}{2L} \log \frac{r_{\rm i} + r_{\rm p} e^{2i\phi_{\rm src}}}{1 + r_{\rm i} r_{\rm p} e^{2i\phi_{\rm src}}} \equiv -\lambda_g - i\epsilon\,, \tag{5.20}$$

where λ_g and ϵ are positive and are the resonant frequency and the decay time. With our choice of signal-recycling parameters above, we get resonant sideband frequencies $\lambda_g/2\pi = 228$Hz and $\lambda_g/2\pi = 1005$Hz. The actual resonant frequency is $\omega_0 - \lambda_g$, i.e., the down-converted signal sideband. Depending on the sign of the SRC detuning, the interferometer response is of interest for only one of the two sidebands.

The PRM transmissivity and the PRC tuning are chosen such that the PRM is impedance matched to the AC and the total carrier power (summed over all optical modes) in the AC is maximized for fixed input light power.

The only interferometer control we do in simulations when mirrors are slightly deformed is to optimize the total carrier light power in the AC by adjusting the tuning of the PRC and the AC. To optimize the carrier light power in the AC, instead of modeling the control signal, we look directly at the power at each equilibrium state, i.e., we do a static pseudo-control and do not model the dynamical response of the interferometer during the control process. With our choice of interferometer parameters given above, and a 125W input light power, the carrier light power in an ideal interferometer is $\simeq$ 825kW, the power recycling factor is $\simeq$ 18, and the carrier light going toward the dark port is $\simeq$ 1W.

Since we are interested in the reduction of the signal sideband power due to mirror deformations, we consider in our simulations only the carrier light and the down-converted signal sideband, and omit the RF sideband and other sidebands used for control purposes, as well as the up-converted signal sideband, since the

interferometer is tuned to be sensitive only to the down-converted signal sideband with the best sensitivity (assuming white noise) at frequency $f_0 - \lambda_g/2\pi$. The distortion of the phase fronts also affect the control sidebands, but we are not concerned with several percent loss of the SNR of the control signals. However, there is a problem associated with tilt control signals, whose SNRs are proportional to the amplitude of the (1,0) and (0,1) Hermite-Gaussian modes excited by mirror tilts. If we choose to suppress HOMs for the signal sideband by using nondegenerate recycling cavities, the SNR of the tilt control signals entering the recycling cavities will also be strongly reduced. Correspondingly, choosing the degeneracy level of the SRC will entail compromises between inputs on the signal and control sidebands. This problem is not considered in this chapter, and is left for future investigation.

After setting up our model of an ideal interferometer, we introduce perturbations to its mirrors. We do not model thermal lensing of the mirrors. We assume that all tilts and misalignments of the mirrors are corrected by the control system. Because of the high computational cost associated with our mode decomposition method, we limit our figure errors to simple profiles so that they generate, at the leading order, coupling between only a few optical modes (≤ 6). One focus of our study is mirror curvature radius errors, which is the most interesting type of deformation, since it can be generated effectively by thermal lensing of the ITMs. We assume that the beamsplitter is perfect, because deformations of the beamsplitter introduce complicated phase-front distortions which have no qualitative difference from those introduced by other mirrors.

At the interferometer output, we assume that there is a mode cleaner that filters out all HOMs in the carrier and signal sidebands, so that the shot noise is proportional to the square root of the output carrier power in the fundamental mode [i.e., (0,0) Gaussian mode]:

$$N_{\text{shot}} \propto \sqrt{I_{00}^{C}}\,. \tag{5.21}$$

Here the superscript "C" stands for carrier, and the subscript labels the mode. The signal power comes from beating the signal sideband against the carrier, both taking only the fundamental mode, so

$$S \propto \sqrt{I_{00}^{C}}\sqrt{I_{00}^{S}}\,, \tag{5.22}$$

where the superscript "S" stands for signal sideband. Assuming shot noise dominates, we have

$$\text{SNR} \propto \sqrt{I_{00}^{S}}\,, \tag{5.23}$$

i.e., the SNR is directly proportional to the signal sideband amplitude in the fundamental mode.

When we take into account radiation-pressure noise, the change of the SNR becomes more delicate. However, since the radiation-pressure noise is determined by the total light power on the test masses, it is presumably less sensitive to the mode structure of the light. When radiation-pressure noise is important, although the loss of the SNR is not given by Eq. (5.23), that equation is still a rough measure of the loss

of the SNR. This argument applies to all other non-optical noise sources. Radiation-pressure noise is thus omitted in our simplified model, and will be studied in more sophisticated future simulations [21].

In the interferometer model described above, we calculate the signal sideband in two steps. In the first step, we propagate the input carrier light (Nd:YAG laser) with frequency $f_0 = 2.82 \times 10^{14}$Hz through the interferometer to build up the static carrier-light field. In the second step, we assume a sinusoidal gravitational wave of frequency f_g propagating perpendicular to the detector plane with only "+" polarization, i.e., effectively, it differentially shakes the ETMs sinusoidally with frequency f_g. To leading order in the GW strain, two signal sidebands of frequencies $f_0 \pm f_g$ are generated at the ETMs with exactly the same mode structures as the carrier field there. We propagate the down-converted sideband through the interferometer to build up the static signal sideband field. Repeating this second step with various GW frequencies, we map out the frequency response of the detector. Repeating both steps with various SRC geometries and levels of degeneracy, we can study the effect of the recycling-cavity degeneracy on the influence of mirror deformations on signal response and the interferometer's noise spectrum.

The EM field in the interferometer (a system of coupled optical cavities) can be written formally as

$$E = E_{\rm pump} + P_{\rm r.t.} E \,. \tag{5.24}$$

Here $E_{\rm pump}$ is the pumping field that contributes directly to the E field, and $P_{\rm r.t.}$ is the round-trip propagator, which consists of free propagation operators and interaction operators that describe the propagation of E through the interferometer and back to itself. The specific forms of $E_{\rm pump}$ and $P_{\rm r.t.}$ depend on location in the interferometer. For example, the field $E_{\rm cir1}$ in Fig. 5.1, i.e., the circulating field in the online AC at the ITM going toward the ETM, can be written as

$$E_{\rm cir1} = t_{\rm i} T_{\rm i1} E_{\rm in1} + r_{\rm i} r_{\rm e} M_{\rm i1} P_{\rm ac1} M_{\rm e1} P_{\rm ac1} E_{\rm cir1} \,, \tag{5.25}$$

where, e.g., $M_{\rm i1}$ and $T_{\rm i1}$ are reflection and transmission operators of the ITM in the online cavity, and we use subscripts "1" and "2" to denote the online and offline cavities. We can write out a set of coupled equations in the form of Eq. (5.24) for all fields labeled in Fig. 5.1, and solve them numerically by iteration, as has been done in the FFT simulation code for optical fields in LIGO [14]. In principle, we can also solve for each field in terms of the input field $E_{\rm in0}$ by directly taking the inverse of all operators of the form $(I - P_{\rm r.t.})$ (I is the identity matirx). In the FFT code, hundreds of modes are included, and it is computationally difficult to take the inverse of all the large matrices, which are sometimes nearly singular. In our simulation however, as we consider only six modes, we find it more efficient to directly invert the matrices instead of iterating the fields.

In Appendix 5.9, we write out the field coupling equations explicitly and solve for all the carrier and signal sideband fields.

5.4 Mirror figure error and optimal degeneracy

In this section, based on results of our simulations of the simplified Advanced-LIGO model set up in Sec. 5.3, we try to answer the question *how much loss of the SNR is caused by mirror deformations with various spatial modes and magnitudes, and how does this loss of the SNR depend on the degeneracy of the SR cavity?*

For mirror deformations, we consider mostly mirror curvature-radius errors. At leading order, we need only consider the (2,0) and (0,2) Hermite-Gaussian modes excited by curvature radius error.

We also consider a case in which, besides the curvature radius error, there is deformation of the SRM with higher-order spatial modes. We are interested in this case since, if the SRC is nondegenerate, the optical eigenmodes of the SRC and the coupled SRC-AC cavities under the mirror deformation are different from those of the coupled PRC-AC cavity, and there might be a substantial loss of the SNR due to the mode mismatch between the carrier light (mostly in the PRC-AC cavity) and the signal sideband light (mostly in the SRC-AC cavity). Thus we would especially like to see how the loss of the SNR depends on the degeneracy of the SR cavity in this case.

For signal sidebands, we consider mostly the resonant signal sideband with frequency $f_0 - \lambda_g/2\pi$ given by Eq. (5.20), and only at the end of this section do we consider signal sidebands with frequencies varying from 50Hz to 1000Hz.

5.4.1 Curvature radius error on the ITMs: Broadband configuration

First, we consider a broadband interferometer with curvature radius errors on the ITMs that simulate the thermal lensing effect, and we assume all other mirrors are perfect. The curvature radii of the ITMs ($R_{\rm ITM}$ = 2076.4m) are changed by $\Delta R_{\rm ITM}$ = 5m, either commonly or differentially. This curvature radius error corresponds to the following mirror figure error:

$$\Delta z(x,y) = 1.04\text{nm}\left[-1 + 2\left(\frac{x}{6\text{cm}}\right)^2 + 2\left(\frac{y}{6\text{cm}}\right)^2\right], \tag{5.26}$$

where $\Delta z(x,y)$ is the mirror surface height error, and $\Delta z(x,0)$ is show in Fig. 5.2.

We show the loss of the SNR in Fig. 5.3. With changes of the SRC degeneracy, characterized by the Guoy phase and the SRC g-factor, we see significant change in the loss of the SNR. In the baseline degenerate design, for common and differential perturbations we lose 4% and 0.4% of the SNR. Note that at leading order the SNR loss is proportional to the square of the size of the error, so we have, for instance, 4 times the above SNR losses when $\Delta R_{\rm ITM}$ = 10m instead of 5m. The bigger of these SNR losses is consistent with the estimate based on geometric optics approximation in Section IV J of Ref. [13].

Figure 5.3 shows that, when the degeneracy is reduced, the SNR loss drops by more than two orders of magnitude, making the curvature error harmless. The most striking features in the plots are the peaks corresponding to huge SNR loss at some nondegenerate SRC configuration. This happens when the Guoy

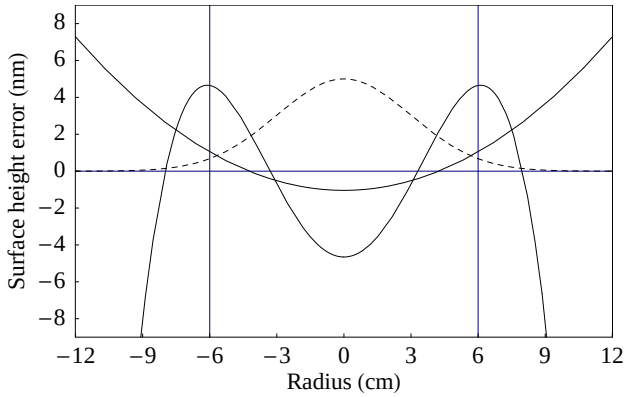

Figure 5.2: Mirror figure errors given in Eqs. (5.26) and (5.27). We show as solid curves the error Δz in units of nanometers along the x-axis [i.e., $\Delta z(x, 0)$]. The dashed curve is the power profile of the fundamental Gaussian mode plotted in arbitrary units. The beam size at the mirror is w = 6cm (c.f. Eq. (5.7)), so the variance of the power profile is σ = 3cm. The peak-to-valley figure errors inside the 2σ (6cm) region are about 2.0nm and 9.3nm for the two cases.

phase of the HOMs (in this case, (2,0) and (0,2) Hermite-Gaussian modes) cancels the SRC detuning ($\phi^{\rm B}_{\rm src}$ = 0.06 for broadband design), so that the HOMs of both the carrier and the signal light are resonant in the SRC while the fundamental modes are detuned. This is clearly a bad choice of SRC degeneracy. We refer to it as the HOM resonant peak. When more HOMs are coupled into the interferometer by perturbations, we should avoid all such cavity configurations in which some HOM (of an order not so high that it suffers strong diffraction loss) has a Guoy phase $\eta_{\rm HOM}$ that nearly cancels the SRC tuning phase.

Figure 5.4 shows the effect of the SRC degeneracy on the loss of carrier light due to differential curvature errors on the ITMs. In addition to the HOM resonant peaks discussed above, there are other noticeable features in the carrier light. In the AC, curvature errors reduce the carrier-power build-up in ways described below. When the SRC becomes nondegenerate, for common and differential curvature errors on the ITMs, the carrier and signal sideband light behaves very differently (compare Figs. 5.3 and 5.4).

For common curvature errors, the HOMs are coupled into the symmetric port of the interferometer, which is accepted by the degenerate PRC but are anti-resonant in it, so they get reflected back into the AC. Since the HOMs do not enter the SRC, its degeneracy causes no difference. In this case the carrier light power is controlled by the AC and is hardly affected by the mirror deformations, thus we do not show it. The SNR loss in this case is due directly to the coupling of signal-light HOMs to the dark port.

For differential curvature error, by contrast, the HOMs are coupled to the anti-symmetric port of the interferometer, and when the SRC is degenerate, because the carrier light is not anti-resonant in it, it behaves like "resonant carrier extraction," and sucks carrier light power out of the AC thus reducing its power build-up. When the SRC is nondegenerate, HOMs are rejected by both the SRC and the AC, and the carrier power builds up as usual in the AC in almost entirely its fundamental mode, without losing any significant power. The SNR loss in this case is due to the loss of carrier power in the AC, since the signal sideband HOMs are

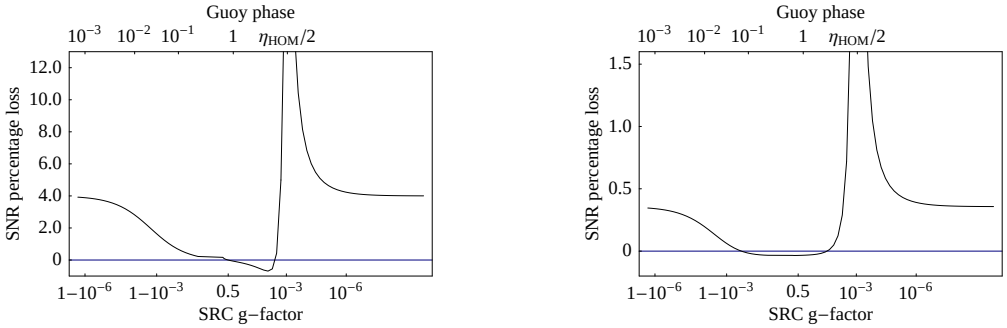

Figure 5.3: Loss of the SNR in Advanced-LIGO interferometers due to mirror curvature radius error on the ITMs, at the resonant signal sideband frequency $f_0 - \lambda/2\pi$, as a function of the SRC degeneracy level. The curvature radius of the ITMs is $R_{\rm ITM} = 2076.4$m and we consider an error $\Delta R_{\rm ITM} = 5$m, which is equivalent to the mirror surface height error given in Eq. (5.26). We consider the two cases where the curvature errors on the two ITMs are common (i.e., curvature radii are $R_{\rm ITM} - \Delta R_{\rm ITM}$) and differential (i.e., curvature radii are $R_{\rm ITM} \pm \Delta R_{\rm ITM}$), and show the loss of the SNR in the left and right panels, respectively. The horizontal axis is the level of degeneracy, measured by two quantities: the g-factor of the SRC and the one-way Guoy phase in the SRC. The horizontal position of the left-most point of the curve corresponds to the degeneracy level of the SRC in the current Advanced-LIGO baseline design.

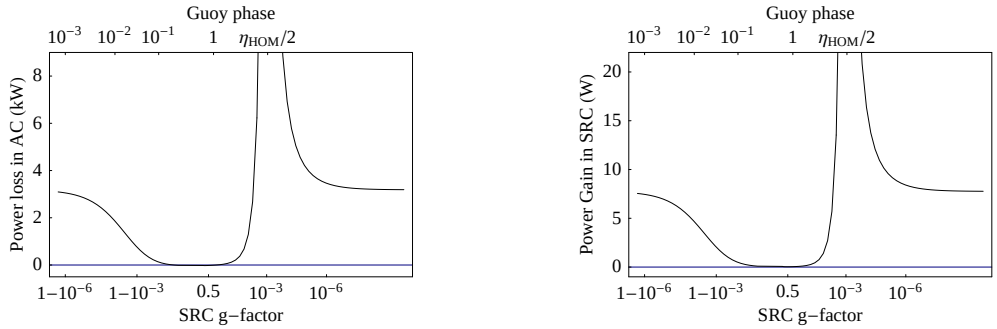

Figure 5.4: Change of the carrier light power in the AC and SRC in Advanced-LIGO interferometers due to differential mirror curvature radius error on the ITMs, as a function of SRC degeneracy. We consider the same differential curvature error as in Fig. 5.3. In the left panel, we show the loss of carrier power (all optical modes) in the AC in units of kW (the ideal AC carrier power is about 825kW); in the right panel we show the increase of the carrier power (all optical modes) in the SRC in units of W (the ideal SRC carrier power is about 1W). The horizontal axis is the level of degeneracy, measured by two quantities: the g-factor of the SRC and the one-way Guoy phase in the SRC. The horizontal position of the left-most point of the curve corresponds to the degeneracy level of the SRC in the baseline Advanced-LIGO design.

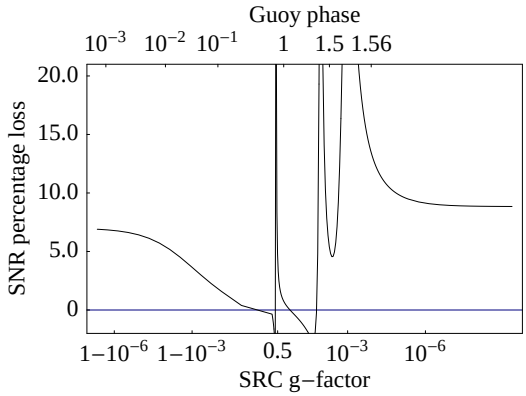

Figure 5.5: Loss of the SNR in Advanced-LIGO interferometers due to mirror curvature radius error on the ITMs and the SRM, and some higher-order mode deformation on the SRM, at the resonant signal sideband frequency $f_0 - \lambda/2\pi$, as a function of SRC degeneracy. We consider a common curvature radius error on the ITMs with $\Delta R_{\rm ITM} = 1$m, i.e., one-fifth the error considered in Fig. 5.3 and 5.4 or equivalently one-fifth the mirror surface height error given by Eq. (5.26). The mirror surface height error of the SRM is given in Eq. (5.27). The horizontal axis is the level of degeneracy, measured by two quantities: the g-factor of the SRC and the one-way Guoy phase in the SRC. The horizontal position of the left-most point of the curve corresponds to the degeneracy level of the SRC in the baseline Advanced-LIGO design.

coupled to the symmetric port and rejected by the PRC, which is not properly detuned for the signal sideband frequency.

In conclusion, common and differential errors in the ACs reduce the SNR in different ways, and the differential errors reduce the carrier build-up significantly. Finally, as indicated above by "resonant carrier extraction," the differential curvature error sends a huge amount of carrier power in HOMs toward the dark port (7.5W in HOMs and 0.3W in fundamental modes inside the SRC for $\Delta R_{\rm ITM} = 5$m), and thus sends reference light that is mostly in HOMs toward the photon detector. This HOM light must be cleaned out by an output mode cleaner.

5.4.2 Different modes of deformation on the SRM and ITMs

In this section, we consider ACs and the SRC with different modes of deformation in the SRM and ITMs. In Fig. 5.5, we show the loss of the SNR as a function of SRC degeneracy level, when there are common curvature radius errors of $\Delta R = 1$m on the ITMs, and a fourth-order polynomial deformation on the SRM with the form

$$\begin{aligned}\Delta z(x,y) &= -4.65\text{nm} + 17.94\text{nm}\left[\left(\frac{x}{6\text{cm}}\right)^2 + \left(\frac{y}{6\text{cm}}\right)^2\right] \\ &\quad -8.64\text{nm}\left[\left(\frac{x}{6\text{cm}}\right)^2 + \left(\frac{y}{6\text{cm}}\right)^2\right]^2 . \end{aligned} \tag{5.27}$$

This Δz is plotted in Fig. 5.2.

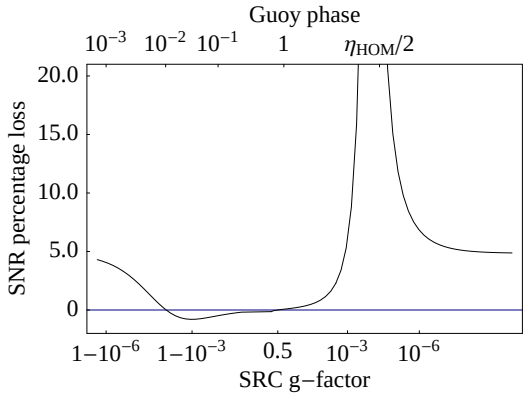

Figure 5.6: Loss of the SNR in narrowband (see Eqs. (5.18) and (5.19) for parameters) Advanced-LIGO interferometers due to common mirror curvature radius errors on the ITMs, at the resonant signal sideband frequency $f_0 - \lambda/2\pi$, as a function of SRC degeneracy. The common error of curvature radius is $\Delta R_{\rm ITM} = 2$m, i.e., two-fifth the error considered in Figs. 5.3 and 5.4 or equivalently two-fifth the mirror surface height error given in Eq. (5.26). The horizontal axis is the level of degeneracy, measured by two quantities: the g-factor of the SRC and the one-way Guoy phase in the SRC. The horizontal position of the left-most point of the curve corresponds to the degeneracy level of the SRC in the current Advanced-LIGO baseline design.

Comparing Fig. 5.5 with Fig. 5.3, we see two more HOM resonant peaks generated by the fourth-order Hermite-Gaussian modes at Guoy phase around 0.8 and 1.4 radian. We see from Fig. 5.5 that, although the optical modes in the AC and the SRC are different, and there is an eigenmode mismatch on the ITMs, the nondegenerate SRC does not simply reject the mismatched part of the signal power, and the loss of the SNR is still very low (away from the HOM resonant peaks). This is because the SRC effectively reflects the HOMs that cause the mode mismatch back into the AC and helps the fundamental mode build-up in the AC, so long as the SRC tuning for the fundamental mode resonance is unchanged. (This tuning depends on how the control system works. Modeling of the control sidebands is being considered in more sophisticated simulations that are under development, e.g., Advanced-LIGO FFT simulations [21]). More precisely, this argument is valid because the coupling of the carrier to the signal sideband happens at the ETM, outside the SRC; if it happened inside the SRC, the non-matching HOMs would be expelled and thus the signal power in the fundamental mode would be reduced.

5.4.3 Curvature radius error on the ITMs: Narrowband configuration

All examples above are simulations for the broadband Advanced-LIGO configuration, i.e., the RSE configuration, in which the signal storage time in the AC is reduced by the SRC. In the narrowband configuration, by contrast, the signal light is truly being "recycled," and the storage time in the SRC is an order of magnitude longer than in the RSE scheme, which could change our broadband-interferometer results significantly. In Fig. 5.6, we show simulation results for the narrowband configuration with differential curvature errors $\Delta R = 2$m on the ITMs. The SNR loss for the baseline degenerate SRC is about 5%, which is very significant.

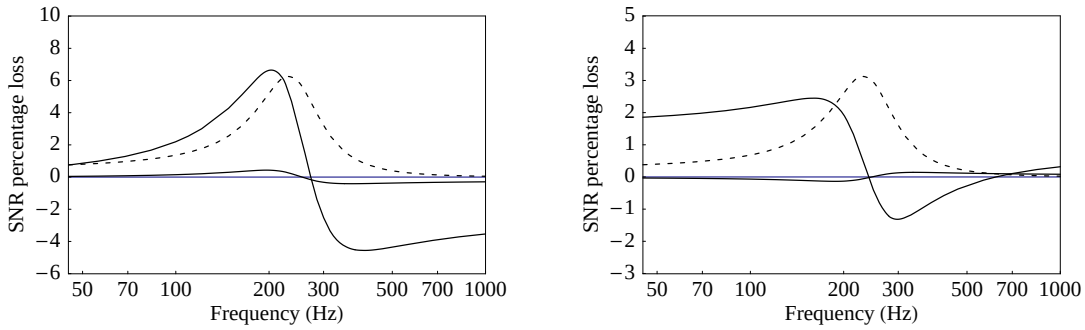

Figure 5.7: Loss of the SNR in an Advanced-LIGO interferometer due to mirror curvature radius error on the ITMs, for signal sidebands with various frequencies. The mirror curvature errors are the same as those consider in Fig. 5.3, and we show in the left and right panels the results for common and differential errors. In each case, we consider two designs of the SRC: one degenerate SRC with the Advanced-LIGO baseline design parameters, and one nondegenerate SRC with one-way Guoy phase $\eta = 0.38$ (i.e., g-factor 0.86) prescribed preliminarily in the MMT design [11]. In each plot the solid curve with larger variations shows the loss of the SNR when the degenerate SRC is used, while the solid curve with smaller variations shows the loss of the SNR when the nondegenerate SRC is used. The dashed curve, plotted in arbitrary units, shows the amplitude of the output signal sideband light in an ideal Advanced-LIGO interferometer with fixed GW strain. The maximum of the dashed curve is at the frequency $f_0 - \lambda_g/2\pi$ with λ_g given by Eq. (5.20).

In Ref. [13], the narrowband configuration also implies the most severe constraint on mirror figure errors. The SRC finesse in the narrowband configuration is much higher than in the broadband Advanced-LIGO configuration, so the HOMs being excited inside the SRC are built up to higher power, when the SRC is degenerate. As for other configurations, the loss of the SNR is reduced by orders of magnitude when the SRC is changed from degenerate to nondegenerate.

5.4.4 Optimal SRC degeneracy

From the examples above, we see that the mode mixing and consequent problems are suppressed by making the SRC nondegenerate. The optimal Guoy phase in the SRC for Hermite-Gaussian modes is the range 0.2 to 1.3 radians. In the examples above we showed the loss of the SNR only at the most sensitive signal sideband frequency [i.e., $f_0 - \lambda_g/2\pi$ given by Eq. (5.20)]. In Fig. 5.7, we show the interferometer response of various signal frequencies assuming that the SRC is either degenerate with the current design parameters or nondegenerate with the MMT design suggested by Müller [11] (the cavity Guoy phase is 0.38 radians, and thus nondegenerate). There is a strong suppression of the SNR loss across the entire Advanced-LIGO sensitive band, and a small shift of the most sensitive frequency (remember however that at low frequency $f < 100$Hz, we should also consider the radiation pressure noise).

At first sight, there seems to be a wide optimal range from which to choose the SRC degeneracy, but our freedom is actually quite limited. One obvious constraint is that we need to avoid those values of the Guoy phase that give rise to the HOM resonant peaks. In a realistic interferometer, with many more HOM

perturbations, there would be a large number of HOM resonant peaks across the optimal Guoy phase range, so the degeneracy should be chosen carefully, through careful simulations.

However, the worst difficulty posed by the above Guoy phase range is a practical one. There are two obvious ways to achieve the desired g-factor: reduce the beam size in the SRC, or increase the length of the SRC. Unfortunately, to achieve the required low degeneracy, we need either a very small beam waist size near the SRM, or a kilometers-long recycling cavity length. In the next section, we discuss the practical alternative designs of these two types.

5.5 Alternative designs

There are two obvious ways to reduce the SRC degeneracy: reduce the beam size and/or increase the optical path length. We discuss two ideas in turn.

To reduce the SRC beam size, we could add a lens in the recycling cavity; but to get a Guoy phase between 0.2 and 1.3 radians, the beam must be focused so strongly that the waist size of the beam is of order 3×10^{-5}m, and the waist location must be tuned precisely to a few millimeters away from the SRM. For a 1×10^{-5}m beam size on the SRM, we will have a 10GW/m^2 power density heating one spot on the mirror, which is too high to be practical. This problem was pointed out qualitatively by Bochner [14] in his FFT simulation work.

We can circumvent this problem by introducing multiple steps of beam focusing, i.e., bringing down the beam size step by step with more optical elements, so there is substantial Guoy phase accumulated during each step with small beam size. It is clearly preferable to use reflective optical elements in this scheme. A practical design based on moving the mode-matching telescopes (MMT) into the recycling cavities has been proposed by Müller and Wise in Ref. [11]. More specifically, the MMTs outside the recycling cavities used to match the beam size from mm scale to cm scale between the light source and the PRM, and from cm scale to mm scale between the SRM and the photo detector are moved into the cavities to reduce the beam size there. Two mirrors are used in each MMT. The first brings down the beam size from $\sim$ 6cm to millimeter scale, and the second tunes the shape of the millimeter-scale beam to achieve the desired degeneracy. Practical parameters for the PRC can be found in Ref. [11], and the coupled recycling cavities and cavities in the MMT are stable in principle. The MMT introduces more mirrors and cavities into the interferometer, and there are more control problems for the new mirrors. Experimental studies of issues about implementing this MMT design are ongoing.

Another way to reduce the SRC degeneracy is to use a longer SRC, though the length must be on the kilometer scale to achieve the necessary g-factor. A natural idea is to bend the SRC into one of the beam tubes of the ACs, and make it 4km long. This design seems to have the immediate problem of light scattering noise in the crowded arm tubes, but it does have important scientific advantages. The 4km SRC idea has been advocated for a long time, and reducing the SRC degeneracy is just one gain among other advantages.

Mizuno [6] suggested using a 4km long SRC to collect power in both signal sidebands and increase the SNR by a factor of 2. Buonanno and Chen [8], in their analysis of beating the SQL with a signal-recycled interferometer, found that the gain in peak sensitivity is vulnerable to optical losses in the short SRC, and km long SRC with fewer light bounces might solve this problem. Moreover, a long SRC introduces a frequency-dependent correlation between the two quadratures of the vacuum field, and might thereby bring interesting changes to the optical noise spectrum of the interferometer. Finally, light scattering in the beam tube may not cause any significant problems according to preliminary estimates, and more investigation of this issue is ongoing.

5.6 Conclusions

We have set up a simplified model of an Advanced-LIGO interferometer, with mirror deformations in the form of figure errors, and we have simulated the carrier and signal sideband optical fields in this model interferometer by a mode decomposition method. Using our simulations, we have investigated the loss of the SNR when SRCs with various degeneracies are used, and we have found an optimal range of SRC degeneracies that minimizes the loss of the SNR.

For the current degenerate SRC design, we found that the loss of the SNR, due to mode mixing between the fundamental mode and HOMs, is severe, and our results are consistent with the geometric optics estimates made in Ref. [13]. Assuming that the loss of the SNR scales quadratically with the size of the mirror figure error, and requiring the SNR loss due to mirror deformation to be smaller than 1%, we found a very severe constraint on the mirror deformations. In the broadband Advanced-LIGO design, If the only type of mirror deformation is curvature-radius error, this error must be smaller than 2.5m–7m on the ITMs, which corresponds to peak-to-valley figure errors smaller than 1nm–3nm in the central region of the mirrors. In reality, the mirror deformation is formed by a combination of many spatial modes, and when we consider the next lowest order spatial modes, as depicted in Eq. 5.27 and Fig. 5.2, we get a constraint $\sim$ 4nm on the SRM. In the narrowband design, the constraint on the ITMs is tightened to $\sim$ 0.4nm. Considering the fact that at leading order, the loss of the SNR grows quadratically with the size of the figure errors, and losses due to figure errors with different spatial modes are added linearly, the constraint on mirror figure errors and thermal effects is very difficult to achieve with current technology. Another minor problem we found with the baseline degenerate SRC is that, when there are differential perturbations on the ACs, a huge amount of carrier light in HOMs is coupled to the dark output port and overwhelms the fundamental-mode reference light. To remove this large HOM light at the output requires a reliable output mode cleaner.

We have shown that a nondegenerate SRC could solve this problem, by suppressing the mode mixing and reducing the loss of the SNR by orders of magnitude, in the Advanced-LIGO sensitive band. We have shown also that a nondegenerate SRC does not simply reject mode mismatched light from the AC; it also helps the fundamental mode to build up.

We propose using a nondegenerate SRC in Advanced LIGO with the one-way Guoy phase between 0.2 and 1.3 radians. There are difficulties in achieving this optimal degeneracy in practice, and we have discussed two possible alternative designs for doing so. In the first design, we move the MMT into the recycling cavities and in the second, we use a 4km long SRC.

A more complete simulation of the optical fields inside an Advanced-LIGO interferometer using FFT propagation methods is under development [21]. This will effectively include hundreds of HOMs, and will model important physical factors such as thermal effects on the mirrors, and control sideband fields. This new simulation is aimed at mapping out the phase fronts of the light in a very realistic Advanced-LIGO model, to an accuracy of $\sim 10^{-6}$. This new simulation, among other goals, will help perfect designs of SRCs with optimal degeneracy.

5.7 Appendix A: Abbreviations and symbols

There is a large number of abbreviations and symbols used in this chapter. We give a full list of them in this appendix, for easy reference.

Abbreviations:

AC	arm cavity
BS	beam-splitter
EM	electromagnetic
ETM	end test mass
FFT	fast Fourier transform
GW	gravitational wave
HOM	higher-order mode
ITM	input test mass
MMT	mode-matching telescope
PRC	power-recycling cavity
PRM	power-recycling mirror
RF	radio frequency
RSE	resonant sideband extraction
SNR	signal-to-noise ratio
SRC	signal-recycling cavity
SRM	signal-recycling mirror
TCS	thermal compensation system

Symbols:

Δz	mirror surface height error
η	Guoy phase
λ	carrier light wavelength
λ_g	resonant signal sideband frequency in the combined SRC-AC cavity
ω_0	carrier light frequency
ω_g	GW sideband frequency
ϕ_α	phase shift in cavity "α"
ϕ_h	phase shift due to GW strain
c	speed of light in vacuum
d	Michelson arm length difference
f_0	carrier light frequency
k	carrier light wave number
L	Length of arm cavity
l_α	common length of recycling cavity "α"
M_α	reflection operator of mirror "α" or of cavity "alpha" as a compound mirror; Exceptions: Michelson operators $M_{\rm C}^{\rm C}$, $M_{\rm D}^{\rm C}$, $M_{\rm C}^{\rm S}$ and $M_{\rm D}^{\rm S}$ defined in Eq. (5.36)
P_α	one-way propagator in cavity "α" or propagator of path "alpha"
r_α	amplitude transmissivity of mirror "α"
T_α	transmission operator of mirror "α"
t_α	amplitude transmissivity of mirror "α"
Z	distortion function

Superscripts:

B	broadband design
C	carrier light
N	narrowband design
S	signal sideband

Subscripts:

ac1	online arm cavity
ac2	offline arm cavity
b	beam-splitter
C	common mode in Michelson arms
D	differential mode in Michelson arms
$\pm d$	a $\pm d$ trip in one of the Michelson arms
e1	end test mass of online arm cavity
e2	end test mass of offline arm cavity
i1	input test mass of online arm cavity
i2	input test mass of offline arm cavity
p	power-recycling mirror
prc	power-recycling cavity
rt ac1	round trip in online arm cavity
rt ac2	round trip in offline arm cavity
s	signal-recycling mirror
src	signal-recycling cavity

5.8 Appendix B: Assumptions and approximations in Advanced-LIGO interferometer model

In this appendix, We list the principal assumptions and approximations adopted in our simplified Advanced-LIGO interferometer model, that are introduced and discussed in various places in the chapter:

(1) We consider only the five lowest-order HOMs and focus mostly on the two lowest-order modes, i.e., modes excited by mirror curvature-radius errors

(2) We assume the sizes of mirrors in the interferometers are large enough for diffraction losses to be negligible.

(3) We assume that the interferometer noise is dominated by the photon shot noise, and ignore radiation-pressure noise.

(4) We assume all degrees of freedom of the interferometer (cavity tuning, optical element alignment, etc.) are fixed to their ideal values as if there were no mirror deformation, except for the tuning of the PRC and the AC. The PRC and AC are tuned to maximize the total carrier light power (sum of power in all optical modes) in the AC, for fixed input light power.

(5) We include in our simulation only the carrier light and one signal sideband, without any sidebands for control purposes.

(6) We choose a microscopic asymmetry between the Michelson arm lengths that sends about 1W of

carrier power to the SRM.

(7) We assume that the beam-splitter is perfect.

(8) We adopt the short distance approximation (Sec. 5.2.1).

(9) We ignore the difference in phase shifts in the short recycling cavities between the carrier and signal sidebands.

(10) We assume that all mirrors are lossless.

5.9 Appendix C: Solving for the optical fields in the interferometer

In this appendix, we write out the explicit form of the interaction operator M in the Hermite-Gaussian modal space, and write equations in the form of Eq. (5.24) for all the carrier and signal sideband fields displayed in Fig. 5.1. We solve these equations analytically in terms of the input field $E_{\rm in0}$, the GW strain, and the propagation and interaction operators. The SNR is proportional to the fundamental mode component of the output signal sideband field $E^{\rm S}_{\rm out}$

The carrier light and the signal light have inputs at different positions (the signal input is effectively at the ETMs), so their solutions are different and have to be treated separately. In the following we will denote with superscripts "C" for carrier and "S" for signal. Furthermore, because of their different frequencies, their propagation operators have to be distinguished as well in the AC; however, for the short recycling cavities, since the fractional difference between the carrier and signal frequencies is on the order of 10^{-11}, the phase difference between carrier and signal light is negligible and we use the same SRC operators. For the same reason, the interaction operators are the same for carrier and signal light, since the perturbation effect has effectively a length scale $\sim$ 10nm.

For Hermite-Gaussian modes, the matrix element of M in the modal space is given in Ref. [17] as

$$\begin{aligned} M_{mn,kl} &= \langle mn|e^{-ikZ(x,y)}|kl\rangle \\ &= \left\langle mn\middle|\exp\Big(-ik\sum_{op,qr}|op\rangle Z_{op,qr}\langle qr|\Big)\middle|kl\right\rangle, \end{aligned} \tag{5.28}$$

where $Z_{op,qr}$ can be calculated through the following quantities:

(i) c_{ij} is given by the expansion of the distortion function $Z(x,y)$ into Hermite polynomial modes:

$$-kZ(x,y) = \sum_{i,j} c_{ij} H_i\left(\frac{\sqrt{2}x}{w(z)}\right) H_j\left(\frac{\sqrt{2}x}{w(z)}\right), \tag{5.29}$$

in which $w(z)$ is the beam size at the reference surface where the operator is defined;

(ii) $h^{ij}_{st,qr}$ is given by the expansion of Hermite polynomial products:

$$H_i(x)H_j(y)H_q(x)H_r(y) = \sum_{st} h^{ij}_{st,qr} H_s(x)H_t(y)\,. \tag{5.30}$$

(iii) $T^{ij}_{op,qr}$ is given by the integral

$$T^{ij}_{op,qr} = \langle op|H_i(x)H_j(y)|qr\rangle|_{z=0}\,, \tag{5.31}$$

which is given analytically when the mirror size is infinite as

$$T^{ij}_{op,qr} = \frac{h^{ij}_{st,qr}}{2}\sqrt{\frac{2^o o!2^p p!}{2^q q!2^r r!}}\,. \tag{5.32}$$

When the mirror size is finite, $T^{ij}_{op,qr}$ has to be calculated numerically.

(iv) $Z_{op,qr}$ is then given by:

$$Z_{op,qr} = -\frac{2}{k}\sum_{i,j} c_{ij} T^{ij}_{op,qr}\,. \tag{5.33}$$

Therefore, given $Z(x,y)$, which embodies information about the mirror distortion, and the beam size at the optical element $w(z)$, we get the representation of the operators $M_{mn,kl}$ in modal space following the steps above.

Now we turn to the optical fields. As described in Sec. 5.3, we solve for the carrier field as the first step. Using results for LIGO that have been derived in Ref. [17] and Ref. [22], and following the conventions in Sec. 5.3, we define the following.

(i) The round-trip propagator in the AC is given by

$$\begin{aligned} P^{\rm C}_{\rm rt\,ac1} &= r_{\rm i1} r_{\rm e1} M_{\rm i1} P^{\rm C}_{\rm ac1} M_{\rm e1} P^{\rm C}_{\rm ac1}\,, \\ P^{\rm C}_{\rm rt\,ac2} &= r_{\rm i2} r_{\rm e2} M_{\rm i2} P^{\rm C}_{\rm ac2} M_{\rm e2} P^{\rm C}_{\rm ac2}\,. \end{aligned} \tag{5.34}$$

again we use subscripts "1" and "2" to denote the online and offline arm cavities.

(ii) The reflection operators of the ACs (for reflecting off the AC from the ITM side) are given by

$$\begin{aligned} M^{\rm C}_{\rm ac1} &= r_{\rm i1}\left(M'_{\rm i1} - \frac{t^2_{\rm i1}}{r^2_{\rm i1}} T_{\rm i1} M^{\dagger}_{\rm i1} P^{\rm C}_{\rm rt\,ac1}(I - P^{\rm C}_{\rm rt\,ac1})^{-1} T_{\rm i1}\right)\,, \\ M^{\rm C}_{\rm ac2} &= r_{\rm i2}\left(M'_{\rm i2} - \frac{t^2_{\rm i2}}{r^2_{\rm i2}} T_{\rm i2} M^{\dagger}_{\rm i2} P^{\rm C}_{\rm rt\,ac2}(I - P^{\rm C}_{\rm rt\,ac2})^{-1} T_{\rm i2}\right)\,, \end{aligned} \tag{5.35}$$

where $M'_{\rm i1}$ and $M'_{\rm i2}$ are reflection operators of the ITMs as seen from the recycling cavity side.

(iii) The Michelson cavity operators are given by

$$\begin{aligned} M_{\rm C}^{\rm C} &= t_{\rm bs}^2 P_{\rm d}^{\rm C} M_{\rm ac1}^{\rm C} P_{\rm d}^{\rm C} + r_{\rm bs}^2 P_{\rm -d}^{\rm C} M_{\rm ac2}^{\rm C} P_{\rm -d}^{\rm C}\,, \\ M_{\rm D}^{\rm C} &= t_{\rm bs} r_{\rm bs} (P_{\rm d}^{\rm C} M_{\rm ac1}^{\rm C} P_{\rm d}^{\rm C} + P_{\rm -d}^{\rm C} M_{\rm ac2}^{\rm C} P_{\rm -d}^{\rm C})\,, \end{aligned} \tag{5.36}$$

where $P_{\rm d}^{\rm C}$ and $P_{\rm -d}^{\rm C}$ are propagators through the differential length d of the Michelson arms [Eq. (5.3)]. By combined with $P_{\rm prc}^{\rm C}$ and $P_{\rm src}^{\rm C}$, i.e., the propagators through the common lengths of the PRC ($l_{\rm prc} = 8.34$m) and SRC ($l_{\rm src} = 8.327$m), we get the propagators from the PRM to the PRM and the SRM (i.e., the "common" and "differential" mode propagators): $P_{\rm prc}^{\rm C} M_{\rm C}^{\rm C} P_{\rm prc}^{\rm C}$ and $P_{\rm src}^{\rm C} M_{\rm D}^{\rm C} P_{\rm src}^{\rm C}$.

The coupled equations for the carrier fields are then

$$\begin{aligned} E_{\rm s}^{\rm C} &= t_{\rm bs} P_{\rm prc}^{\rm C} P_{\rm d}^{\rm C} E_{\rm re1}^{\rm C} - r_{\rm bs} P_{\rm prc}^{\rm C} P_{\rm -d}^{\rm C} E_{\rm re2}^{\rm C}\,, \\ E_{\rm a}^{\rm C} &= r_{\rm bs} P_{\rm src}^{\rm C} P_{\rm d}^{\rm C} E_{\rm re1}^{\rm C} + t_{\rm bs} P_{\rm src}^{\rm C} P_{\rm -d}^{\rm C} E_{\rm re2}^{\rm C}\,, \\ E_{\rm sr}^{\rm C} &= -r_{\rm p} M_{\rm p} E_{\rm s}^{\rm C} + t_{\rm p} T_{\rm p} E_{\rm in0}\,, \\ E_{\rm ar}^{\rm C} &= -r_{\rm s} M_{\rm s} E_{\rm a}^{\rm C}\,, \\ E_{\rm in1}^{\rm C} &= t_{\rm bs} P_{\rm prc}^{\rm C} P_{\rm d}^{\rm C} E_{\rm sr}^{\rm C} + r_{\rm bs} P_{\rm src}^{\rm C} P_{\rm d}^{\rm C} E_{\rm ar}^{\rm C}\,, \\ E_{\rm in2}^{\rm C} &= -r_{\rm bs} P_{\rm prc}^{\rm C} P_{\rm -d}^{\rm C} E_{\rm sr}^{\rm C} + t_{\rm bs} P_{\rm src}^{\rm C} P_{\rm -d}^{\rm C} E_{\rm ar}^{\rm C}\,, \\ E_{\rm re1}^{\rm C} &= M_{\rm ac1}^{\rm C} E_{\rm in1}^{\rm C}\,, \\ E_{\rm re2}^{\rm C} &= M_{\rm ac2}^{\rm C} E_{\rm in2}^{\rm C}\,, \end{aligned} \tag{5.37}$$

and the circulating fields inside the AC are given in terms of $E_{\rm in1}^{\rm C}$ and $E_{\rm in2}^{\rm C}$ by

$$\begin{aligned} E_{\rm cir1}^{\rm C} &= t_{\rm i1} P_{\rm ac1}^{\rm C} \left(I - P_{\rm rt\,ac1}^{\rm C}\right)^{-1} T_{\rm i1} E_{\rm in1}^{\rm C}\,, \\ E_{\rm cir2}^{\rm C} &= t_{\rm i2} P_{\rm ac2}^{\rm C} \left(I - P_{\rm rt\,ac2}^{\rm C}\right)^{-1} T_{\rm i2} E_{\rm in2}^{\rm C}\,. \end{aligned} \tag{5.38}$$

Solving Eq. (5.37), we have

$$\begin{aligned} E_{\rm sr}^{\rm C} &= t_{\rm p}\Big(I + r_{\rm p} M_{\rm p} P_{\rm prc}^{\rm C} M_{\rm C}^{\rm C} P_{\rm prc}^{\rm C} - r_{\rm p} r_{\rm s} M_{\rm p} P_{\rm prc}^{\rm C} M_{\rm D}^{\rm C} P_{\rm src}^{\rm C} \times \left(I + r_{\rm s} M_{\rm s} P_{\rm src}^{\rm C} M_{\rm C}^{\rm C} P_{\rm src}^{\rm C}\right)^{-1} M_{\rm s} P_{\rm src}^{\rm C} M_{\rm D}^{\rm C} P_{\rm prc}^{\rm C}\Big)^{-1} T_{\rm p} E_{\rm in0}\,, \\ E_{\rm ar}^{\rm C} &= -\left(I + r_{\rm s} M_{\rm s} P_{\rm src}^{\rm C} M_{\rm C}^{\rm C} P_{\rm src}^{\rm C}\right)^{-1} r_{\rm s} M_{\rm s} P_{\rm src}^{\rm C} M_{\rm D}^{\rm C} P_{\rm prc}^{\rm C} E_{\rm sr}^{\rm C}\,. \end{aligned} \tag{5.39}$$

All other carrier fields can be easily calculated from $E_{\rm sr}^{\rm C}$ and $E_{\rm ar}^{\rm C}$.

Assuming a monochromatic GW wave passing through the interferometer and shaking the ETMs differentially with strain $h_0 \cos \omega_g t$, the carrier light that is incident on the ETMs (i.e., $E_{\rm cir1}^{\rm C}$ and $E_{\rm cir2}^{\rm C}$) is coupled to

the motion of the ETMs and generates signal sidebands at frequencies $\omega \pm \omega_g$ with the EM fields given by

$$\begin{aligned} E^{\rm S}_{\rm sig1} &= i\phi_h r_{\rm e1} M_{\rm e1} E^{\rm C}_{\rm cir1}\,, \\ E^{\rm S}_{\rm sig2} &= -i\phi_h r_{\rm e2} M_{\rm e2} E^{\rm C}_{\rm cir2}\,, \end{aligned} \tag{5.40}$$

where $\phi_h = 2kh_0L$ is the phase shift due to the GW strain. These fields are the input for the signal-light field in the interferometer.

For the signal sideband field, we define the round-trip propagator of the AC:

$$\begin{aligned} P^{\rm S}_{\rm rt\,ac1} &= r_{\rm i1} r_{\rm e1} M_{\rm e1} P^{\rm C}_{\rm ac1} M_{\rm i1} P^{\rm C}_{\rm ac1}\,, \\ P^{\rm S}_{\rm rt\,ac2} &= r_{\rm i2} r_{\rm e2} M_{\rm e2} P^{\rm C}_{\rm ac2} M_{\rm i2} P^{\rm C}_{\rm ac2}\,, \end{aligned} \tag{5.41}$$

and we define for the signal sideband the reflection operators of the ACs $M^{\rm S}_{\rm ac1}$ and $M^{\rm S}_{\rm ac2}$, and Michelson cavity operators: $M^{\rm S}_{\rm C}$ and $M^{\rm S}_{\rm D}$, in the same way as their carrier-light counterparts were defined in Eq. (5.36), but using signal sideband propagators.

The coupled equations for the signal fields are similar to Eq. (5.37); we only need to change all quantities for the carrier fields in Eq. (5.37) to their counterparts for the signal fields, and change the positions of the input fields in three of the equations:

$$\begin{aligned} E^{\rm S}_{\rm sr} &= -r_{\rm p} M_{\rm p} E^{\rm S}_{\rm s}\,, \\ E^{\rm S}_{\rm re1} &= M^{\rm S}_{\rm ac1} E^{\rm S}_{\rm in1} + t_{\rm i1} T_{\rm i1} P^{\rm S}_{\rm ac1} \left(I - P^{\rm S}_{\rm rt\,ac1}\right)^{-1} E^{\rm S}_{\rm sig1}\,, \\ E^{\rm S}_{\rm re2} &= M^{\rm S}_{\rm ac2} E^{\rm S}_{\rm in2} + t_{\rm i2} T_{\rm i2} P^{\rm S}_{\rm ac2} \left(I - P^{\rm S}_{\rm rt\,ac2}\right)^{-1} E^{\rm S}_{\rm sig2}\,. \end{aligned} \tag{5.42}$$

Solving Eq. (5.42) for $E^{\rm S}_{\rm a}$ we obtain the output signal field:

$$E^{\rm S}_{\rm out} = t_{\rm s} T_{\rm s} E^{\rm S}_{\rm a} = t_{\rm s} T_{\rm s} \left(I + r_{\rm s} P^{\rm S}_{\rm src} M^{\rm S}_{\rm C} P^{\rm S}_{\rm src} M_{\rm s}\right)^{-1} \left(-r_{\rm p} P^{\rm S}_{\rm src} M^{\rm S}_{\rm D} P^{\rm S}_{\rm prc} M_{\rm p} E^{\rm S}_{\rm s} + E^{\rm S}_{\rm siga}\right), \tag{5.43}$$

where

$$\begin{aligned} E^{\rm S}_{\rm s} &= \left(I + r_{\rm p} P^{\rm S}_{\rm prc} M^{\rm S}_{\rm C} P^{\rm S}_{\rm prc} M_{\rm p} - r_{\rm p} r_{\rm s} P^{\rm S}_{\rm prc} M^{\rm S}_{\rm D} P^{\rm S}_{\rm src} M_{\rm s} \left(I + r_{\rm s} P^{\rm S}_{\rm src} M^{\rm S}_{\rm C} P^{\rm S}_{\rm src} M_{\rm s}\right)^{-1} P^{\rm S}_{\rm src} M^{\rm S}_{\rm D} P^{\rm S}_{\rm prc} M_{\rm p}\right)^{-1} \\ &\quad \times \left(E^{\rm S}_{\rm sigs} - r_{\rm s} P^{\rm S}_{\rm prc} M^{\rm S}_{\rm D} P^{\rm S}_{\rm src} M_{\rm s} \left(I + r_{\rm s} P^{\rm S}_{\rm src} M^{\rm S}_{\rm C} P^{\rm S}_{\rm src} M_{\rm s}\right)^{-1} E^{\rm S}_{\rm siga}\right), \\ E^{\rm S}_{\rm sigs} &= t_{\rm i1} t_{\rm bs} P^{\rm S}_{\rm prc} P^{\rm S}_{\rm d} T_{\rm i1} P^{\rm S}_{\rm ac1} \left(I - P^{\rm S}_{\rm rt\,ac1}\right)^{-1} E^{\rm S}_{\rm sig1} - t_{\rm i2} r_{\rm bs} P^{\rm S}_{\rm prc} P^{\rm S}_{\rm -d} T_{\rm i2} P^{\rm S}_{\rm ac2} \left(I - P^{\rm S}_{\rm rt\,ac2}\right)^{-1} E^{\rm S}_{\rm sig2}\,, \\ E^{\rm S}_{\rm siga} &= t_{\rm i1} r_{\rm bs} P^{\rm S}_{\rm src} P^{\rm S}_{\rm d} T_{\rm i1} P^{\rm S}_{\rm ac1} \left(I - P^{\rm S}_{\rm rt\,ac1}\right)^{-1} E^{\rm S}_{\rm sig1} + t_{\rm i2} t_{\rm bs} P^{\rm S}_{\rm src} P^{\rm S}_{\rm -d} T_{\rm i2} P^{\rm S}_{\rm ac2} \left(I - P^{\rm S}_{\rm rt\,ac2}\right)^{-1} E^{\rm S}_{\rm sig2}\,. \end{aligned} \tag{5.44}$$

According to Eq. (5.23), the SNR is proportional to the amplitude of the output signal sideband field $E^{\mathrm{S}}_{\mathrm{out}}$ in the fundamental optical mode. The fractional loss of the SNR is then the fractional loss of the fundamental mode amplitude in $E^{\mathrm{S}}_{\mathrm{out}}$ when mirror deformations are introduced through the mirror reflection and transmission operators M_α and T_α.

5.10 Bibliography

[1] P. Fritshel, Proc. SPIE **4856-39**, 282 (2002).

[2] A. Abramovici et al., Science **256**, 325 (1992).

[3] J.Y. Vinet, B. Meers, C.N. Man, and A. Brillet, Phys. Rev. D **38**, 433 (1988); B. J. Meers, *ibid*. 2317 (1988).

[4] J. Mizuno, K.A. Strain, P.G. Nelson, J.M. Chen, R. Schilling, A. Rüdiger, W. Winkler, and K. Danzmann, Phys. Lett. A **175**, 273 (1993).

[5] K.S. Thorne, "The scientific case for mature LIGO interferometers" LIGO Document Number P000024-00-R, `http://www.ligo.caltech.edu/docs/P/P000024-00.pdf`; C. Cutler and K. S. Thorne, "An overview of gravitational-wave sources," gr-qc/0204090.

[6] J. Mizuno, Ph.D. thesis, Max-Planck-Institut für Quantenoptik, Garching, 1995.

[7] G. Heinzel, Ph.D. thesis, Max-Planck-Institut für Quantenoptik, Garching, 1999.

[8] A. Buonanno, and Y. Chen, Phys. Rev. D **64**, 042006 (2001).

[9] J.A. Arnaud, Appl. Opt. **8**, 189–195 (1969).

[10] R. Lawrence, Ph.D. thesis, MIT, 2003.

[11] G. Müller and S. Wise, "Mode Matching in Advanced LIGO," LIGO Document Number T020026-00-D, `http://www.ligo.caltech.edu/docs/T/T020026-00.pdf`

[12] G. Müller, private communication.

[13] E. D'Ambrosio, R. O'Shaughnessy, S. Strigin, K.S. Thorne, and S. Vyatchanin, gr-qc/0409075, Submitted to Phys. Rev. D.

[14] B. Bochner, Ph.D. thesis, MIT, 1998.

[15] Y. Chen, private communication.

[16] A.E. Siegman, *Lasers*, (University Science, Mill Valley, 1986).

[17] Y. Hefetz, N. Mavalvala, and D. Sigg, "Principles of Calculating Alignment Signals in Complex Resonant Optical Interferometers," LIGO Document Number P960024-A-D, http://www.ligo.caltech.edu/docs/P/P960024-A.pdf

[18] J. Vinet, P. Hello, C. Man, and A. Brillet, J. Phys. I France **2**, 1287 (1992).

[19] http://www.ligo.caltech.edu/advLIGO/scripts/ref_des.shtml

[20] A. Buonanno and Y. Chen, Phys. Rev. D. **67**, 062002 (2003).

[21] Y. Pan, P. Willems, and H. Yamamoto, "FFT Simulation Note 1: Formulation", LIGO Document Number T050218-00-E, http://www.ligo.caltech.edu/docs/T/T050218-00.pdf

[22] D. Sigg, "Modal Model Update 1: Interferometer Operators," LIGO Document Number T960113-00-D, http://www.ligo.caltech.edu/docs/T/T960113-00.pdf